Functional and structural methods for minimally invasive treatment of epilepsy

Document status and date:
Published: 29/03/2018

Document Version:
Publisher's PDF, also known as Version of Record (includes final page, issue and volume numbers)

Please check the document version of this publication:

• A submitted manuscript is the version of the article upon submission and before peer-review. There can be important differences between the submitted version and the official published version of record. People interested in the research are advised to contact the author for the final version of the publication, or visit the DOI to the publisher's website.
• The final author version and the galley proof are versions of the publication after peer review.
• The final published version features the final layout of the paper including the volume, issue and page numbers.

[Link to publication](#)

Functional and structural methods for minimally invasive treatment of epilepsy

Cover design by Stephan Meesters.

Functional and structural methods for
minimally invasive treatment of epilepsy

PROEFSCHRIFT

ter verkrijging van de graad van doctor aan de
Technische Universiteit Eindhoven, op gezag van de
rector magnificus, prof.dr.ir. F.P.T. Baaijens, voor een
commissie aangewezen door het College voor
Promoties in het openbaar te verdedigen
op donderdag 29 maart 2018 om 13:30 uur

door

Stephan Petrus Lambertus Meesters

geboren te Vlijmen

Dit proefschrift is goedgekeurd door de promotoren en de samenstelling van de promotiecommissie is als volgt:

Voorzitter:	prof.dr.ir. O.J. Boxma
1^e promotor:	prof.dr. L.M.J. Florack
2^e promotor:	prof.dr. P.A.J.M. Boon (Academisch Centrum voor Epileptologie Kempenhaeghe, Universitair Ziekenhuis Gent)
Co-promotor:	dr. P.P.W. Ossenblok (Academisch Centrum voor Epileptologie Kempenhaeghe)
Onafhankelijke leden:	dr. A. Vilanova Bartroli (Technische Universiteit Delft)
	prof.dr. L. Lemieux (University College London)
	dr. J.C. de Munck (VU Medisch Centrum)
Overige leden:	dr. R. Duits
	prof.dr.ir. B.M. ter Haar Romeny
Adviseur:	dr. A. Fuster

Het onderzoek of ontwerp dat in dit proefschift wordt bescreven is uitgevoerd in overeenstemming met de TU/e Gedragscode Wetenschapsbeoefening.

Abbreviations

ANT . . Anterior Nucleus of the Thalamus
CSD . . Constrained Spherical Deconvolution
CT . . . Computed Tomography
DBS . . Deep-brain stimulation
DENS . Depth Electrode Navigation Software
DIPY . . Diffusion Imaging in Python
DTI . . Diffusion Tensor Imaging
DWI . . Diffusion Weighted Imaging
ECoG . Electrocorticography
EEG . . Electroencephalography
EZ . . . Epileptogenic Zone
FBC . . Fiber to Bundle Coherence
FDR . . False Discovery Rate
FM . . . Fast Marching
fMRI . . functional Magnetic Resonance Imaging
FOD . . Fiber Orientation Distribution
GLM . . General Linear Model
HU . . . Hounsfield Unit

HARDI High Angular Resolution Diffusion Imaging
ICA . . Independent Component Analysis
IEDs . . Interictal Epileptic Discharges
LGN . . Laternal Geniculate Nucleus
MEG . . Magneto-electroencephalography
ML-TP . Meyer's Loop to Temporal Pole
MMT . . Mamillothalamic tract
MRI . . Magnetic Resonance Imaging
ODE . . Ordinary Differential Equation
OR . . . Optic Radiation
PDD . . Principal Diffusion Direction
PDE . . Partial Differential Equation
RFBC . Relative Fiber to Bundle Coherence FBC
ROI . . Region Of Interest
SEEG . . Stereoelectroencephalography
SNR . . Signal-to-Noise Ratio
SOZ . . Seizure Onset Zone
TLE . . Temporal Lobe Epilepsy
TLR . . Temporal Lobe Resection

Publications

2017   **Stephan Meesters**, Pauly Ossenblok, Albert Colon, Louis Wagner, Olaf Schijns, Paul Boon, Luc Florack and Andrea Fuster. *Modeling of intracerebral interictal epileptic discharges: evidence for network interactions. Clinical Neurophysiology.* Clinical Neurophysiology (submitted).

2017   Remco Duits*, **Stephan Meesters***, Jean-Marie Mirebeau* and Jorg Portegies*. *Optimal paths for variants of the 2D and 3D Reeds-Shepp car with applications in image analysis.* Journal of Mathematical Imaging and Vision (accepted). **(*Joint main authors)**

2017   **Stephan Meesters**, Pauly Ossenblok, Louis Wagner, Olaf Schijns, Paul Boon, Luc Florack, Anna Vilanova and Remco Duits. *Stability metrics for optic radiation tractography: Towards damage prediction after resective surgery.* Journal of Neuroscience Methods. Vol. 288, pages 34-44

2016   Shouliang Qi, **Stephan Meesters**, Klaas Nicolay, Bart M. ter Haar Romenij, and Pauly Ossenblok. *Structural brain network: What is the benefit of LiFE optimization of whole brain tractography?* Frontiers in Computational Neuroscience, 10(12)

2015   Shouliang Qi, **Stephan Meesters**, Klaas Nicolay, Bart M Ter Haar Romeny, and Pauly Ossenblok. *The influence of construction methodology on structural brain network measures: A review.* J Neurosci Methods, 253:170–182

2015   **Stephan Meesters**, Pauly Ossenblok, Albert Colon, Olaf Schijns, Luc Florack, Paul Boon, Louis Wagner, and Andrea Fuster. *Automated identification of intracranial depth electrodes in computed tomography data.* IEEE 12th International Symposium on Biomedical Imaging (ISBI), pages 976–979

2015   Jorg Portegies, Rutger Fick, Gonzalo Sanguinetti, **Stephan Meesters**, Gabriel Girard and Remco Duits. *Improving Fiber Alignment in HARDI by Combining Contextual PDE Flow with Constrained Spherical Deconvolution.* PLoS One. `https://doi.org/10.1371/journal.pone.0138122`

2015   Jorg Portegies, Gonzalo Sanguinetti, **Stephan Meesters** and Remco Duits. New approximation of a scale space kernel on SE(3) and applications in neuroimaging. Scale Space and Variational Methods in Computer Vision (5th International Conference)

2014   **Stephan Meesters**, Pauly Ossenblok, Bart ter Haar Romeny, Olaf Schijns, Louis Wagner, Paul Hofman and Anna Vilanova. *Diffusion-weighted tractography to reconstruct the optic radiation in support of temporal lobe epilepsy surgery.* Insights Imaging (2014) 5 (Suppl 1):S135–S36

Contents

Part 2: Structural methods

Chapter 1 | **Introduction**

1.1 Introduction

Epilepsy is a chronic neurological disease [66] that affects an estimated 50 million people worldwide. The incidence of epilepsy in developed countries is around 50 per 100,000 capita and in The Netherlands an estimated 180,000 people are affected [145]. Epilepsy is characterized by recurrent seizures caused by excessive or synchronous neuronal activity in the brain [66]. Seizures can occur suddenly and without warning, leading to abnormal behavior and sensations that may cause serious injury or even be life-threatening to the patient. About 70% of epilepsy patients can be treated with antiepileptic drugs [133]. However, if seizures persist despite drug treatment, or if the patient cannot tolerate the side effects of the drug treatment, then invasive treatment may be a possible solution. Focal epilepsy may be treatable by resective epilepsy surgery, which entails the removal of the epileptic tissue that causes seizures, referred to as the epileptogenic zone (EZ). In some cases, the EZ can be related to structural brain abnormalities visible at magnetic resonance imaging (MRI), for example as result of a stroke, trauma, infection, or of a genetic cortical migration disorder. If noninvasive examinations, such as MRI and video-electroencephalography (video-EEG) seizure monitoring, do not result in a single hypothesis on the EZ then the patient may become a candidate for preoperative invasive EEG recordings. The most common epilepsy syndrome with focal seizures is temporal lobe epilepsy (TLE). In Fig. 1-1 the locations of the temporal lobe (left) and the amygdala and hippocampus (right) are illustrated, which are brain structures commonly associated with medial TLE. These patients may become seizure-free after an anterior temporal lobectomy [233]. However, an adverse event such as a severe memory decline may occur, but also a visual field deficit due to disruption of the optic radiation (OR).
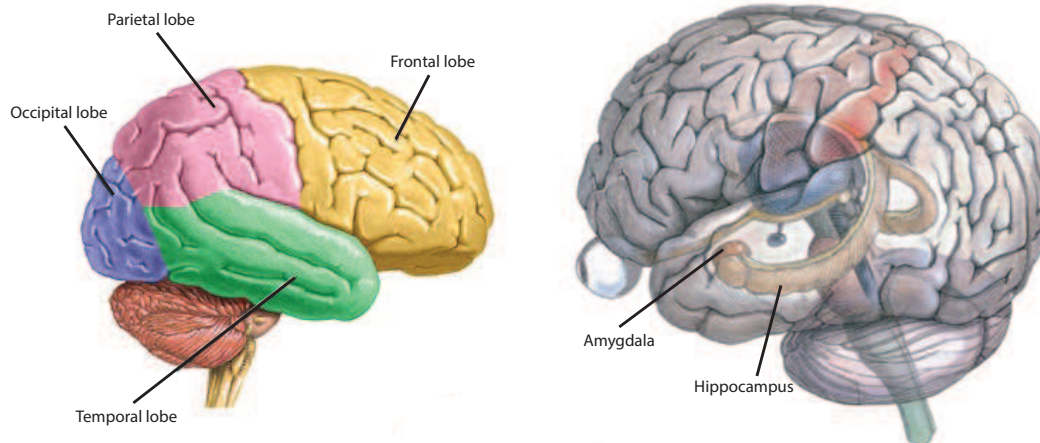
Figure 1-1: Left: The lobes of the human brain. Right: An illustration of brain structures that are commonly involved in TLE. (Images adapted from A.D.A.M.)

If the risk of functional deficits outweighs the possible benefits from surgical intervention, or in case of multiple epileptic foci, a possible alternative is deep-brain stimulation (DBS), which entails the direct application of an electrical current to cortical or subcortical brain regions [82, 110, 218]. While the precise mechanism of action remains unknown, DBS has proven to be effective in seizure inhibition by the stimulation of key brain structures that are responsible for seizure propagation [199]. One such key structure is the anterior nucleus of the thalamus (ANT) [65]. The ANT is part of the thalamo-cortical circuit, the so-called Papez circuit, which is most often involved in TLE.

Epilepsy as a network disease

In recent years it has become commonly accepted that epilepsy is a network disease [167, 219, 9, 106, 200]. Rather than analyzing local functional properties of anatomical brain regions, in a network approach the network interactions and connectivity at short and long range are emphasized [200]. Within this concept, seizures are understood to be the result of abnormal network dynamics [87]. The propagation of seizures in an epileptic network is a complex process, involving multiple distributed brain regions [10], and may involve aberrant network pathways [87]. A standard method for identifying network activity in case of epilepsy is long-term seizure monitoring based on video-EEG recording,
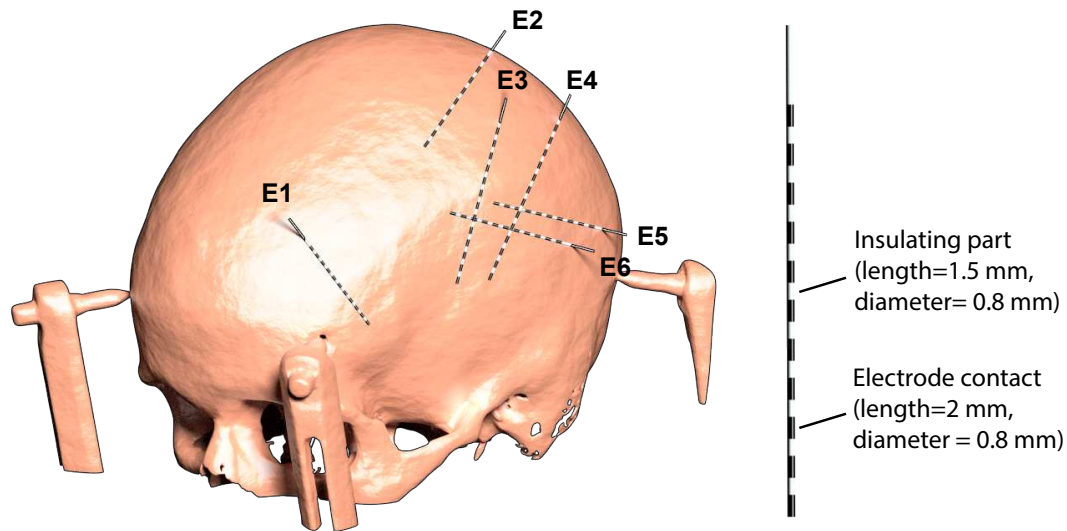
Figure 1-2: Schematic illustration of the depth electrodes used for SEEG recordings. Left: the electrodes implanted into the skull, which has a stereotactic frame attached that is used to guide the positioning of electrodes. Right: The dimensions of the electrode contacts and inter-contact insulating parts.

with as main interest the identification of the seizure onset zone (SOZ). This type of examination can be performed both with surface EEG or invasive EEG recordings. Depth electrode EEG, or stereotactic EEG (SEEG), is considered to be the best choice if there are multiple hypotheses on possible locations of the SOZ or if the epilepsy is suspected to originate in deep-sited anatomical structures [203]. SEEG involves implanting depth electrodes through small openings in the skull, which is illustrated in Fig. 1-2. There is a vast amount of literature showing that the spatiotemporal source distribution underlying interictal epileptic discharges (IEDs), i.e. discharges that may occur in the EEG in between seizures, recorded with high density EEG [204], magneto-electroencephalography (MEG) [154] or combined EEG and functional MRI (EEG-fMRI) [220], represents the origin and propagation of epileptic activity throughout a neural network. IEDs are typically of short time-duration and may occur in isolation or in brief bursts usually shorter than a few seconds. In Fig. 1-3 the typical waveforms of seizure activity (left) and IEDs (right) recorded with surface EEG are illustrated. The implantation of depth electrodes is based on the hypotheses about the location of the epileptic foci derived from long term video-EEG recording. Therefore, SEEG recordings potentially reflect the activity of the nodes of the
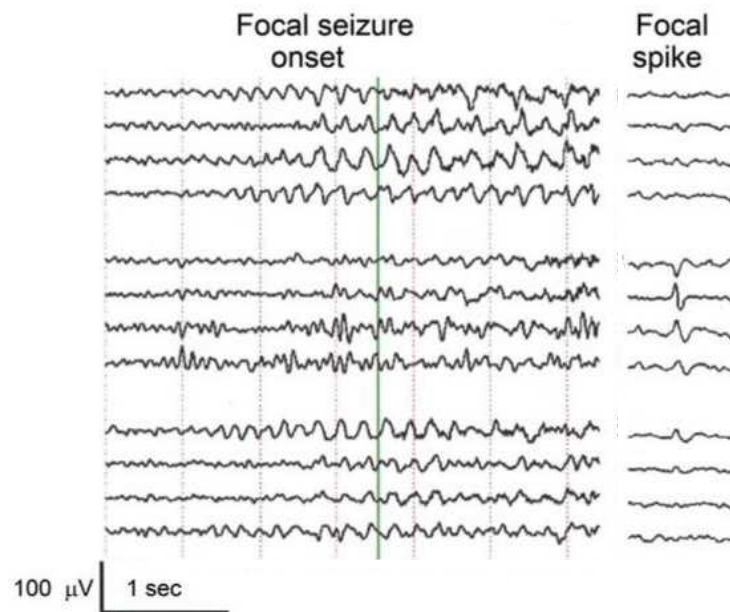
Figure 1-3: Epileptiform patterns in EEG commonly include focal spikes, generalized spikes, spike-waves, and a seizure activity. Shown at the left is seizure with a focal onset and at the right a focal spike. Figured adapted from [67].

epileptic network, what makes them, especially, suitable for studying the spatiotemporal interactions of these networks. Moreover, in several studies the correlation between IEDs and ictal discharges has been investigated [77, 45, 5, 6], yielding evidence that detailed analysis of the onset of the IEDs is indicative for the SOZ.

Apart from a functional description of network connectivity, which can be seen as the physiologic process of "communication" between brain areas, structural networks are considered the supporting hardware [219]. A structural network can be inferred from diffusion-weighted imaging (DWI), which is an MRI technique for measuring the directionality of diffusion of water molecules in the brain and can be used to reconstruct white matter pathways. Research in recent years has focused on answering the question to what extent the functional networks are constrained by structural networks [31], whether these networks are different for epilepsy patients [216, 106], and whether alterations in structural networks can be identified [22, 174].

1.2   Aim of the thesis

Recent developments of functional and structural brain imaging techniques are becoming increasingly important to guide minimally invasive surgical treatment. Resective surgery is a trade-off between removing as much epileptic tissue to render a patient seizure free, while avoiding damage to brain structures that are involved in function. The studies reported on in this thesis focus on the development of new methods, based on functional (SEEG) and structural modalities (MRI, DWI and computed tomography (CT)), for presurgical evaluation. For an introduction to the basics of these modalities the reader is referred to Appendix A.

SEEG recordings generally reflect a vast number of IEDs, which are difficult to interpret due to complex underlying network interactions. An analysis framework is developed to unravel the network interactions underlying the IEDs. However, in order to make correct physiological assumptions when reviewing the SEEG recordings, it is important to accurately locate the depth electrodes. To this end, a software package is developed to automatically detect and visualize the intracranial depth electrodes based on computed tomography (CT) images. Furthermore, it will be shown that a network approach is imperative in case of patients with complex epilepsies and is considered a valuable addition to the routine review of SEEG recordings, with the potential to increase the success rate of epilepsy surgery. For the development of new methods based on SEEG as a functional modality, the following research questions are posed:

- Can we automatically detect and visualize depth electrodes?
- Can we model the network interactions underlying IEDs?

In order to minimize the risk of functional deficits as result of anterior temporal lobe resection, a framework is developed for the robust reconstruction of the OR. The OR is a white matter structure that facilitates vision, which can be reconstructed using diffusion-weighted tractography by generating streamlines between the thalamus and the visual

cortex. However, results of tractography often reflect spurious (aberrant) streamlines, which hinder an accurate distance measurement between the temporal pole and the tip of the OR, which is crucial for temporal lobe resective surgery. Tractometry measures are introduced to quantitatively measure the alignment of streamlines and to identify and remove spurious streamlines.

In order to be able to estimate the connectivity strength of white matter pathways, a connectivity measure for structural networks is developed. Estimating structural network connectivity using DWI is generally done by counting the number of streamlines that connect two brain regions. However, streamline counting is considered a controversial method [96] because there is a strong dependence on the type of tractography algorithm used and tractography in general suffers from biasing effects due to length, curvature and branching [94, 74]. To quantitatively estimate a measure of connectivity, a new method is introduced based on the anisotropic fast marching (FM) algorithm, which enables the computation of a shortest distance, or geodesic, distance map that inherently reflects connectivity. Experiments on artificial datasets demonstrate its potential as an alternative to tractography for measuring structural connectivity. Preliminary results are discussed of the estimation of structural connectivity of the Papez circuit, which is mainly of interest in relation with alternative treatments for epilepsy, such as DBS. Regarding the development of methods based on a structural modality, the following research questions are posed:

- Can we robustly reconstruct the OR in support of resective epilepsy surgery?
- Can we provide a quantitative measure of structural connectivity?

1.3   Outline

This thesis consists of two parts and details the methodologies developed on basis of functional modalities (Chapters 2 and 3) and structural modalities (Chapters 4 to 7).

In Chapter 2 an algorithm is introduced to automatically detect the implanted intracranial depth electrodes based on CT images. A software package is developed for the visualization of the detected depth electrodes relative to brain anatomy. Chapter 3 focuses on the framework for SEEG signal analysis to model the network interactions underlying the IEDs.

In Chapter 4 an introduction is given of methods for modeling DWI data, via tensors or higher-order models, and of the basic principles of tractography. Furthermore, in this chapter new methods are introduced for the denoising of DWI-derived modeling results and for the reduction of false positive streamlines. These methods are implemented in Diffusion Imaging in Python (DIPY) [73] and are described with code examples. In Chapter 5 the newly developed methodology for structural analysis is applied for a robust reconstruction of the OR in support of resective epilepsy surgery. The estimation of structural connectivity using FM is detailed in Chapter 6, while in Chapter 7 future prospects are discussed for applying these techniques to study the thalamocortical connections that may be involved in TLE. An introduction to the basics of structural and functional modalities, namely EEG, SEEG, MRI and CT, is given in Appendix A. In Appendix B details regarding the formal mathematical notation of the space of positions and orientations are given.

Part 1

Functional methods

Stereoelectroencephalography

Chapter 2 | Detection of intracranial depth electrodes

Knowledge of the exact location of intracranial depth electrodes is important in order to properly interpret the EEG in relation to the anatomy. For the fast and accurate identification of the position of these electrodes, a procedure has been developed for the automatic detection in computed tomography data. Depth electrode navigation software is developed to visualize the detected electrodes relative to the anatomy, using 2D and 3D viewports.

Chapter based on:

Meesters, S., Ossenblok, P., Colon, A., Schijns, O., Florack, L., Boon, P., Wagner, L., and Fuster, A. (2015). Automated identification of intracranial depth electrodes in computed tomography data. In Biomedical Imaging (ISBI), 2015 IEEE 12th International Symposium on, pages 976–979

2.1 Introduction

Intracranial depth electrode placement is a common procedure to identify brain areas that are responsible for epileptic seizures, i.e. the epileptogenic zone (EZ). Intracranial depth electrodes are implanted upon hypotheses of the locations of one or multiple EZ regions according to prior measurements such as non-invasive electroencephalography (EEG) examinations and magnetic resonance imaging (MRI).

The actual position of the depth electrodes may differ from the initially planned position and may thus result in inappropriate physiologic and anatomical assumptions about the EZ. The position of implanted depth electrodes is usually estimated visually using post-implant computed tomography (CT) or MRI, which is time consuming. Computer-assisted detection of depth electrodes can aid the neurologist in this task and provide benefits in terms of speed and accuracy. In this chapter, a method for automatic identification of depth electrodes in CT images is introduced. A problem commonly encountered in CT images of patients with intracerebral depth electrodes is metal streak artifacts due to scattering of the photons against the metal surfaces of the electrode. The proposed algorithm for depth electrode detection is designed to be insensitive to these artifacts. The detection results of depth electrode implantation locations are compared against visual inspection by neurologists of the Academic Center of Epileptology Kempenhaeghe. Furthermore, a software tool is developed to support the physician by providing interactive 2D and 3D visualizations of the detected electrodes in relation to the brain anatomy seen in MRI.

2.2 Materials and methods

2.2.1 Data acquisition and preprocessing

The procedure for the detection of depth electrodes was applied on the data of eight patients (N=8) who were candidates for epilepsy surgery and underwent pre-operative depth

electrode recording. Each patient had platinum depth electrodes (DIXI medical, Besançon, France) implanted in suspected EZs. These electrodes have 5 to 18 contact areas with a diameter of 0.8 mm and a length of 2 mm, spaced 1.5 mm apart. Post-implantation CT images were acquired with a spatial resolution of $0.47{\times}0.47{\times}1$ mm^3 and $512{\times}512{\times}164$ matrix. The contact points cause characteristic artifacts, such as those shown in Fig. 2-1b. Furthermore, T1-weighted scans were performed using a 3 Tesla MR scanner (Achieva, Philips Health Care, Best, The Netherlands) before and after electrode implantation with a spatial resolution of 1 mm^3 isotropic, TE = 3.7 ms, TR = 8.1 ms and a field-of-view of $16{\times}24.4{\times}24.4$ mm. The patient data was acquired according to clinical procedures and was collected retrospectively. Each patient signed a statement that there was no a-priori objection against the anonymous use of his or her clinical data for scientific research.

The preprocessing involves resampling the CT images to an isotropic spatial resolution of 1 mm^3 in order to match the resolution of the MR images. Subsequently, the MRI datasets are coregistered to the CT dataset using the *FLIRT* function in FMRIB Software Library v5.0 (FSL) [91]. Optimal settings for MRI-to-CT registration were investigated by

(a)   (b)
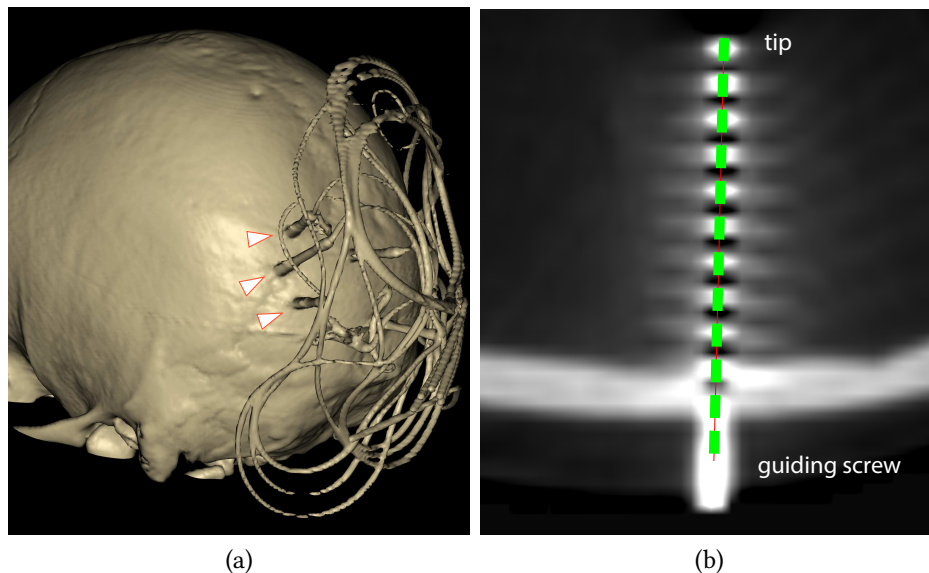
Figure 2-1: (a) Depth electrode guiding screws and attached wires. (b) Metal scattering artifacts showing high intensity near the contact areas and attenuation at the inter-contact areas. The green line indicates the localization of the depth electrode, corresponding to each contact point.

Rooijen [222] and were adopted in this study. Brain extraction is performed on the pre-implantation MRI dataset using the *BET* function [197] of FSL. *BET* is also used to remove electrode cables from the CT data, such as those depicted in Fig. 2-1a.

2.2.2 Depth electrode detection algorithm

The algorithm is divided into the three steps detailed below.

i. Line structure filter to detect guiding screws

The initial step in automatic identification of depth electrodes is the detection of the surgically implanted guiding screws, fixed to the skull, that are used to lead and hold the intracerebral electrodes (Fig. 2-1a). These screws are tubular structures which can be extracted using the 3D multi-scale filter proposed by Sato et al. [185]. The filter is available in the Insight Segmentation and Registration Toolkit (ITK) [243]. For each voxel in the CT volume, the eigenvalues of the 3x3 Hessian matrix are computed such that $\lambda_1 \geq \lambda_2 \geq \lambda_3$. The Hessian matrix is composed of second-order Gaussian derivatives of image intensity at scale σ. This scale parameter allows for the enhancement of line structures of variable width. Voxels which satisfy the requirements corresponding to a line structure are enhanced, characterized by $\lambda_1 \simeq 0$ and $\lambda_2 \simeq \lambda_3 \ll 0$. The similarity to a bright line structure is computed for each voxel according to the vesselness intensity value $L = f(\lambda_1, \lambda_2) \cdot \lambda_2$ where the function f is given by

$$
f(\lambda_1, \lambda_2) = \begin{cases}
-e^{-\frac{\lambda_1^2}{2(\alpha_1 \lambda_2)^2}} & \lambda_1 \leq 0, \lambda_2 \neq 0 \\[2mm]
-e^{-\frac{\lambda_1^2}{2(\alpha_2 \lambda_2)^2}} & \lambda_1 > 0, \lambda_2 \neq 0 \\[2mm]
0 & \lambda_2 = 0
\end{cases}
\tag{2.1}
$$

with the additional requirement that $\alpha_2 = 5\alpha_1$. This constraint is empirically chosen such that the line structures are enhanced anisotropically, which appeared to be suitable for the detection of guiding screws in CT data.
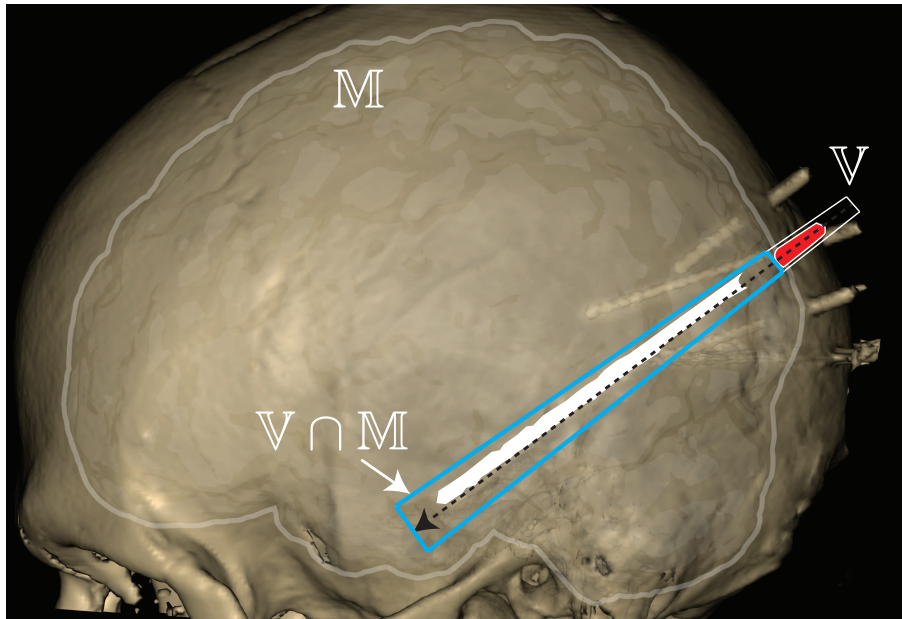
Figure 2-2: Three regions used in the optimization algorithm are shown: the depth electrode search region $\mathbb{V}$, the brain mask region $\mathbb{M}$ and the intersection of both regions (marked in blue) $\mathbb{V} \cap \mathbb{M}$. The red shape is a guiding screw and the white shape a depth electrode. The arrow indicates the detected orientation.

ii. Labeling and axis detection of guiding screws

The resulting image with enhanced line structures is binarized by thresholding at 50% of the maximum voxel intensity. Subsequently, connected component labeling is applied in order to segregate the largest components which most likely correspond to the guiding screws from smaller components that may arise from noise. Components with a summed intensity below 5% of the maximum summed intensity are assumed to be noise and removed. Geometric properties of each component are computed such as volume, centroid location and the orientations given by the principal axes of inertia [158]. Since the number N of implanted depth electrodes is known, the N largest components will in most cases correspond to all guiding screws.

iii. Determine the most likely tip location for each depth electrode

The procedure for detection provides an initial location and orientation for each depth electrode. The next step is to locate the tip of each depth electrode relative to the anatomy.

To this end, a novel optimization algorithm is proposed that samples the original CT image intensity $u\colon \mathbb{R}^3 \to \mathbb{R}$ inside the region in which it is expected that the tip of the depth electrode can be found. This region is defined as the set of coordinates $\mathbb{V}$ and is cone shaped (Fig. 2-2) such that it can incorporate uncertainty in the orientation. A local coordinate frame is defined with the origin $\mathbf{O}$ at the centroid of the component and the axes aligned along the principal axes of inertia $\mathbf{v}_1, \mathbf{v}_2, \mathbf{v}_3$. The optimization algorithm considers each voxel in $\mathbb{V}$ and favors long distances from the origin, such that the search does not prematurely end in regions of low intensity, e.g. due to artifacts. The algorithm optimizes the integrated intensity along the line from $\mathbf{O}$ to the tentative end point. This allows the algorithm to traverse through regions of artifacts while preventing it from overshooting beyond the actual end point. In CT data, the Hounsfield unit (HU) corresponds to radiodensity and has typical values for different types of tissues and materials (e.g. >1000 HU for metal and -1000 HU for air). Since artifacts may lead to inconsistencies in HU values, a safe value of 500 is used as a threshold between air and metal. Voxels below this value are assigned the HU value corresponding to air, which makes these regions unfavorable to traverse. Since the end point is known to be located in brain tissue, a brain mask denoted by $\mathbb{M}$ is used which was obtained from the brain-extracted MR image. The total region in which the end point is searched for is the set intersection $(\mathbb{V} \cap \mathbb{M}) \subset \mathbb{R}^3$. The optimization algorithm is defined to maximize the distance and integrated intensity for the end point vector $\mathbf{x}$ inside the region $\mathbb{V} \cap \mathbb{M}$, i.e. the vector $\mathbf{x}$ that maximizes U, as follows

$$U = \max_{\mathbf{x} \in \mathbb{V} \cap \mathbb{M}} \int_C H(\mathbf{s})ds, \tag{2.2}$$

where C is the straight line segment between the origin $\mathbf{O}$ and the tentative end point $\mathbf{x}$, $\mathbf{s}$ is the position vector and the function H incorporates the penalty for traversing regions of low intensity according to

$$H(\mathbf{s}) = \begin{cases} u(\mathbf{s}) & \text{if } u(\mathbf{s}) \geq 500 \\ -1000 & \text{otherwise.} \end{cases} \tag{2.3}$$

The algorithm is initially run with scale $\sigma = 1$ for the line structure filter. In case not all electrodes are detected, higher values for σ are used (e.g. $\sigma = 2$ or $\sigma = 2.5$).

2.2.3 Visualization

The depth electrode navigation software (DENS) has been developed to enable the physician to assess the positioning of the electrodes in relation to the anatomy. This tool provides automatic detection of depth electrodes, by use of the algorithm outlined in this chapter, and offers visualization of electrodes on top of the underlying anatomy. The electrodes are visualized together with the post-implantation CT (3D skull reconstruction) and pre-implantation MRI. An example visualization is shown in Fig. 2-3a, which displays the depth electrodes, the pre-implantation MRI, and the skull in 2D and/or 3D viewports (render windows). Figure 2-3b shows the verification of an electrode placed in the hippocampus. A novel method of interaction is introduced, allowing the user to slide an orthogonal plane showing an MRI slice along the depth electrode for interactive inspection, as shown in Fig 2-3b. As a result, the position of the contact points of the electrodes can be evaluated, and corrected if necessary (see Fig. 2-1b), interactively in a 3D viewport in relation to the anatomy.
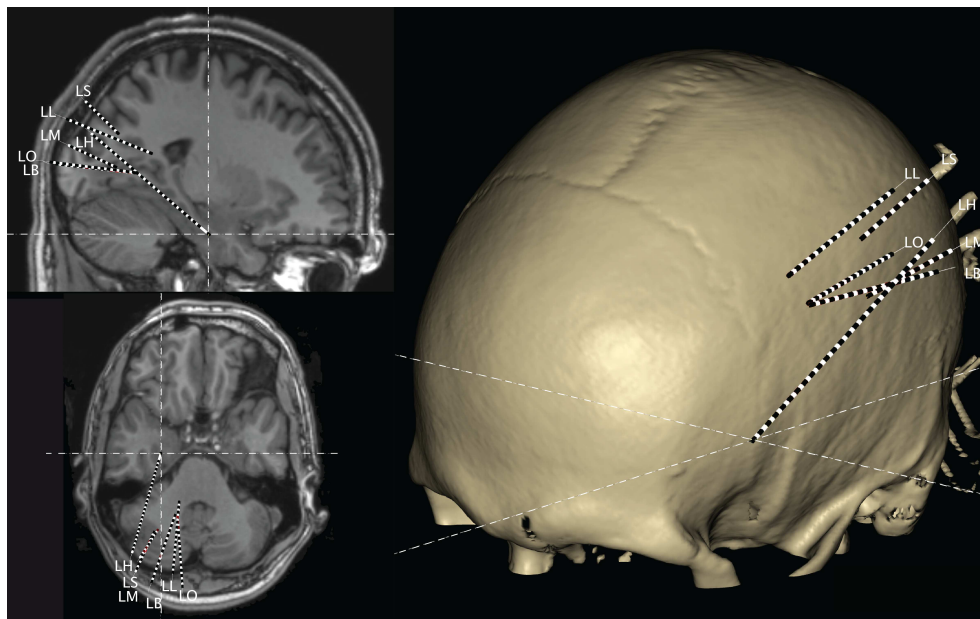
(a)
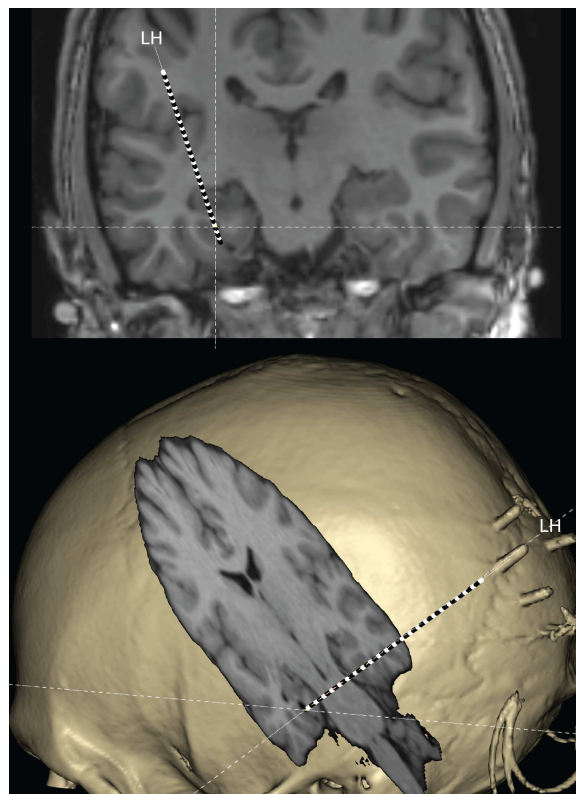
(b)

Figure 2-3: (a) Visualization of the detected depth electrodes, shown together with pre-implantation MR images in sagittal (top-left) and axial (bottom-left) views. 3D visualization with a surface rendering of the skull in CT data is shown on the right. (b) The LH depth electrode is verified to be inside the left hippocampus. The electrode is shown in pre-implantation MRI (top) and in post-implantation CT and MRI (bottom).

DENS provides an easy-to-use workflow that focuses on visualization of implanted depth electrodes. In Fig. 2-4 the user dialog is shown for the pre-processing of data, which requires the specification of a working directory, and the paths to CT and MR image data files. The minimal input required to run the electrode detection algorithm is the post-implantation CT image. However, for optimal results the user should specify an MRI image, since this is used for the generation of the brain mask region $\mathbb{M}$ (see Fig. 2-2) and is applied to reduce the number of false-positive electrodes detected. After the detection is completed, the user can manipulate the depth electrode positioning manually, and change the name of the depth electrodes, using the menu bar on the right, shown in Fig. 2-5. Several options for visualization style are available, such as hiding or showing the skull and cortex surface and changing the opacity, brightness and contrast of the anatomical image. The user can save the results in a project file for later use.

The software tool is written in C++ and based on the following libraries: Visualization Toolkit (VTK) [187] for visualization of medical images and 3D surfaces; Insight Segmentation and Registration Toolkit (ITK) [243] for computations within the depth electrode detection algorithm; and the Qt Development Kit (Nokia, Espoo, Finland), which facilitates the user interface. The depth electrode contact points are rendered as geometric primitives and labeled by a text field. A 3D surface of the skull and of the cortex outer layer is obtained through isosurface generation [119].
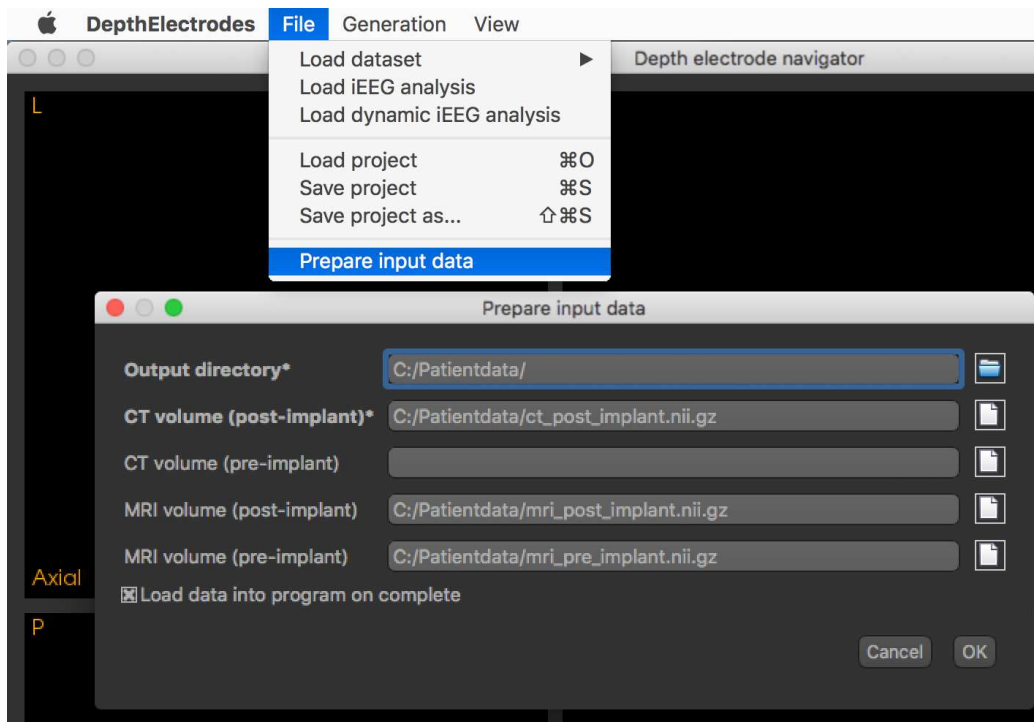
Figure 2-4: Interface for the pre-processing of medical image data. The user is required to specify a project directory and the paths to medical image files.
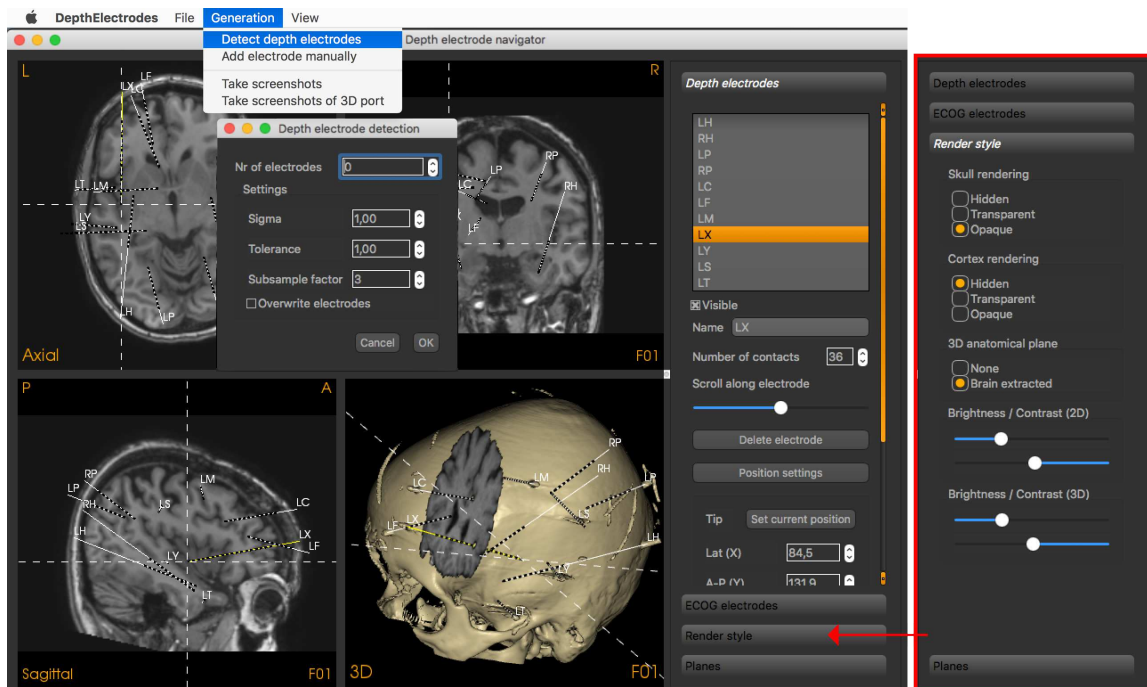
Figure 2-5: Visualization of depth electrodes after automatic detection by use of the 'Detect depth electrodes' dialog. The user can alter the depth electrodes' name, positioning and visualization style by the menu bar on the right.

2.3   Results

The algorithm to detect the depth electrodes was evaluated for 8 patients who were candidates for epilepsy surgery. The automatic detection algorithm was able to find 68 out of the total of 69 electrodes. Two false positives occurred, which required manual deletion. The detection algorithm performed independently of the location or orientation of the depth electrodes. The accuracy of the localization of the depth electrodes is evaluated based on the position of the guiding screw and the tip relative to the anatomy. To this end, the deviation was measured between the automatically obtained position and the manually placed position (see Fig. 2-1b). The average deviation between the detected tip locations and the manually verified locations was 1.2 ± 0.5 mm. Seven outliers with a high deviation (6.4 ± 2.7 mm, maximally 11 mm) related to electrodes, which were affected by metal artifacts. In three cases a correction of the guiding screw location was necessary of maximally 0.9 mm. The average time needed for detection per patient was 5 minutes for data preprocessing, 10 seconds for automatic depth electrode detection, and 30 seconds up to several minutes per depth electrode for manual adjustment.

2.4   Discussion

A software tool called DENS has been developed for the automatic identification and visualization of depth electrodes. By doing so, this software tool distinguishes itself from a software package such as EpiNav™ (CMIC, UCL, London, UK) [148] that is aimed at epilepsy surgery planning and provides advanced visualization, but requires a manual specification of post-implantation depth electrodes. The automatic identification was shown to be successful even in case of a heterogeneous distribution of the depth electrodes throughout the brain. DENS provides an easy-to-use workflow that focuses on visualization of implanted depth electrodes. It has been shown that the algorithm was able to find the electrodes accurately and within a clinically acceptable time frame. Several depth electrodes appeared to be curved rather than straight, leading to mislocalization. In

one case, the curvature was caused during surgery by pushing the electrode against the falx cerebri, which is a membrane that separates the left and right cerebral hemispheres. In other cases the curvature was caused by brain shift during surgical intervention. Furthermore, several depth electrodes were implanted close to the os petrosum, which is part of the temporal bone at the base of the skull, causing the tip location to be estimated slightly within the skull. However, using DENS, it is possible to manually adjust the locations of the base (the guiding screw centroid) and the end tip by reference of the images from post-implantation CT or post-operative MRI.

The current work has focused on detecting depth electrodes based on CT images. Detecting the depth electrodes in a post-implantation MR image may be possible [222]. However, the contrast between depth electrodes and brain tissue is significantly lower when compared to the post-implantation CT image, and the anatomy may be distorted due to metal artifacts.

It is crucial to plan the trajectories such that critical neurovascular structures are avoided. To determine the safest trajectories, computer-aided planning can be employed such as the pipeline by Nowell et al. [148, 149], which uses 3D multimodality image integration. Multiple techniques exist for the surgical implantation of depth electrodes: the stereotactic (frame-based) method [203]; the frameless method [147]; or a robotic trajectory guidance system [75]. The actual location of implantation may differ from the initially planned location depending on the accuracy of the method used with a deviation in the order of 2 to 3 mm [217]. It is expected that the accuracy of depth electrode implantation will improve over time, e.g. with the advent of intra-operative CT [109], which can aid in achieving a higher success rate for implanting a depth electrode in the EZ. Future work will focus on estimating the accuracy relative to each depth electrode contact point instead of at the guiding screw and tip locations, including in particular the ability to adjust for curved depth electrodes, which may be achieved by including a curvature term inside the optimization algorithm. The algorithms developed for depth electrode detection and visualization might also be suitable for detection of electrodes implanted for deep brain stimulation.

Chapter 3 | Modeling of intracerebral interictal epileptic discharges

Intracerebral EEG recordings are considered to be the best choice for preoperative invasive evaluation when the epilepsy of the patient is suspected to originate in deep-sited anatomical structures. The interictal epileptic discharges occurring in these recordings are in general abundant compared to ictal discharges, but difficult to interpret due to complex underlying network interactions. In the current study an analysis framework is developed to model these network interactions.

3.1   Introduction

The clinical assessment of stereoelectroencephalography (SEEG) recordings is primarily aimed at identifying the brain area that is responsible for the seizures of the patient, referred to as the seizure onset zone (SOZ). Knowledge of the location of the SOZ and its relation to functional areas, as well as seizure propagation pathways, is crucial for the surgical treatment of drug-resistant epilepsy patients [13]. In a recent review Bartolomei et al. [10] outlined the concept of the epileptogenic network and the contribution of SEEG signal analysis to this concept, which is mainly based on the analysis of the spatiotemporal dynamics of multiple brain areas involved in the epileptogenic process. Wendling, Bartolomei and coworkers [230, 12, 229] used non-linear correlation methods to characterize the dynamic interactions between neural populations involved in the epileptogenic network, including time delays and directionality of these couplings. The correlation coefficient h^2, introduced by Pijn and Lopes da Silva [166, 41] and further elaborated on by Kalitzin et al. [99], estimates the non-linear relationship between signals. Similarly to Wendling, Bartolomei and coworkers [230, 12, 229] in this study the correlation coefficient h^2 is used to estimate the coupling strength. However, a shortcoming of the estimation of time delays based on a time-varying correlation function is that its results may exhibit large variations that are physiologically implausible [221]. Therefore, to overcome this problem, in this study a regularization procedure is introduced to avoid large variations in the time delay estimated between spatially neighboring signals.

The non-linear correlation studies of couplings between neural populations were mainly introduced for the analysis of seizure activity. However, SEEG recordings also reflect a vast amount of interictal epileptic discharges (IEDs) [196], which are in general abundant compared to ictal discharges. Several methods to analyze interictal activity in SEEG recordings have been reported. The first attempts involved basic techniques such as spectral analysis and linear cross correlation [2]. Later studies [28, 231] investigated which brain structures frequently co-activated during the evolvement of IEDs. Amini et al. [3] used the linear wavelet cross-correlation coefficient as a coupling measure and estimated

leading brain areas based on time delays. More recently, Bartolemei et al. [11] identified the irritative zone (the region which initiates the IEDs) by calculating the spike frequency index (SI) for each brain area involved in the IEDs occurring in SEEG recordings. The SI demonstrated a 75% concordance of the irritative zone and the SOZ in case of cortical dysplasia and 56% concordance in all other cases studied (N=32). The conclusion of the authors was that when the IEDs arise from complex network interactions the spike frequency index probably is not a suitable descriptor to identify the SOZ.

In this study a network analysis approach is followed to identify the spatiotemporal interactions of the neuronal populations involved in the IEDs. The time-varying correlation estimated by the non-linear correlation coefficient h^2 is used together with the IED density function as input in the general linear model (GLM) [221]. The output of the GLM indicates the brain areas with SEEG signals that are highly synchronized compared to background activity during the evolvement of the IEDs. To investigate the interdependency of these areas, independent component analysis (ICA) is applied followed by a clustering of its resulting spatial distributions. The averaged spike clusters yield information about the spatiotemporal interactions and the directionality of the interactions, indicating which of the brain areas involved might be related to the SOZ.

The framework of analysis developed in this study was evaluated for five patients who underwent successful surgery. The result of the quantitative analysis of the IEDs of these patients was compared to the SOZ as identified by visual review and the resection that rendered the patient seizure free. Additionally, the analysis was performed for two so-called 'failures', patients for whom the clinical hypothesis based on SEEG recordings did not lead to a satisfactory surgical outcome. The analysis approach as introduced in this study appears to be, especially, suitable to unravel the complex network interactions underlying the IEDs of these patients. Overall, it will be shown that our approach offers the perspective of analyzing interictal SEEG recordings for presurgical evaluation, with the potential to increase the success rate of surgical intervention.

3.2 Materials and methods

3.2.1 Patients and electroclinical details

The analysis framework was applied on SEEG recordings of seven patients (N=7) with drug-resistant epilepsy (see for patient characteristics Table 3.1). Extensive pre-surgical assessment was performed at the Academic Center for Epileptology, location Kempenhaeghe (Heeze, The Netherlands), including long-term video-EEG monitoring and an epilepsy protocol for 3T magnetic resonance imaging (MRI) measurements to study the presence of anatomical abnormalities (Table 3.1, column 3). The electro-clinical hypotheses (Table 3.1, column 4) guided the placement of the depth electrodes. The resection strategy was determined according to the hypothesis of the SOZ (Table 3.1, column 5), which was based on the standard review of the SEEG recordings. Five of the seven patients included in this study were seizure-free after surgery or had a satisfactory seizure reduction (Engel class 1&2). The follow-up period for seizure assessment was one year. For these five patients there were abnormalities visible at MRI. Further details of these patients can be found in Van Houdt et al. [221], who compared the results of EEG-correlated functional MRI (fMRI) analysis to the SEEG recordings of these five patients. The other two patients were diagnosed with an MRI-negative epilepsy and were not seizure free after operation (Engel 3&4). The patient data were acquired solely according to clinical procedures. Each of the patients signed a statement authorizing the anonymous use of his or her clinical data for scientific research.

3.2.2 Data acquisition and preprocessing

Each patient was implanted with several platinum depth electrodes (DIXI medical, Besançon, France). These electrodes have 5 to 18 contacts of 2 mm each with an intercontact distance of 1.5 mm. The diameter of the electrodes is 0.8 mm. Besides depth electrodes, in patients 3 and 4 subdural strip electrodes with 4–8 contacts (DIXI medical, Besançon, France) were implanted. A contact in white matter tissue was chosen as the common

reference electrode for all channels. The implantation of the electrodes was performed at the Academic Center of Epileptology, location Maastricht University Medical Center (Maastricht, The Netherlands). A pre-implantation structural MRI scan (Intera 3.0 Tesla, Philips Medical Systems, Best, The Netherlands) was acquired with gadolinium contrast-enhancement. After implantation a computed tomography (Sensation 16, Siemens, Berlin,

Patients	Age/ Gender	Lesion	(Electro)-clinical hypothesis	SOZ	Resection	Engel class outcome
1	42/F	Porencephalic cyst frontal R; hippocampal sclerosis R	Temporal R; Parietal R; Insula R	Mesial Temporal R	Anterior temporal R and amygdalo-hippocampectomy R	2
2	24/M	Hippocampal sclerosis L; infarct occipital L	Temporal L; Occipital L	Mesial Temporal L	Anterior temporal L and amygdalo-hippocampectomy L	1
3	39/M	Nodular heterotopia occipital L and R; cortical dysplasia mesial temporal R and occipital R	Temporal R; Occipital R	Mesial Temporal R	Anterior temporal R and amygdalo-hippocampectomy R	2
4	46/F	Hippocampal sclerosis L	Temporal L; Temporoparietal junction L; Insula L	Mesial Temporal L; Lateral Temporal L	Extended anterior temporal L and amygdalohippocampectomy L	1
5	48/M	Infarct Temporo-occipital R	Occipital R; Temporal R	Mesial Temporo-occipital R	Temporo-occipital R	1
6	44/F	Negative	Temporal L; Insula L; Cingulum L	Cingulum L	Anterior Cingulum L	4
7	15/F	Negative	Frontal R; Frontal L	Middle Frontal gyrus (F2) R	Middle Frontal gyrus (F2) R	3

Table 3.1: Patient characteristics and the clinical hypotheses based on preimplantation neuroradiological (MRI) and electro-clinical examinations of the patients. The resection was guided by the hypothesis regarding the seizure onset zone (SOZ) as result of the presurgical video-SEEG recordings. The outcome of surgery is given for each of the seven patients studied in terms of the Engel Epilepsy Surgery Outcome Scale.

Germany) and structural MR scan (Intera 3.0 Tesla, v.s.) were acquired to verify the positions of the electrodes and the absence of postoperative hematomas. When no further complications occurred, the long-term recording was performed at the Academic Center for Epileptology, location Kempenhaeghe (Heeze, The Netherlands).

The EEG was examined by an experienced EEG specialist who identified on average 471±282 IED's, which amounts to 19.6±11.8 IEDs per hour in the 24 hour recordings used. The number of IEDs identified at the SEEG recordings of each of the patients studied is listed in Table 3.2 (column 2). Isolated IEDs (spikes, sharp waves and spike-and-wave discharges) were annotated at the maximum of the spike amplitude of the IEDs. An interval centered around the maximum of each IEDs was selected with a time duration of 2.5s, which reduces the amount of SEEG data that is required to be processed. Data was recorded at a sample rate of 600 Hz (Stellate Harmony 6.1 C, Natus Medical Inc., San Carlos, USA). Fieldtrip [153] was used to read the data in EDF+ format and to apply bandpass filtering in the frequency range of 1-70 Hz in order to reduce high-frequency noise. Both monopolar and bipolar derivations were created within MATLAB (The MathWorks Inc., Natick, MA, 2015). The SEEG analysis framework developed in this study uses C++, MATLAB and Mathematica 10.0 (Wolfram Research, Inc., Champaign, IL). OpenMP was used for multi-thread processing.

3.2.3   Overview of analysis framework

The SEEG analysis, outlined in Fig. 3-1 (top row), consists of three steps addressing the following questions: 1) is the activity underlying the SEEG signals synchronized during the IEDs?, 2) which brain areas are involved in the generation of the activity underlying the IEDs?, and 3) what is the interdependency between multiple active brain areas and can we identify the area that corresponds to the irritative zone?. Visualization of the analysis results relative to the cortical anatomy is outlined in Fig. 3-1, bottom row, which utilizes the depth electrode navigation software tool introduced in Chapter 2. The methodology is illustrated by the analysis of the SEEG recordings of one of the patients studied.
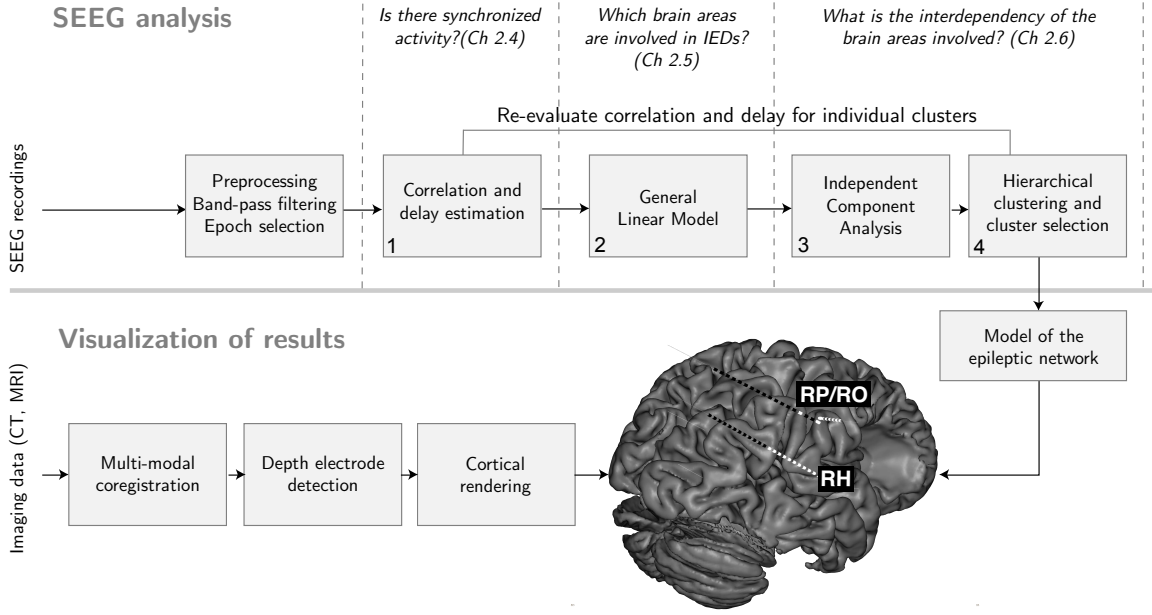
Figure 3-1: Overview of the developed methodology, outlining the analysis of SEEG recordings (top) and the visualization of its results (bottom).

3.2.4 Synchronous epileptic activity

To estimate the synchronization of each possible combination of SEEG signals during the occurrence of the IEDs, a non-linear correlation analysis is applied. The correlation coefficient h_{XY}^2 is used in the analysis, which models the degree to which any arbitrary signal Y can be interpreted as a transformed version of signal X [166, 41, 99]. In other words, we estimate a signal $\hat{Y}$ given by $\hat{Y} = S(X)$ where S is the perturbation function. The difference between the true Y and the estimated $\hat{Y}$ is defined as the unexplained variance. The non-linear coefficient $0 \leq h_{XY}^2 \leq 1$ is then given by

$$h_{XY}^2 = \frac{\sum\limits_{i=1}^{n}(Y_i - \overline{Y})^2 - \sum\limits_{i=1}^{n}(Y_i - S(X_i))^2}{\sum\limits_{i=1}^{n}(Y_i - \overline{Y})^2}, \tag{3.1}$$

where X_i and Y_i are samples of the signals X and Y, respectively, n is the number of samples and $\overline{Y}$ is the average amplitude of signal Y. Originally, the perturbation function S was defined by a piece-wise linear approximation of the regression curve modeled from

the scattergram of X and Y [41]. A linear approximation was chosen by these authors because of its computational efficiency. The downside of this method is that the scattergram is required to be divided into bins, which makes its results dependent on the size of the bins. In this study, however, we opt to use a cubic spline instead of a piece-wise linear function, because the cubic spline describes the data better with a lower unexplained variance as result and does not require binning. The parameters of the cubic spline function can be found by using a linear least-squares fit.

The analysis to identify synchronized activity is outlined in a flowchart shown in Fig. 3-2 (top row). The correlation analysis is performed on windows centered around the maximum of the IED (see Fig. 3-2, top left) with a window size of 250 ms, which is large enough to encompass the spike-and-wave discharges [46]. In addition to the improved perturbation function, in our approach a method is introduced for the accurate estimation of the time delay between the SEEG signals. The time delay is estimated based on the averaged correlation function of all IEDs, as shown in Fig. 3-2 (top middle), instead of the commonly used time delay estimation based on a single IED [230]. The correlation function is calculated for the time windows of analysis w_k centered around the kth IED, while shifting one signal relative to the other with a time-shift of $-50ms \leq \tau \leq 50ms$. The correlation function is denoted by $h_{ij}^2(w_k, \tau_{ij})$, where $(i,j) = 1, ..., \#_{\text{contacts}}$ are indices for the depth electrode signals and τ_{ij} denotes the time-shift variable between channels i and j.

The averaged correlation for all IED-centered windows of analysis $\bar{h}_{ij}^2(\tau_{ij})$ is computed according to

$$\bar{h}_{ij}^2(\tau_{ij}) = \frac{1}{N} \sum_{k=0}^{N} h_{ij}^2(w_k, \tau_{ij}), \tag{3.2}$$

where N is the number of IEDs. From its corresponding graph (see Fig. 3-2, top middle) the time delay $(\tau_{ij})_{\text{max}}$ is estimated as the time-shift that results in a maximum averaged correlation value:

$$(\tau_{ij})_{\text{max}} = \arg\max_{\tau_{ij}} \bar{h}_{ij}^2(\tau_{ij}). \tag{3.3}$$
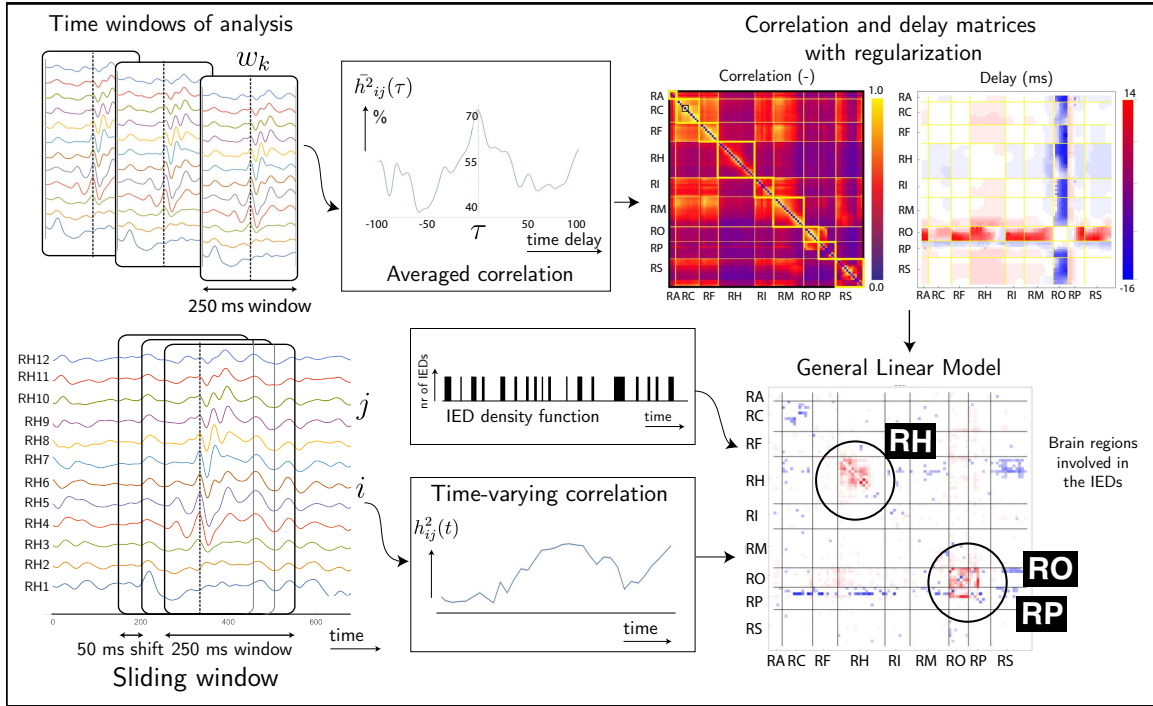
Figure 3-2: Overview of the analysis applied to the SEEG recordings of patient 1, as indicated in steps 1 and 2 of the flowchart for SEEG analysis (see Fig. 3-1). Top row: The non-linear correlation is computed for windows centered around the maximum of IEDs, shown by the vertical dotted line (left), from which the time delay can be estimated (middle) and summarized in correlation and time delay matrices (right). Shown in the middle is the averaged correlation as function of the estimated time delay. Bottom row: A sliding window analysis is performed (left) in which the changes in non-linear correlation over time are computed (middle). These time-varying correlation functions are together with the IED density function the input of the General Linear Model (GLM). The result of the GLM analysis reveals at which contact points SEEG signals are recorded that are significantly involved in the IEDs (right).

Regularization of the delay matrix

However, because multiple local maxima may be present that are nearly equal to the global maximum $\max_{\tau_{ij}} \bar{h}^2_{ij}(\tau_{ij})$ the time delay estimation may be unstable and lead to outliers in the delay matrix. In order to provide a robust estimation of the time delays, a regularization procedure is introduced that incorporates spatial information. In this procedure the average correlation function $\bar{h}^2_{ij}(\tau_{ij})$ is maximized, while simultaneously requiring a certain smoothness between neighboring entries in the delay matrix. Since two neighboring SEEG contact points measure activity from an overlapping area, it is assumed that

the correlation and associated estimated delay vary continuously between neighboring matrix entries. Based on this assumption, a smoothness constraint is implemented within the energy term used for regularization, formulated according to

$$E_\Omega = \sum_{(i,j)\in\Omega} \bar{h}_{ij}^2(\tau_{ij}^*) - \lambda|\Delta\tau_{ij}^*|, \qquad (3.4)$$

where $\bar{h}_{ij}^2(\cdot)$ is the average correlation function (see Eq. (3.2)), τ_{ij}^* is the time delay value to be optimized at the indices for depth electrode signals (i, j), and λ is a weighting term for the degree of smoothness applied to the delay matrix. Here, Ω is an area of the delay matrix corresponding to the contact points of any two electrodes, for example containing the time delays from every signal measured by the RC electrode to every signal measured by the RH electrode (see Fig. 3-3, middle). Optimization is performed within Ω to ensure that the smoothness is evaluated in the same anatomical areas. The Laplace operator $\Delta = \nabla \cdot \nabla$ is used to measure the variation between neighboring values in the delay matrix within Ω. In order to ensure smoothness to all neighboring values, a 9-connected discrete approximation of the two-dimensional Laplace operator is used. The nine-point
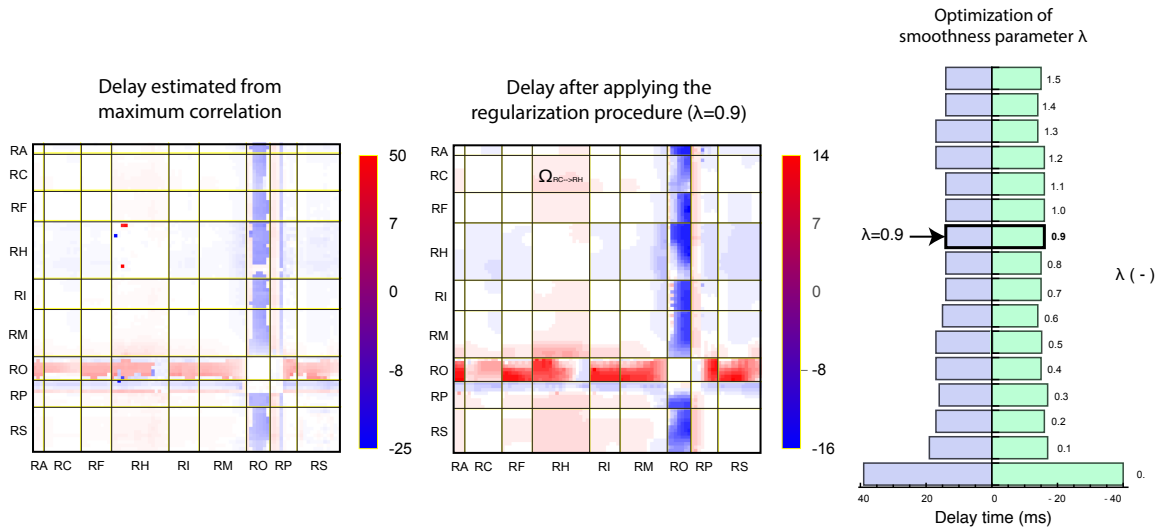
Figure 3-3: Example of the regularization procedure for patient 1. Left: Delay matrix estimated from the estimation of maximum correlation. Middle: Delay matrix obtained after the regularization procedure. Right: Selection of an appropriate smoothness parameter λ through a stability analysis.

Laplacian is given by $\Delta u = -h^{-2}[8u_{i,j} - u_{i-1,j} - u_{i+1,j} - u_{i,j-1} - u_{i,j+1} - u_{i-1,j-1} - u_{i-1,j+1} - u_{i+1,j-1} - u_{i+1,j+1}]$ [116] with a stepsize $h = 1$.

The time delay τ_{ij}^* is optimized by maximizing the energy function E_Ω, following a three-step procedure:

1. Initial values for the maximum correlation and the corresponding delay are computed for all entries in Ω based on the time-shifts that resulted in maximum correlation.

2. A direct search method is applied which optimizes each matrix entry (i, j) individually by computing the energy term for a range of delay values ($\pm$ 10 ms around τ_{ij}^*). The delay value corresponding to the highest energy is updated according to $\tau_{ij}^* = (\tau_{ij}^*)_{\text{new}}$.

3. Step 2 is repeated until convergence is reached, i.e. $\tau_{ij}^* \approx (\tau_{ij}^*)_{\text{new}}$ within a tolerance level, or until the maximum number of iterations is reached.

The smoothness parameter λ can be estimated through a stability analysis in which the minimum and maximum delay values of the matrix are inspected for increasing λ (see Fig. 3-3, right). The appropriate value of λ is the point at which the minimum and maximum delay values no longer change for an increment of λ.

After the procedure for smoothness regularization of the delay matrix, which is described in detail below, the problem of outliers is solved, with as result a more plausible range of delay values. Shown are the regularized correlation and delay matrices (see Fig. 3-2, top right) that were obtained for 843 IEDs occurring in the first 24 hours of the SEEG recording of patient 1. In order to compute the full correlation matrix $\boldsymbol{h^2} = \left\{ (h_{ij}^2)_{\text{max,regularized}} \right\}$ and the full delay matrix $\boldsymbol{\tau} = \left\{ (\tau_{ij})_{\text{max,regularized}} \right\}$, it is necessary to evaluate both the combinations $i \to j$ and $j \to i$ since the correlation coefficient is asymmetric, i.e. $\bar{h}_{ij}^2 \neq \bar{h}_{ji}^2$ [166].

Local maximum based correlation analysis

Recordings of epileptic activity using SEEG may reflect a large variability in the waveform of the IEDs. As a result, the regularization procedure may yield implausible results for delay estimation for the SEEG recordings of some patients. To resolve this issue, a re-evaluation is performed of the correlation function $h_{ij}^2(w_k, \tau_{ij})$. The first step is the detection of the local maxima of the correlation function. In order to prevent the detection of maxima caused by white noise, only the local maxima that survived a blurring of scale $\sigma = 10$ (corresponding to a kernel of size 10 ms) were maintained. The results of local maxima detection for both $h_{ij}^2(w_k, \tau_{ij})$ and its transpose $h_{ji}^2(w_k, \tau_{ij})$ are shown in Fig. 3-4. Subsequently, the locations of the local maxima and their correlation coefficient are included in a weighted distribution, where each delay at the q-th local maximum $\tau_q = \tau_{ij}(w_k, q)$ is weighted by its corresponding correlation $h_q^2 = h_{ij}^2(w_k, \tau_q)$. The delay between any two EEG signals i and j is then estimated by the weighted arithmetic mean according to $\hat{\tau}_{ij} = \frac{1}{k} \sum_{k}^{\#\text{IEDs}} \frac{1}{q} \left(\sum_{q}^{\#\text{maxima}} h_q^2 \tau_q \right) / \left(\sum_{q}^{\#\text{maxima}} h_q^2 \right)$.

Since the correlation function for an individual spike may contain noise, several preprocessing enhancement steps are applied. Firstly, a second-order Gaussian derivative filter with scale $\sigma = 10$ is applied to the monopolar EEG data for each spike. This procedure increases the spike amplitude while reducing low-amplitude background activity. Furthermore, since low-frequency background activity is known to produce relatively high correlation in some cases, a total variation measure is applied to weigh the correlation function according to EEG activity. In practice this leads to a reduction of peaks in the correlation function associated with background activity. The correlation function for each spike is weighted according to $h_{ij}^2(w_k, \tau_{ij}) \cdot log(\text{TV}_{w_k,i}/\text{TV}_{w_k,ref})$, where TV is the total variation $\text{TV}_{w_k,i} = \sum_{t=0}^{T} \|y_i'(t)\|$ and y_i is the EEG signal for the ith channel within window w_k and T is the time length of the window. The derivative y_i' is calculated by a first-order Gaussian derivative filter ($\sigma = 5$). The total variation for a given channel i is compared to a reference value $\text{TV}_{w_k,ref}$ that is associated with background activity. The logarithm is used in order to get a weighting that is zero when the total variation is equal to the reference.
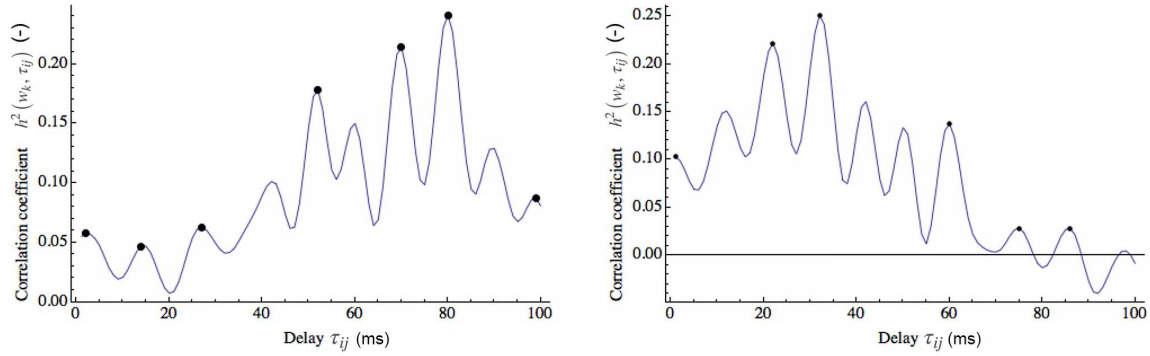
Figure 3-4: Example outcome of the correlation profiles of $h_{ij}^2(w_k, \tau_{ij})$ (left) and its transpose $h_{ji}^2(w_k, \tau_{ij})$ (right). The local maxima are denoted by black dots. It can be observed that the local maxima are anti-symmetric around the origin $\tau = 0$.

To apply the local maximum based correlation analysis to SEEG recordings it is, first of all, required to select one or several reference signals to which the time delay is estimated. The use of multiple reference signals can be beneficial to obtain more stable delay estimation results. The average time delay of every signal with respect to the reference signals is denoted by τ_{IJ}, and its transposed delay estimation is denoted by τ_{JI} The final estimate of the time delay is computed by the averaged norm of both delays according to $\tau_{I\leftrightarrow J} =$
$\frac{1}{2}\left(\sum_{i}^{\#\text{electrodes}} \|\tau_{IJ}\| + \sum_{i}^{\#\text{electrodes}} \|\tau_{JI}\|\right).$

3.2.5 Brain regions involved in the IEDs

To estimate the likeliness of a brain area to generate epileptiform activity, the GLM is applied, which is a method for multiple regression analysis. The GLM is used to model the statistical relation between the occurrence of the IEDs and the associated time-varying correlation of the SEEG signals. This approach is based on the assumption that mutual correlations between electrodes increase during epileptiform activity [24]. The univariate GLM is evaluated for all pairs i and j and is formulated as follows

$$h_{ij}^2(t) = \beta_{ij} \, \mathrm{IED}(t) + \alpha_{ij} + \gamma_{ij} t + \eta_{ij} \, \mathrm{CONF}(t) + \epsilon(t), \tag{3.5}$$

where $h_{ij}^2(t)$ is the dependent variable describing the time-varying correlation. The time-varying changes in the correlation $h_{ij}^2(t)$ are computed using the sliding window approach, in which the correlation is estimated by overlapping time windows with a length of 250 ms and a sliding step of 50 ms (Fig. 3-2, bottom left). At a 600 Hz sampling rate, these windows correspond to 150 and 30 samples, respectively. The current study expands upon the GLM analysis for SEEG, introduced by Van Houdt et al. [221], by taking the delay estimation into account. In order to achieve optimal values in time-varying correlation $h_{ij}^2(t)$, in this study a correction for the time delay is applied to each combination $i, j = 1, ..., \#_{\text{contacts}}$ according to the delay matrix computed for the considered patient. Formally the time-varying correlation is computed according to

$$h_{ij}^2(t) = h_{ij}^2 \left(w(t), (\tau_{ij})_{\text{max,regularized}} \right) \tag{3.6}$$

where $w(t)$ is the sliding window centered around time t.

The correlation function is modeled by a linear combination of independent variables (i.e. regressors). The predictor of interest is the IED density function (Fig. 3-2, bottom middle) denoted by $\mathrm{IED}(t)$, obtained by counting the number of IEDs that occur within the sliding window throughout the SEEG recording selected for analysis. The other independent variables are confounding variables: a constant, a linear trend, and the confounder density

function $\mathrm{CONF}(t)$. The model residual is given by $\epsilon(t)$. Artifacts from physiological origin that may occur in the EEG, e.g. paroxysmal activity, were identified and marked by a technician and are included in the confounder density function $\mathrm{CONF}(t)$, which counts the number of artifacts that occur during the sliding window.

The GLM is expected to yield high regression coefficients β_{ij} for contact points that are highly synchronized during the occurrence of IEDs. After the initial estimation of the matrix of regression coefficients $\boldsymbol{\beta} = \{\beta_{ij}\}$, several procedures are employed to distinguish epileptically active regions from false positive regions. First, the $\boldsymbol{\beta}$-matrix is thresholded according to a significance level in order to reduce false positives. The p-values obtained from the GLM procedure are adjusted according to the false discovery rate (FDR) [241] to correct for multiple testing, with every entry of the $\boldsymbol{\beta}$-matrix thresholded at $q < 0.01$. Here, q is the FDR-adjusted p-value. In extension to the method as introduced by Van Houdt et al. [220], a symmetry requirement on the regression coefficient is imposed, since synchronization during the occurrences of IEDs is expected to occur in both directions, i.e. $\beta_{ij} \approx \beta_{ji}$. Non-symmetric matrix elements can indicate the presence of a false positive. In order to remove the non-symmetric part of the $\boldsymbol{\beta}$-matrix, entries for which the condition $|[\mathrm{asym}(\boldsymbol{\beta})]_{ij}| = |\frac{1}{2}(\beta_{ij} - \beta_{ji})| > \frac{1}{2}\sigma$ holds are removed, where σ is the standard deviation of the distribution of significant $\boldsymbol{\beta}$-matrix values. Lastly, a selection of the highest $\boldsymbol{\beta}$-matrix values is done in order to select the most likely regions of focal activity. To select a suitable threshold, Otsu's method [155] is applied, which is based on the estimation of Gaussian distributions in the $\boldsymbol{\beta}$-matrix histogram. The final $\boldsymbol{\beta}$-matrix is shown in Fig. 3-2 (bottom right), indicating for the example patient two distinct anatomical regions (encircled in black) targeted by three electrodes (RO, RP and RH). In this case, electrodes RO and RP target the same anatomical region. In conclusion, the GLM reduces the number of signals to be analyzed and thereby facilitates further analysis.

3.2.6 Interdependency assessment

In order to evaluate the interdependency of the brain areas involved in IEDs, ICA is applied to create spatial distributions of each individual IED, followed by hierarchical clustering to identify spike clusters that have similar underlying spatiotemporal interactions. ICA [97, 37] is a statistical model where observed data is represented by a weighted sum of estimated source signals. This is expressed by $\mathbf{y}(t) = W\mathbf{x}(t)$ where $\mathbf{x}(t)$ is the observed data, $\mathbf{y}(t)$ are the estimated independent components and W is the unmixing matrix. Numerous variations of ICA are available and have been used in the context of EEG analysis [117, 42]. The current study employs the InfoMax ICA decomposition introduced by Makeig et al. [121], which is a commonly used algorithm available in signal processing toolboxes such as EEGLab [47]. A first requirement for Infomax ICA is that the sources must be statistically independent of each other, which is fulfilled when the sources have a low mutual information. The measure of statistical independence is the mechanism for source decomposition used by InfoMax ICA. The second requirement is that the observed data is stationary and not normally distributed. The EEG signals fulfill these requirements, since EEG is quasi-stationary, i.e. it is stationary within short time intervals during normal brain activity [183], while it is assumed that the EEG activity is not normally distributed. Lastly, InfoMax ICA requires the estimated weighting matrix W to be square and full rank.

InfoMax ICA is applied for each individual IED (Fig. 3-5, top left) thus generating a corresponding spatial weighting distribution W (Fig. 3-5, top right). The spatial weighting distribution provides a footprint of each individual IED, which can subsequently be clustered to identify groups of IEDs and investigate whether independent focal areas can be identified. To this end, Ward's method is applied [227], which is a general agglomerative hierarchical clustering procedure that merges clusters at each step based on a distance metric. The Frobenius norm of the matrix W, given by $\|W\|_F \equiv \sqrt{\sum_{i=1}^{m} \sum_{j=1}^{n} |W_{ij}|^2}$, is the distance metric used in order to cluster the spatial distributions. Since the most interesting information is contained within the first few independent components, the latter containing mostly noise, the distance metric is only calculated on the first 10 components

(i.e. columns) of the weighting matrices. An average of the IEDs and the spatial distribution of the independent components of these discharges is shown in Fig. 3-5 (bottom left). The hierarchical clustering is based on the similarity of the spatial distributions of the independent components of the individual IEDs. The number of clusters that can be discriminated as output of the clustering procedure can be estimated based on a dendrogram (Fig. 3-5, bottom row).
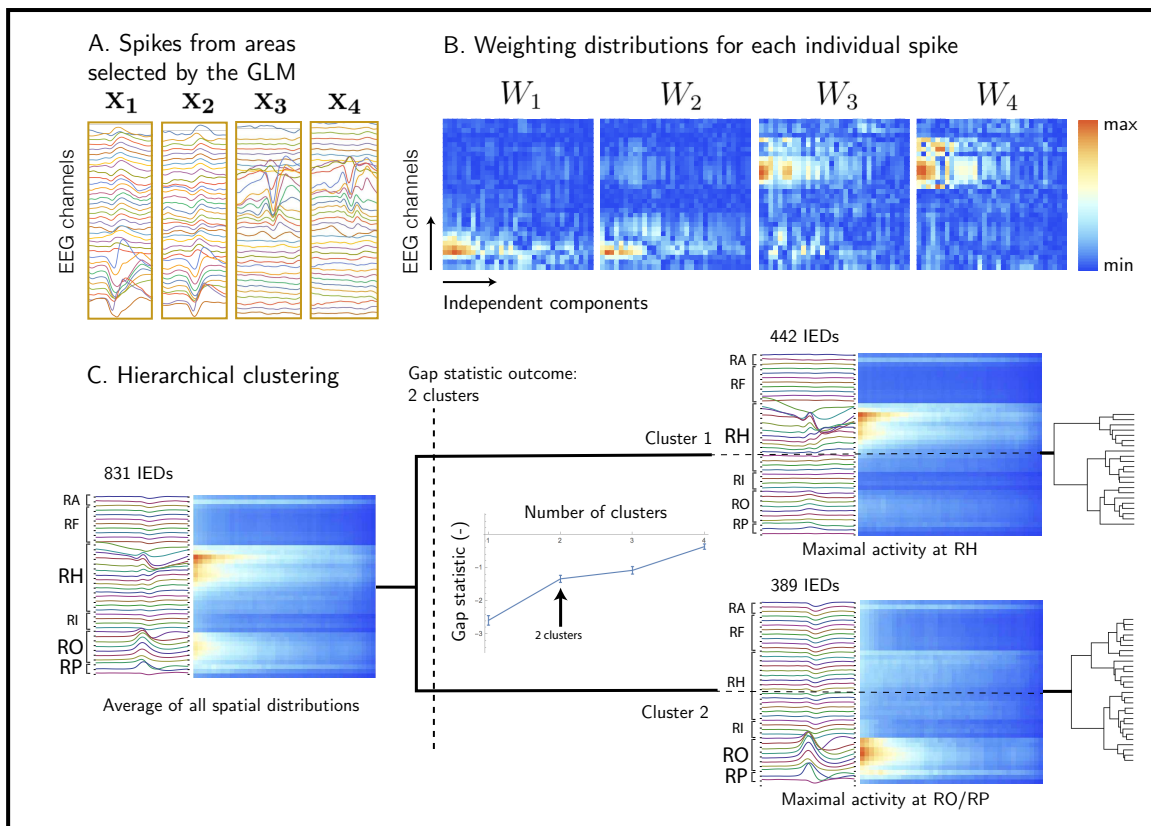
Figure 3-5: Overview of the clustering procedure to assess the interdependency of focal brain areas applied for patient 1, as indicated in steps 3 and 4 of the flowchart of the SEEG analysis procedure (see Fig. 3-1). ICA is applied for each spike x_1, x_2, $\cdots$ individually (A), resulting in a spatial distribution matrix W for each spike, denoted by W_1, W_2, $\cdots$. (B). Shown at the bottom left is the average of all IEDs selected for further analysis and of their spatial distributions. Hierarchical clustering is applied to the set of individual spatial distributions, which results in a dendrogram (C). The gap statistic [208] is used to estimate the number of clusters, indicating two spike clusters for this patient. The corresponding averaged spatial distributions for each cluster are shown, displaying a clear separation of the epileptic activity at either the electrode RH or at the crossing of the tips of the electrodes RO/RP.

In order to estimate the number of clusters quantitatively, the gap statistic [208] is employed. The gap statistic compares the clustering of SEEG recordings against a second clustering result of a randomly generated dataset of the same dimensions and the same range of values. The gap statistic compares the within-cluster dispersion between both clustering results, which is a measure of the average distance between the elements within all clusters. The within-cluster dispersion is expected to become lower as the number of clusters increases, since elements within a cluster are increasingly alike. The difference between within-cluster dispersion measured in both datasets forms the gap statistic. Based on the gap statistics two well-separated spike clusters that differ in spatiotemporal distribution, i.e. the shape of the IEDs and the anatomical area at which these discharges are maximal can be distinguished (Fig. 3-5, bottom row, right). More details on the gap statistic applied to hierarchical clustering can be found in Tibshirani et al. [208].

In some cases the gap statistic can be inconclusive. In those cases, an alternative approach to estimate the number of clusters is used. In this approach the number of clusters is manually estimated based on the expected number of independent focal areas. The intermediate results are then clustered for a second time using a K-means algorithm to discover groups of similar clusters or deviating clusters. Again, Otsu's method [155] is applied, but now for selecting the contact points of electrodes with the highest response by considering the accumulated weighting of the first 10 components.

Visualization

To visualize the brain areas and their interactions, the depth electrode navigation software tool introduced in Chapter 2 is employed. The spatial distribution of the activity underlying the IEDs recorded with the depth electrodes is visualized in a 2D- and 3D-viewport against pre-implantation MRI or against the cortical rendering (see for example Figs 3-6 to 3-9). Furthermore, a model of the underlying interactions of the brain areas is visualized by the use of arrows, given with the estimated association strength (in %) and with the delay, indicating whether the brain areas are lagging or leading. In addition, each arrow corresponds to the depicted associated correlation, which is a measure of coupling strength.

3.3   Results

To evaluate the analysis framework the SEEG recordings were analyzed retrospectively for five patients (patients 1 to 5) who all underwent successful epilepsy surgery (Engel class 1&2). Furthermore, it will be shown that the network analysis approach developed in this study is also successful for the patients included with a focal partial epilepsy who were not seizure free after surgery (patient 6 and 7, Engel class 3&4). The results, as summarized for the seven patients in Table 3.2, are evaluated against the electroclinical hypotheses, the SOZ, the resected area and the surgical outcome. Furthermore, the activation patterns underlying the IEDs are displayed at the depth electrodes in relation to the brain anatomy for each of the seven patients studied.

3.3.1   Evaluation of the analysis framework

The analysis framework was evaluated for the five patients with disrupted anatomy visible at MRI (see Table 3.1, column 3) who underwent successful surgery. Patient 1 had a right frontal porencephalic cyst from birth with partial involvement of the right insular and temporal regions. For this patient, nine electrodes were implanted in the right hemisphere, targeting the hippocampus, temporal operculum, insula, cingulum, frontal and occipital lobes, and the area surrounding the patient's porencephalic cyst (Fig. 3-6, bottom left). The contact points at which the IED activity was maximal according to visual review are listed in column 3 of Table 3.2. These results can be compared to the quantified maximal IED activity as determined by the result of the analysis framework (Table 3.2, column 4). For this patient there are two spike clusters active, one in the right hippocampus (electrode RH) and one at the site of the right insula, at the crossing of the RO and RP electrode (Fig. 3-6, right top row). The spatial distribution of the individual clusters is displayed color-coded at the corresponding electrodes in a sagittal and axial MR scan (Fig. 3-6, right bottom row). The spike cluster that is maximal at the right hippocampus coincides with the SOZ as indicated by the yellow box in the sagittal MRI scan. The overlap

Patients	#IEDs	IED activity (visual review)	IED activity (quantified)	SOZ activity	Overlap IED activity (quantified) and SOZ
1	831	RH 2-11; RP 1-3; RF 2-4	Focal areas: 1) RH 3-9; 2) RO 1-6; RP 1-4	RH 7-10	Focal areas: 1) 75%; 2) 0%
2	260	LH 1-6; LH 10-11	LH 1-5	LH 1-11	45%
3	177	RSP 1-3; RH 1-8	RH 1,2,5-8; RSA 1-3; RSL 3-4; RSP 2	RH 6-11	50%
4	883	LH 1-9; LST 2-4; LSO 4-6; LE 6-8	LH 4-8; LE 5-7 LSO 1-5; LST 2-3	LH 7-8; LSP 8	67%
5	502	LH 1-10; RH 1-10; RO 2-6; RZ 1-4; RI 4-6	RO 2-8; RZ 1-7; RI 2-4; RT 3-4	RO 1-6; RZ 1-4	90%
6	270	LH 1-10; LT 3-4; LF 1-2; LP 1-2	LH 6-9; LX 3-9;	LC 2-4	0%
7	379	RY 7-12; RX 8-12; RC 3-8; LC 6-8; LX 9-12	Focal areas: 1) LC 4-8; LX 5-12; LA 14-16; 2) RY 7-12; RX 10-14; RC 4-5,8; RA 6-7,10	RY 10-13; RX 8-12	Focal areas: 1) 56%; 2) 0%

Table 3.2: Results for the patient group, showing the number of IEDs analyzed (#IEDs), the IED activity as determined by visual review and as result of applying the analysis framework (IEDs quantified), and the SOZ as result of visual review of the SEEG recordings. The overlap of IED activity (quantified) with the SOZ is indicated in percentages in the last column. For patients 1 and 7 the overlap is indicated for two focal areas identified. The location is described by the depth electrode label and involved contact points. The depth electrodes are labeled by their anatomical position (e.g. LH = left hippocampus, RH = right hippocampus, RO=right occipital, RP=right parietal, RT=right temporal), which may, in some cases, refer to a different region depending on the patient studied.

Model of the spatiotemporal interactions   Significantly active spike clusters
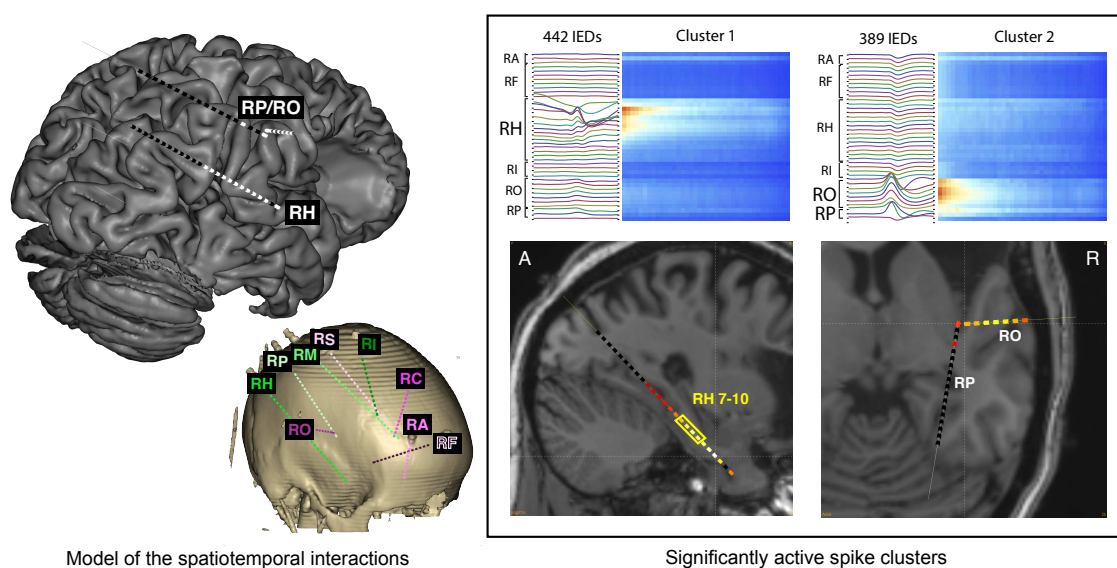
Figure 3-6: The results of the SEEG analysis for patient 1, indicating the spatiotemporal pattern of the two spike clusters (upper right) and visualizing the significant activation at the electrodes RH, RO and RP (bottom right). The yellow box indicates the overlap of the activity underlying the IEDs and the SOZ. The model of the spatiotemporal interactions (top left) displays the electrodes with significantly involved activity underlying the IEDs indicated by the white dots. The nine electrodes implanted for this patient are displayed together with the 3D-CT scan of the patient's head (bottom left).

as indicated in column 6 of Table 3.2 is computed by the intersection of: 1) the set of contact points identified by quantified IED activity, and 2) the set of contact points that correspond to the SOZ according to clinical review. The overlap is normalized by the number of contact points corresponding to the SOZ. For the first cluster, the overlap between the quantified IED activity and the SOZ is measured at 75%, indicating a good concordance. The second cluster involving the RO and RP electrodes targeting the right insula showed no overlap with the SOZ. The patient underwent a right anterior temporal lobe resection and amygdalohippocampectomy, which led to satisfactory seizure reduction.

In Fig. 3-7 an overview is given of the analysis results for patients 2, 3 and 4. The semiology of patient 2 indicated left temporal lobe epilepsy. The question when planning the implantation of the depth electrodes was whether the left hippocampus was involved in seizure generation and whether there could be an epileptogenic area related to the MRI abnormalities due to an earlier infarction at the left occipital lobe. Five depth electrodes

Figure 3-7: Results of the SEEG analysis for patients 2 (A), 3 (B) and 4 (C). In the left column the implanted electrodes are shown together with the 3D-CT scan and the spatiotemporal model of the interactions underlying the IEDs. The association strength ratios are denoted in percentages and the estimated delays are given in milliseconds. The middle column shows the output of Independent Component Analysis followed by hierarchical clustering, indicating the number of spike clusters and their spatiotemporal patterns. In the right column, the activity corresponding to these spike clusters is projected on anatomical MRI slices with the location of the SOZ indicated by the yellow box.

were implanted in the left occipital lobe and a single depth electrode was implanted in the left hippocampus (Fig. 3-7A, left). The EEG signals that were, according to the GLM, significantly involved in the IEDs were mainly recorded with the electrodes LH, LB and LM. However, after ICA and subsequent spike clustering, a single spike cluster could be identified with a maximum at electrode LH (Fig. 3-7A, middle). The maximum, centered around LH5, coincided with the SOZ, as indicated by the yellow box in the sagittal MR scan (Fig. 3-7A, right). The overlap between the quantified IEDs and the SOZ is 45% (see Table 3.2, column 6). The patient was rendered seizure-free after a standard left temporal lobe resection and amygdalohippocampectomy. For patient 3, three depth electrodes were implanted in the right temporal and occipital lobes (RH, RC, RI). Furthermore, three subdural strip electrodes were placed (Fig. 3-7B, left) in the right anterior basal temporal (RSA), posterior basal temporal (RSP) and lateral temporal regions (RSL). According to the GLM the EEG signals recorded with electrodes RH, RSA, RSL and RSP were significantly involved in the IEDs. ICA with subsequent cluster analysis yielded two spike clusters (Fig. 3-7B, middle), which was supported by the gap statistics. The spike cluster shown at the top row is dominant at electrode RH, whereas the second spike cluster shown at the bottom row is dominant at the subdural strip RSP. Note that the spikes recorded at the subdural RSP strip are inversed in polarity because the RSP strip was placed posterior basal to the hippocampal electrode. The most significant activity is recorded at the tip of the RH-electrode, however, the SOZ is located more posterior in the right hippocampus (see the yellow box in Fig. 3-7B, right, top row). The overlap between the quantified IEDs and the SOZ is 50% (see Table 3.2, column 6). A right anterior temporal lobe resection and amygdalohippocampectomy led to a satisfactory seizure reduction.

The recordings of patient 4 (Fig. 3-7C) reflected large IEDs at the left temporal and left occipital lobes. For this patient seven depth electrodes were implanted in brain areas including the left and right hippocampus (LH and RH), left insula (LX, LY) and left parietal (LE, LO, LS) lobes. In addition, five subdural strip electrodes were implanted in the right basal (RSB) and lateral temporal (RSL) regions, the left anterior basal temporal lobe (LST), left temporo-occipital (LSO) and parietal lobes (LSP). According to the GLM, EEG signals

measured with the electrodes LH, RH, LX, LY, LSO, LST, and RSL were significantly involved in the IEDs. However, after ICA, together with hierarchical clustering, two clearly distinct spike clusters were obtained that were both dominated by activity at the electrodes located at the left temporal lobe (Fig. 3-7C, middle). Cluster 1 reflects simultaneous activity from LH and LSO mainly and with a smaller amplitude LST, while for cluster 2 the activity recorded with the LH electrode dominates. The left hippocampus targeted by the LH electrode coincides with the SOZ (Fig. 3-7C, right) showing a 67% overlap (see Table 3.2, column 6). For this patient, a left extended temporal lobe resection and amygdalohippocampectomy was performed rendering this patient seizure-free.

A. Interictal activity

B. GLM after filtering

D. Model of the spatiotemporal interactions

C. Significantly active spike clusters
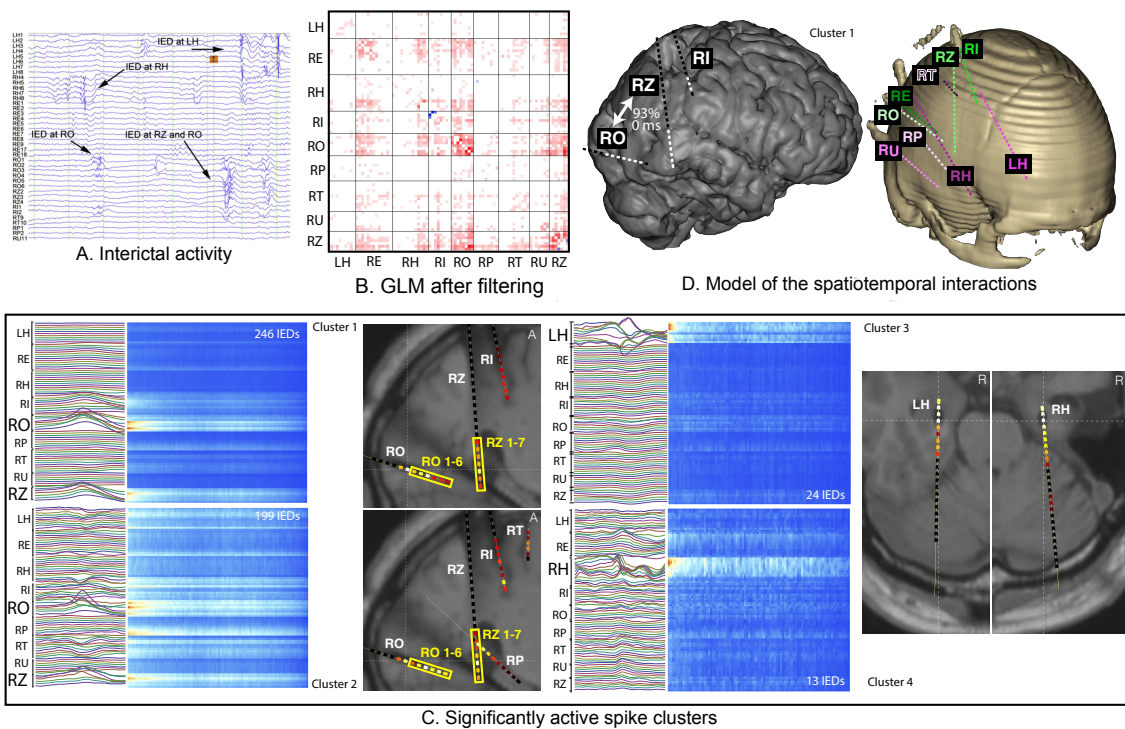
Figure 3-8: Results of the SEEG analysis for patient 5. A) The SEEG recording showing IEDs at the depth electrodes. B) The output of the General Linear Model indicating that most of the SEEG signals are significantly involved in the epileptic discharges. C) The spatiotemporal distribution of the distinct spike clusters involved. At the left, the spike clusters are shown with maximal activity at electrodes RO and RZ. The overlap with the SOZ is indicated by the yellow boxes. At the right, the spike clusters with maximal activity at, respectively, the electrodes targeting the left (LH) and right (RH) hippocampus. D) The model of the network organization which shows the depth electrodes that are part of the epileptic network (left). The association strength ratios are denoted in percentages and the estimated delays are given in milliseconds. The implanted depth electrodes are shown together with the CT-scan at the right.

Patient 5 had a cystic lesion due to a perinatal infarction in the temporo-occipital lobe of the right hemisphere. Eight depth electrodes were implanted adjacent to the infarction, with in addition one electrode implanted in the left and right hippocampus (Fig. 3-8D, right). The GLM reflects a diffuse pattern, indicating significant activity measured by all electrodes (Fig. 3-8B). Therefore, no electrodes were excluded from further analysis. ICA was applied followed by hierarchical clustering. The interactive method was employed for estimating the number of clusters since the gap statistic was inconclusive. Cluster 1 is mainly dominated by activity recorded at several contact points of RO and RZ, whereas cluster 2 reflects more diffuse activity with involvement apart from the activity at RO and RZ of the electrodes LH, RI, RP and RT, albeit of lower intensity. Further visual review indicated that for cluster 1 the activity dominated alternately at electrode RO and RZ, whereas cluster 2 mainly reflects distributed activity over six of the implanted electrodes. The analysis results of this patient reveal two additional spike clusters, with dominant activity at both the left and right hippocampal electrodes (Fig. 3-8C, right). These clusters consist of, respectively, 24 and 13 IEDs, amounting to less than 5% of the total number of IEDs occurring in the selected SEEG recordings of this patient. It appeared that the pathological brain area targeted by the electrodes RO and RZ coincided with the SOZ, as indicated by the yellow boxes at Fig. 6C, with an overlap of 90% (see Table 3.2, column 6). An extended resection of the brain area including the cystic lesion was performed rendering this patient seizure-free.

3.3.2   Network analysis approach

A network underlying the IEDs is assumed to consist of nodes, which are the brain areas involved in the evolvement of the IEDs, and the connections between these nodes. The connections are expressed by the association strength (in %), while the estimated time delay (in ms) indicates the direction, i.e. whether the node is leading or lagging. The scope of the network analysis procedure was, however, limited for the five patients who participated in the evaluation study because the implantation strategy of the depth electrodes was mainly guided by the abnormalities visible at MRI. The two spike clusters of

patient 1, located adjacent to the porencephalic cyst and probably originating in the right hippocampus and insular area, were independently active. For patient 2 a single spike cluster was identified with an origin in the left hippocampus. The spatiotemporal interactions of the spike clusters identified for both patient 3 and 4 are restricted to, respectively, the right and left temporal lobe (see Fig. 3-7B,C). For these patients there was a negligible time delay between the spikes recorded at the hippocampal electrodes and the subdural electrode strips. Thus, the SOZ of 4 out of 5 patients evaluated (patient 1-4) originated in either the left or right hippocampus and a standard or more extended temporal lobe resection plus amygdalohippocampectomy led for each of these patients to a satisfactory seizure outcome. The SEEG recordings with the most complex interactions of the MRI-positive epilepsy patients were recorded for patient 5 (Fig. 3-8A). Spike clusters with the most dominant activity were identified at the RO and RZ electrodes with varying spike amplitude but without significant time delay between these electrodes. Furthermore, the electrodes placed in the left and right hippocampus revealed independent interictal spiking (Fig. 3-8C), but did not interact with the RO and RZ electrodes. In summary, there is no evidence for interactions with distant brain areas for the 5 patients included in the evaluation study with an epilepsy related to pathologic brain tissue identified at MRI.

However, the network analysis approach appeared, especially, suitable for patients who had, according to visual review, an epilepsy with underlying complex network interactions. For one of the two patients studied (patient 6), who was not seizure free after SEEG guided resections, electro-clinical review indicated focal partial seizures with secondary generalization. Visual review of the SEEG recordings pointed at a neocortical left temporal lobe epilepsy, possibly with involvement of the contralateral temporo-parietal regions. For this patient, in total nine electrodes were implanted in the left hemisphere and two electrodes were implanted in the right hemisphere, including a depth electrode in each of the hippocampi (Fig. 3-9D, right). Visual analysis of seizure data identified the left anterior cingulum targeted by depth electrode LC as the SOZ. However, the patient was not seizure-free after resection of this area. The SEEG recordings of this patient mainly reflect IEDs recorded at the depth electrodes implanted in the left frontal and temporal

A. Interictal activity   B. GLM after filtering   D. Model of the spatiotemporal interactions

C. Significantly active spike clusters

Figure 3-9: Results of the SEEG analysis for patient 6. A) The SEEG recording showing the IEDs at a selection of depth electrodes. B) The output of the General Linear Model displaying which SEEG signals are significantly involved in the epileptic network. Positive β values (red) indicate increased correlation during IEDs, while the negative β values indicate a decorrelation during IEDs. C) The three distinct spike clusters with the complete network involved (left), dominant activity at electrode LH (middle) or dominant activity at the electrodes LY/LX (right). D) The model of the spatiotemporal interactions underlying spike cluster 1 (left), with the association strength ratios denoted in percentages and the estimated delays given in milliseconds. The implanted electrodes are visualized relative to the 3D-CT scan (right).

lobes (Fig. 3-9A). GLM analysis (Fig. 3-9C) revealed significant activity measured from six depth electrodes (LH, LX, LC, LF, LY and LT). Subsequently, ICA followed by hierarchical clustering yielded three spike clusters (Fig. 3-9C, upper row) with involvement mainly of five electrodes (LH, LC, LY, LX and LT). Spike cluster 1 reflects the activity underlying the discharges recorded at the electrode targeting the left hippocampus (LH), which is leading the activity recorded, respectively, at the electrodes targeting the left temporal pole

(LT), anterior insula (LX) and anterior cingulum (LC). Spike cluster 2 is mainly recorded at the electrode targeting the left hippocampus and its direct neighborhood, while the third spike cluster was maximal at the LY electrode targeting the left insula. The interactions between brain areas for cluster 1 are visualized in (Fig. 3-9D) in which the delay values are depicted, showing the LH-LX electrodes as the focal area. These electrodes are leading according to the delay estimation, with small delays towards LY and LT and larger delays to LC and LF. The network interactions as identified by the analysis framework applied in this study all point to the left hippocampus as being responsible for the initiation of the IEDs of this patient. The interictal activity (quantified) is not concordant with the clinical hypothesis regarding the SOZ and has 0% overlap (see Table 3.2, column 6).

Patient 7 was diagnosed with an epilepsy of unknown origin with secondary generalization and with either a left, right or bilateral frontal onset. For this patient, 9 electrodes were implanted in the right hemisphere and 6 in the left hemisphere (Fig. 3-10D). GLM analysis indicated significant activity measured mainly from LC, LX, RA, RC, RX and RY (Fig. 3-10B). ICA followed by hierarchical clustering yielded three spike clusters (Fig. 3-10C, upper row). All clusters indicate activity from the left and right insular and cingulate regions, however, with dominant activity recorded from the right insular region (RY) and from the area of the cinguli (LC, RA and RC). According to the clinical hypothesis based on these depth electrode recordings the SOZ was located in the area of the right middle frontal gyrus. However, resection of this area did not lead to a satisfactory seizure reduction.

Possibly due to the varying shape of the IEDs within each spike cluster, delay estimation by the regularization procedure did not lead to plausible results for this patient, showing mostly delays estimated around 0 ms. In order to resolve these issues, a local maximum based analysis of the correlation function is applied, as described in Section 3.2.4. The results corresponding to the second cluster are shown in Fig. 3-11 for the delay of every electrode with respect to the reference electrode RY denoted by τ_{IJ} (A) and the transposed delay estimation denoted by τ_{JI} (B). For the delay computation, three reference electrodes RY9, RY10 and RY11 were used, which displayed similar activity throughout all spikes. It
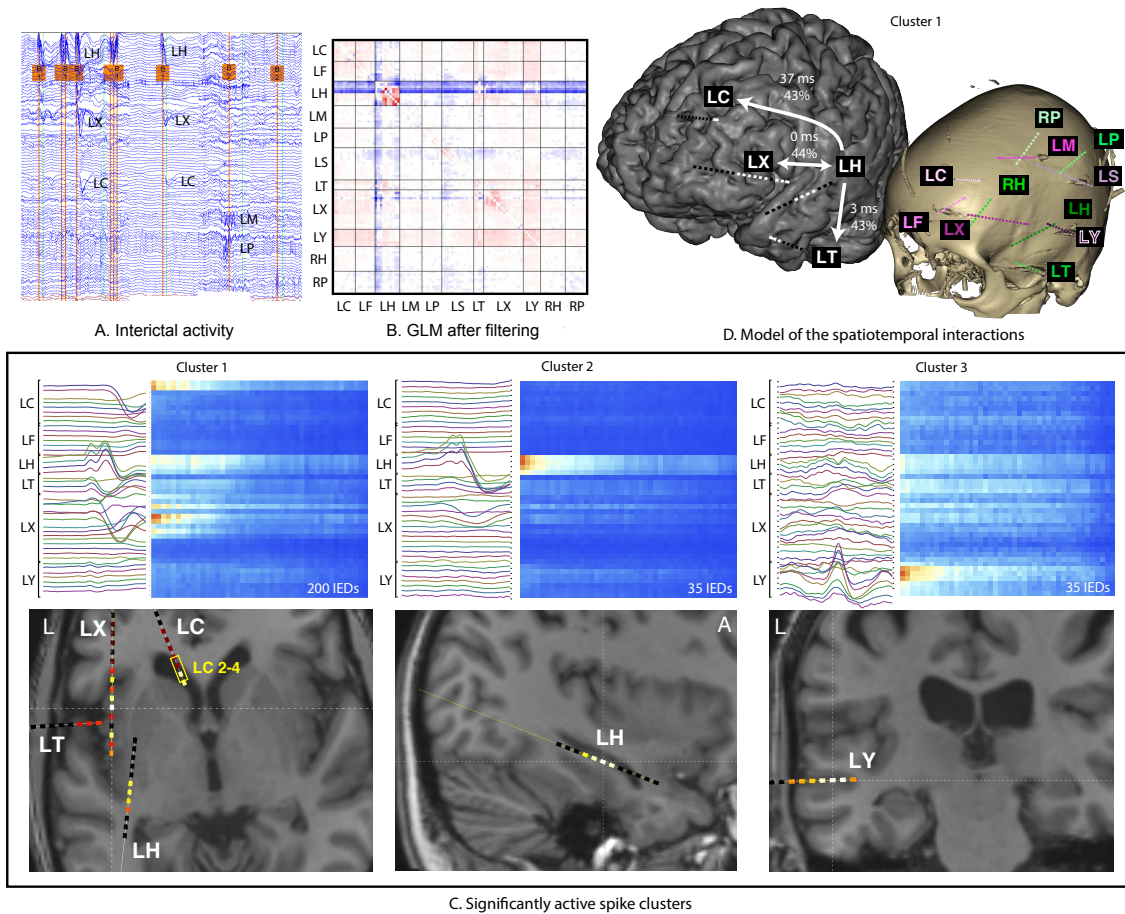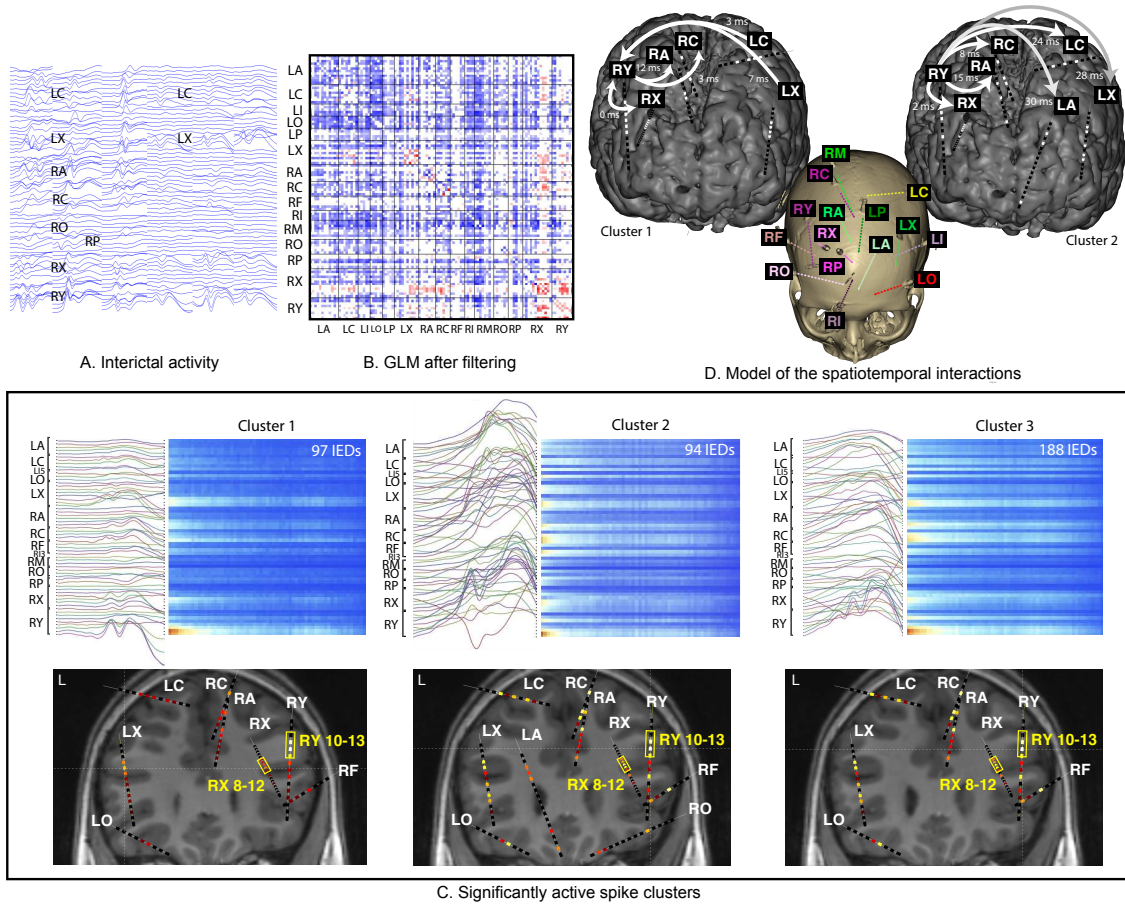
Figure 3-10: Results of the SEEG analysis for patient 7. A) The SEEG recording showing the IEDs at different depth electrodes. B) The output of the General Linear Model displaying which SEEG signals are significantly involved in the epileptic network. Positive β values (red) indicate increased correlation during IEDs, while the negative β values indicate a decorrelation during IEDs. C) Independent Component Analysis followed by hierarchical clustering indicates three spike clusters. All spikes clusters display complex activity involving multiple involved electrodes. D) The model of the network organization showing that the activity recorded at LX is leading for cluster 1 (left) and the activity recorded at electrode RY for cluster 2 (right). The implanted electrodes are displayed relative to the 3D-CT scan (middle).

can be observed that the delay estimation τ_{IJ} and its inverse τ_{JI} are approximately anti-symmetric and behave according to the condition $\tau_{IJ} \approx -\tau_{JI}$, where I and J denote whole electrodes. The anti-symmetry observed here is an indication of the reliability of the delay computation. The final estimate of the time delay for cluster two is shown in Fig. 3-11C, indicating the right hemisphere as a clear onset region, showing large delays up to 30 ms to the left cingulum (Fig. 3-10C, middle), but indicates simultaneous activa-

(A) Delay to RY electrode   (B) Delay to RY electrode (transpose)   (C) Average norm delay to RY electrode
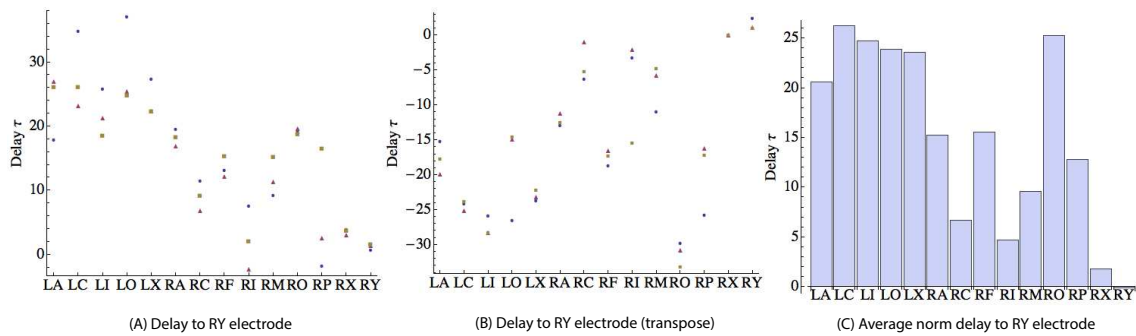
Figure 3-11: Results of the delay computed using the local maximum based analysis (see Section 3.2.4), showing the delays from electrode RX to all others (A), the delays from all electrodes to electrode RX (B) and the average normed delay in both directions (C).

tion of the sources targeted by LX and RY, but also including LC and RC. Using the same procedure, the first cluster indicates that the activity from the left insula and cingulum precede the activity seen in the right hemisphere (Fig. 3-10C, left). The third cluster appears to be a mixture of clusters 1 and 2, showing distributed activity originating from both the left and the right hemisphere (Fig. 3-10C, right). In conclusion, the results of the analysis framework indicate that the most dominant IEDs of this patient, both in number and amplitude, are initiated in the right middle frontal gyrus and right anterior insula. However, the activity originating in the left middle frontal gyrus and left anterior insula also contributes to the IEDs of this patient. Furthermore, as result of the network analysis approach it appears that the electrodes in the left middle frontal gyrus and left anterior insula are leading in cluster 1. For cluster 2, concordance of the focal areas identified in the right hemisphere, at electrodes RX and RY, and the SOZ is measured at 56% (see Table 3.2, column 6). Evidently, the focal area identified by cluster 1 at electrodes LX and LC did not overlap with the SOZ as identified by visual review of the SEEG recordings. After surgical intervention of the right middle frontal gyrus the seizures started to reoccur, but now clearly with a left hemispheric origin, thus indicating that surgical intervention was successful for the seizures arising from the right hemisphere.

3.4 Discussion

A framework developed to map the spatiotemporal interactions of interictal stereo-EEG recordings was evaluated, retrospectively, for epilepsy surgery candidates (N=7). For five of these patients who underwent successful surgery it was investigated whether multiple focal brain areas were interacting. Furthermore, the leading brain area was identified and related to the electro-clinical hypotheses with regard to the SOZ. The additional value of the analysis framework was further demonstrated by the presentation of the results for two patients with complex network interactions underlying their IEDs. These patients had no satisfactory seizure outcome despite long term SEEG recordings guiding their surgery. The analysis framework applied to the SEEG recordings of these two patients yielded spike clusters originating in leading brain areas, which did not coincide with the resected area. The results presented here provide evidence that for these patients systematic network analysis of the activity underlying the IEDs would have been of importance in addition to routine review of SEEG recordings to guide resective surgery.

3.4.1 Methodology: limitations and improvements

In order to study the couplings and time delays between SEEG signals during the occurrence of IEDs non-linear correlation analysis was applied. Contrary to the commonly used method (see e.g. Wendling et al. [230]; van Houdt et al. [221]) the time delay estimation is based on the average correlation function of a large number of IEDs. In this study a matrix representation is used for the correlation and time delay estimates in order 1) to avoid errors due to highly varying correlation values at distinct contact points of a particular electrode, and 2) to enable regularization of the delay estimations. The newly introduced regularization procedure led to a delay matrix that contains fewer outliers and reflects a range of delay values that is within a more plausible range based on physiological expectations. In case of high variability of the interictal spike activity, like for patient 7, the delay estimation appears to be inaccurate despite regularization. Therefore, an al-

ternative approach for delay estimation was introduced, which diminishes the influence of IEDs of deviating shape, resulting in a more accurate delay estimation for such cases.

The current study adopts and extends the use of the GLM approach firstly introduced by van Houdt et al. [221] for the purpose of the identification of these brain areas that generate highly synchronized activity during the occurrence of the IEDs. The application of the GLM is a crucial step preceding ICA based on individual IEDs, because it reduces the number of signals to be analyzed, leading to better modeling outcomes and significantly reduced computation time. The outcome of the GLM is represented in a β-matrix, which, contrary to the approach introduced by van Houdt et al. [221], does not require the averaging of the time-varying correlation of multiple depth electrode signals. Nonsignificant and false positive matrix entries could in most cases be removed successfully from the β-matrix through statistical significance testing and through symmetry filtering. Correcting for multiple comparisons through the FDR method effectively imposes stricter requirements on the p-value, which, especially for large matrices, is important to reduce false positives. Imposing a requirement on symmetry was effective in reducing outliers in the β-matrix. However, if it is not possible to reduce the number of SEEG signals, as was the case for patient 5, a high number of multicolinear variables remain, which have an adverse effect on the performance of ICA because 1) an artifactual source present in the EEG may be spread out over multiple components, and 2) a single SEEG signal is representing multiple components. A possible solution is to apply principal component analysis (PCA) as a dimension reduction step before applying ICA [89]. An unexpected outcome of the GLM analysis was that its results reflect negative values for several patients, which were retained regardless of the filtering procedure based on FDR-adjusted p-values or by imposing a symmetry requirement. Negative β-values may be the result of sudden unexplained discharges or changes of the SEEG signals that could not be adequately compensated for by the confounder density function. Overall, the GLM has proven to be useful for selecting the brain areas that generate the highly synchronized activity underlying the IEDs.

The application of ICA followed by hierarchical clustering appeared to be an effective method for identifying spike clusters with a distinct spatiotemporal pattern. The cluster-

ing of spatial distributions was inspired by Van 't Ent et al. [223] who applied spike cluster analysis of IEDs occurring in the magnetoencephalogram (MEG). The foremost limitations of the hierarchical clustering method are that it may be unclear how many spike clusters should be selected, and, secondly, which of the selected clusters reflect focal activity. In the current study, the optimal number of clusters was quantitatively determined by the gap statistic. However, the optimal number of clusters may include, regardless of the restrictive statistics, clusters with a very low number of spikes, like for patient 5 with a spike cluster originating in the left and right hippocampus. The relevance of these spike clusters remains unclear, also because they were not interacting with the spike cluster which was concordant with the SOZ. The gap statistic did not produce a conclusive answer for patient 5 (see Fig. 3-8) and patient 6 (see Fig. 3-9) since the criterion for determining the number of clusters as described by Tibshirani et al. [208] could not be met. For these cases it was possible to successfully use the interactive method described in Section 3.2.6 to estimate the number of clusters. In future work it should be investigated whether the use of advanced ICA models can yield sources with a greater statistical independence and therefore provide more robustness to noise. Examples of this type of advanced models are convolutive ICA [59] or mean-field approaches [85], which incorporate reverberations and convolutive mixing, and may be more appropriate for dealing with SEEG data than the InfoMax algorithm as applied in this study.

3.4.2   Clinical perspective

The first 24 hours of SEEG recordings generally do not reflect any seizures, but may contain a large number of IEDs and can therefore provide an initial overview of the epileptic activity patterns related to the epilepsy of a patient. In practice this could lead to a reduction of the recording time needed.

However, an important prerequisite for analysis of these SEEG data using the framework of analysis as presented is the accurate annotation of IEDs. Considerable time and effort by a skilled EEG technician is required to annotate long-term SEEG recordings. It is,

therefore, of utmost importance to proceed towards a (semi-)automatic framework for SEEG analysis through the automatic detection of IEDs.

A major limitation of any intracranial EEG-recording is the spatial resolution that can be achieved. For the five successfully operated patients the implantation strategy was mainly guided by the abnormalities visible at MRI, which limits the network analysis approach. For example, for patient 1 (see Fig. 3-6) a relatively low number of electrodes were placed in the temporal lobe, thus limiting further investigation of interactions between the left hippocampus and insular cortex. Interactions between these regions would be expected based on the classification of network interactions reported on by Kahane and Bartolomei [98]. The same limitation of spatial sampling was seen for patient 2 (see Fig. 3-7A), for whom an electrode was targeting the left hippocampus, but there were no electrodes implanted in the left temporal lobe. The implantation of depth electrodes for the two failure patients was not guided by abnormalities visible at MRI. The epileptic events of these patients were characterized by rapid, and for one of the patients generalized, propagation of the activity underlying the IEDs. Therefore, these patients received a more distributed implantation of electrodes in both hemispheres than the 5 patients who had abnormalities visible at MRI. It was shown for these patients with complex focal epilepsy, for whom seizures could not provide a conclusive clinical image, that network analysis of IEDs is potentially a valuable tool to describe the spatiotemporal interactions of the epileptic discharges and to identify the SOZ. Overall, the approach as introduced in this study might increase the success rate of resective surgery, or could be helpful to select these patients who should be further investigated as candidates for alternative treatments.

3.5   Conclusion

A framework of analysis was developed to identify the network interactions underlying the IEDs occurring in SEEG recordings. The interdependency was assessed between brain areas that reflected highly synchronized neural activity. The time delay between nodes of the network was estimated by a new robust method and was used to map the spatiotemporal network interactions. The additional value of a network analysis approach became apparent, especially, for MRI-negative patients with a complex epilepsy. In conclusion, the analysis of IEDs by the analysis framework introduced in this study is considered a valuable addition to the routine review of SEEG recordings, with the potential to increase the success rate of epilepsy surgery.

Part 2

Structural methods

Diffusion-Weighted Imaging

Chapter 4 | Framework for contextual processing

A framework is developed for the denoising of diffusion weighted imaging data and for the improvement of tractography results. The framework uses Diffusion Imaging in Python, which is a free and open source software project for computational neuroanatomy.

Chapter based on:

[1]*Meesters, S., Sanguinetti, G., Garyfallidis, E., Portegies, J., and Duits, R. (2016). Fast implementations of contextual PDE's for HARDI data processing in DIPY. Proceedings of the 16th Annual Meeting of the International Society for Magnetic Resonance in Medicine.*

[2]*Meesters, S., Sanguinetti, G., Garyfallidis, E., Portegies, J., Ossenblok, P., and Duits, R. (2016). Cleaning output of tractography via fiber to bundle coherence, a new open source implementation. Proceedings of the 22nd Annual Meeting of the Organization for Human Brain Mapping.*

4.1 Introduction

In the context of minimally invasive epilepsy treatment, it may be possible to decrease the risk of a functional deficit by mapping brain white matter structures that are in close proximity to the planned resection area or may be involved in the propagation of epileptic activity. Diffusion-weighted imaging (DWI) is a magnetic resonance imaging (MRI) technique to investigate the white matter architecture of the brain in vivo [138]. By the use of a method called tractography, it is possible to reconstruct the geometry of white matter bundles. However, a downside of DWI is that its acquired images may have a low signal-to-noise ratio (SNR). In this study, an open-source framework is introduced for the denoising of DWI data based on *contextual enhancement.* In this framework an implementation [128] is provided of a denoising method that retains the information of crossing fiber bundles [54, 52, 40, 51, 170]. The framework is based on Diffusion Imaging in Python (DIPY) [73], which is freely accessible to the neuroimaging community and can be readily included in existing processing pipelines.

Despite the effectiveness of contextual enhancement in reducing noise in diffusion imaging data, the results of tractography may contain spurious (aberrant) streamlines that are unlikely to physically exist due to their deviating geometry. Fiber to bundle coherence (FBC) measures were developed to identify and remove these spurious streamlines [127, 170]. Notably, these FBC measures are based on the same mathematical framework introduced for crossing-preserving denoising. An open-source implementation of the FBC measures is included in the framework [129].

Provided is the necessary background information on the acquisition (Section 4.2) and modeling (Section 4.3) of DWI data and the basic principles of tractography. Subsequently, the mathematics behind the methods in the framework are explained and code examples are given of the application of these methods to: 1) crossing-preserving denoising of a coronal slice of DWI data (Section 4.6); and 2) remove spurious fibers from tractography results of the optic radiation (Section 4.7).

4.2   Diffusion-weighted imaging

The basic principle of DWI is to measure the diffusion constant of water molecules. Diffusion is also called intra-voxel incoherent motion, random motion or Brownian motion, and results from random thermal agitation [138]. It is unrelated to physiological motion: even water molecules in a static compartment can exhibit IVIM unless the water is frozen. Albert Einstein characterized this random motion according to $\sigma = \sqrt{2Dt}$, where σ is the mean (average) diffusion distance, D the diffusion coefficient, and t the diffusion time [61].

To explain the concept of applying diffusion to reconstruct the white matter architecture of the brain, one may compare the diffusion of water to a drop of ink on a piece of paper. After a time lapse it will spread due to thermal motion of its molecules and the stain reveals something about the underlying fiber structure of the paper. If the stain is elongated this is called anisotropic diffusion, suggesting a higher fiber density in the direction of the stain [139]. Applied to the human brain, anisotropy in diffusion reveals information about the local direction of nerve fibers. The basic premise is that in white matter tissues the random walk of water molecules is restricted by barriers and can move more easily along the axonal bundles [139, 138, 108]. In a short time frame, these restrictions do not affect the diffusion coefficient. However, during a longer time period the observed diffusion coefficient is restricted. For this reason we speak of an *apparent* diffusion coefficient [225].

In MRI, sensitization to water diffusion is achieved by using the Pulsed Gradient Spin-Echo (PGSE) sequence [202]. Following this sequence, the hydrogen spins are first dephased by applying a gradient, which labels each spin with a dependency on location. After a certain time duration, a rephasing gradient is applied to refocus the spins. Molecules that have moved in random directions due to diffusion cannot be refocused, leading to a measurable loss of signal. The experiment can be designed in such a way that the typical signal loss lies between 10–90% [138]. The attenuation of the measured signal S depends on the diffusion constant D and the diffusion weighting b-value, according to the Stejskal-Tanner equation

[202] as follows

$$S = S_0 e^{-bD}. \tag{4.1}$$

The b-value is defined by the gradient strength $G = |\mathbf{G}|$, the gyromagnetic ratio γ and diffusion weighting times δ and Δ in units of s/mm^2 according to

$$b = \gamma^2 G^2 \delta^2 \left(\Delta - \frac{\delta}{3} \right). \tag{4.2}$$

The b-value is usually changed by controlling the gradient strength G. This is preferred over changing the separation Δ of the two gradient pulses, in order to have unaffected relaxation times.

The diffusion coefficient D is measured along the direction of G, and can be estimated from two acquisitions with different b-values. The chosen value of b for the first acquisition is usually close to zero. In Eq: 4.1 this effectively leads to the acquisition of S_0, which has a negligible amount of sensitivity to diffusion. The second experiment measures S_1 and uses a non-zero b-value. The diffusion coefficient is then found according to

$$D = -\frac{1}{b} \ln \left(\frac{S_1}{S_0} \right). \tag{4.3}$$

In Fig. 4-1 an anatomical image weighted by the diffusion coefficient is compared against common MRI weighting schemes, such as proton density, T1, and T2 (c.f. Appendix A).
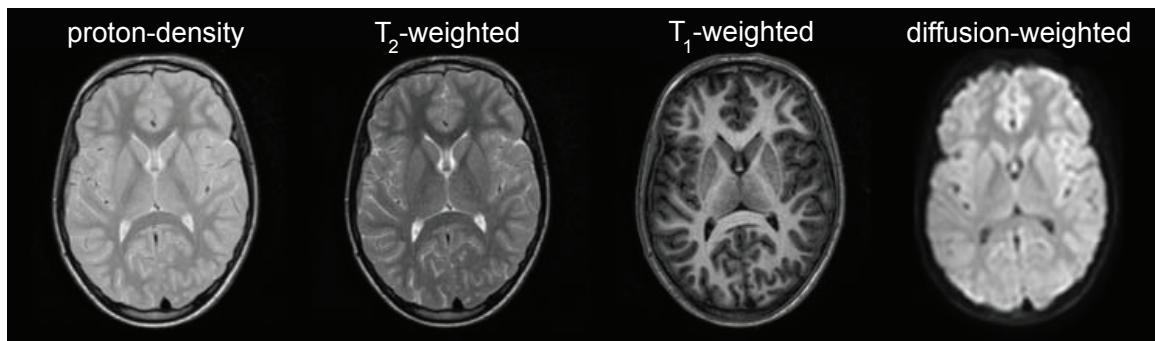

Figure 4-1: Various types of intensity weighting in MRI. Adapted from Mori [139].

4.3 Diffusion modeling

In order to gain insight in brain connectivity using DWI, it is necessary to infer biologically meaningful parameters from the data through the application of *mathematical models*. The diffusion coefficient that is estimated is highly dependent on the orientation in which the scan was made. Except for regions of high diffusion isotropy, such as the ventricular system of the brain containing free-flowing cerebrospinal fluid, a large variability in the diffusion coefficient is seen along uniform directions on the sphere. Expanding upon Eq. (4.1), the diffusion in the gradient sensitizing direction $\mathbf{g}$ can be modeled according to

$$S(\mathbf{x}, \mathbf{g}, \tau) = S_0(\mathbf{x}) e^{-b \mathbf{g}^T \mathbf{D}(\mathbf{x}, \tau) \mathbf{g}}, \tag{4.4}$$

where $\mathbf{g} = \frac{\mathbf{G}}{\|\mathbf{G}\|} \in \mathbb{R}^3$, for a field gradient $\mathbf{G}$ applied in an arbitrary direction, and $\mathbf{D} = \mathbf{D}(\mathbf{x}, \tau) \in \mathbb{R}^{3 \times 3}$ is the second-order *diffusion tensor* [15] at a position $\mathbf{x} \in \mathbb{R}^3$ and τ is the effective diffusion weighting time. Due to the quadratic restriction imposed in Eq. (4.4), a minimum of six measurements are required to construct the tensor as there are six unknown variables to estimate (i.e. the elements of the symmetric matrix $\mathbf{D}$). In practice, a larger number of measurements is used to achieve a better SNR, leading to a more robust estimation of the diffusion tensor. For a common diffusion tensor imaging (DTI) protocol with a b-value of 1000 s/mm^2 the number of gradient directions is usually around 30. Furthermore, the protocol requires the acquisition of at least one b=0 image.

The diffusion tensor can be analyzed to provide information on tissue micro-structure. The mean diffusivity characterizes the mean-squared displacement of molecules and the overall restriction of the diffusion of water molecules, as follows

$$\text{Mean diffusivity} = \frac{1}{3} \text{tr}(\mathbf{D}). \tag{4.5}$$

The three principal diffusivities of $\mathbf{D}$ correspond to its eigenvalues ($\lambda_1 \geq \lambda_2 \geq \lambda_3 > 0$) along its principal directions represented by the eigenvectors ($\mathbf{v_1}, \mathbf{v_2}, \mathbf{v_3}$). Classically,

the diffusion tensor is visualized using ellipsoids whose major and minor axes are scaled by the eigenvalues and whose orientations are determined by the eigenvectors [14], as illustrated in Fig. 4-2. Such a visual primitive is called a glyph. Besides the ellipsoid shape, other types of glyph visualization exist, such as superquadratic glyphs [62] or Reynolds glyphs [136].
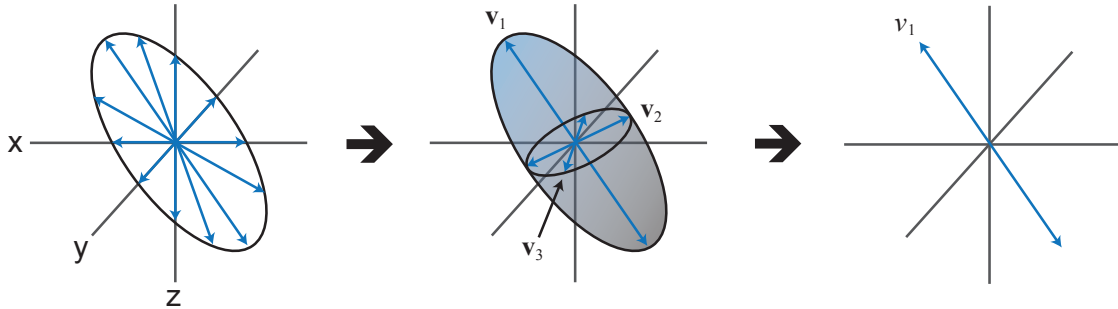
Figure 4-2: The visualization of a diffusion tensor as an ellipsoid glyph.

The shape of the diffusion tensor can be quantified by tensor anisotropy measures, which are based on the eigenvalues of the tensor. The fractional anisotropy (FA) is the most widely used anisotropy measure and effectively measures the difference of the tensor ellipsoid's shape from that of a perfect sphere [151]. The FA measure is given by

$$\text{FA} = \sqrt{\frac{1}{2}} \frac{\sqrt{(\lambda_1 - \lambda_2)^2 + (\lambda_2 - \lambda_3)^2 + (\lambda_3 - \lambda_1)^2}}{\sqrt{\lambda_1^2 + \lambda_2^2 + \lambda_3^2}}. \tag{4.6}$$

The degree of anisotropy is related to the presence of oriented structures, ranging from 0 (isotropic) to 1 (anisotropic). In Fig. 4-3 the glyphs of a coronal section of the human brain are shown, illustrating isotropic glyphs in the ventricular system as a result of unobstructed diffusion, and anisotropic glyphs in the corpus callosum as a result of highly aligned fibers.
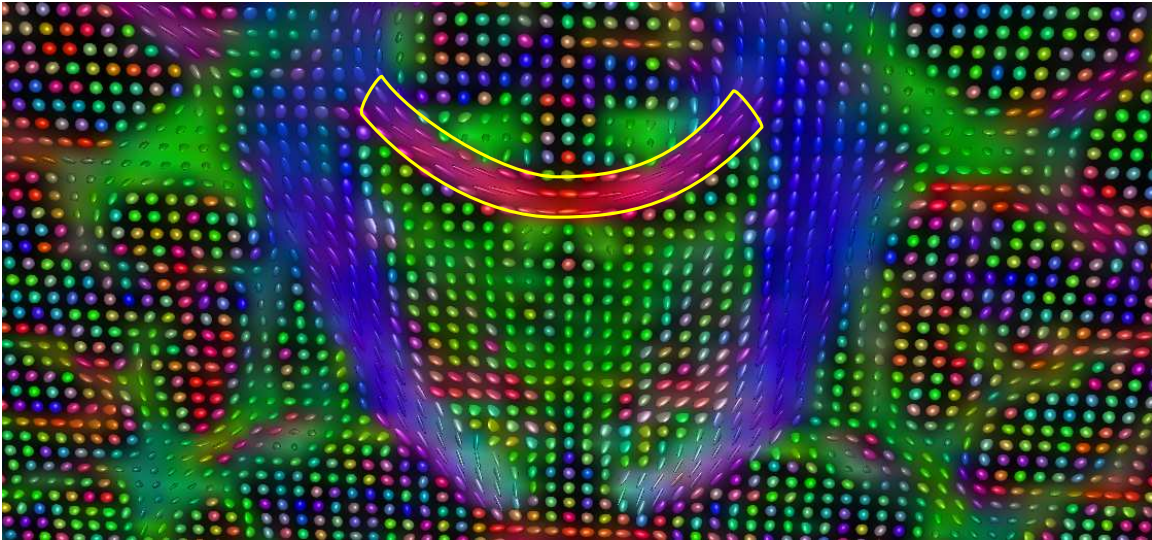
Figure 4-3: Ellipsoid glyphs shown at the corpus callosum region, outlined in yellow. The glyphs are color-coded according to the direction of the largest eigenvector of the tensor (red=left-right, green=anterior-posterior, blue=inferior-superior).

Higher-order models of diffusion

Due to its robustness, conceptual simplicity and moderate acquisition demands, the diffusion tensor model is the most commonly used technique to model the diffusion signal. However, a limitation of DTI is that it can extract only a single fiber direction from the DWI data [212]. The diffusion tensor model is therefore not suitable for describing regions of crossing fiber tracts, such as the cross-over region between the corpus callosum and the corona radiata, leading to low FA values [17]. To overcome the limited angular resolution of the DTI acquisition scheme, a high angular resolution diffusion imaging (HARDI) acquisition scheme [215] may be used, which uses a larger number of gradient directions (30-100), and typically a larger b-value (1000 to 3000 s/mm^2). Commonly associated with HARDI acquisition schemes is the use of higher-order models for characterizing diffusion. Examples of such higher-order models are multi-tensor reconstruction [215], the q-ball model [214], the diffusion orientation transform [157], constrained spherical deconvolution [209, 212], higher-order tensor fitting [189], Mean Apparent Propagator (MAP-MRI) [156], and multi-tensor MAP-MRI [246].

Fiber orientation density function

Using the Q-ball model it is possible to estimate an orientation distribution function (ODF) from the HARDI data, which computes a probability distribution of diffusion displacement based on the Funk-Radon transform [214]. The ODF is a probability distribution that is defined in the space of positions and orientations $\mathbb{R}^3 \times S^2$. While it was not the original purpose of Q-ball imaging, the ODF can be used for estimating multiple fiber orientations, which is especially useful for resolving regions of crossing fibers. In Fig. 4-4 the representations of diffusion tensors and the ODF are shown side-by-side.

The current state-of-the-art method for estimating the *fiber orientation distribution* (FOD), is constrained spherical deconvolution (CSD) [211, 209, 212]. Central in the approach of CSD is the estimation of a response function that represents the diffusion displacement
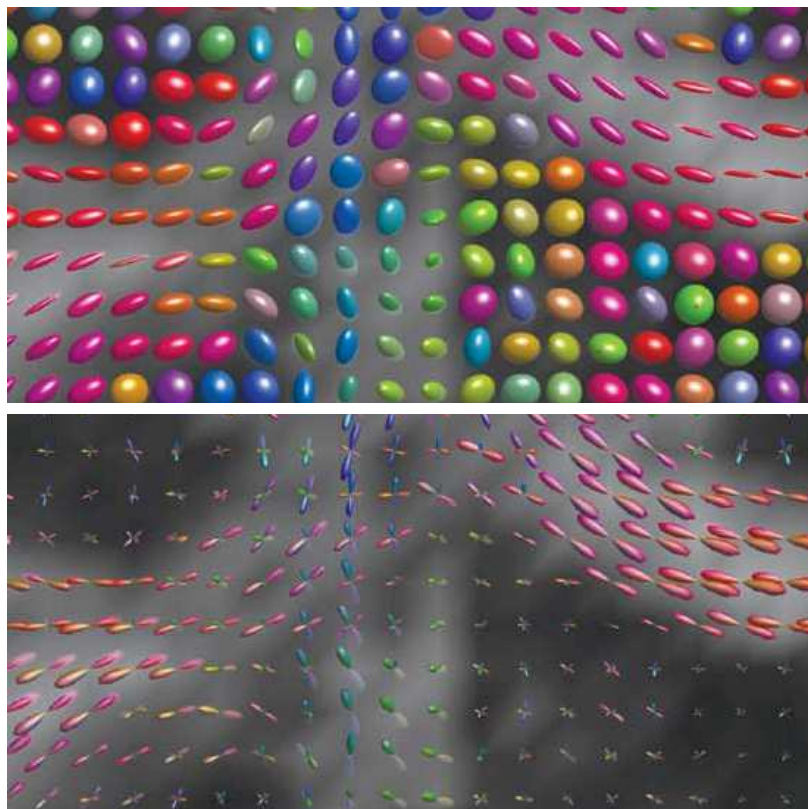

Figure 4-4: Comparison of diffusion tensors glyphs (top) and ODF glyphs (bottom) in the corpus callosum region, superimposed on a FA map. The tensor glyphs are color-coded by their main orientation, and the ODF glyphs are colored by their local orientation. Adapted from Jeurissen [92].

that corresponds to a single fiber population. The signal $s(\mathbf{n})$ that is measured in a voxel containing multiple fiber orientations can be modeled as the sum of weighted response functions. Such a signal is expressed by a spherical convolution of the response function R and the FOD function W

$$s(\mathbf{n}) = (W *_{S_2} R)(\mathbf{n}) \tag{4.7}$$

The FOD function W, which is the remaining unknown variable, can be estimated by the so-called spherical deconvolution method [211] of Eq. (4.7). To perform spherical deconvolution it is convenient to transform the data into a spherical harmonics representation. For more details regarding spherical harmonics, the reader is referred to [84]. In this representation, a convolution operation simply consists of a matrix multiplication, and deconvolution is done by matrix inversion. However, inverse solutions such as the spherical deconvolution operation are ill-posed and susceptible to noise. To resolve this issue, Tikhonov regularization is used with a positivity constraint to minimize the appearance of artifactual negative values in the FOD [212], leading to dramatically reduced noise sensitivity.

4.4   Tractography

The characterization of the diffusion data by a tensor or by a higher-order model gives an indication of the main orientation of fibers at every point in the brain. Connecting these local directions, it is possible to reconstruct pathways and identify anatomical connections in the human brain. This process is referred to as *tractography*, which in its simplest deterministic form starts from a seed location and generates a pathway by a sequence of discrete, locally optimal decisions. The pathway is terminated according to some criteria, e.g. if the pathway enters a region of low FA value in which the next direction is uncertain, such as illustrated in Fig. 4-5a (red cross).

(a) PDD   (b) Probabilistic
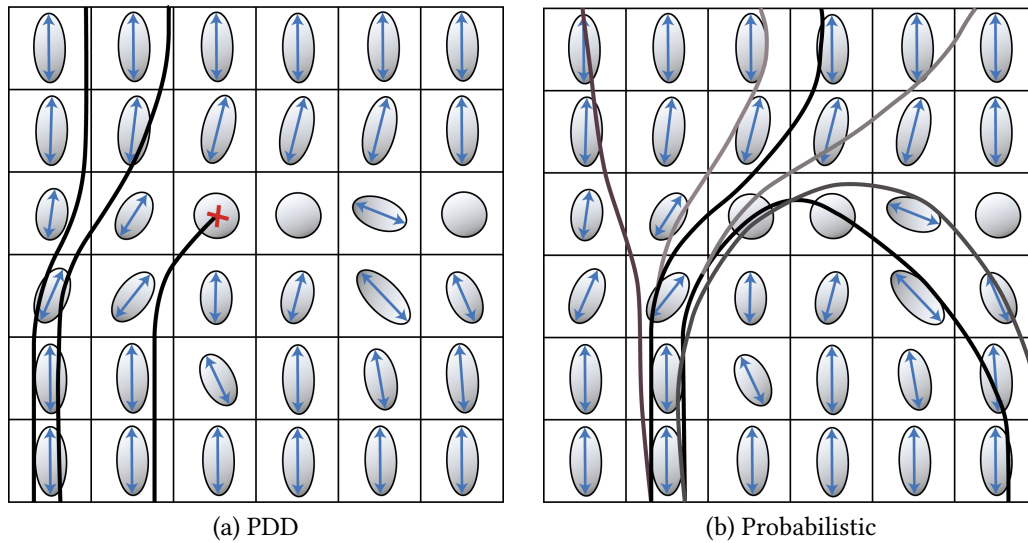
Figure 4-5: Principal diffusion direction (PDD) (a) and probabilistic (b) methods of trac-
tography. The image shows a grid of diffusion tensors and their principal directions. In
PDD tracking, tracts are terminated in regions with low anisotropy. In probabilistic track-
ing, the tracts are not terminated but the propagation direction is taken randomly, which
allows the algorithm to find new routes.

A basic algorithm for deterministic tractography is the principal diffusion direction (PDD)
method [16], in which a tract is obtained by following the main eigenvector $\mathbf{v_1}$ of the dif-
fusion tensor. Algorithms of this type have the advantage of simplicity and speed and the
generated streamlines can be easily visualized and analyzed. However, a severe limitation
of PDD tractography is that it cannot account for the uncertainty in the data [48, 193].
Uncertainty in the data arises from noise and from the used models that are never per-
fectly accurate. A second limitation is that it does not allow for distributed connectivity
since there is a unique solution for each pathway.

To overcome the limitations of PDD tractography, different classes of algorithms have
been developed based on *probabilistic* and *geodesic* tractography. Probabilistic tractogra-
phy is characterized by the generation of a large amount of streamlines and the use of
relatively loose constraints on streamline termination. In Fig. 4-5 the difference is illus-
trated between PDD and probabilistic tractography methods, showing that probabilistic
tractography is able to traverse through regions of unclear fiber orientation. An impor-
tant advantage is the ability to generate probabilistic maps of streamline connectivity

between brain regions. These maps can e.g. be used for the estimation of a voxel-based connectivity index to map potential structural abnormalities related to pathology.

An independent class of tractography algorithms is geodesic tractography, which is based on finding the path that is globally optimal with respect to some underlying distance metric. Instead of generating streamlines through a series of local decisions, geodesic tractography can infer connectivity by globally optimizing a certain cost function [150, 112, 70, 71]. By doing so it can avoid potential errors caused by a noisy local diffusion profile. A globally optimal path may be obtained by solving the static of time dependent Hamilton-Jacobi (HJ) equation, which describes the distance from an initial point to any point of the domain induced by a front propagation subject to a local speed function [190]. One method to solve the static HJ equation is the (anisotropic) Fast Marching technique, which will be discussed in Chapter 6.

4.5   Framework for Diffusion Imaging in Python

DIPY (Diffusion Imaging in Python) [73] is an open-source DWI analysis library based on the Python language. The DIPY library provides a broad spectrum of methods for processing DWI data, which includes the pre-processing of diffusion data, modeling of diffusion data, fiber tractography and post-processing, and visualization. In Fig. 4-6 an overview is given of the functions in the DIPY framework. The NeuroImaging in Python (NIPY) community, which DIPY is part of, is based around high-performance Python libraries that are tailored towards the processing of neuroimaging data. DIPY makes use of Numpy, which provides efficient numerical computations of linear algebra operations on matrices, vectors and tensors. Furthermore, Scipy is used, a Python library for interfacing with the neuroimaging formats available, such as the commonly used NIfTI-1 format. Lastly, Cython is used for its high-speed modules, which is a subset of the Python programming language designed to provide C-like performance with code written mostly in Python. See Fig. 4-6 for an overview of the used Python libraries together with DIPY. In the next two sections the implementation in DIPY of contextual enhancement and of fiber to bundle coherence measures will explained and demonstrated.
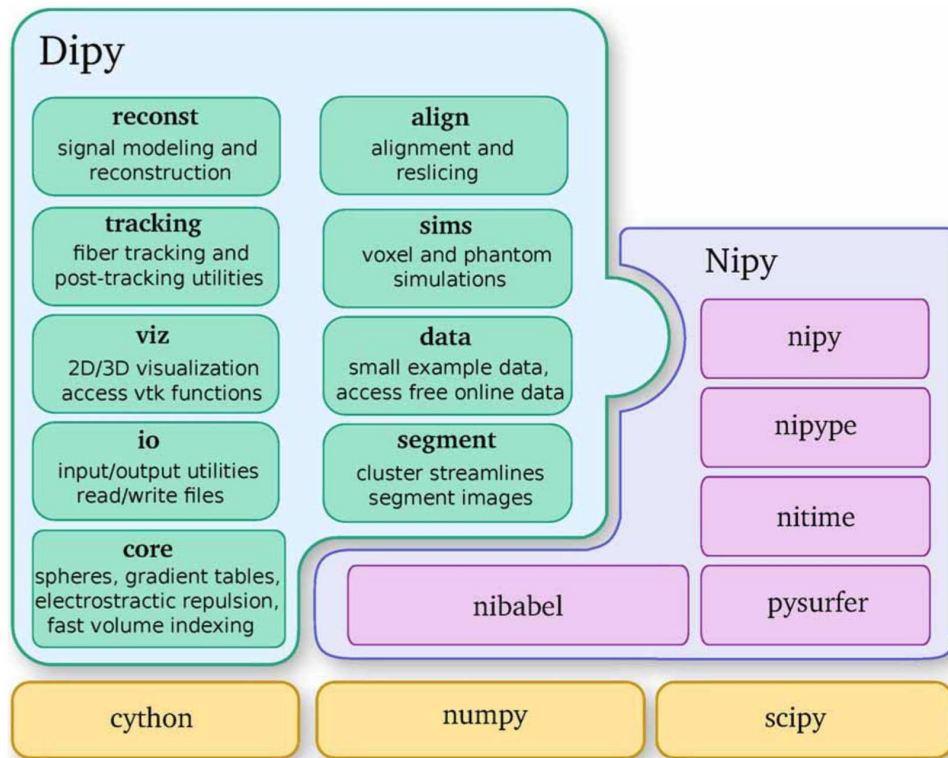
Figure 4-6: Overview of the functions in the DIPY framework and its integration in the NIPY framework. Furthermore, it depends on the Python libraries Numpy, Scipy and Cython. Adapted from [73].

4.6 Contextual enhancement of DWI data

A shortcoming of DWI is that it is inherently a low-SNR and slow imaging technique [139]. Especially at high b-values, such as those used by the HARDI acquisition scheme, the SNR of the acquired image becomes significantly reduced. Developments in MRI acquisition have made it possible to reach a higher SNR, for example through the use of a birdcage head coil, parallel imaging techniques such as sensitivity encoding (SENSE) [173] or generalized autocalibrating partially parallel acquisitions (GRAPPA) [79], averaging of the same image acquired multiple times, a higher field MRI strength such as 7T or even 9.4T [224], or by using an ultra-high strength gradient of up to 300 mT/m [63].

However, in a clinical setting it may not be feasible to perform a HARDI acquisition and a higher field MRI system may not be available. Another approach is to improve the SNR

by applying denoising to the diffusion data. Conventional methods for denoising MRI data are anisotropic diffusion filtering [163] and wavelet-based filters [146]. More recent approaches are non-local means filtering [123] or non-local principal component analysis (PCA) [124]. A third approach, which is considered in this thesis, is to perform denoising on the ODF fields that are derived from the diffusion data. In this chapter contextual PDE's [54, 51, 170] are implemented for the denoising of ODF fields with the aim to enhance the alignment of elongated structures in the data such that crossings are maintained while reducing noise and other small incoherent structures.

The contextual enhancement method is based on the Fokker-Planck diffusion equations [160], which describe Brownian motion on the space of positions and orientations $\mathbb{R}^3 \times S^2$. This domain carries a non-flat geometrical differential structure, which naturally expresses a notion of alignment between neighboring points. The coupling between positions and orientations is denoted by $\mathbb{R}^3 \rtimes S^2$, which arises from the embedding of the space of positions and orientations in the group of rigid-body motions SE(3). Further mathematics details are provided in Appendix B. Let $(\mathbf{y}, \mathbf{n}) \in \mathbb{R}^3 \rtimes S^2$ be a point in this space, where $\mathbf{y}$ and $\mathbf{n}$ denote the spatial and angular part, respectively. Furthermore, let $W_F : \mathbb{R}^3 \rtimes S^2 \times \mathbb{R}_0^+ \to \mathbb{R}$ be the function representing the evolution of the initial FOD field F, i.e. the change of the field as denoising is applied to it. Then, the contextual PDE with evolution time $t \geq 0$ is given by:

$$\begin{cases} \partial_t W_F(\mathbf{y}, \mathbf{n}, t) = (D_{\text{spat}}(\mathbf{n} \cdot \nabla_{\mathbf{y}})^2 + D_{\text{ang}}\Delta_{S^2})W_F(\mathbf{y}, \mathbf{n}, t), \\ W_F(\mathbf{y}, \mathbf{n}, 0) = F(\mathbf{y}, \mathbf{n}). \end{cases} \tag{4.8}$$

Here, $t \geq 0$ is the evolution time, $D_{\text{spat}} > 0$ is the coefficient for spatial smoothing strictly in the direction of $\mathbf{n}$. D_{ang} is the coefficient for angular smoothing and Δ_{S^2} is the Laplace-Beltrami operator on the sphere S^2. In this evolution process, $W_F(\mathbf{y}, \mathbf{n}, t)$ represents the transition density of a moving particle with position $\mathbf{y}$ and orientation $\mathbf{n}$ at the time $t \geq 0$, given that it started with the initial FOD field $F(\mathbf{y}, \mathbf{n})$ at $t = 0$. In Fig. 4-7A the stochastic process corresponding to this PDE is illustrated for a large number of moving particles.
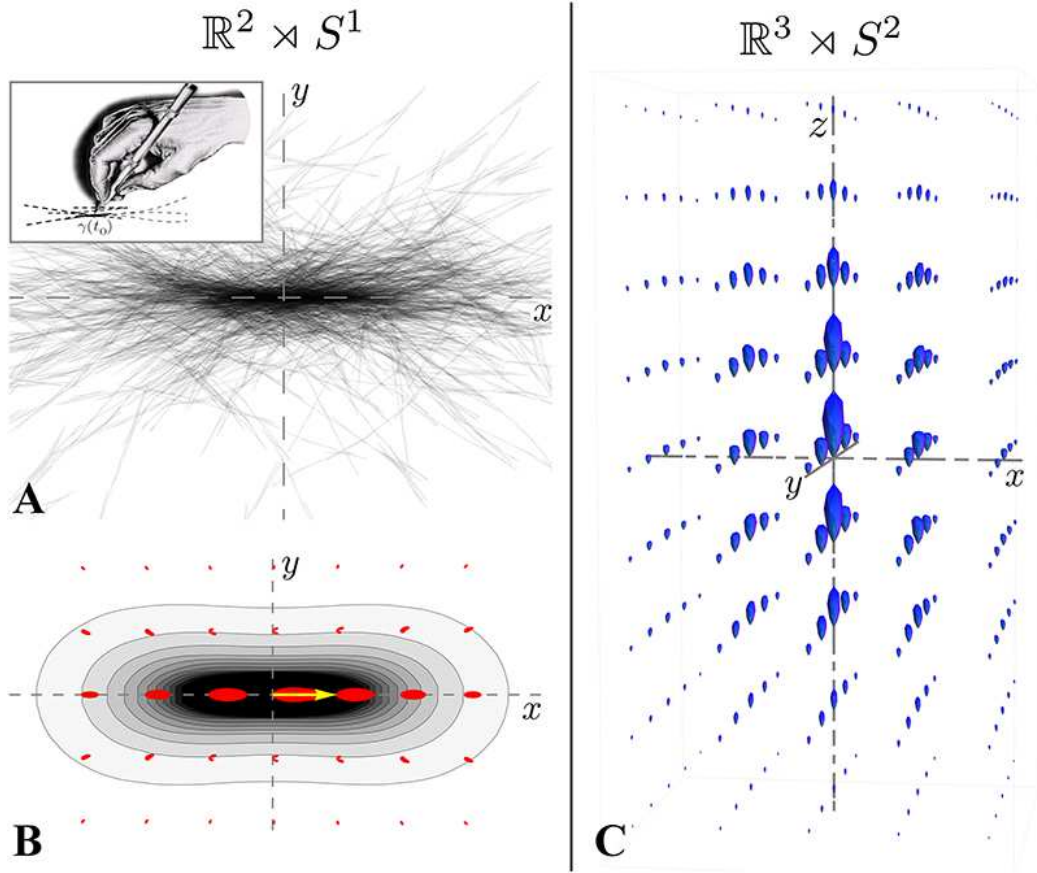
Figure 4-7: A) Random paths simulating the stochastic process. B) The contour enhancement kernel arises from the accumulation of infinitely many sample paths. The red glyphs are a representation of the contour enhancement kernel at each grid point. C) The contour enhancement kernel oriented in the positive z-direction. Figure adapted from [170].

The PDE equation is solved via a shift-twist convolution (denoted by $*_{\mathbb{R}^3 \rtimes S^2}$) of the corresponding *contour enhancement kernel* p_t with the initial FOD field $F(\mathbf{y}, \mathbf{n})$:

$$W(\mathbf{y}, \mathbf{n}, t) = (p_t *_{\mathbb{R}^3 \rtimes S^2} F)(\mathbf{y}, \mathbf{n})$$
$$= \int_{\mathbb{R}^3 \rtimes S^2} p_t(R_{\mathbf{n}'}^T(\mathbf{y} - \mathbf{y}'), R_{\mathbf{n}'}^T \mathbf{n}) F(\mathbf{y}', \mathbf{n}') d\sigma(\mathbf{n}') d\mathbf{y}'. \qquad (4.9)$$
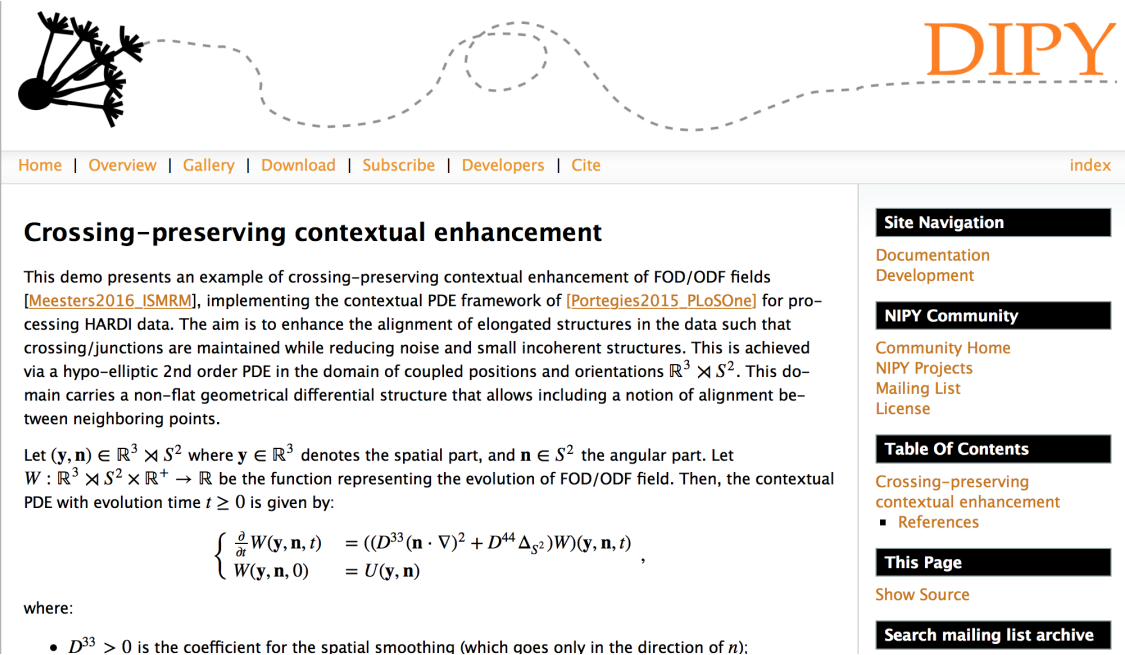
Here, $p_t(\mathbf{y}, \mathbf{n})$ denotes the kernel corresponding to the evolution process in Equation 4.8, which equals the probability density of finding a random oriented particle at position $\mathbf{y}$, with orientation $\mathbf{n}$, at time $t \in R^+$ given that it started at position $\mathbf{0}$ and upward orientation $\mathbf{e_z} \in S^2$ at time 0. The kernel thus has a probabilistic interpretation: it represents the limiting distribution of infinitely many random walkers in $\mathbb{R}^3 \times S^2$ that randomly

move forward or backward, randomly change their orientation, but cannot move sideways [54, 51, 170]. In Fig. 4-7B and C the kernel is illustrated in 2D and 3D, respectively. Furthermore, $p_t(R_{\mathbf{n}'}^T(\mathbf{y} - \mathbf{y}'), R_{\mathbf{n}'}^T\mathbf{n})$ is the probability density of finding a random oriented particle at the position $\mathbf{y}$ with orientation $\mathbf{n}$, given that it started at the position $\mathbf{y}'$ with orientation $\mathbf{n}'$ at the time $t = 0$. Here, $R_{\mathbf{n}}$ is a 3D rotation that maps the vector $\mathbf{e_z} = (0, 0, 1)$ onto $\mathbf{n}$ and $d\sigma(\mathbf{n}')$ is the usual surface measure on the sphere S^2. For exact formulas for the kernel $p_t(\mathbf{y}, \mathbf{n})$, and the Gaussian approximations that we used for our computations, see [168, 170].

The shift-twist convolutions as given in Eq. (4.9) are implemented using the Cython language and the optional multithread processing via the OpenMP library. Following ideas by Rodrigues et al. [178], further speedup is achieved by computing lookup-tables containing rotated versions of the kernel p_t sampled over a discrete set of orientations. In order to ensure rotationally invariant processing, the discrete orientations are required to be equally distributed over a sphere, which is achieved by an electrostatic repulsion model [95].

Demonstration in DIPY

An example illustrating the method is performed on the Stanford HARDI dataset [180] (150 orientations, b=2000s/mm^2) to which Rician noise is added to lower its SNR. Code examples in Python elicit the procedure and show the DIPY routines that are used. The demonstration shown here is available on the DIPY website `www.dipy.org`.

Figure 4-8: Screenshot of the DIPY website showing the contour enhancement demonstration page.

➤ The initial step is to download and parse the Standard HARDI dataset, which can be approached by the *fetch_stanford_hardi* and *read_stanford_hardi* routines of DIPY. Subsequently, Rician noise is added to the dataset in order to lower the SNR to 4.

```python
import numpy as np
from dipy.data import fetch_stanford_hardi, read_stanford_hardi
from dipy.core.gradients import gradient_table


# Read data
fetch_stanford_hardi()
img, gtab = read_stanford_hardi()
data = img.get_data()


# Add Rician noise
from dipy.segment.mask import median_otsu
from dipy.sims.voxel import add_noise
b0_slice = data[:, :, :, 1]
b0_mask, mask = median_otsu(b0_slice)
data_noisy = add_noise(data, 10.0, np.mean(b0_slice[mask]),
                       noise_type='rician')
```

➤ The FOD field is obtained by applying CSD to the dataset with added noise. The CSD model is available in DIPY by using the *ConstrainedSphericalDeconvModel* routine. For this routine a so-called gradient table is required containing the b-vecs (list of gradient orientations) and the list of corresponding b-values. Furthermore, the response function is required, which can be estimated using the *auto_response* routine.

```
from dipy.reconst.csdeconv import auto_response
from dipy.reconst.csdeconv import ConstrainedSphericalDeconvModel
response, ratio = auto_response(gtab, data, roi_radius=10, fa_thr=0.7)
csd_model_orig = ConstrainedSphericalDeconvModel(gtab, response)
csd_fit_orig = csd_model_orig.fit(data_small)
csd_shm_orig = csd_fit_orig.shm_coeff
```

➤ The next step is the creation of the enhancement kernel. For this purpose the newly created routine called *EnhancementKernel* is used, which takes the angular and spatial diffusion coefficients and the diffusion time as parameters. The resulting enhancement kernel is afterwards saved in a lookup table and stored on the hard-drive for subsequent use. For those parameters, the kernel is sampled on a 7x7x7 spatial grid and in 100 orientations. The number of orientations is an optional parameter, whereas the resolution of the kernel is determined automatically based on the input parameters.

```
from dipy.denoise.enhancement_kernel import EnhancementKernel
Dang = 1.0; Dspat = 0.02; t = 1
k = EnhancementKernel(Dang, Dspat, t)
```

➤ The shift-twist convolution is performed with the newly created routine called *convolve*, which has as input parameters the spherical harmonic representation of the noisy data, the lookup table, and the spherical harmonic order.

```
from dipy.denoise.shift_twist_convolution import convolve
csd_shm_enh = convolve(csd_shm_noisy, k, sh_order=8)
```

➤ Optionally, in order to recover more sharp angular distributions, the Spherical Deconvolution Transform (SDT) [48] can be applied by using the *odf_sh_to_sharp* routine in DIPY.

```
from dipy.reconst.csdeconv import odf_sh_to_sharp
csd_shm_enh_sharp = odf_sh_to_sharp(csd_shm_enh, sphere, sh_order=8,
                                    lambda_=0.1)
```

In Fig. 4-9 the results are shown of applying enhancement to the example dataset with added Rician noise. It can be observed that the structure of the original dataset (top-left) is significantly disrupted by the added noise (bottom-left). After enhancement the glyphs appear better aligned and structures appear more coherent (bottom-right). Crossings that were well-aligned with neighboring structures were retained. The improvement is sup-
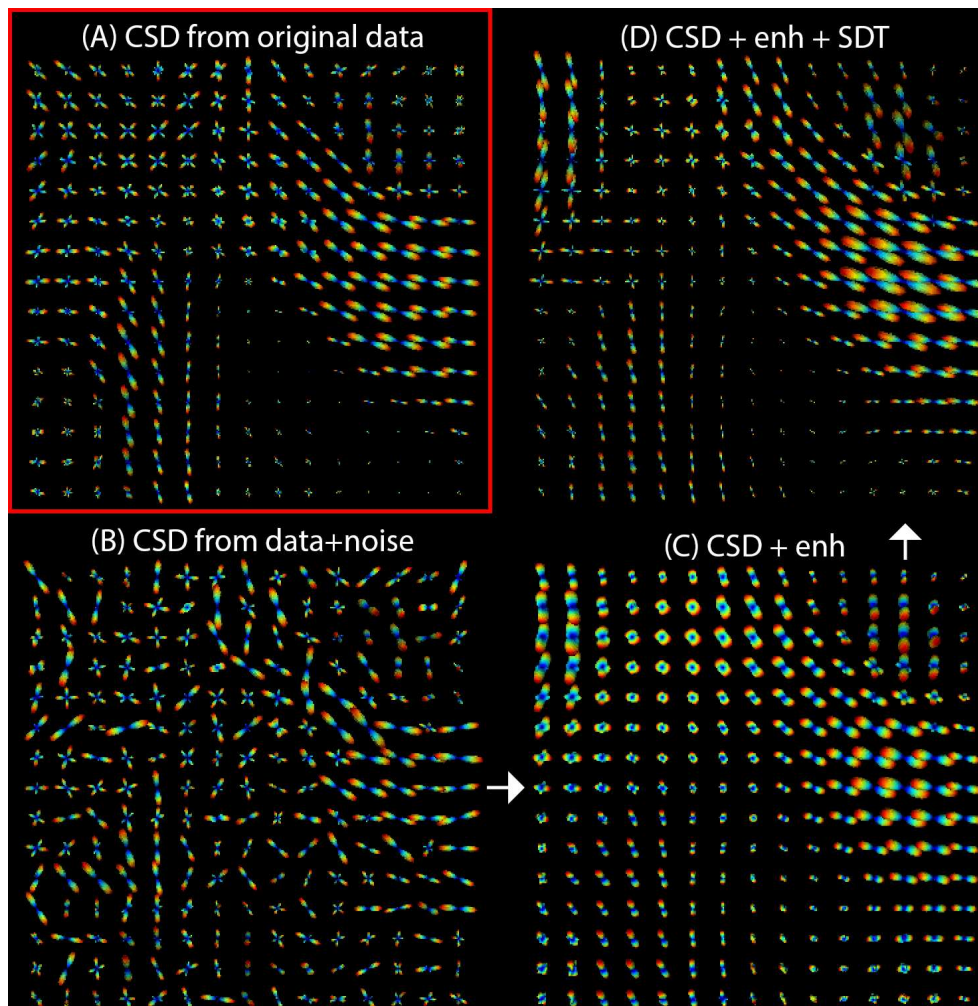
Figure 4-9: A) FOD field (only a slice 15x15 is displayed) of the original data obtained via CSD. B) CSD of the data+noise (SNR=4) C) Contextual enhancement eliminates small data incoherence and enhance elongated structures. D) Sharp angular distributions are obtained by subsequently applying the Spherical Deconvolution Transform [48].

ported quantitatively by the computation of the average angular error [43] w.r.t to the original data, which is $23.5°$ for the enhanced data and $33.8°$ for the noisy data. The SDT improves the FOD field by sharpening the peaks (top-right). Regarding computation time, after a one-time computation of the lookup-table (taking several minutes) for the same experiment a speed up of 209% is achieved w.r.t. the finite difference implementation proposed by [40] (explicit scheme, $\Delta t = 0.05$[1]).

Although contextual PDE's have proven to be useful in different clinical applications [170, 171], their use has been limited due to the lack of flexible implementations or high computational demands. The new open source module available in DIPY makes the framework presented here widely available to the neuroimaging community and flexible to be included within the existing DWI processing pipeline of DIPY. The novel implementation of the shift-twist convolution via multithreading and lookup-tables allows for large scale experiments. A similar framework can be applied to other contextual PDE applications, e.g. morphological convolutions on ODF fields [51].

4.7   Fiber to bundle coherence measures

The tractograms obtained from probabilistic tractography often reflect spurious (aberrant) streamlines. These spurious streamlines are by definition not well-aligned with neighboring streamlines and can lead to false conclusions regarding structural connectivity or the anatomical shape of a white matter structure. Fiber to bundle coherence (FBC) tractometry measures [127, 170] are introduced to quantitatively measure the alignment of streamlines and to identify and remove spurious streamlines. An open-source module is proposed, included in the DIPY library, in which the FBC measures are implemented efficiently using multithreading and pre-computed lookup tables.

---

[1]The step size chosen here is within stability criteria provided in [40].

In order to compute the FBC, streamlines are lifted to 5D curves by including the local orientation of the tangent to the streamline. A lifted streamline γ_i can be written as

$$\gamma_i = \left\{ (\mathbf{y}_i^k, \mathbf{n}_i^k) \in \mathbb{R}^3 \times S^2 \mid k = 1, \ldots, N_i \right\}, \tag{4.10}$$

where $\mathbf{y}$ and $\mathbf{n}$ contain the positions and orientations of streamline elements, N_i is the number of points in the streamline and i denotes the index within the streamline bundle $\Gamma = \bigcup_{i=1}^N \{\gamma_i\}$. To include a notion of alignment between neighboring streamline tangents, we embed the lifted streamlines into the differentiable manifold of the rigid-body motion Lie group SE(3). Within this differential structure, a measure is defined that quantifies the alignment of any two lifted streamline points with respect to each other in the space of positions and orientations $\mathbb{R}^3 \rtimes S^2$ [140, 36, 53]. In order to compute this measure, kernel density estimation is applied using a (hypo-elliptic) Brownian motion kernel (see Figure 4-10, top left). The FBC measure results from evaluating the kernel density estimator along each element of all lifted streamlines, shown in Figure 4-10 (top right) where the FBC is color-coded for each streamline.

A spurious streamline can be identified by a low FBC that occurs anywhere along its path. For this purpose, a scalar measure for the entire streamline is introduced, called the relative FBC (RFBC), which computes the minimum average FBC in a sliding window along the streamline $\gamma_i \in \Gamma$ relative to the bundle Γ. The RFBC for a streamline γ_i is calculated according to

$$\text{RFBC}^\alpha(\gamma_i, \Gamma) = \frac{\text{AFBC}^\alpha(\gamma_i, \Gamma)}{\text{AFBC}(\Gamma)}. \tag{4.11}$$

The numerator $\text{AFBC}^\alpha(\gamma_i, \Gamma)$ gives the minimum average FBC of any segment of length α along the streamline γ_i. The denominator $\text{AFBC}(\Gamma)$ is used for normalization and is the average FBC of all the streamlines in the bundle, computed over the entire length of each streamline. The segment length α was determined empirically as 2 mm (corresponding to 10 streamline points when using a stepsize of 0.2 mm), which is considered small enough to characterize local deviations of the streamline but contains enough streamline points for stable quantification of local FBC.
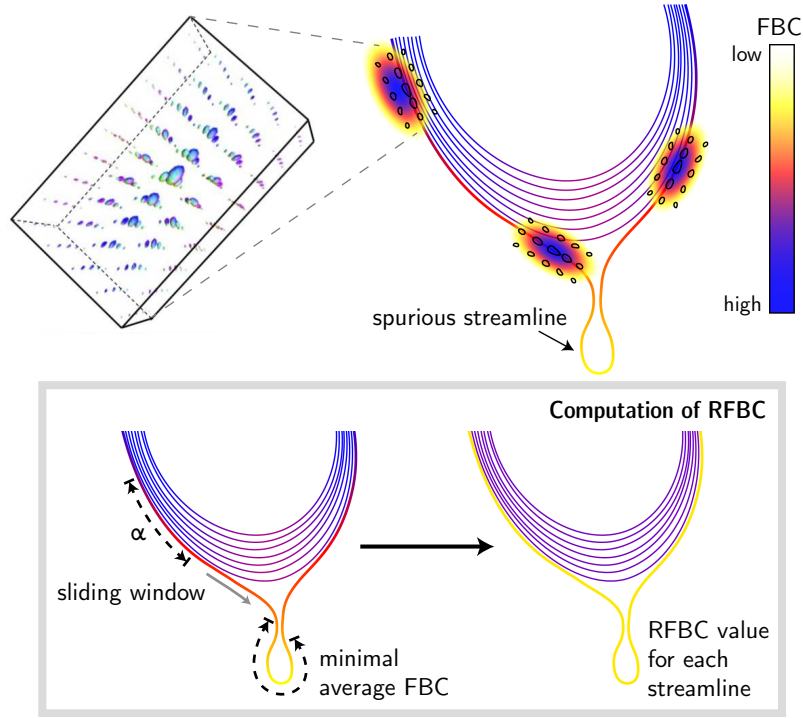
Figure 4-10: Top: The *fiber to bundle coherence* FBC measure is determined via kernel density estimation. A Brownian motion kernel on $\mathbb{R}^3 \rtimes S^2$ is used (shown left) [168, 169], which is defined on the space of positions and orientations. The streamlines are color-coded according to their FBC measure, scaled from high (blue) to low (white). Bottom: The RFBC is computed using a sliding window of size α, producing a single value for each streamline.

Mathematical details

Each equidistantly sampled streamline $\gamma_i = \left\{ \gamma_i^k \mid k = 1, \ldots, N_i \right\}$ with $\gamma_i^k = (\mathbf{y}_i^k, \mathbf{n}_i^k) \in \mathbb{R}^3 \times S^2$ is represented by delta distributions $\delta_{(\mathbf{y}_i^k, \mathbf{n}_i^k)}$. Here, N_i denotes the number of streamline points of streamline γ_i and $\mathbf{y}_i^k$ and $\mathbf{n}_i^k$ denote the position and tangent orientation of the streamline point γ_i^k, respectively. The full lifted output of the tractography is given by

$$F_\Gamma(\mathbf{y}, \mathbf{n}) = \frac{1}{N} \sum_{\sigma=1}^{2} \sum_{i=1}^{N} \sum_{k=1}^{N_i} \delta_{(\mathbf{y}_i^k, (-1)^\beta \mathbf{n}_i^k)}(\mathbf{y}, \mathbf{n}), \qquad (4.12)$$

where $\Gamma = \bigcup_{i=1}^{N} \{\gamma_i\}$ denotes the streamline bundle and N indicates the number of streamlines in the bundle Γ. The summation over β is used to account for antipodal symmetry (we identify $\mathbf{n}_i \sim -\mathbf{n}_i$) of each tangent orientation $\mathbf{n}_i$.

The Brownian motion kernel p_t (see Figure 4-10, top left) is, first of all, evaluated using pre-defined values for the spatial diffusion D_{spat}, angular diffusion D_{ang} and diffusion time t (see Section 4.6). Then, the Local FBC (LFBC) is the result of evaluating the kernel $p = p_{t,\text{fixed}}$ along each element of the lifted streamline.

$$\text{LFBC}(\mathbf{y}, \mathbf{n}, \Gamma) = (p *_{\mathbb{R}^3 \rtimes S^2} F)(\mathbf{y}, \mathbf{n}) \tag{4.13}$$

$$:= \int_{\mathbb{R}^3} \int_{S^2} p(R_{\mathbf{n}'}^T(\mathbf{y} - \mathbf{y}'), R_{\mathbf{n}'}^T \mathbf{n}) \, F_\Gamma(\mathbf{y}', \mathbf{n}') \, d\sigma(\mathbf{n}') \, d\mathbf{y}'.$$

As a result, by superposition in (4.13), $\text{LFBC}(\mathbf{y}, \mathbf{n}, \Gamma)$ denotes the probability density of finding a random oriented particle at $\mathbf{y}$ and pointing at orientation $\pm\mathbf{n}$ at time $t > 0$ given that it started at some point of the bundle Γ at $t = 0$.

A whole streamline measure, the relative FBC (RFBC), is calculated by the minimum of the moving average LFBC along the streamline γ_i

$$\text{RFBC}^\alpha(\gamma_i, \Gamma) = \frac{\text{AFBC}^\alpha(\gamma_i, \Gamma)}{\text{AFBC}(\Gamma)}, \tag{4.14}$$

where $\text{AFBC}^\alpha(\gamma_i, \Gamma)$ indicates the minimal average LFBC over a small segment of the streamline with length α, given by

$$\text{AFBC}^\alpha(\gamma_i, \Gamma) = \min_{a \in [0, l_i - \alpha]} \frac{1}{\alpha} \int_a^{a+\alpha} \text{LFBC}(\gamma_i(s), \Gamma) \, ds. \tag{4.15}$$

Here, l_i is the total length of the spatially projected curve of streamline $\gamma_i = (\mathbf{y}_i, \mathbf{n}_i)$. Furthermore, $\text{AFBC}(\Gamma)$ is the average FBC of the entire streamline bundle Γ

$$\text{AFBC}(\Gamma) = \frac{1}{N_\Gamma} \sum_{i=1}^{N_\Gamma} \text{FBC}(\gamma_i, \Gamma), \tag{4.16}$$

where

$$\text{FBC}(\gamma_i, \Gamma) = \frac{1}{l_i} \int_0^{l_i} \text{LFBC}(\gamma_i(s), \Gamma) \, ds. \tag{4.17}$$

Further details of the computation of FBC can be found in [170].

Demonstration in DIPY

The FBC measures are implemented as part of DIPY using the Cython language. To be able to use the lookup table containing the rotated versions of the contour enhancement kernel, each (continuous) streamline tangent orientation must be matched with the closest (discrete) orientation on the sphere. For efficient implementation of orientation matching, a *k*-d tree is used, which is a multi-dimensional (K=3) data structure [21] that is used to partition the discrete orientations on the sphere in small subsets. When matching a streamline tangent to a discrete orientation of the sphere, the algorithm finds the partition that the tangent vector falls into, and subsequently only requires the angular distance computations between the tangent and the discrete orientations within this partition.

➤ The first step in performing tractography in DIPY is to create a region of interest of the white matter region of the brain, which is useful for reducing unnecessary computations. To this end, a FOD field is first created using the Constant Solid Angle (CDA) ODF Model by using the *CsaOdfModel* routine. CSA is a good choice to estimate general fractional anisotropy (GFA), which the tissue classifier can use to restrict tractography to those areas where the ODF shows significant restricted diffusion. The *ThresholdTissueClassifier* requires the ODF peaks, extracted with the *peaks_from_model* routine, and a threshold on GFA.

```python
from dipy.reconst.shm import CsaOdfModel
from dipy.direction import peaks_from_model
from dipy.data import default_sphere
csa_model = CsaOdfModel(gtab, sh_order=6)
csa_peaks = peaks_from_model(csa_model, data, default_sphere,
                relative_peak_threshold=.6,
                min_separation_angle=45,
                mask=selectionmask)
# Tissue classifier
from dipy.tracking.local import ThresholdTissueClassifier
classifier = ThresholdTissueClassifier(csa_peaks.gfa, 0.25)
```

➤ Using the *ConstrainedSphericalDeconvModel* routine a FOD field is created that will be used for streamline generation.

```python
from dipy.reconst.csdeconv import auto_response
from dipy.reconst.csdeconv import ConstrainedSphericalDeconvModel
response, ratio = auto_response(gtab, data, roi_radius=10, fa_thr=0.7)
csd_model = ConstrainedSphericalDeconvModel(gtab, response)
csd_fit = csd_model.fit(data_small)
```

➤ At each streamline generation step the FOD is sampled using the *ProbabilisticDirectionGetter* routine. The parameters for this routine is the FOD field in the form of spherical harmonic coefficients, the maximal bending angle and the sampling orientations on the sphere.

```python
from dipy.direction import ProbabilisticDirectionGetter
prob_dg = ProbabilisticDirectionGetter.from_shcoeff(csd_fit.shm_coeff,
                              max_angle=30.,
                              sphere=default_sphere)
```

➤ The optic radiation is reconstructed by tracking streamlines from the calcarine sulcus (visual cortex V1) to the lateral geniculate nucleus (LGN). Seeding from the calcarine sulcus is done by manually selecting a region-of-interest (ROI) cube of dimensions $3 \times 3 \times 3$ voxels. The *seeds_from_mask* is used to convert the mask to a set of coordinates, transformed by a supplied affine matrix, and with a certain density per voxel.

```python
from dipy.tracking import utils
mask = np.zeros(data.shape[:-1], 'bool')
rad = 3
mask[26-rad:26+rad, 29-rad:29+rad, 31-rad:31+rad] = True
seeds = utils.seeds_from_mask(mask, density=[4, 4, 4], affine=affine)
```

➢   Probabilistic tractography is then performed using the *LocalTracking* routine in DIPY. This routine uses the probabilistic direction getter, the tissue classifier, the seed locations and the affine matrix as inputs.

```python
from dipy.tracking.local import LocalTracking
streamlines = LocalTracking(prob_dg, classifier, seeds, affine,
                            step_size=.2)
# Compute streamlines and store as a list.
streamlines = list(streamlines)
```

➢   In order to select only the streamlines that enter into the LGN, another ROI is created from a cube of size $5 \times 5 \times 5$ voxels. The *near_roi* command is used to find the streamlines that traverse through this ROI.

```python
# Set a mask for the lateral geniculate nucleus (LGN)
mask_lgn = np.zeros(data.shape[:-1], 'bool')
rad = 5
mask_lgn[35-rad:35+rad, 42-rad:42+rad, 28-rad:28+rad] = True


# Select all the streamlines that enter the LGN and discard all others
filtered_fibers2 = utils.near_roi(streamlines, mask_lgn, tol=1.8,
                  affine=affine)
sfil = []
for i in range(len(streamlines)):
  if filtered_fibers2[i]:
    sfil.append(streamlines[i])
streamlines = list(sfil)
```

➢   Using the *EnhancementKernel* routine that was introduced earlier, a lookup table is created or loaded from the hard disk if it already exists.

```python
from dipy.denoise.enhancement_kernel import EnhancementKernel
Dspat = 1.0;  Dang = 0.02; t = 1
k = EnhancementKernel(Dspat, Dang, t)
```

➤ The FBC measures are computed using the new routine called *FBCMeasures*, taking the streamlines and the lookup tables as input. An optional parameter is the segment length α, which is 10 streamline points by default (corresponding to 2 mm based on tractography step size).

```python
from dipy.tracking.fbcmeasures import FBCMeasures
fbc = FBCMeasures(streamlines, k)
```

➤ After the computation of the FBC measures, a threshold ϵ can be chosen on the minimal relative FBC (RFBC) required to maintain a streamline. In this example we show the results for threshold 0 (i.e. all streamlines are included) and 0.125 (removing the 12.5 percent most spurious streamlines).

```python
# Calculate LFBC for original streamlines
fbc_sl_orig, clrs_orig, rfbc_orig = \
                fbc.get_points_rfbc_thresholded(0, emphasis=0.01)


# Apply a threshold on the RFBC to remove spurious streamlines
fbc_sl_thres, clrs_thres, rfbc_thres = \
                fbc.get_points_rfbc_thresholded(0.125, emphasis=0.01)
```

The results of FBC measures are visualized in Fig. 4-11, showing the original streamlines colored by LFBC (top row), and the streamlines after the cleaning procedure via RFBC thresholding (bottom row).
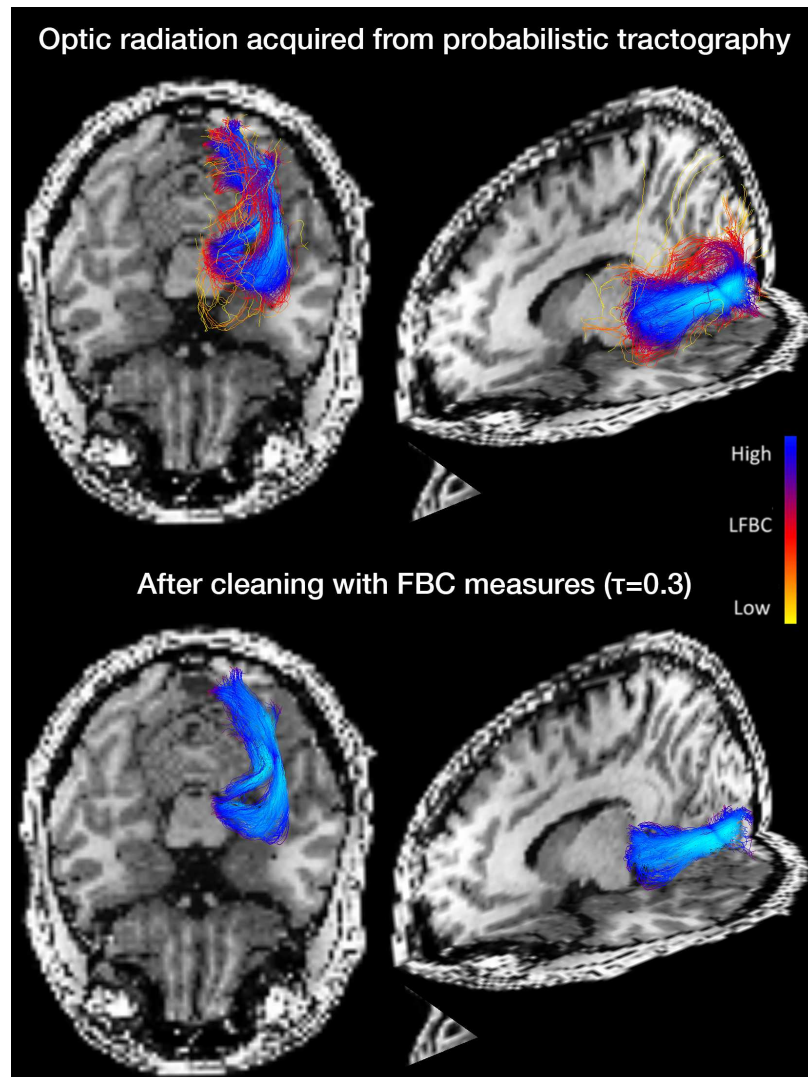
Figure 4-11: The fiber to bundle coherence (FBC) measures are demonstrated for the reconstruction of the OR. The OR is obtained through probabilistic tractography (shown at the top row). The streamlines are color-coded by the local FBC measures (LFBC). The tractography result is cleaned (shown at the bottom row) by removing streamlines with a relative FBC (RFBC) lower than the threshold $\epsilon = 0.125$.

4.7.1 Conclusion

A framework was developed for the contextual enhancement of DWI data and the removal of spurious fibers from tractography results. These newly developed methods can be readily included in a processing pipeline and are optimized to allow for large-scale experiments. In the next chapter (Chapter 5) a method is introduced for a quantitative and robust estimation of the parameter ϵ, which is important to balance the removal of spurious streamlines and retaining relevant streamlines, especially, in the Meyer loop. The contextual enhancement of FOD fields can be useful to denoise the DWI data that is used for experiments with the fast marching algorithm (Chapter 6 & Chapter 7).

Chapter 4

Chapter 5 | Robust reconstruction of the optic radiation

A framework is developed for the robust reconstruction of the optic radiation in support of temporal lobe epilepsy surgery to avoid a visual field deficit. Results of tractography often reflect spurious streamlines, which hinder an accurate identification of the tip of the Meyer's loop. Stability metrics are introduced for the automated removal of spurious streamlines near the Meyer's loop.

Chapter based on:

5.1   Introduction

The optic radiation (OR) is a collection of white matter fiber bundles which carries visual information from the thalamus to the visual cortex [181]. Numerous studies [242, 205, 35, 236, 25, 90] have accomplished to reconstruct the OR, by tracking pathways between the lateral geniculate nucleus (LGN) and the primary visual cortex using diffusion-weighted tractography. In the curved region of the OR, configurations with multiple fiber orientations appear, such as crossings, because white matter tracts of the temporal stem intermingle with the fibers of the Meyer's loop [104]. Therefore, it is especially challenging to reconstruct the Meyer's loop, which is the most vulnerable bundle of the OR in case of surgical treatment of epilepsy in which part of the temporal lobe is removed [90].

Tractography based on constrained spherical deconvolution (CSD) [209, 48] has been shown to have good fiber detection rates [235] and has been applied in several studies to reconstruct the OR [115, 125]. Furthermore, probabilistic tractography is considered superior in comparison to deterministic tractography for resolving the problem of crossing fibers in the Meyer's loop [114]. The probabilistic tracking results between the LGN and the visual cortex for a healthy volunteer are illustrated in Figure 5-1 (left). The tracking results are shown (Figure 5-1, right) in a composite image along with other brain structures such as the ventricular system, and furthermore indicates the distance from the tip of the Meyer's loop to the temporal pole (ML-TP).

In Chapter 4 it was discussed how spurious (deviating) streamlines commonly occur in tractograms obtained from probabilistic tractography. These spurious streamlines may hinder an accurate measurement of the ML-TP distance, which is required for estimating the potential damage to the OR after temporal lobe resection (TLR). Methods have been proposed for the identification and removal of spurious streamlines, for example based on outlier detection [240, 125, 103], based on the prediction of diffusion measurements by whole-brain connectomics [164], or based on the uncertainty in the main eigenvector
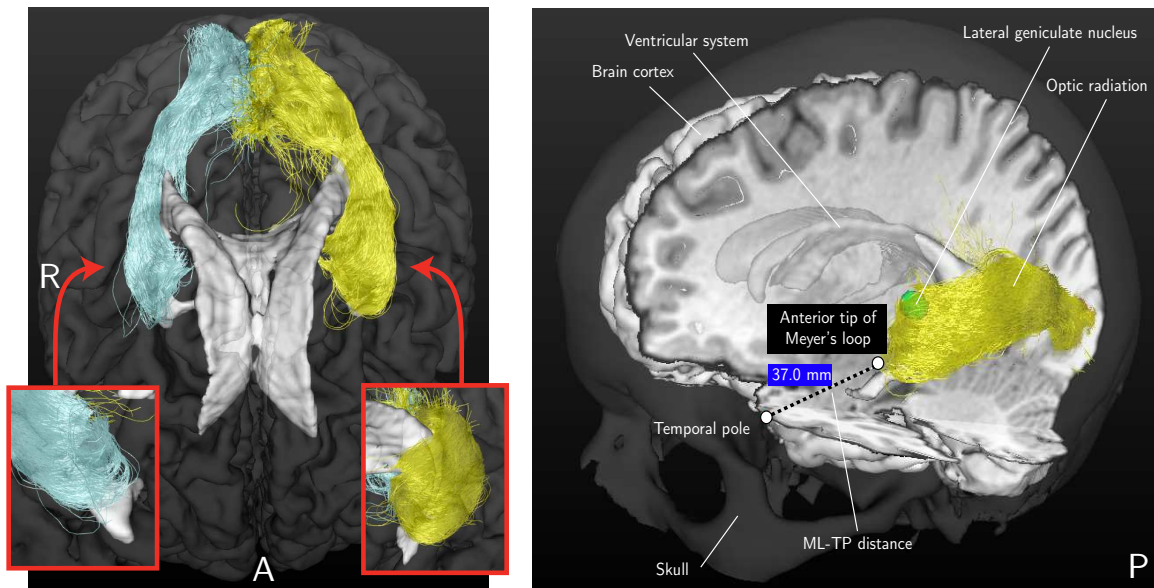
Figure 5-1: Left: An example of the reconstruction result of the OR using probabilistic tractography from an axial view. As inserts, close-ups are shown of the anterior tips of the reconstructions of the OR from a coronal view. Right: The tracking results are shown for the same volunteer in a composite image along with other brain structures such as the ventricular system. The Meyer's loop to Temporal Pole (ML-TP) distance measurement is indicated.

of the diffusion tensor [159]. Most of these methods for reducing spurious streamlines are based on density estimation in $\mathbb{R}^3$. In addition, the fiber to bundle coherence (FBC) tractometry measure introduced in Chapter 4 is based on density estimation in the space of positions and orientations $\mathbb{R}^3 \times S^2$.

To achieve a reliable reconstruction of the full extent of the Meyer's loop, an appropriate selection of streamlines is required such that spurious streamlines are removed while preserving streamlines that are anatomically more likely to exist. For this purpose the FBC parameter ϵ (c.f. Chapter 4) is estimated based on the measured variability in ML-TP distance. Here we respect an a-priori constraint on the maximal ML-TP distance variability for a test-retest procedure on streamline tracking and determine the corresponding minimal threshold $\epsilon_{\text{selected}}$ on the FBC measures. This threshold removes a minimal amount of spurious streamlines while allowing for a stable estimation of the ML-TP distance. The procedure for selecting the optimal threshold is named the stability metrics and provides a reliable OR reconstruction that is robust under stochastic realizations of probabilistic

tractography.

The validity of the distance measurements is evaluated based on pre- and post-operative comparisons of the reconstructed OR of patients who underwent a TLR. It is investigated whether it is feasible to assess pre-operatively for each individual patient the potential damage to the OR as an adverse event of the planned TLR. The deviation between the prediction of the damage to the OR and the measured damage in a post-operative image is compared, giving an indication of the overall error in distance measurement.

5.2 Materials and methods

5.2.1 Subjects

Eight healthy volunteers without any history of neurological or psychiatric disorders were included in our study. All volunteers were male and in the age range of 21–25 years. Furthermore, three patients were included who were candidates for temporal lobe epilepsy surgery. For each patient a standard pre- and post-operative T1-weighted anatomical 3D-MRI was acquired. Patient 1 (46/F) was diagnosed with a right mesiotemporal sclerosis and underwent a right TLR, including an amygdalohippocampectomy. Patient 2 (23/F) was diagnosed with a left mesiotemporal sclerosis and underwent an extended resection of the left temporal pole. Lastly, Patient 3 (38/M) was diagnosed with a cavernoma located in the basal, anterior part of the left temporal lobe and had an extended lesionectomy. All patients had pre- and post-operative perimetry carried out by consultant ophthalmologists. The study was approved by the Medical Ethical Committee of Kempenhaeghe, and informed written consent was obtained from all subjects.

5.2.2 Data acquisition

Data was acquired on a 3.0 T magnetic resonance (MR) scanner, using an eight-element SENSE head coil (Achieva, Philips Health Care, Best, The Netherlands). A T1-weighted scan was obtained for anatomical reference using a Turbo Field Echo (TFE) sequence with timing parameters for echo time (TE = 3.7 ms) and repetition time (TR = 8.1 ms). A total of 160 slices were scanned with an acquisition matrix of 224x224 with isotropic voxels of 1x1x1 mm, leading to a field of view of 224x224x160 mm. Diffusion-weighted imaging (DWI) was performed using the Single-Shot Spin-Echo Echo-Planar Imaging (SE-EPI) sequence. Diffusion sensitizing gradients were applied, according to the diffusion tensor imaging (DTI) protocol, in 32 directions with a b-value of 1000 s/mm^2 in addition to an image without diffusion weighting. A total of 60 slices were scanned with an acquisition matrix of 112x112 with isotropic voxels of 2x2x2 mm, leading to a field of view of 224x224x120 mm. A SENSE factor of 2 and a halfscan factor of 0.678 were used. Acquisition time was about 8 minutes for the DWI scan and 5 minutes for the T1-weighted scan. The maximal total study time including survey images was 20 minutes.

5.2.3 Data preprocessing

The preprocessing of the T1-weighted scan and DWI data is outlined in Figure 5-2 (top-left box). All data preprocessing is performed using a pipeline created with NiPype [76], which allows for large-scale batch processing and provides interfaces to neuroimaging packages (FSL, MRtrix). The T1-weighted scan was first aligned to the anterior commissure to posterior commissure (AC-PC) axis by affine coregistration (12 degrees-of-freedom) to the MNI152 template using the FMRIB Software Library v5.0 (FSL) [91]. Secondly, affine coregistration, considered suitable for within-subject image registration, was applied between the DWI volumes to correct for motion. Eddy current induced distortions were corrected within the Philips Achieva scanning software and did not require further post-processing. The DWI b=0 volume was subsequently affinely coregistered
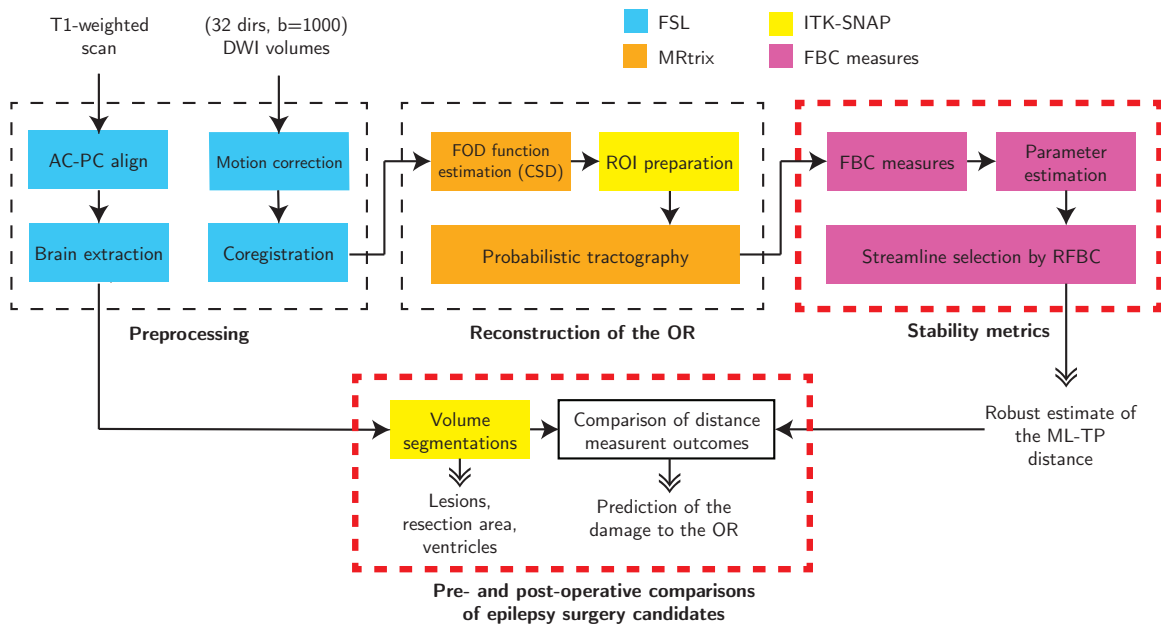
Figure 5-2: A schematic overview of the analysis procedures followed to reconstruct the optic radiation (OR) and to acquire a robust estimate of the Meyer's Loop to Temporal Pole (ML-TP) distance. The stages in which data are processed are indicated by the dashed boxes. The red dashed boxes indicate the new contributions of the study. The various software packages are color-coded. The inputs of the pipeline are a diffusion-weighted imaging (DWI) dataset and an anatomical T1-weighted MRI image. Outputs of the pipeline are shown with double-headed arrows. Abbreviations: FOD, Fiber Orientation Density; CSD, Constrained Spherical Deconvolution; ROI, Region of Interest; FBC, Fiber to Bundle Coherence; RFBC, Relative FBC.

to the axis-aligned T1-weighted scan using normalized mutual information, and the resulting transformation was applied to the other DWI volumes. The DWI volumes were resampled using linear interpolation. After coregistration, the diffusion orientations were reoriented using the corresponding transformation matrices [111].

5.2.4 Probabilistic tractography

Probabilistic tractography of the OR (outlined in Figure 5-2, top-middle box) is based on the Fiber Orientation Density (FOD) function. With probabilistic tractography, streamlines are generated between two regions of interest (ROIs): the LGN, located in the thalamus, and the primary visual cortex (see Figure 5-1). The LGN was defined manually on

the axial T1-weighted image using anatomical references (lateral and caudal to the pulvinar of the thalamus) [69] using a sphere of 4 mm radius, corresponding to a volume of 268 mm^3. The ipsilateral primary visual cortex was manually delineated on the axial and coronal T1-weighted image. The primary visual cortex ROI's used have an average volume of 1844 mm^3.

In the current study the FOD function is estimated using CSD, which is implemented in the MRtrix software package [210]. During tracking, the local fiber orientation is estimated by random sampling of the FOD function. In the MRtrix software package, rejection sampling is used to sample the FOD function in a range of directions restricted by a curvature constraint imposed on the streamlines. Streamlines are iteratively grown until no FOD function peak can be identified with an amplitude of 10% of the maximum amplitude of the FOD function [92, 210]. In MRtrix tracking, 20,000 streamlines are generated, which provides a good balance between computation time and reconstruction ability. A step size of 0.2 mm and a radius of curvature of 1 mm were used. These settings are reasonable for our application of reconstructing the OR and are recommended by Tournier et al. [210]. The FOD function was fitted with six spherical harmonic coefficients, which is suitable for the DTI scanning protocol used in this thesis.

Anatomical constraints are applied when reconstructing the OR in order to prevent the need for manual pruning of streamlines and to reduce a subjective bias. Firstly, streamlines are restricted within the ipsilateral hemisphere. Secondly, fibers of the OR are expected to pass over the temporal horn of the ventricular system [195]. The ventricular system is manually delineated using ITK-SNAP image segmentation software [244]. Streamlines that cross through the area superior-laterally to the temporal horn are retained. Thirdly, an exclusion ROI is created manually of the fornix to remove streamlines that cross this region, which is in close proximity to the LGN and Meyer's loop. Furthermore, in order to remove long anatomically implausible streamlines, the maximum length of the streamlines is set to 114 mm based on a fiber-dissection study of the OR by Peltier et al. [162].

5.2.5   Stability metrics

To control the removal of spurious streamlines the threshold parameter ϵ was introduced in Chapter 4, which is defined as the lower bound criterion on the relative fiber to bundle coherence (RFBC) that retains a streamline. More precisely, every streamline $\gamma_i \in \Gamma$ that meets the condition $\text{RFBC}^\alpha(\gamma_i, \Gamma) \geq \epsilon$ is retained. However, a careful selection of this threshold is required in order to prevent an underestimation of the full extent of the Meyer's loop. A method is introduced for the standardized selection of the minimal threshold $\epsilon_{\text{selected}}$ through test-retest evaluation of the variability in ML-TP distance. To this end, probabilistic tractography of the OR is repeated multiple times, followed by the computation of the RFBC measure in each repetition. Subsequently, a parameter sweep is performed in which ϵ is varied between $0 \leq \epsilon \leq \epsilon_{\text{max}}$ where ϵ_{max} corresponds to the state where all streamlines are removed from Γ. During every step of the parameter sweep, the ML-TP distance is calculated for all test-retest repetitions by computing the Hausdorff distance [177] between the temporal pole and the OR. Using these distance measurements, the mean and the standard deviation (variability) of the ML-TP distance are determined for each value of ϵ.

The procedure is illustrated for a healthy subject in Figure 5-3, showing the mean and standard deviation of the ML-TP distance for increasing values of ϵ. Initially, a high variability is seen at $\epsilon = 0$, indicating the presence of spurious streamlines near the anterior tip of the Meyer's loop. At $\epsilon = 0.075$ most spurious streamlines are removed and a variability in the order of several millimeters is seen. The variability rises and falls during $0.1 \leq \epsilon \leq 0.3$. A stable region is obtained at $\epsilon \approx 0.3$, however at this point too many streamlines have been discarded as a result of the condition $\text{RFBC}^\alpha(\gamma_i, \Gamma) \geq \epsilon$ and thereby the ML-TP distance will be overestimated. In order to estimate the minimal threshold $\epsilon_{\text{selected}}$, in which the ML-TP distance is neither under- nor overestimated, a maximum is set for the variability of 2 mm. This maximum is based on the maximal accuracy of 2-5 mm that may be achieved during resective surgery. In the selection procedure, ϵ is set at the first occurrence of low variability, i.e.

$$\epsilon_{\text{selected}} = \min\{\epsilon > 0 \mid \sigma(\epsilon) \leq 2\text{mm}, \sigma'(\epsilon) = 0, \sigma''(\epsilon) > 0\} \tag{5.1}$$

where $\sigma(\epsilon)$ denotes the standard deviation in ML-TP for the chosen ϵ. After crossing the 2 mm threshold on variability, $\epsilon_{\text{selected}}$ is placed on the local minimum of $\sigma(\epsilon)$. Using this procedure, in the example shown in Figure 5-3 the ML-TP is estimated for $\epsilon = 0.075$ at 36 mm. This ML-TP distance is within the range of 22 to 37 mm as reported by Ebeling & Reulen [60], who performed a dissection study on 25 human cadavers.

For the patients studied, the distance measurement outcomes are compared to the predicted damage of the OR after surgery, as outlined in Figure 5-2 (bottom row, red dashed box). The resection area is manually delineated in the post-operative T1-weighted image using ITK-SNAP [244]. The resection length is measured from the temporal pole, at the anterior tip of the middle sphenoid fossa, up to the posterior margin of the resection. The predicted damage is determined by the distance between the pre-operative ML-TP distance and the resection length. The difference between the predicted damage and the observed damage, given by the distance between pre- and post-operative ML-TP distances, is named the margin of error. The margin of error indicates the maximal error in distance measurements, which includes both the variability in probabilistic tractography and unaccounted sources of error such as brain shift or distortions.
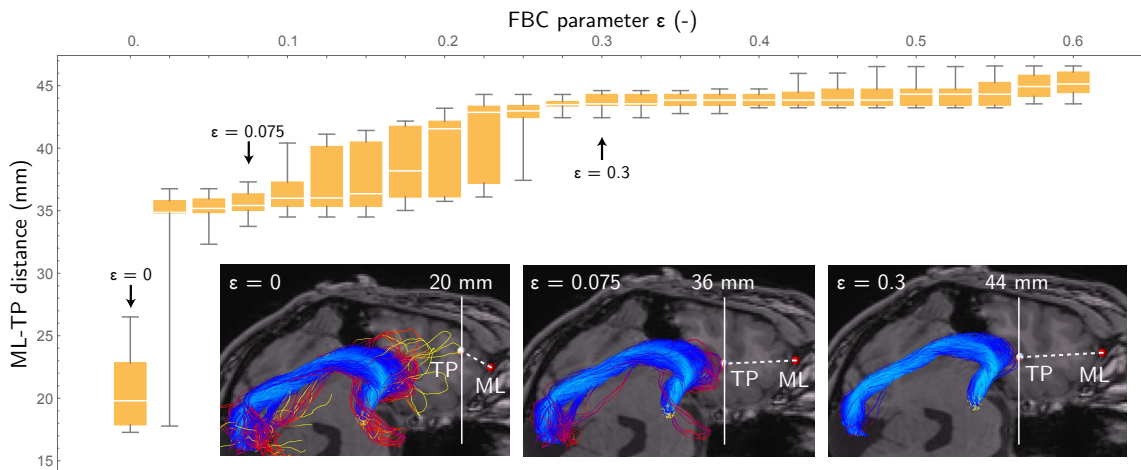
Figure 5-3: Boxplot showing the mean and standard deviation of the estimated ML-TP distances for test-retest evaluation of the reconstruction of the OR for an example healthy volunteer. A sweep from low to high ϵ is performed to evaluate the effect of removing streamlines on the stability of the estimated ML-TP distance.

5.3   Results

5.3.1   Robust estimation of ML-TP distance

The effect of the removal of spurious streamlines on the ML-TP distance measurement using the FBC measures is demonstrated for eight healthy volunteers. For each volunteer the mean ML-TP distance and its standard deviation are listed in Table 5.1 for the left and right hemisphere, together with its corresponding test-retest variability. The additional value of the FBC measures for a robust ML-TP distance measurement is further evaluated for three patients who underwent a TLR.

Volunteer	ML-TP distance		ϵ	
	Left (mm)	Right (mm)	Left (-)	Right (-)
1	36.4 ± 1.5	32.1 ± 1.3	0.075	0.15
2	30.0 ± 0.6	27.8 ± 1.0	0.13	0.14
3	33.4 ± 1.5	23.5 ± 0.9	0.2	0.35
4	34.9 ± 1.7	31.4 ± 0.2	0.45	0.1
5	36.8 ± 1.4	32.2 ± 1.0	0.075	0.33
6	28.3 ± 0.3	25.8 ± 0.6	0.025	0.28
7	32.3 ± 0.4	23.4 ± 1.1	0.15	0.05
8	22.5 ± 0.5	30.7 ± 1.0	0.125	0.18

Table 5.1: Listed are the ML-TP distances estimated for the left and right hemispheres of the healthy volunteers studied (N=8) and the corresponding selected values for the FBC thresholding parameter ϵ.

The parameter estimation based on test-retest evaluation is illustrated in Figure 5-4 for the reconstructed OR of the left hemisphere for the eight healthy volunteers studied, showing for a range of parameter ϵ (0 - 0.6) the standard deviation (left) and the mean (right) of the estimated ML-TP distance. The test-retest evaluation was performed with 10 repeated tractograms of the OR, which was empirically determined to be a good balance between group size and computation time. For all volunteers evaluated, a high standard deviation

of the ML-TP distance (over 2 mm) was observed at low values of ϵ (0.0 - 0.05), which indicates the presence of spurious streamlines with a very low RFBC. The corresponding mean ML-TP distance reflects large jumps for an increase of the value of ϵ from 0 to 0.05, showing an average increase for the eight healthy volunteers of 8 mm. For each healthy volunteer the $\epsilon_{\text{selected}}$ is selected according to Equation 5.1. The $\epsilon_{\text{selected}}$ corresponds to a mean ML-TP distance that is depicted by the arrows in Figure 5-4 (right) for the eight healthy volunteers studied. After the initial high variability of the ML-TP distance, a stable region occurred for all healthy volunteers in which the standard deviation was below 2 mm. The healthy volunteers 1, 4 and 5 indicated regions of instability (standard deviation
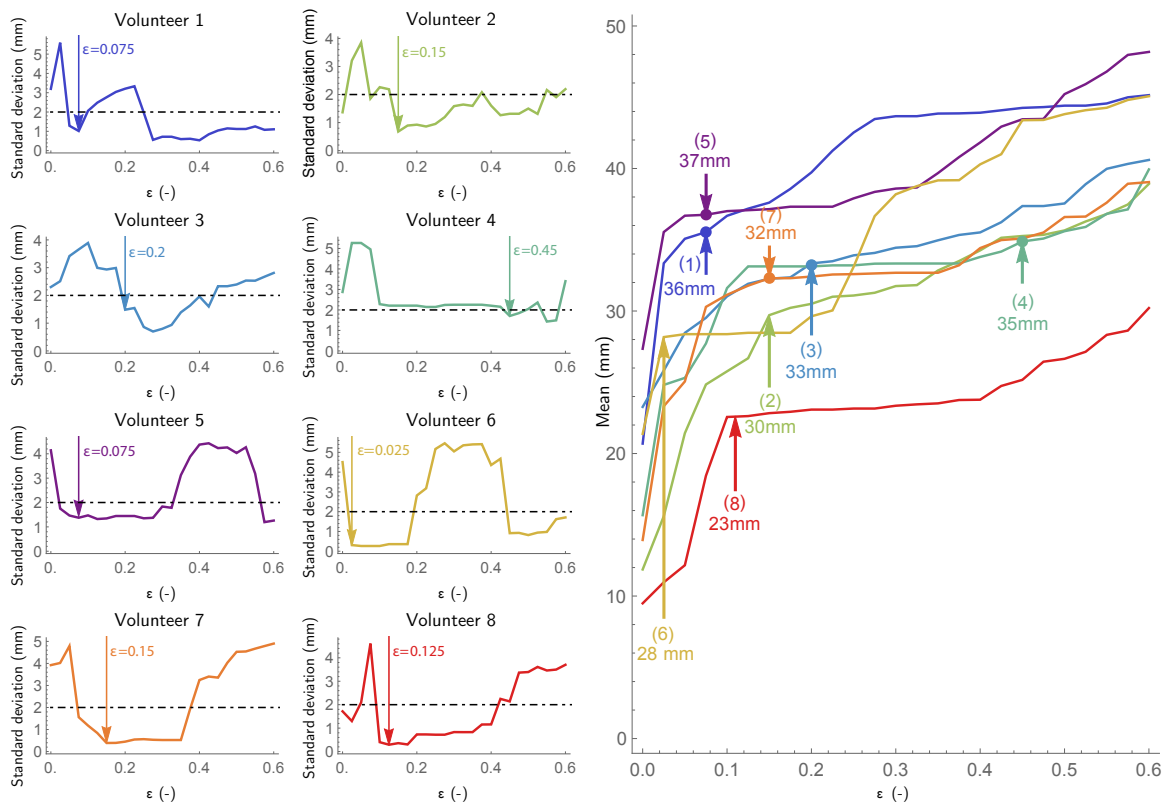
Figure 5-4: Shown is the parameter estimation for the reconstructed left OR of the eight healthy volunteers studied. Left: The standard deviation of the ML-TP distance is shown as a function of ϵ. For each healthy volunteer a suitable choice of ϵ is made at the point where the standard deviation first drops below the threshold of 2 mm and reaches a local minimum, shown by the black dotted line. Right: The estimated mean ML-TP distance is shown as a function of ϵ. The $\epsilon_{\text{selected}}$ for each volunteer is indicated by an upwards pointed arrow, indicated along with the values of the associated estimate of the ML-TP distance.

over 2 mm) for relatively high values of ϵ (i.e. $\epsilon \geq 0.2$). This can be attributed to gaps within the reconstructed OR with a lower number of streamlines compared to the main streamline bundle. Lastly, it can be observed that for volunteer 4 the selected ϵ is large compared to the other healthy volunteers. However, for this volunteer the mean ML-TP distance is stable from $\epsilon = 0.15$ onward and therefore does not reflect an overestimation of the ML-TP distance.

On the group level the ML-TP distances listed in Table 5.1 are on average 31.7 ± 4.7 mm for the left hemisphere and 28.4 ± 3.8 mm for the right hemisphere. The mean variability in probabilistic tractography on the individual level for the group of healthy volunteers is 1.0 mm and 0.9 mm for the left and right hemispheres, respectively. Large deviations in ML-TP distance were observed between the left and right hemispheres, especially, for volunteers 3, 7 and 8.

5.3.2   Pre- and post-operative comparisons

The importance of the robust ML-TP distance measurement is illustrated for three patients who underwent resective epilepsy surgery. Figure 5-5 displays the pre-operative (first and last columns) and post-operative reconstructions (second and third columns) of the OR and indicates for both hemispheres the estimated ML-TP distances (first and second column). Given is also the resection length (third column) and the pre-operative reconstruction of the OR along with the predicted damage, indicated by the red colored streamlines (fourth column). The pre- and post-operative distance measurements and the corresponding values of ϵ are listed for both the left and right hemisphere in Table 5.2. Furthermore, the predicted damage is listed in Table 5.2 and reflects the distance between the pre-operative ML-TP distance and the resection length. Finally, the margin of error is indicated, defined as the difference between the predicted damage and the observed damage.
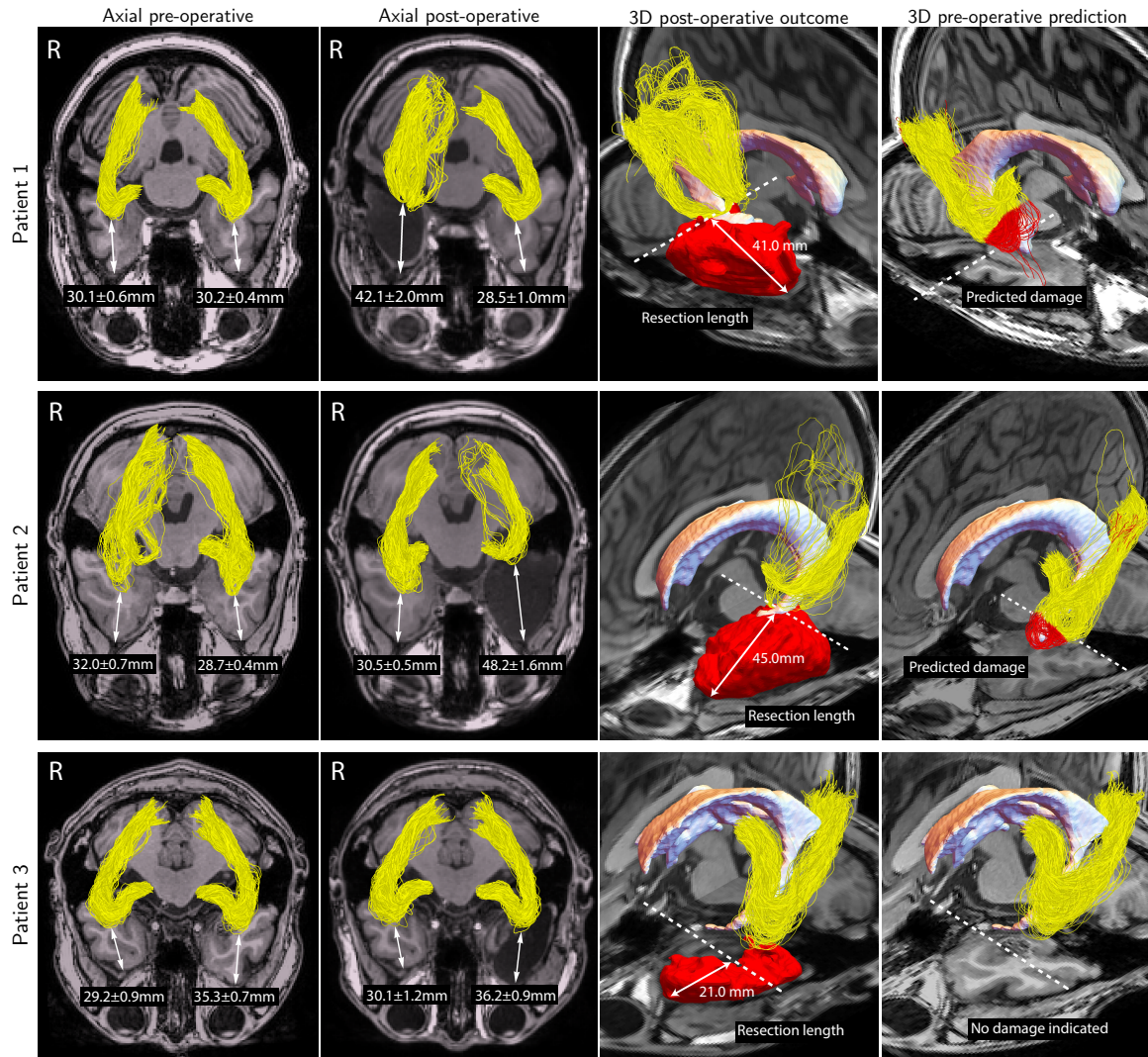
Figure 5-5: Tractography and distance measurement results for the three patients included in the study. The first and second columns show the reconstructions of the OR before and after surgery, respectively. For each reconstruction the ML-TP distance and associated variability are displayed. The third and fourth columns show a 3D view of the reconstruction of the OR in the affected hemisphere after and before surgery, respectively. The resection area is displayed in red and the predicted damage is indicated by color-coded red streamlines.

The tractography results indicate that for patients 1 and 2 the OR is damaged, likely resulting in a disrupted Meyer's loop for both patients. The perimetry results of these patients indicated a visual field deficit (VFD) of 60 degrees for patient 2, which was smaller than the VFD measured for patient 1 at 90 degrees despite the larger resection of patient 2 (see Table 5.2). Note, that for patient 3, for whom there was no damage to the OR, the reconstruction of the OR is well reproducible for both hemispheres, with a difference of maximally 3.0 mm including the variability in ML-TP distance. The difference between the predicted damage and the observed damage was small for these patients, indicating a maximum error of the predicted damage of the OR of 5.6 mm or less. The reproducibility of the reconstruction results obtained following the procedures as here described is further confirmed by the unaffected hemispheres of each individual patient, which show a similar anterior extent for both pre- and post-operative reconstructions of the OR. The ML-TP distance of the OR reconstructed for the OR of the non-pathologic hemisphere showed deviations for the two different scans of maximally 3.1 mm, 2.7 mm and 3.0 mm

Patient	ML-TP distance		ϵ				
	Pre-op (mm)	Post-op (mm)	Pre-op (-) / Post-op (-)	Resection length (mm)	Predicted damage (mm)	Observed damage (mm)	Margin of error (mm)
Patient 1							
Left	30.2±0.4	28.5±1.0	0.10 / 0.20	-	-	-	-
Right	30.1±0.6	42.1±2.0	0.48 / 0.18	41.0	10.9±0.6	12.0±2.6	4.3
Patient 2							
Left	28.7 ± 0.4	48.2 ± 1.6	0.13 / 0.4	45.0	16.3±0.4	19.5±2.0	5.6
Right	32.0 ± 0.7	30.5 ± 0.5	0.13 / 0.2	-	-	-	-
Patient 3							
Left	35.3 ± 0.7	36.2 ± 0.9	0.10 / 0.18	21.0	0.0	0.0	1.6
Right	29.2 ± 0.9	30.1 ± 1.2	0.22 / 0.18	-	-	-	-

Table 5.2: The results listed for the pre- and post-operative comparison of the reconstruction of the OR for both hemispheres of the three epilepsy surgery candidates included in our study. Distance measurements of the anterior extent of the OR to the temporal pole (ML-TP) are displayed along with the variability in probabilistic tractography for the corresponding $\epsilon_{\text{selected}}$. Furthermore, the resection lengths, predicted and observed damages, and the measured margins of error are listed for the affected hemispheres.

for Patient 1, Patient 2 and Patient 3, respectively, including the variability measure. The overall mean ML-TP distance pre-operatively is 31.4 ± 3.5 mm for the left hemisphere and 30.4 ± 1.4 mm for the right hemisphere. The mean variability in probabilistic tractography is 0.5 mm and 0.7 mm for the left and right hemispheres, respectively.

5.4 Discussion

Stability metrics were introduced for a robust estimation of the distance between the tip of the Meyer's loop and temporal pole. Standardized removal of spurious fibers was achieved, firstly by quantification of spurious streamlines using the FBC measures, and secondly by a procedure for the automatic selection of the minimal threshold $\epsilon_{\text{selected}}$ on the FBC measures. The results presented indicate that a reliable localization of the tip of the Meyer's loop is possible and that it is feasible to predict the damage to the OR as result of a TLR performed to render patients seizure free.

5.4.1 Procedures for the reconstruction of the OR

For the estimation of the FOD function, CSD was applied on diffusion data obtained with the prevalent DTI acquisition scheme, thus allowing for a broad clinical applicability. In the current study, the DTI acquisition scheme (b=1000, 32 directions) has a relatively low number of directions of diffusion. Since the tip of the Meyer's loop has a high curvature, its reconstruction could especially benefit from a high angular resolution diffusion imaging (HARDI) acquisition scheme [215], which measures a larger number of directions of diffusion such as 64 or 128 directions. However, unlike DTI, HARDI is not commonly applied within a medical MRI diagnosis. Instead, the DTI data may be improved by applying the contextual enhancements introduced in Chapter 4. Additionally, in order to improve the image quality of the diffusion measurements it may be beneficial to apply denoising. This may, for example, be achieved by a recently proposed denoising approach based on non-local principal component analysis (PCA) [124].

The MRtrix software package was employed for the estimation of the FOD function and for performing probabilistic tractography. As an alternative to the rejection sampling method that is implemented in MRtrix for sampling the FOD during tracking, the importance sampling method as introduced in Friman et al. [68] could be used. In contrast to the hard constraints used in rejection sampling, the importance sampling method provides a soft constraint on the space of positions and orientations, which is in line with the mathematical framework introduced in Chapter 4.

The seed regions of the LGN and visual cortex are highly influential for the tractography results [113]. It may be possible to improve the fiber orientation estimation at the white matter to gray matter interface, such as near the LGN and visual cortex ROIs, by applying the recently introduced informed constrained spherical deconvolution (iCSD) [179]. iCSD improves the FOD by modifying the response function to account for non-white matter partial volume effects, which may improve the reconstruction of the OR. In the current study, the LGN was identified manually and could possibly be improved by using a semi-automatic method such as presented by Winston et al. [237]. Another approach proposed by Benjamin et al. [20] is to place different ROIs around the LGN and within the sagittal stratum, or by seeding from the optic chiasm [100]. A recent study suggested using seeding around the Meyer's loop with an a-priori fiber orientation [33].

5.4.2 Application of the stability metrics

The FBC measures are used for the quantification of spurious streamlines. These FBC measures are based on the estimation of streamline density in the space of positions and orientations $\mathbb{R}^3 \times S^2$. An advantage of the FBC method is that it is generally applicable, regardless of the type of diffusion model and the tracking algorithm being used, since it depends only on the outcome of tractography. A possible limitation of the FBC measures is the number of streamlines that can be processed, since for densely populated regions of streamlines the method is computationally expensive. However, through the use of several optimization steps detailed in Chapter 4 such as pre-computed lookup tables for the Brownian motion kernel, multi-threaded processing, subsampling of streamlines, and

the exclusion of far-away streamline points, the computation times remain manageable.

In order to remove spurious fibers while preventing an underestimation of the full extent of the Meyer's loop, a procedure for estimating $\epsilon_{\text{selected}}$ was introduced based on the test-retest evaluation of the variability in ML-TP distance. Using this methodology, a robust measurement of the ML-TP distance was achieved in the left and right hemispheres of eight healthy volunteers. The variability in the reconstruction results of the OR stems mostly from data acquisition (e.g. signal-to-noise, partial volume effects, and patient motion) [226]. Therefore, $\epsilon_{\text{selected}}$ may vary between pre- and post-operative scans in the non-affected hemisphere (see Table 5.2). If a robust measurement of the ML-TP distance cannot be achieved due to a large variability, this would be an indication that the tractography results and/or the DWI acquisition may be suboptimal. The mean ML-TP distances for both brain hemispheres, measured to be 30.0 ± 4.5 mm for the healthy volunteer group and 30.9 ± 2.4 mm for the patient group (pre-operatively), are within the range of the ML-TP distance reported on by Ebeling & Reulen [60] and outcomes from other OR reconstruction methodologies. For example, ConTrack [194] showing 28 ± 3.0 mm, Streamlines Tracer technique (STT) showing 37 ± 2.5 mm [238] and 44 ± 4.9 mm [144], Probability Index of Connectivity (PICo) showing 36.2 ± 0.7 mm [44], tractography on Human Connective Project (HCP) multi-shell data showing 30.7 ± 4.0 mm [100], and MAGNET showing 36.0 ± 3.8 mm [33]. It appeared, furthermore, that the mean ML-TP distances for both the healthy volunteers and the patients was larger in the left hemisphere compared to the right hemisphere, which is not consistent with a recent study by James et al. [90] that indicated significantly higher ML-TP distances in the right hemisphere.

A possible limitation of the parameter estimation procedure is that its application is tailored towards OR tractography. Unlike the FBC measures, which can be used for any tractogram, the parameter estimation procedure may not be generally applicable for other fiber bundles since a distance measurement between well-defined landmarks is required. However, a possible approach for generalized parameter selection is to fit the streamline bundle on a manifold such as used by BundleMAP [103] and optimize $\epsilon_{\text{selected}}$ by minimizing the spread on the manifold.

5.4.3 Towards damage prediction for epilepsy surgery

The methodology for the estimation of the ML-TP distance is applied for the surgical candidates, firstly to assess the validity of the distance measurements, and secondly to indicate its additional value for temporal lobe epilepsy surgery. An indication of the validity of distance measurements was given by the margin of error, which was the largest for patient 2 amounting to 5.6 mm. The margin of error observed for the three patients can be lowered, e.g. by correcting for brain shifts that occur due to resection and cerebrospinal fluid (CSF) loss [228] and by correcting for distortions present in MR echo-planar imaging [93, 86]. The measurement of the ML-TP distance may be further complicated due to a shifted location of the temporal pole, or even its complete absence. However, the reproducibility of the pre- and post-operative reconstructions of the OR in the non-pathological hemisphere indicates that the effects of brain shift and imaging distortions may be limited. Small deviations in the ML-TP distance were seen (see Table 5.2), which suggests a good reproducibility, albeit for a limited number of patients.

In the standardized estimation procedure of $\epsilon_{\text{selected}}$ the maximal variability was set at 2 mm, both for the OR reconstructions of the healthy volunteers and the patients, which is based on the maximal surgical accuracy that can be achieved during standard or tailored anterior temporal lobectomy before the leakage of cerebrospinal fluid (CSF). A surgical accuracy below 2 mm has been reported [207] if a stereotactic frame is used or robotic assistance is involved. After the leakage of CSF however, cortical displacement up to 24 mm may be seen [83], while other sources of inaccuracy are likely present such as echo-planar imaging distortion, partial volume effects, and image noise. However, despite these inaccuracies the pre- and post-operative comparison of the OR reconstructions indicates that the procedures developed in this thesis are a valid tool to assess the robustness of the distance measurements.

It appeared that the robust estimation of the ML-TP distance enabled to predict the damage of the OR after surgery, which was concordant with the actual damage for the three patients studied. Based on the damage prediction the margin of error was estimated, giv-

ing an indication of the overall error in distance measurement. The perimetry results of two of the patients studied indicated damage of either the left or right visual field, corresponding to a disruption of the Meyer's loop. A relatively small VFD was indicated for patient 2 despite the large temporal lobe resection. This result may be indicative of the large inter-patient variability in OR anatomy and function, but may also be the result of the non-standardized procedures for visual field testing in-between hospitals. It is recommended to evaluate the developed methodology further in a clinical trial including a sizable group of patients who are candidate for a TLR in order to be able to assess what the relation is between a VFD and the damage to the OR after a TLR.

5.5 Conclusion

It was shown for a group of healthy volunteers included in this thesis that standardized removal of spurious streamlines provides a reliable estimation of the distance from the tip of the Meyer's loop to the temporal pole that is stable under the stochastic realizations of probabilistic tractography. Pre- and post-operative comparisons of the reconstructed OR indicated, furthermore, 1) the validity of a robust ML-TP distance measurement to predict the damage to the OR as result of resective surgery, and 2) the high reproducibility of the reconstructions of the non-pathological hemisphere. In conclusion, the developed methodology based on diffusion-weighted MRI tractography is a step towards applying optic radiation tractography for pre-operative planning of resective surgery and for providing insight in the possible adverse events related to this type of surgery.

Chapter 5

Chapter 6 | Optimal paths by fast marching

An approach is presented for finding the optimal paths for the Reeds-Shepp car by the use of the fast marching algorithm with highly anisotropic Finsler metrics on the manifold of positions and orientations. In the proposed model a data-driven functional is minimized involving constraints for curvature, length and sideways motion. A variant of this model is investigated that constrains forward motion by removing the reverse gear of the vehicle.

6.1   Introduction

In this chapter a new method for the quantitative estimation of connectivity is introduced, which is based on finding the shortest path. Specifically, shortest paths in the space of positions and orientations $\mathbb{R}^3 \rtimes S^2$ are considered (c.f. Chapter 4). Reeds and Shepp [175] considered the problem of finding the shortest paths for a car that can move forward and backward, turn the steering wheel, but cannot perform sideways motion. Given a suitably defined metric, the shortest pathways, or minimizing geodesics, that arise from such a set of constraints may be good candidates for blood vessels or neural fibers in the brain. A method that is capable of solving a geodesic distance map and provide such optimal paths is fast marching (FM) [213, 191]. Originating from the field of optimal control theory, FM is an efficient algorithm that uses a single-pass iterative scheme to solve a continuous distance map.

An example is given of the application of optical control theory to find the shortest path of a Reeds-Shepp car, defined by coordinates in a 2D space with some orientation θ. A path in this space is defined by $\gamma = (x(\cdot), y(\cdot), \theta(\cdot))$. The control system for this car is defined by a system of differential equations depending on the control variables $t \mapsto \tilde{u}(t) \in \mathbb{R}, t \mapsto \tilde{v}(t) \in \mathbb{R}$ given by

$$
\begin{cases}
\dot{x}(t) = \tilde{u}(t) \cos \theta, \\
\dot{y}(t) = \tilde{u}(t) \sin \theta, \\
\dot{\theta}(t) = \tilde{v}(t).
\end{cases}
\quad \Leftrightarrow \quad
\dot{\gamma}(t) = \tilde{u}(t) \begin{bmatrix} \cos \theta \\ \sin \theta \\ 0 \end{bmatrix} + \tilde{v}(t) \begin{bmatrix} 0 \\ 0 \\ 1 \end{bmatrix},
$$

where $\dot{\gamma}$ is the tangent vector of the pathway. The optimal solution of such a system is a curve with Lipschitz regularity that minimizes the cost function

$$
\inf \left\{ \int_0^1 \sqrt{\tilde{u}(t)^2 + \tilde{v}(t)^2} dt \mid \gamma(0) = \mathbf{p}, \gamma(1) = \mathbf{q}, \gamma(t) \in \mathrm{Lip}([0, 1], \mathbb{R}^2 \rtimes S) \right\},
$$

where $\mathbf{p}$ and $\mathbf{q}$ are the beginning and end points of the pathway parametrized by arc length, respectively. The resulting shortest path is illustrated in Fig. 6-1, which shows that
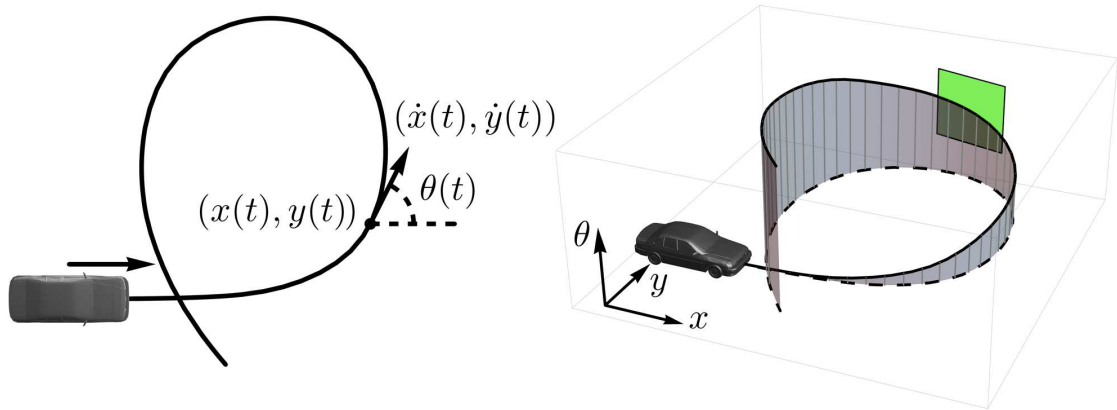
Figure 6-1: A car can only move in its current orientation or change its current orientation. In other words, when the path $\gamma(t) = (x(t), y(t), \theta(t))$ is considered as indicated in the left figure, the tangent $\dot{\gamma}(t)$ is restricted to the span of $(\cos \theta(t), \sin \theta(t), 0)$ and $(0, 0, 1)$, of which the green plane on the right is an example.

the constraint on sideways motion can be achieved by constraining the tangent vector $\dot{\gamma}(t)$ to remain in the span of $(\cos \theta(t), \sin \theta(t), 0)$ and $(0, 0, 1)$, denoted by the green rectangle.

To define the length of a pathway γ it is necessary to have a notion of distance. This can be achieved by defining a Riemannian manifold $\mathcal{M}$. A manifold can be seen as a topological space, which may be curved but locally has a tangent space that represents a flat Euclidean space. The Riemannian manifold is a smooth real-valued manifold equipped with an inner product $g_{\mathbf{p}}$ on the tangent space $T_{\mathbf{p}}\mathcal{M}$ at each point $\mathbf{p} \in \mathbb{R}^d$ for some dimension $d \geq 2$ that varies smoothly over the manifold. The constraint of sideways motion leads to a special case of the Riemannian manifold called a sub-Riemannian manifold in which the curve tangent is only allowed within horizontal subspaces (as indicated by the green plane in Fig. 6-1). The sub-Riemannian structure takes into account both the spatial and angular distance [51], which is illustrated in Fig. 6-2a. The optimization of curves in a sub-Riemannian (SR) manifold have been extensively studied in the two-dimensional case [184, 165, 36, 51, 27, 126, 1, 134, 26, 182], in the three-dimensional case [56], and more generally for the n-dimensional case [55]. Examples of the relation between optimal control theory and SR geometry can be found in the books of Agrachev and Sachkov [1] and Montgomery [135]. Applications in robotics and visual modeling of SR geometry and control theory can be found in e.g. Stefani et al. [201].
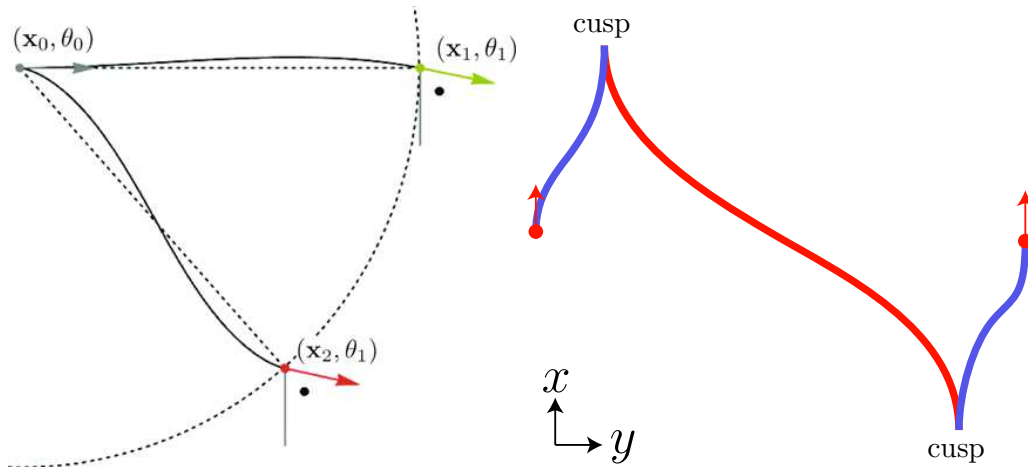
Figure 6-2: Left: Schematic illustration of the coupling between positions and orientations. Both pathways have the same spatial and angular distance between them, but in a sub-Riemannian framework the points $(\mathbf{x}_0, \theta_0)$ and $(\mathbf{x}_1, \theta_1)$ are more connected than $(\mathbf{x}_0, \theta_0)$ and $(\mathbf{x}_2, \theta_2)$. Right: spatial projection of a pathway following the Reeds-Shepp car constraints, which connects two points in $\mathbb{R}^2 \rtimes S^1$ by two cusps. The blue part of the line indicates forward motion and the red part indicates backward motion. Figures adapted from Duits et al. [51].

In Fig. 6-2b an optimal path is shown between two points in $\mathbb{R}^2 \rtimes S^1$, indicated by the red arrows. To reach the minimal distance the Reeds-Shepp car has to move in reverse (indicated by the red part of the line), which results in two cusps. To prevent the creation of cusps, which are undesirable in image analysis applications such as tracking of blood vessels or neural fibers, a variant of the Reeds-Shepp car is considered in which the reverse gear is removed, thus forcing a spatial propagation that is forward.

The chapter begins with an explanation of the mathematics and algorithms used in Fast Marching, explaining the variations of the eikonal equation based on Euclidean or Riemannian or Finslerian geometry, how to numerically solve it, and how to compute the geodesics from a minimal distance map. Secondly, variants of the Reeds-Shepp car are discussed and the extension of the Finsler metric by data-driven factors that can vary with position and orientation. A software tool is introduced for performing FM experiments and is demonstrated for phantom DWI data. Experiments on the phantom DWI data demonstrate the results of finding the shortest-path using the new methodology and highlights the differences between the Riemannian and Finslerian metrics.

6.2   The fast marching method

FM was conceived [213, 191] for finding the shortest path, or geodesic, between any two points by computing a distance map with respect to some underlying distance metric. FM is comparable to Dijkstra's method [49] for finding the shortest path in the sense that FM computes a continuous (smooth) distance map through the use of an interpolated value function, while Dijkstra's method is restricted to nodes in a fixed grid that can result in discontinuities in the distance map.

6.2.1   The eikonal equation

FM approximates the geodesic distance map $U(\mathbf{x})$ by finding a viscosity solution to the *eikonal equation.* The eikonal equation is a non-linear partial differential equation (PDE) that is often encountered in problems of wave propagation and is used to compute the arrival times of the propagating wavefront. The eikonal equation for an initial boundary problem of a wavefront stating at the arrival time of zero is given by

$$\begin{cases} \|\nabla U(\mathbf{x})\| = \mathcal{C}(\mathbf{x}), & \text{for all } \mathbf{x} \in \Omega \setminus \{\mathbf{x}_\mathrm{S}\}, \\ \quad U(\mathbf{x}_S) = 0, \end{cases} \tag{6.1}$$

which can be interpreted as the time it takes to move from points in the source region $\mathbf{x}_S$ to any other point $\mathbf{x}$ in the domain $\Omega \subset \mathbb{R}^d$ for some dimension $d \geq 2$. Here, $\|\cdot\|$ denotes the usual Euclidean norm. The cost of moving is denoted by $\mathcal{C}(\mathbf{x}) > 0$. N.B.: for a positive position-dependent speed $\mathcal{C}(\mathbf{x}) > 0$ this equation is equivalent to the static Hamilton-Jacobi equation [191].

6.2.2   Algorithm

To solve the eikonal equation presented in Eq. (6.1) an iterative one-pass algorithm is applied. Starting from a set of initial source points where $U(\mathbf{x}_S) = 0$, a monotonically advancing front propagates throughout the domain Ω. As is illustrated in Fig. 6-3 (left), points on the grid are labeled as either "Accepted", for which $U(\mathbf{x})$ is determined, "Trial" for the points that form the front, and "Far" for points that have yet to be visited. In each iteration the trial point $\mathbf{x}_{\min}$ that minimizes $U(\mathbf{x}_{\min})$ is selected and is marked as accepted. For all neighborhood points of $\mathbf{x}_{\min}$, determined by the local stencil, the local geodesic distance is computed. Far points in this neighborhood are relabeled as Trial points. If a point was already labeled as a Trial point, then the geodesic distance is updated if it is lower than the previously computed distance for that point. The iterative algorithm is continued until the entire domain is visited and all points are labeled Accepted. In Fig. 6-3 (right) a trivial example is shown of isocontours computed with a constant cost, which result in circles. The red line shows the shortest path between a seed point $\mathbf{x}_S$ and target points $\mathbf{x}_{Q1}$ and $\mathbf{x}_{Q2}$.
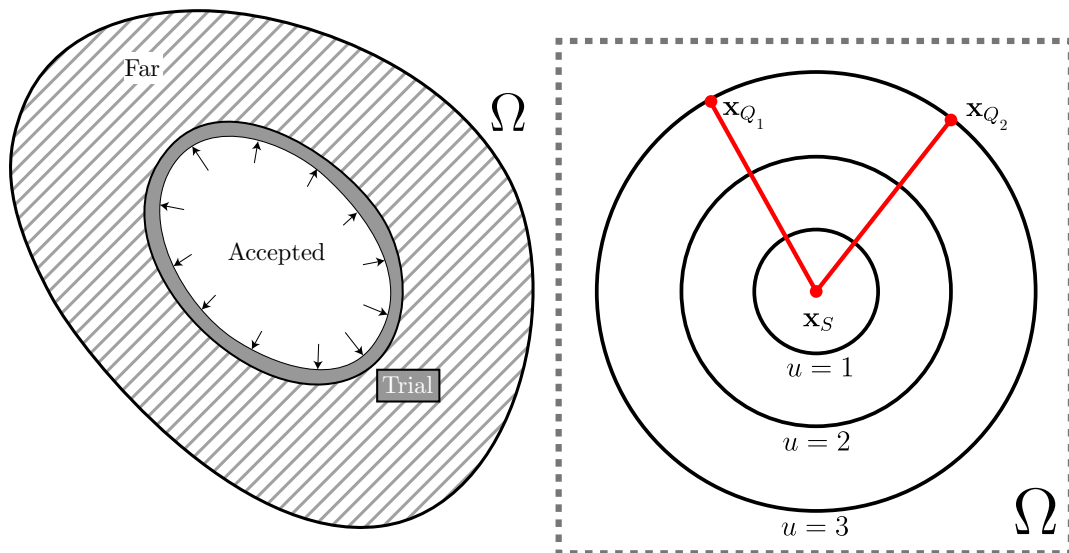

Figure 6-3: Left: Schematic illustration of the fast marching algorithm in which a front starting from a seeding region propagates through the domain. Right: Example of a shortest path between a seed point $\mathbf{x}_S$ and two different end points $\mathbf{x}_{Q1}$ and $\mathbf{x}_{Q2}$ for a 2D field with constant cost $\mathcal{C} = 1$.

6.2.3   Riemannian metric

The length induced by the minimal geodesic distance map $U(\mathbf{x})$ on every position $\mathbf{x} \in \mathbb{R}^d$ of the domain domain $\Omega \subset \mathbb{R}^d$ depends on the metric that is used. On a Riemannian manifold $\mathcal{M}$ that is defined on position space $\mathbb{R}^d$ we have a bilinear form $\mathcal{M}_\mathbf{x} : T_\mathbf{x}(\mathbb{R}^d) \times T_\mathbf{x}(\mathbb{R}^d) \to \mathbb{R}$ that is given by $\mathcal{M}_\mathbf{x}(\dot{\mathbf{x}}, \dot{\mathbf{x}}) = \dot{\mathbf{x}} \cdot M(\mathbf{x})\dot{\mathbf{x}}$ where $M(\mathbf{x}) \in \mathbb{R}^d \times \mathbb{R}^d$ is the matrix representation of $\mathcal{M}(\mathbf{x})$ and where $\dot{\mathbf{x}} \in T_\mathbf{x}(\mathcal{M})$. Then, a norm for each $\mathbf{x}$ can be defined according to $\|\cdot\|_{\mathcal{M}(\mathbf{x})} = \sqrt{\dot{\mathbf{x}} \cdot \mathcal{M}(\mathbf{x})\dot{\mathbf{x}}}$ on $T_\mathbf{x}(\mathbb{R}^d)$. Using this notation, the eikonal equation can be written as

$$
\begin{cases}
\|\nabla U(\mathbf{x})\|_{\mathcal{M}(\mathbf{x})} = 1, & \text{for all } \mathbf{x} \in \Omega \setminus \{\mathbf{x}_S\}, \\
U(\mathbf{x}_S) = 0.
\end{cases}
\tag{6.2}
$$

The Riemannian length of a pathway with Lipschitz regularity $\gamma : [0,1] \to \Omega$ is given by

$$
\text{Length}_{\mathcal{M}}(\gamma) := \int_0^1 \|\gamma'(t)\|_{\mathcal{M}(\gamma(t))} \, \mathrm{d}t.
$$

Then the geodesic distance between any two points on the domain $\mathbf{x}_1, \mathbf{x}_2 \in \Omega$ is given by

$$
\begin{aligned}
d_{\mathcal{M}}(\mathbf{x}_1, \mathbf{x}_2) := \inf\{ \text{Length}_{\mathcal{M}}(\gamma) \mid \gamma \in \Gamma, \, \gamma(0) = \mathbf{x}_1, \\
\gamma(1) = \mathbf{x}_2\},
\end{aligned}
\tag{6.3}
$$

with $\Gamma := \text{Lip}([0,1], \mathbb{M})$ The normalized minimizers of Eq. (6.3) are called minimal geodesics between $\mathbf{x}_1$ and $\mathbf{x}_2$.

Remark

In literature the meaning of a "metric" can in some cases be ambiguous and refer to either the metric tensor field $\mathcal{M}$, the metric tensor at $\mathbf{x}$ given by $\mathcal{M}(\mathbf{x})$, the norm associated to the metric sensor given by $\|\cdot\|_{\mathcal{M}(\mathbf{x})}$, the distance metric $d_{\mathcal{M}}(\cdot, \cdot)$ or the matrix representation $M(\mathbf{x})$ with respect to a standard basis $(\partial_{\mathbf{x}_1}|_\mathbf{x}, (\partial_{\mathbf{x}_2}|_\mathbf{x})$. In the remainder of the text it will depend on the context which of these objects is referred to.

6.2.4   Finsler metric

A generalization of Riemannian geometry is Finsler geometry. Whereas in Riemannian geometry the metric tensor is a function of position, in Finsler geometry it is a function of position as well as a directional argument [8]. Generally, Finsler geometry is Riemannian geometry without the quadratic restriction. The use of a Finsler metric allows for more complex geometry because the cost can be specified for any point on the sphere S^2. Furthermore, it allows for asymmetry, i.e. $\mathcal{F}(\mathbf{x}, \mathbf{n}) \neq \mathcal{F}(\mathbf{x}, -\mathbf{n})$ for a Finsler structure $\mathcal{F}$, which will be essential for imposing a forward propagation restriction later on in the chapter. In contrast to several studies that chose a single tensor representation to describe Finsler geometry [4, 72] The base manifold used in this study is $\mathbb{M} := \mathbb{R}^d \rtimes S^{d-1}$ to circumvent the problem of overlapping fronts [190, 58].

A Finsler structure $\mathcal{F}$ on the manifold $\mathbb{M} := \mathbb{R}^d \rtimes S^{d-1}$ for some dimension $d \in \{2, 3\}$ is a function on the tangent bundle of $\mathbb{M}$ given by

$$\mathcal{F} : T(\mathbb{M}) \to [0, \infty),$$

where the tangent bundle is given by $T(\mathbb{M}) := \cup_{\mathbf{p} \in \mathbb{M}} T_{\mathbf{p}}(\mathbb{M})$ and where $T_{\mathbf{p}}\mathbb{M}$ is the tangent space. Let $(\mathbf{p}, \dot{\mathbf{p}}) \in T(\mathbb{M})$ be a pair consisting of a point $\mathbf{p} \in \mathbb{M}$ and a tangent vector $\dot{\mathbf{p}} \in T_{\mathbf{p}}(\mathbb{M})$ at this point. The spatial and angular components of a point $\mathbf{p} \in \mathbb{M}$ are denoted by $\mathbf{x} \in \mathbb{R}^d$ and $\mathbf{n} \in S^{d-1}$, and this convention carries over to the tangent:

$$\mathbf{p} = (\mathbf{x}, \mathbf{n}), \qquad\qquad \dot{\mathbf{p}} = (\dot{\mathbf{x}}, \dot{\mathbf{n}}) \in T_{\mathbf{p}}(\mathbb{M}).$$

We say that $\dot{\mathbf{x}}$ is proportional to $\mathbf{n}$, that we write as $\dot{\mathbf{x}} \propto \mathbf{n}$, iff there exists a $\lambda \in \mathbb{R}$ such that $\dot{\mathbf{x}} = \lambda \mathbf{n}$.

Based on a continuous Finsler function $\mathcal{F}$, the eikonal equation formulation becomes

$$\begin{cases} \mathcal{F}^*(\mathbf{p}, dU(\mathbf{p})) = 1, & \text{for all } \mathbf{p} \in \Omega \setminus \{\mathbf{p}_\text{S}\}, \\ U(\mathbf{p}_S) = 0, \end{cases} \tag{6.4}$$

where U is the unique viscosity solution [39, 38], $\mathcal{F}^*$ is the dual metric of $\mathcal{F}$ and dU is the differential of the distance map U. The dual metric is given by

$$\mathcal{F}^*(\mathbf{p}, \hat{\mathbf{p}}) := \sup_{\dot{\mathbf{p}} \in T_\mathbf{p}\mathbb{M}\setminus\{0\}} \frac{\langle \hat{\mathbf{p}}, \dot{\mathbf{p}} \rangle}{\mathcal{F}(\mathbf{p}, \dot{\mathbf{p}})}, \tag{6.5}$$

for all points on the co-tangent bundle $(\mathbf{p}, \hat{\mathbf{p}}) \in T^*(\mathbb{M})$. Finally, the length of a pathway with a Finsler metric is given by

$$\text{Length}_\mathcal{F}(\gamma) := \int_0^1 \mathcal{F}(\gamma(t), \dot{\gamma}(t)) \, \mathrm{d}t.$$

For a detailed explanation regarding the theory of Riemannian and Finsler geometry, dual spaces and dual metrics, see the books by Bao et al. [8] and Shen et al. [192].

Remark

The common terminology 'Finsler metric' is used for $\mathcal{F}$, although in literature it may also be referred to as the 'Finsler function', 'Finsler norm' or 'Finsler structure', despite the fact that $\mathcal{F}$ is not a metric (distance) in the classical sense. If $\mathcal{F}(\mathbf{p}, \dot{\mathbf{p}}) = \mathcal{F}(\mathbf{p}, -\dot{\mathbf{p}})$ for all $\mathbf{p} \in \mathbb{M}$ and tangent vectors $\dot{\mathbf{p}} \in T_\mathbf{p}(\mathbb{M})$, then the induced quasi-distance $d_\mathcal{F}$ is a true metric, satisfying $d_\mathcal{F}(\mathbf{p}, \mathbf{q}) = d_\mathcal{F}(\mathbf{q}, \mathbf{p})$ for all $\mathbf{p}, \mathbf{q} \in \mathbb{M}$. However, to avoid confusion of the word metric, we will only refer to $d_\mathcal{F}$ as a distance or quasi-distance. Furthermore, throughout the document the words path and curve will be used synonymously.

6.2.5 Numerical viscosity solution to the eikonal equation

To numerically solve the eikonal equation, given in Eq. (6.5), by local geodesic distance updates, two main types of approaches exist: an upwind discretization form of the eikonal equation [191] or the use of the Hopf-Lax update scheme [213].

In this work we use the numerical solver of Mirebeau et al [130], which is based on the Hopf-Lax update scheme to discretize the eikonal PDE according to

$$
\begin{cases}
U(\mathbf{p}) = \Lambda U(\mathbf{p}), & \text{for all } \mathbf{p} \in Z \setminus \{\mathbf{p}_S\}, \\
U(\mathbf{p}_S) = 0,
\end{cases}
\tag{6.6}
$$

where Z is the discretized orthogonal grid of the domain Ω [130, 34]. The Hopf-Lax update operator Λ is defined by

$$
\Lambda U(\mathbf{p}) := \min_{\mathbf{z} \in \partial S(\mathbf{p})} \left\{ \mathcal{F}(\mathbf{p}, \mathbf{p} - \mathbf{z}) + I_{S(\mathbf{p})} U(\mathbf{z}) \right\},
\tag{6.7}
$$

where $S(\mathbf{p})$ is the stencil centered at point $\mathbf{p} \in Z$ and $I_{S(\mathbf{p})}$ is a piecewise linear interpolator on the edge of a stencil. This operator is a discretization of Bellman's optimality principle, in which $\mathcal{F}(\mathbf{p}, \mathbf{p} - \mathbf{z})$ represents the distance from $\mathbf{p}$ to a point $\mathbf{z}$ on the edge of the stencil, and $I_{S(\mathbf{p})} U(\mathbf{z})$ represents the distance from source $\mathbf{p}_S$ to $\mathbf{z}$.

In Fig. 6-4 this procedure is illustrated for a stencil with discrete points on Z. For each "simplex" denoted by T, which is a triangular portion of the stencil, the Hopf-Lax operator is performed on discrete grid points according to

$$
U(T) = \min_{\eta \in X} \left\{ \mathcal{F}\left(\mathbf{p}, \sum_{i=1}^{d} \eta_i(\mathbf{p}_i^T - \mathbf{p}) \right) + \sum_{i=1}^{d} \eta_i U(\mathbf{p}_i^T), \right\}
\tag{6.8}
$$

where $(\eta_i, \cdots, \eta_d), \sum_i^d \eta_i = 1$ are normalized interpolation weights along vertices $\mathbf{p}_i^T$ of the stencil for dimension d. In Fig. 6-4 the weights η_i are optimized resulting in an optimal

point $\mathbf{z}$. The minimal action map $U(\mathbf{p}) := u_{\text{new}}$ is given by

$$u_{\text{new}} = \min_{T \in S(\mathbf{p})} U(T). \tag{6.9}$$

To facilitate the accurate computation of the distance map u by the FM method, Mirebeau et al. [130] introduced a construction method for anisotropic stencils that adapt locally to the underlying metric used. Importantly, these stencils should satisfy an acuteness property depending on the geometry defined by $\mathcal{F}$. The stencil construction is suitable for 3D anisotropic Riemannian metrics [130], arbitrary 2D Finsler metrics [131] and anisotropic and non-symmetric (non reversible) Finsler metrics.
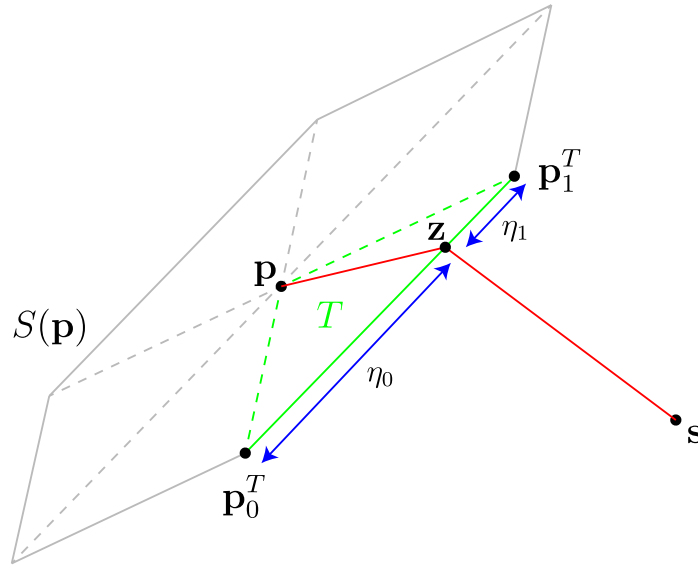
Figure 6-4: Illustration of Bellman's optimality principle where $\mathbf{s}$ is the source point, $\mathbf{p}$ is a point to which the distance is being measured, and $\mathbf{z}$ is the intersection of the boundary of the stencil $S(\mathbf{p})$ and the geodesic from $\mathbf{s}$ to $\mathbf{p}$. The point $\mathbf{z}$ is estimated by linear interpolation between two points $\mathbf{p}_0^T$ and $\mathbf{p}_1^T$ of the simplex T using the interpolation weights η_0 and η_1 in the case of dimension $d = 2$.

6.3   Cusps and keypoints

In Fig. 6-5 examples are shown of a cusp (left) and a keypoint (right).

The definition of a *cusp point* $\mathbf{x}(t_0)$ on a spatial projection of a geodesic $t \mapsto (\mathbf{x}(t), \mathbf{n}(t))$ in $\mathbb{M} := \mathbb{R}^d \rtimes S^{d-1}$ for some dimension $d \in \{2, 3\}$ is a point where

$$\tilde{u}(t_0) = 0, \text{ and } \dot{\tilde{u}}(t_0) \neq 0,$$

$$\text{where } \tilde{u}(t) := \mathbf{n}(t) \cdot \dot{\mathbf{x}}(t) \text{ for all } t. \tag{6.10}$$

In other words, a cusp point is a point where the spatial control aligned with $\mathbf{n}(t_0)$ vanishes and switches sign locally.

The definition of a *keypoint* is a point $\tilde{\mathbf{x}}$ on the spatial projection of a geodesic $\gamma(t) = (\mathbf{x}(t), \mathbf{n}(t))$ in $\mathbb{M}$ subject to the condition that there exist $t_0 < t_1$, such that $\mathbf{x}(t) = \tilde{\mathbf{x}}$ and $\dot{\mathbf{n}}(t) \neq 0$ for all $t \in [t_0, t_1]$, i.e., a point where an in-place rotation (or 'vertical motion') takes place.

For detailed explanations of cusps and keypoints and proofs regarding their occurrence, the reader is referred to the journal paper [58].

6.4   The Reeds-Shepp model and forward variant

We now give the exact formulation of the Finsler metric $\mathcal{F}_0$ underlying the Reeds-Shepp car model. Additionally, to prevent the creation of cusps, a variant $\mathcal{F}_0^+$ of the Reeds-Shepp car is introduced in which the reverse gear is removed by restricting a forward spatial propagation. The metrics introduced here include data-dependent costs in order to favor paths that follow the structures of interest, e.g. a neural fiber pathway or a blood vessel.

The Reeds-Shepp and forward Reeds-Shepp Finsler metrics are given by

$$
\mathcal{F}_0(\mathbf{p}, \dot{\mathbf{p}})^2 := \begin{cases} \mathcal{C}_1^2(\mathbf{p})|\dot{\mathbf{x}} \cdot \mathbf{n}|^2 + \mathcal{C}_2^2(\mathbf{p})\|\dot{\mathbf{n}}\|^2 & \text{if } \dot{\mathbf{x}} \propto \mathbf{n}, \\ \\ +\infty & \text{otherwise.} \end{cases} \tag{6.11}
$$

$$
\mathcal{F}_0^+(\mathbf{p}, \dot{\mathbf{p}})^2 := \begin{cases} \mathcal{C}_1^2(\mathbf{p})|\dot{\mathbf{x}} \cdot \mathbf{n}|^2 + \mathcal{C}_2^2(\mathbf{p})\|\dot{\mathbf{n}}\|^2 & \text{if } \dot{\mathbf{x}} \propto \mathbf{n} \text{ and} \\ & \dot{\mathbf{x}} \cdot \mathbf{n} \geq 0, \\ +\infty & \text{otherwise,} \end{cases}
$$

$$\tag{6.12}$$

for all $\mathbf{p} = (\mathbf{x}, \mathbf{n}) \in \mathbb{M}$ and $\dot{\mathbf{p}} = (\dot{\mathbf{x}}, \dot{\mathbf{n}}) \in T_{\mathbf{p}}(\mathbb{M})$. Here, the data-dependent cost functions $\mathcal{C}_1 = \mathcal{C}_1(\cdot)$ and $\mathcal{C}_2 = \mathcal{C}_2(\cdot)$ are assumed to be continuous on $\mathbb{M}$, and uniformly bounded from below by a positive constant $\delta > 0$. Note that their physical units are distinct: if one wishes $d_{\mathcal{F}}$ to have the dimension $[T]$ of a travel time, then $\mathcal{C}_1^{-1}$ is a physical, (strictly) spatial velocity $[\text{Length}][T]^{-1}$, and $\mathcal{C}_2^{-1}$ is an angular velocity $[\text{Rad}][T]^{-1}$. For simplicity one often sets $\mathcal{C}_1 = \xi \mathcal{C}_2$, where $\xi^{-1} > 0$ is a unit of spatial length related to the maximally

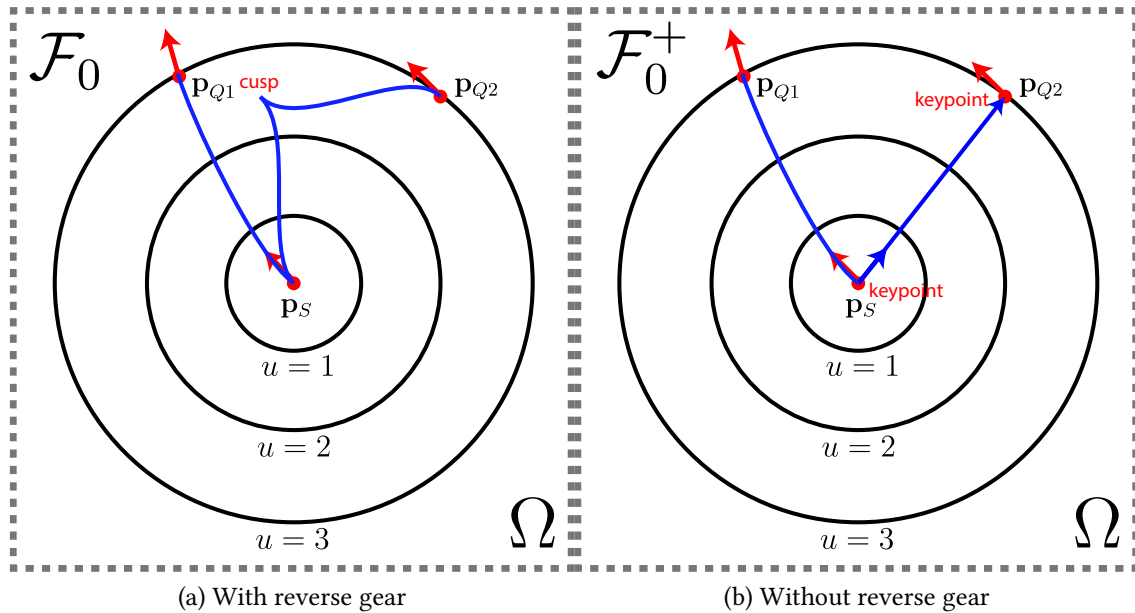(a) With reverse gear   (b) Without reverse gear

Figure 6-5: The difference between shortest-paths obtained used the Reeds-Shepp car (left) and forward-constrained Reeds-Shepp car (right) for a seed point $\mathbf{p}_S$ and two different end points $\mathbf{p}_{Q1}$ and $\mathbf{p}_{Q2}$.

allowed radius of curvature. The special case $\mathcal{C}_1(\mathbf{p}) = \xi\mathcal{C}_2(\mathbf{p}) = \xi$ for all $\mathbf{p} \in \mathbb{M}$ is referred to as the uniform cost case. In Fig. 6-5 the difference between both metrics is illustrated, and it can be seen that the cusps that occurs when using the metric $\mathcal{F}_0$ is replaced by two keypoints when using the metric $\mathcal{F}_0^+$.

The $\mathcal{F}_0$ and $\mathcal{F}_0^+$ metrics are sub-Riemannian due to their infinite cost for side-ways motion. To allow for stable numerical computations with the FM method and include these metrics in the eikonal equation, approximating metrics are introduced that are denoted by $\mathcal{F}_\varepsilon$ and $\mathcal{F}_\varepsilon^+$. The parameter $0 < \varepsilon \leq 1$ controls the amount of side-stepping action allowed. The metrics converge to a sub-Riemannian metric for $\varepsilon \to \infty$, of which proof is provided in the journal article [58]. In practical use, the approximations result in a highly anisotropic Riemannian and Finslerian metrics. The metric $\mathcal{F}_\epsilon$ is in line with previous approximations [36, 19, 184] for the case $d = 2$. Both approximations penalize the deviation from the constraints of collinearity $\dot{\mathbf{x}} \propto \mathbf{n}$, and in addition, $\mathcal{F}_\varepsilon^+$ penalizes negativity of the scalar product $\dot{\mathbf{x}} \cdot \mathbf{n}$, appearing in Eq. (6.11) and Eq. (6.12). For that purpose, we introduce some additional notation: for $\dot{\mathbf{x}} \in \mathbb{R}^d$ and $\mathbf{n} \in S^{d-1}$ we define

$$\|\dot{\mathbf{x}} \wedge \mathbf{n}\|^2 := \|\dot{\mathbf{x}}\|^2 - |\dot{\mathbf{x}} \cdot \mathbf{n}|^2, \tag{6.13}$$

$$(\dot{\mathbf{x}} \cdot \mathbf{n})_- := \min\{0, \dot{\mathbf{x}} \cdot \mathbf{n}\}, \tag{6.14}$$

$$(\dot{\mathbf{x}} \cdot \mathbf{n})_+ := \max\{\dot{\mathbf{x}} \cdot \mathbf{n}, 0\}. \tag{}$$

These are respectively the norm of the orthogonal projection[1] of $\dot{\mathbf{x}}$ onto the plane orthogonal to $\mathbf{n}$, and the negative and positive parts of their scalar product. The two metrics $\mathcal{F}_\varepsilon, \mathcal{F}_\varepsilon^+ : T(\mathbb{M}) \to \mathbb{R}_+$ are defined for each $0 < \varepsilon \leq 1$, as follows:

$$\mathcal{F}_\varepsilon(\mathbf{p}, \dot{\mathbf{p}})^2 := \mathcal{C}_1(\mathbf{p})^2(|\dot{\mathbf{x}} \cdot \mathbf{n}|^2 + \varepsilon^{-2}\|\dot{\mathbf{x}} \wedge \mathbf{n}\|^2) + \mathcal{C}_2(\mathbf{p})^2\|\dot{\mathbf{n}}\|^2, \tag{6.15}$$

$$\mathcal{F}_\varepsilon^+(\mathbf{p}, \dot{\mathbf{p}})^2 := \mathcal{C}_1(\mathbf{p})^2((\dot{\mathbf{x}} \cdot \mathbf{n})_+^2 + \varepsilon^{-2}\|\dot{\mathbf{x}} \wedge \mathbf{n}\|^2 + \varepsilon^{-2}(\dot{\mathbf{x}} \cdot \mathbf{n})_-^2) + \mathcal{C}_2(\mathbf{p})^2\|\dot{\mathbf{n}}\|^2. \tag{6.16}$$

---

[1]The quantity $\|\dot{\mathbf{x}} \wedge \mathbf{n}\|$ is also the norm of the wedge product of $\dot{\mathbf{x}}$ and $\mathbf{n}$, but defining it this way would require introducing some algebra which is not needed in the rest of this thesis.

In contrast to the more common definition of Finsler metrics, we will *not* assume the Finsler metric to be smooth on $T(\mathbb{M}) \setminus (\mathbb{M} \times \{\mathbf{0}\})$, but use a weaker condition instead. Following [34], we require that the sets

$$\mathcal{B}_{\mathcal{F}}(\mathbf{p}) := \{\dot{\mathbf{p}} \in T_{\mathbf{p}}\mathbb{M} \,|\, \mathcal{F}(\mathbf{p}, \dot{\mathbf{p}}) \leq 1\}, \tag{6.17}$$

are closed and vary continuously with respect to the point $\mathbf{p} \in \mathbb{M}$ in the sense of the Hausdorff distance. The shortest path problem can now be reformulated by defining the distance $d_{\mathcal{F}}(\mathbf{p}, \mathbf{q})$ into a time optimal control problem:

$$d_{\mathcal{F}}(\mathbf{p}, \mathbf{q}) = \inf\{T \geq 0 \mid \exists \gamma \in \Gamma_T, \; \gamma(0) = \mathbf{p},$$
$$\gamma(T) = \mathbf{q}, \forall_{t \in [0,T]} \; \dot{\gamma}(t) \in \mathcal{B}_{\mathcal{F}}(\gamma(t))\}, \tag{6.18}$$

where $\Gamma_T := \mathrm{Lip}([0, T], \mathbb{M})$. The levelsets $\mathcal{B}_{\mathcal{F}}(\mathbf{p})$ are illustrated in Fig. 6-6 for both the $\mathcal{F}_0$ and $\mathcal{F}_0^+$ metrics. Additional details regarding these levelsets are available in the journal article [58].
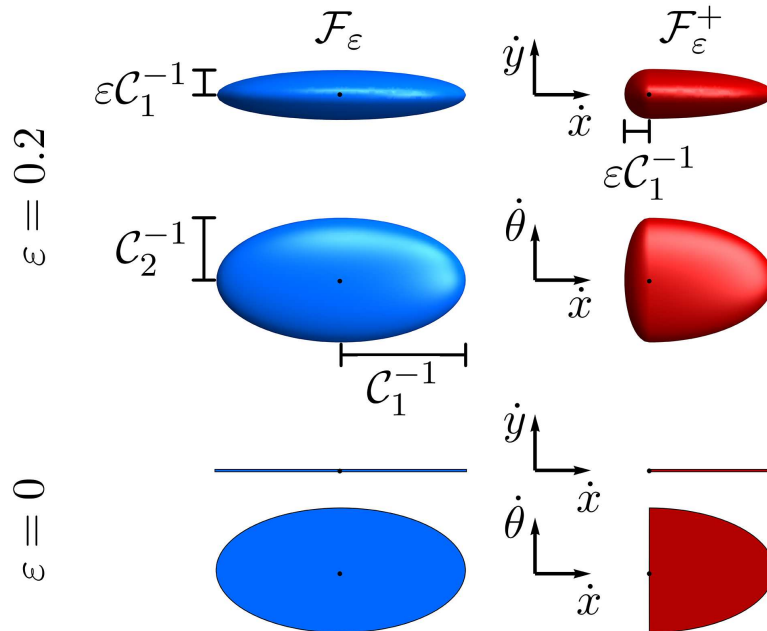

Figure 6-6: Levelsets for $d = 2$ of the (approximating) metrics $\mathcal{F}_{\varepsilon}(\mathbf{0}, (\dot{x}, \dot{y}, \dot{\theta})) = 1$ (left) and $\mathcal{F}_{\varepsilon}^+(\mathbf{0}, (\dot{x}, \dot{y}, \dot{\theta})) = 1$ (right), with $\varepsilon = 0.2$ (top) and $\varepsilon = 0$ (bottom). In this example, $\mathcal{C}_2(\mathbf{0}) = 2\mathcal{C}_1(\mathbf{0})$.

6.4.1 Backtracking

The application of the FM algorithm with the introduced Finsler metrics allows for the creation of a geodesic distance map. In order to compute a shortest path, or geodesic, a gradient descent method is applied. Since the geodesics are defined in the space of positions and orientations, an *intrinsic* gradient descent is applied in which both the spatial derivative $\nabla_{\mathbb{R}^d} U(\cdot)$ and the angular derivative $\nabla_{S^{d-1}} U(\cdot)$ of the distance map are required to be computed.

If γ is a minimizing geodesic from $\mathbf{p}_S$ to some $\mathbf{p} \in \mathbb{M}$, then it obeys the ordinary differential equation (ODE):

$$\begin{cases} \dot{\gamma}(t) = L\, \mathrm{d}_{\hat{\mathbf{p}}}\mathcal{F}^*(\gamma(t), \mathrm{d}U(\gamma(t))),\ L := d_{\mathcal{F}}(\mathbf{p}_S, \mathbf{p}), \\ \gamma(0) = \mathbf{p}_S, \quad \gamma(1) = \mathbf{p}. \end{cases} \tag{6.19}$$

for any $t \in [0,1]$ such that the differentiability of U and $\mathcal{F}^*$ holds at the required points. We denoted by $\mathrm{d}_{\hat{\mathbf{p}}}\mathcal{F}^*$ the differential of the dual metric $\mathcal{F}^*$ with respect to the second variable $\hat{\mathbf{p}}$, hence $\mathrm{d}_{\hat{\mathbf{p}}}\mathcal{F}^*(\mathbf{p}, \hat{\mathbf{p}}) \in T_{\mathbf{p}}^{**}(\mathbb{M}) \cong T_{\mathbf{p}}(\mathbb{M})$ is indeed a tangent vector to $\mathbb{M}$, for all $(\mathbf{p}, \hat{\mathbf{p}}) \in T^*\mathbb{M}$. For a proof of the ODE in Eq. (6.19) the reader is referred to the journal paper [58]. This ODE can be rewritten for the Riemannian approximation paths of the Reeds-Shepp car, provided that U is differentiable at $\gamma(t) = (\mathbf{x}(t), \mathbf{n}(t))$, such that

$$\dot{\gamma}(t) = L\, \mathcal{G}_{\gamma(t);\varepsilon}^{-1} \mathrm{d}U(\gamma(t))$$
$$\Leftrightarrow$$
$$\begin{cases} \dot{\mathbf{n}}(t) = L\, \mathcal{C}_2(\gamma(t))^{-1}\, \nabla_{S^{d-1}} U(\gamma(t)), \\ \dot{\mathbf{x}}(t) = L\, \mathcal{C}_1(\gamma(t))^{-1}\, D_{\mathbf{n}(t)}^{\varepsilon} \nabla_{\mathbb{R}^d} U(\gamma(t)). \end{cases} \tag{6.20}$$

where the gradient fields $\dot{\gamma}(t) \mapsto \mathcal{G}_{\mathbf{p};\varepsilon}^{-1} \mathrm{d}U(\dot{\gamma}(t))$ arise from a polarization of the symmetric Finsler norm $\mathcal{F}_{\varepsilon}(\gamma(t), \cdot)$:

$$\begin{aligned} \mathcal{G}_{\gamma(t);\varepsilon}(\dot{\gamma}(t), \dot{\gamma}(t)) &= |\mathcal{F}_{\varepsilon}(\gamma(t), \dot{\gamma}(t))|^2 \\ &= \mathcal{C}_1^2(\gamma(t))((\dot{\mathbf{x}} \cdot \mathbf{n})^2 + \varepsilon^{-2}\|\dot{\mathbf{x}} \wedge \mathbf{n}\|^2) + \mathcal{C}_2^2(\gamma(t))\|\dot{\mathbf{n}}\|^2 \,. \end{aligned} \tag{6.21}$$

The shortest-path from any target point in the domain Ω can now be computed by integration of Eq. (6.20) for example by forward Euler or Runge-Kutta numerical integration.

For the approximation paths of the car without reverse gear we have, provided that the forward-constrained distance map U^+ is differentiable at $\gamma^+(t) = (\mathbf{x}^+(t), \mathbf{n}^+(t))$, that

$$\dot{\gamma}^+(t) = L \begin{cases} \mathcal{G}^{-1}_{\gamma^+(t);\varepsilon} \mathrm{d}U^+(\gamma^+(t)) & \text{if } \gamma^+(t) \in \mathbb{M}_+, \\ \widetilde{\mathcal{G}}^{-1}_{\gamma^+(t);\varepsilon} \mathrm{d}U^+(\gamma^+(t)) & \text{if } \gamma^+(t) \in \mathbb{M}_-, \end{cases} \tag{6.22}$$

with $\widetilde{\mathcal{G}}_{\mathbf{p};\varepsilon}(\dot{\mathbf{p}}, \dot{\mathbf{p}})$ given by

$$\widetilde{\mathcal{G}}_{\mathbf{p};\varepsilon}(\dot{\mathbf{p}}, \dot{\mathbf{p}}) := \mathcal{C}_1^2(\mathbf{p})\, \varepsilon^{-2}\, \|\dot{\mathbf{x}}\|^2 + \mathcal{C}_2^2(\mathbf{p})\|\dot{\mathbf{n}}\|^2, \tag{6.23}$$

and with a disjoint Riemannian manifold splitting $\mathbb{M} = \mathbb{M}_+ \cup \mathbb{M}_- \cup \partial\mathbb{M}_\pm$. The two splitted manifolds are given by

$$\mathbb{M}_+ := \{\mathbf{p} \in \mathbb{M} \mid \nabla_{\mathbb{R}^d} U^+(\mathbf{p}) \cdot \mathbf{n} > 0\}, \tag{6.24}$$

$$\mathbb{M}_- := \{\mathbf{p} \in \mathbb{M} \mid \nabla_{\mathbb{R}^d} U^+(\mathbf{p}) \cdot \mathbf{n} < 0\}. \tag{6.25}$$

Here, the manifold $\mathbb{M}_+$ is equipped with metric tensor $\mathcal{G}_\varepsilon$, $\mathbb{M}_-$ is equipped with metric tensor $\widetilde{\mathcal{G}}_\varepsilon$ and

$$\partial\mathbb{M}_\pm := \overline{\mathbb{M}_+} \setminus \mathbb{M}_+ = \overline{\mathbb{M}_-} \setminus \mathbb{M}_-, \tag{6.26}$$

denotes the transition surface (surface of keypoints). Additional details regarding the process of backtracking of geodesics are available in the journal article [58].

6.5   Tool for fast marching experiments

In order to facilitate the experiments of FM with high-dimensional cost functions in $\mathcal{M}$, a software tool has been made that was co-developed with Stefan Mariën (Scientific programmer at the Academic Center for Epileptology Kempenhaeghe). This software tool is tailored to the specific needs of the project, allowing the user to specify the necessary parameters to the algorithm and receive and visualize its outputs from within the same application. The tool interfaces to the FM algorithm created by Jean-Marie Mirebeau, which is based on anisotropic stencils using lattice-basis reduction [130]. In Fig. 6-7 the main user interface of the software tool is shown.
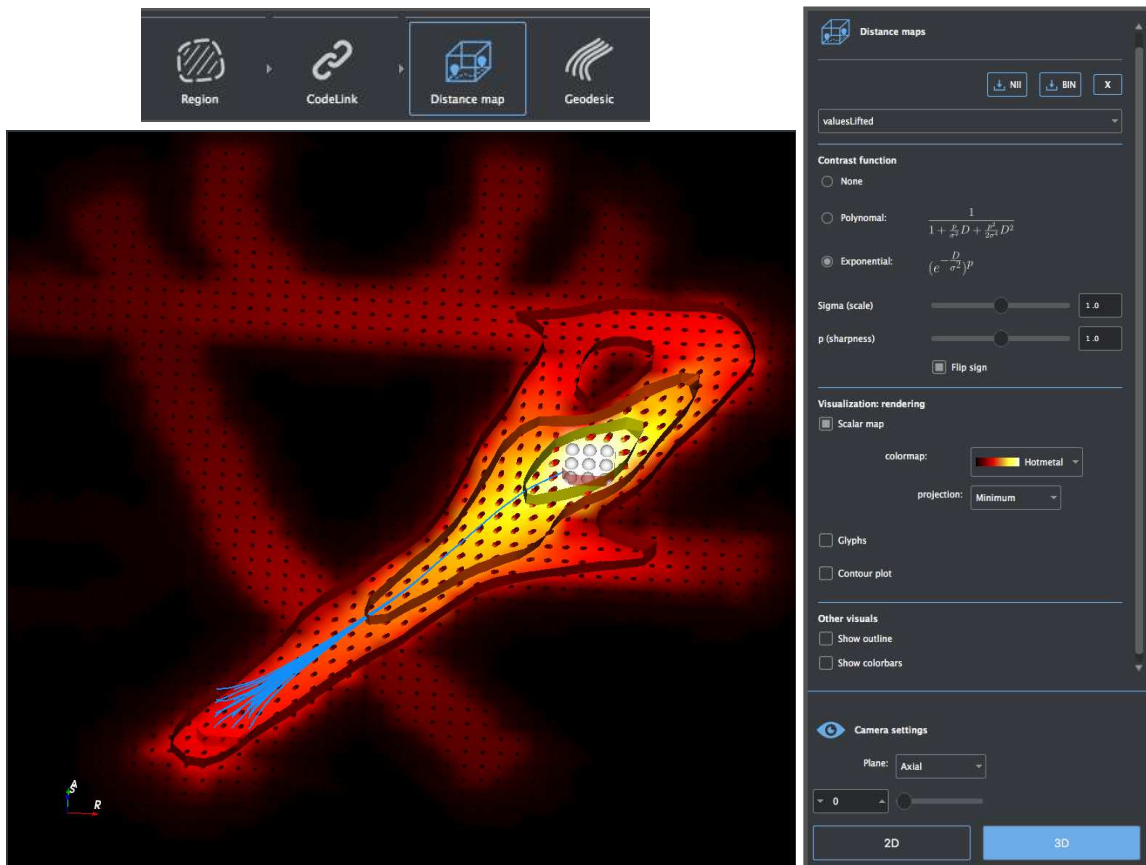
Figure 6-7: Interface of the software tool for performing fast marching experiments. The top bar allows the user to navigate between different panels, such as the "Distance maps" panel shown on the right. The main viewport (rendering area) shows the visualization of a distance map, which includes a scalar map weighted by a contrast function, isocontours showing equidistant boundaries, glyphs, and the geodesics between two ROIs in blue.
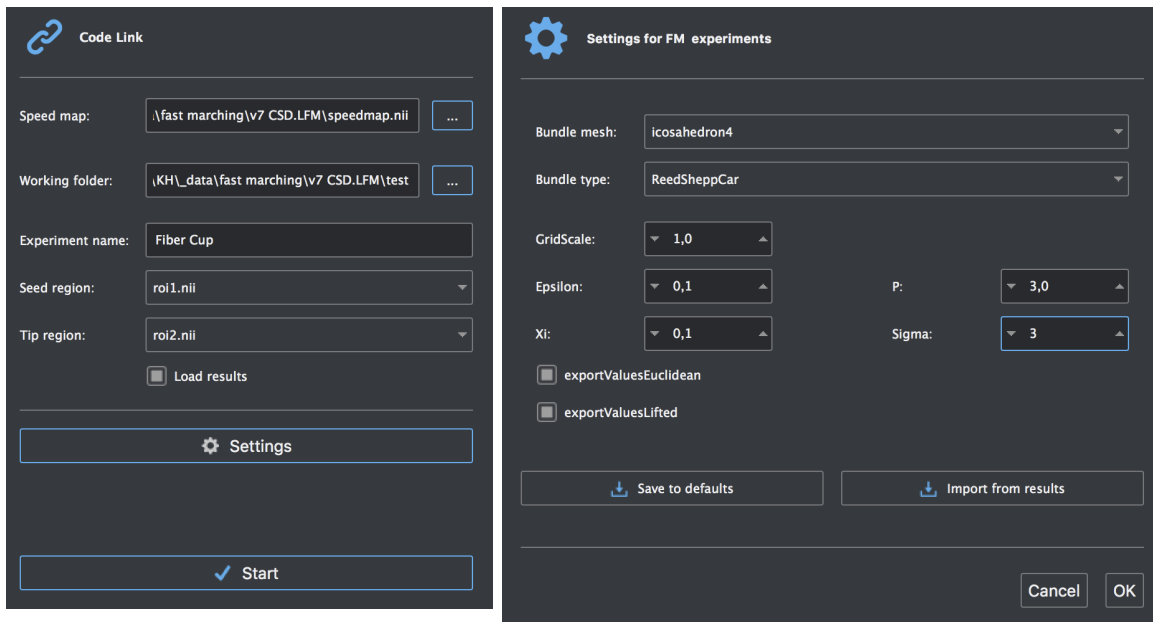
Figure 6-8: The tool features a codelink option, used to call the fast marching software with a set of input parameters such as the cost map $\mathcal{C}$, the seed and target regions, and various parameters such as ϵ, ξ, the type of Reeds-Shepp car used ($\mathcal{F}$ or $\mathcal{F}^+$ variants) and the spherical tessellation.

The software tool features the following user interface panels, each with its own dedicated functions and parameters:

- **Region** Import Region of Interests (ROIs). These ROIs are binary scalar maps that can be used either as seed voxels to initialize the FM (i.e., regions were $U(\mathbf{p}_s{=}0)$ for a set of voxels) or as end points from which a geodesic is drawn.

- **CodeLink** This provides the connection to the FM algorithm, allowing the user to specify necessary input parameters and options for output results. See Fig. 6-8 for the graphical user interface windows associated to this part.

- **Distance map** This panel (see Fig. 6-7, right) provides visualization options for the geodesic distance map. For visualization clarity, the user can specify a contrast function such as $1/\exp\left(\left(\frac{D}{\sigma^2}\right)^p\right)$ or the second-order Taylor expansion of the denominator of the contrast function $1/\left(1 + \left(\frac{D}{\sigma^2}\right)^p + \frac{1}{2}\left(\frac{D}{\sigma^2}\right)^{2p}\right)$ where $D = d_{\mathcal{F}_\epsilon}(\mathbf{p}_s, \mathbf{p})$.

- **Geodesic** Visual options for the geodesics obtained from FM. The user can set a static color of the geodesics, make the coloring orientation-based, and show arrows for each point on the geodesic to indicate its orientation.

The tool for FM experiments is illustrated in the experiments performed in the following section.

6.6   Experimental results

The potential of anisotropic FM for path tracking is demonstrated by experiments on synthetic DWI datasets. In these experiments the benefits of anisotropic metrics compared to isotropic metrics are demonstrated by performing geodesic backtracking for various model parameter variations. Furthermore, the experiments illustrate the differences for the different metrics $\mathcal{F}_\varepsilon$ and $\mathcal{F}_\varepsilon^+$.

The experiments were performed using an anisotropic FM implementation for $d = 3$ written in C++ that was based on the implementation for $d = 2$ described in [130]. Further data analysis was performed using Mathematica 11.0 (Wolfram Research, Inc., Champaign, IL), applying Wolfram LibraryLink (Wolfram Research, Inc., Champaign, IL) to interface with the FM library.

The data acquired from DWI can be readily adapted into the cost function, since the diffusion measurements are distributions $(\mathbf{y}, \mathbf{n}) \mapsto U(\mathbf{y}, \mathbf{n})$ within the manifold $\mathbb{M}$ for $d = 3$. From these measurements a FOD can be created, for example by applying CSD or another modeling procedure (see Chapter 4), yielding a probability of finding a fiber at a certain position and orientation [214].

Backtracking is performed through forward Euler integration of the backtracking PDE involving the intrinsic gradient, following Section 6.4.1. The spatial derivative $\nabla_{\mathbb{R}^d} U(\gamma(t))$ was implemented as a first-order Gaussian derivative. The angular derivatives $\nabla_{S^{d-1}} U(\gamma(t))$ was implemented by a first-order spherical harmonic derivative, which can be computed analytically in a spherical harmonic basis [172].

Construction of the cost function

The synthetic DWI data is created by generating/simulating a Fiber Orientation Density (FOD) of a desired structure. Within the domain in $\mathbb{R}^3 \times S^2$ a distribution of δ-spikes is created with peaks at the positions of the desired structures in the orientation of the bundle. Each δ-distribution is convolved with an FOD kernel that was extracted from real DWI data and reflects the response function that is typical for a single orientation of fibers, i.e. an FOD with a single sharp peak. Spherical rotation of the FOD kernel is done in the spherical harmonics domain by use of the Wigner D-matrix to prevent interpolation issues. From all distributions an FOD function $W : \mathbb{R}^3 \times S^2 \to \mathbb{R}^+$ is composed. We use the FOD function W to define the cost function $\frac{1}{1+\sigma} \leq \mathcal{C} \leq 1$ via

$$\mathcal{C}(\mathbf{p}) = \frac{1}{1 + \sigma \left| \frac{W_+(\mathbf{p})}{\|W_+\|_\infty} \right|^p},$$

where $\sigma \geq 0$, $p \in \mathbb{N}$, with $\| \cdot \|_\infty$ the sup-norm and $W_+(\mathbf{p}) = \max\{0, W(\mathbf{p})\}$. The cost function $\mathcal{C}(\mathbf{p})$ induces the following spatial and angular cost functions $(\mathcal{C}_1, \mathcal{C}_2)$:

$$\mathcal{C}_1(\mathbf{p}) = \xi\mathcal{C}(\mathbf{p}), \qquad \mathcal{C}_2(\mathbf{p}) = \mathcal{C}(\mathbf{p}).$$

The implementation of nonuniform cost is comparable to the application of vessel tracking in retinal images in $d = 2$ by Bekkers et al. [19].

Influence of model parameters

The first synthetic dataset consists of a curved and a straight bundle (tube), which cross at two locations as shown in Fig. 6-9. The experiments using metric $\mathcal{F}_\varepsilon$ demonstrate the effect of the model parameters on the geodesic back-traced from the bottom-left to the seed location at the bottom-right of the curved bundle. A distance map is computed for parameter configuration A (Fig. 6-9, right) in which suitable values are used for the data-term σ, and the fast-marching parameters ξ and ε. Furthermore, fixed values are used for
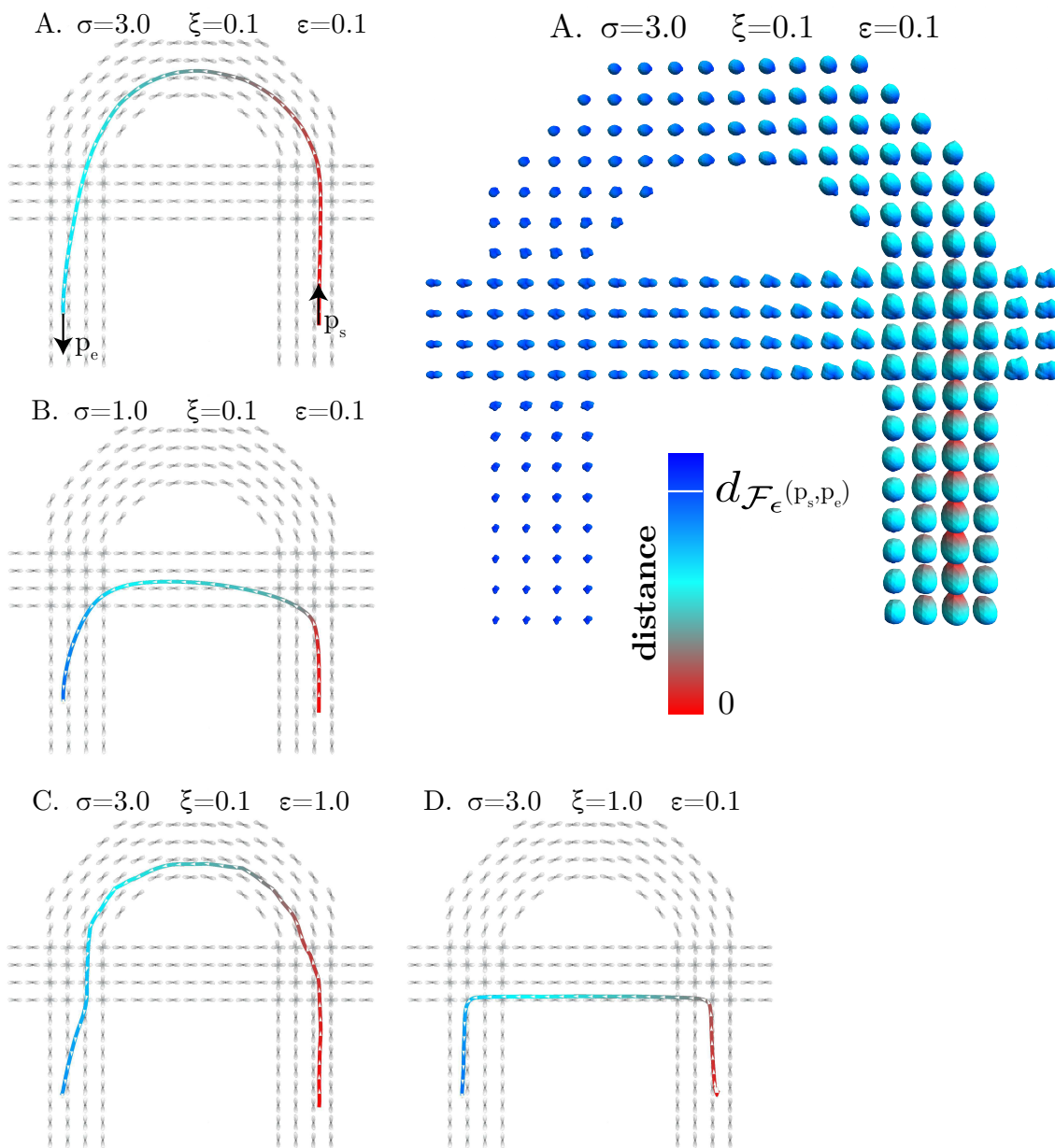
Figure 6-9: Comparison of the results of backtracking on a 2D plane in a synthetic DWI dataset on $\mathbb{M} = \mathbb{R}^3 \times S^2$. In case A the default parameters for σ, ξ and ε are applied resulting in a global minimizing geodesic (left) and its corresponding distance map (right). Case B reflects the influence of the data-term σ. Case C reflects the isotropic Riemannian case. Case D reflects a high cost for moving spatially and results in curves that resemble a piecewise linear curve. The distance map is illustrated using a glyph visualization in which the size of the glyph corresponds to $\exp\left(-(d_{\mathcal{F}_\varepsilon}(\mathbf{p}_s, \mathbf{p}_e)/s)^p\right)$ where $\mathbf{p}_s$ is the seed location, $\mathbf{p}_e$ is a location on a glyph, and s and p are chosen based on visualization clarity.

data sharpening $p = 3$, spatial smoothing $\sigma s = 0.5$, forward-Euler integration step size $\delta t = 0.04$, and a gridscale of 1. By use of these parameters the global minimizing geodesic (Fig. 6-9.A, left) is shown to take the longer, curved route. In parameter configuration B the data-term σ is lowered, which creates a geodesic that is primarily steered by internal curve-dependent costs and is shown to take the shortcut route (Fig. 6-9.B). Setting $\varepsilon = 1$ in configuration C leads to a Riemannian case where the geodesic resembles a piecewise linear curve. In configuration D the relative cost of spatial movement relative to angular movement is high, leading to geodesics with shortcuts. Overall, the configuration **A** with a relatively strong data term, large bending stiffness ($\xi^{-1} = 10$), and a nearly SR geometry ($\varepsilon = 0.1$) results in a pathway that avoids the unwanted shortcut.

Positive control constraint

For the application of FM with DWI data as input it is desirable that the resulting geodesic is not overly sensitive to the boundary conditions, i.e. the placement and orientation of the geodesic tip. Furthermore, since neural fibers do not form cusps, these are undesirable in the backtracking results. In Fig. 6-10 the backtracking results are shown for the cases without reverse gear $\mathcal{F}_\varepsilon^+$ (top) and the model with reverse gear $\mathcal{F}_\varepsilon$ (bottom). The distance map for $\mathcal{F}_\varepsilon^+$ was computed by the iterative method implementing the forward Reeds-Shepp car, while for $\mathcal{F}_\varepsilon$ the FM method was used. Overall, with the positive control constraint it can be observed that small changes in tip orientation cause large variations in the traced geodesic in $(\mathbb{M}, d_{\mathcal{F}_\varepsilon})$, whereas the traced geodesic in $(\mathbb{M}, d_{\mathcal{F}_\varepsilon^+})$ is both more stable and more plausible.
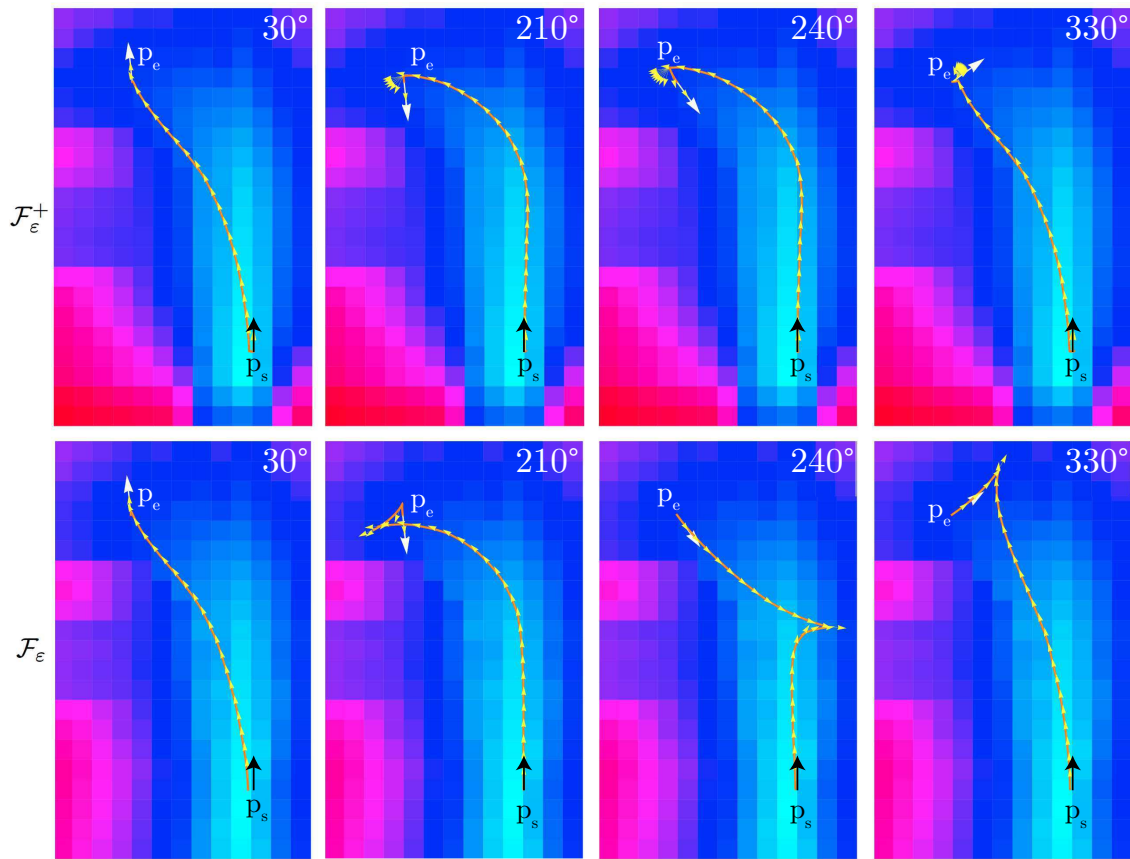
Figure 6-10: Backtracking of minimizing geodesics of the model $(\mathbb{M}, d_{\mathcal{F}_\varepsilon^+})$ without reverse gear (top) and the model with reverse gear $(\mathbb{M}, d_{\mathcal{F}_\varepsilon})$ (bottom) using the model parameters of configuration A ($\sigma = 3.0$, $\xi = 0.1$ and $\varepsilon = 0.1$) for various end conditions.

Robustness to neighboring structures

A problem that arises when tracking a bundle-like structure of interest, using e.g. FM or tractography, is that nearby structures in the data may interfere and lead to incorrect tracking results. For example, a geodesic may partially traverse a neighboring structure in which the cost is lower. The following example, taken from the joint-author paper [JMIV], demonstrates that the use of a sub-Riemannian metric instead of a Riemannian metric can result in geodesics that are more robust to inference from neighboring structures.

The geometry of the dataset is shown in Fig. 6-11 (top-left) and consists of one bundle that has torsion (green), that crosses with another bundle (blue), and a third bundle (red) that is parallel with the first in one part. The cost in these bundles is constructed similarly to the first phantom DWI experiment, but the cost in the red bundle is twice as low as in the other bundles. A close-up of the synthesized FOD distribution is shown in Fig. 6-11 (top-right).
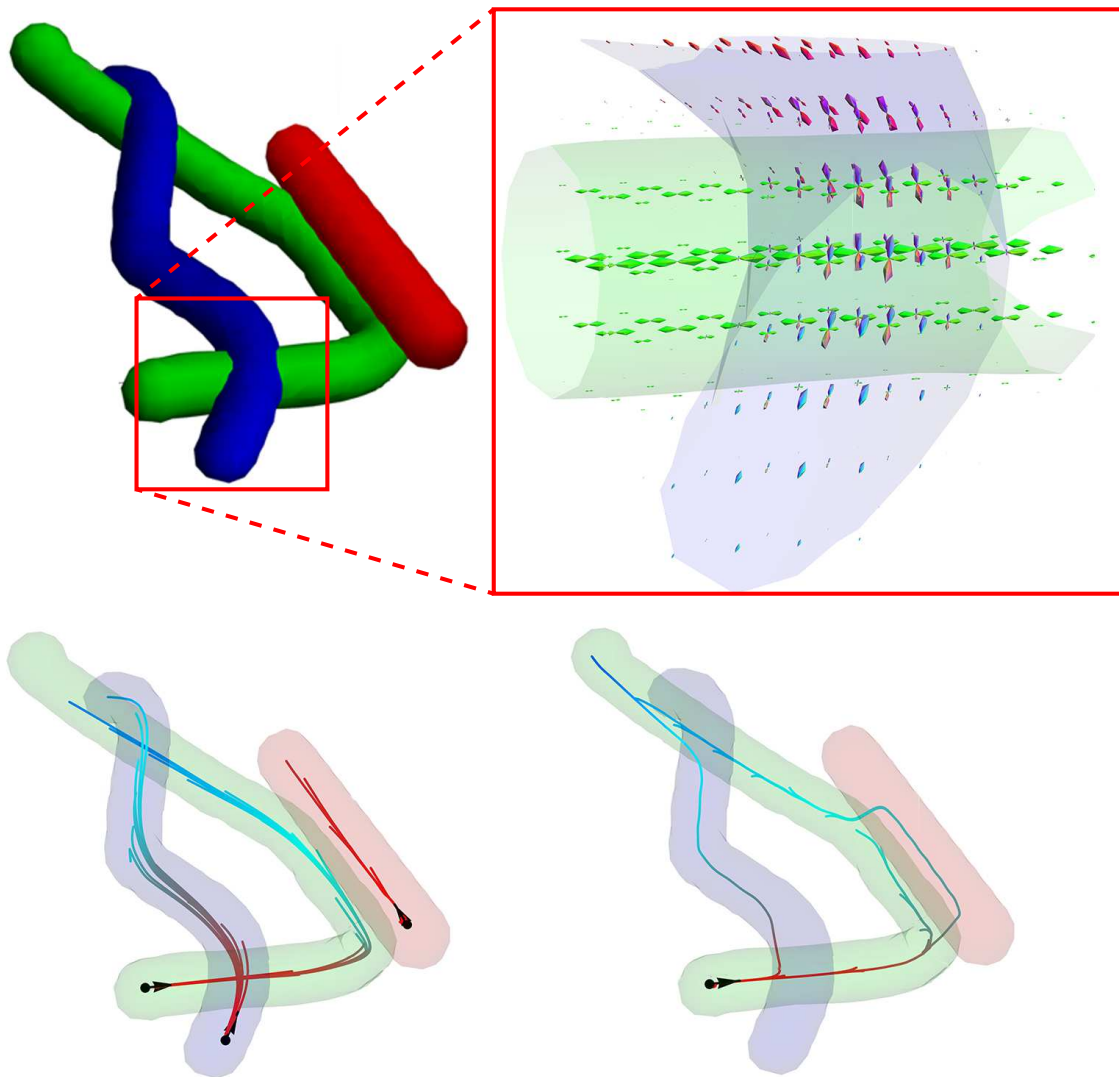
Figure 6-11: 3D configuration of the bundles (top-left) and a visualization of part of the synthetic DWI data (top-right). The backtracking of geodesics in $(\mathbb{M}, d_{\mathcal{F}_\varepsilon})$ from several points inside the curves to end points of the bundle is successful when using $\varepsilon = 0.1$ (bottom-left). When using $\varepsilon = 1$ the dominant red bundle can cause the paths from the green bundle to deviate from the correct structure (bottom-right).

To have comparable parameters as in the previous experiment, despite increasing the amplitude in one of the bundles by a factor 2, we choose to construct the cost using parameter $p = 3$, and $\sigma = 3 \cdot 2^p = 24$. Furthermore, the cost parameters are $\mathcal{C}_1 = \xi\mathcal{C}_2 = \mathcal{C}$, with $\xi = 0.1$. From various seeding regions inside the green, blue or red bundle, the shortest paths to the target region at the end of the bundles is computed by the FM algorithm. In Fig. 6-11 (bottom-right) it can be observed that for $\varepsilon = 1$, which corresponds to having an isotropic Riemannian metric, the geodesic partially traverses into the green bundle with much lower cost. However, for $\varepsilon = 0.1$, which corresponds to an almost (close approximation) of an SR geodesic, it can be observed (see Fig. 6-11, bottom-left) that the shortest path accurately follows the shape of the bundles. Overall, it can be observed that the SR geodesics in $(\mathbb{M} = \mathbb{R}^3 \times S^2, d_{\mathcal{F}_\varepsilon})$ with $\varepsilon \ll 1$, are less attracted to parallel, dominant structures than isotropic Riemannian geodesics.

6.7 Discussion

An extension to the existing optimal control methodology has been presented for solving the problem of finding optimal paths to the Reeds-Shepp car and its variant without a reverse gear, both for $d = 3$. The use of the constrained model without a reverse gear has shown to lead to more meaningful shortest paths in the experiments performed on phantom DWI data.

The hard constraint on curvature as in the original paper by Reeds and Shepp [175] was supplanted for the more flexible Riemannian or Finslerian metrics. These metrics $\mathcal{F}_0$ and $\mathcal{F}_0^+$ are designed to allow for curves that have a constraint in sideways motion, with a positive proportionality constant in the case of $\mathcal{F}_0^+$. Based on theoretical analysis it was shown, as detailed in the journal paper [58], that both models are globally controllable, but only the unconstrained model is also locally controllable. To make numerical evaluation of these metrics possible, approximating metrics $\mathcal{F}_\varepsilon$ and $\mathcal{F}_\varepsilon^+$ have been introduced that convert to a sub-Riemannian metric as $\varepsilon \to 0$. The distance map converges pointwise and the geodesics converge uniformly, implying that for sufficiently small ε we indeed have a reasonable approximation of the $\varepsilon = 0$ case.

To obtain solutions for the optimal control problem of finding the shortest paths, the minimization problem is formulated as an eikonal equation and solved by the FM method. To estimate the accuracy of a numerical solution, which depends in large part on the discretization scheme used, a comparison between exact and numerical geodesics was performed in the journal article [58]. For sub-Riemannian geodesics in the Euclidean motion group SE(3) with uniform cost a sufficient accuracy was observed for not too extreme begin and end conditions, i.e. paths that do not require extraordinary curvature.

The experiments performed on phantom DWI data confirm that the combination of the eikonal PDE formulation, the Fast-Marching method and the construction of the non-uniform cost from the images, results in geodesics that follow the desired paths. The advantages of the model $(\mathbb{M}, d_{\mathcal{F}_\varepsilon})$ with $0 < \varepsilon \ll 1$ over the model $(\mathbb{M}, d_{\mathcal{F}_1})$ were evident in the sense that the minimizing geodesics better follow the curvilinear structure and deal with crossings and nearby parallel bundles (even if torsion is present). Furthermore, we have shown the advantage of model $(\mathbb{M}, d_{\mathcal{F}_\varepsilon^+})$ with $0 < \varepsilon \ll 1$, compared to $(\mathbb{M}, d_{\mathcal{F}_\varepsilon})$ in terms of stability, with keypoints instead of cusps.

Future work should focus foremost on a quantitative assessment of the performance in 3D path tracking problems with medical data, for example on Magnetic Resonance Angiography and on DWI of the brain. Furthermore, to obtain a more adaptive vessel/fiber tracking it should be investigated whether locally adaptive frames [57] can be integrated into the Finsler metrics $\mathcal{F}_\varepsilon$, $\mathcal{F}_\varepsilon^+$.

Chapter 7 | **Future prospects**

Anisotropic fast marching in $\mathbb{R}^3 \rtimes S^2$ is a promising method for the estimation of structural connectivity as an alternative to tractography-based methods. A connectivity measure is proposed that is based on the minimized average distance between any two regions of interest. Preliminary experiments were performed to evaluate the estimation of structural connectivity with fast marching in support of deep brain stimulation.

7.1   Introduction

Deep brain stimulation (DBS) has proven to be effective in seizure inhibition by the stimu-
lation of the anterior nucleus of the thalamus (ANT) [102, 65], which is an important node
within the Papez circuit. The anatomical connections of the Papez circuit are illustrated
in Fig. 7-1. Starting from the hippocampal formation, signals from the cortical association
areas are transferred via the fornix to the mammillary bodies. The mamillothalamic tract
(MMT) relays the information further to the ANT. From there, the ANT projects fibers to
the cingulate gyrus and subsequently projects back to the hippocampus, completing the
circuit. The components within the Papez circuit share a functional dependence, shown
by the fact that other stimulation targets in the Papez circuit can also lead to seizure re-
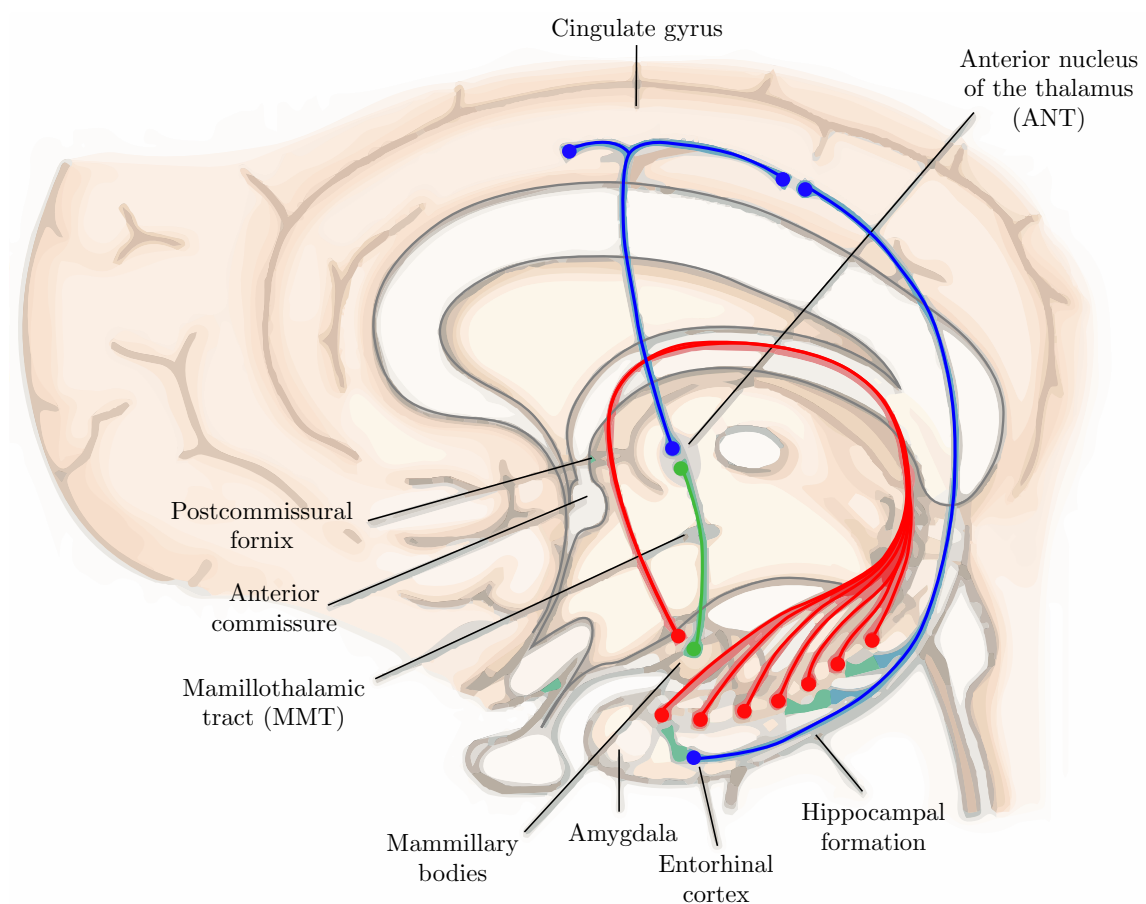

Figure 7-1: The Papez circuit with the brain regions involved and the connections between
them. Figure adapted from [232].

duction, such as the fornix [107, 105, 120] or the MMT [7]. Structural connectivity analysis to estimate the connectivity strength within the Papez circuit may provide clues towards the efficacy of DBS to treat the epilepsy of a patient.

Tractography methods (c.f. Chapter 4) are considered useful when evaluating the *geometry* of white matter structures such as the Papez circuit [137]. For example, in case of temporal lobe epilepsy, it is known that a localized thalamocortical network may be affected [18]. Structural connectivity within these networks was estimated by, amongst others, Keller et al. [101] by counting the number of streamlines between the thalamus and a lobular target, which may yield unreliable results. In Fig. 7-2 the results are illustrated of probabilistic tractography applied to reconstruct the geometry of the Papez circuit by use of the MRtrix algorithm [210], for which the ANT as a well as the cingulate cortex were used as seeding regions. These results indicate that, despite a large number of false positive streamlines, the anatomy of the Papez circuit can be reconstructed by selecting the voxels with a high streamline density.

However, streamline counting for the purpose of estimating structural connectivity is considered a controversial method [96] due to the strong dependence on the type of tractography algorithm and the inherent shortcomings of tractography [94, 74]. As an alternative, the anisotropic FM method introduced in Chapter 6 is considered a promising method. FM provides the geodesic distance map, which describes the shortest paths from a seed region to any other point in the domain. The geodesic distance map can be used to compute a *connectivity measure*, which reflects the minimized average distance between any two regions of interest in the domain. The computation of the connectivity measure will be demonstrated for an MRI phantom that resembles a coronal slice of the human brain, while feasibility experiments demonstrate the possibility to reconstruct the so-called Papez circuit based on human brain data in support of DBS.
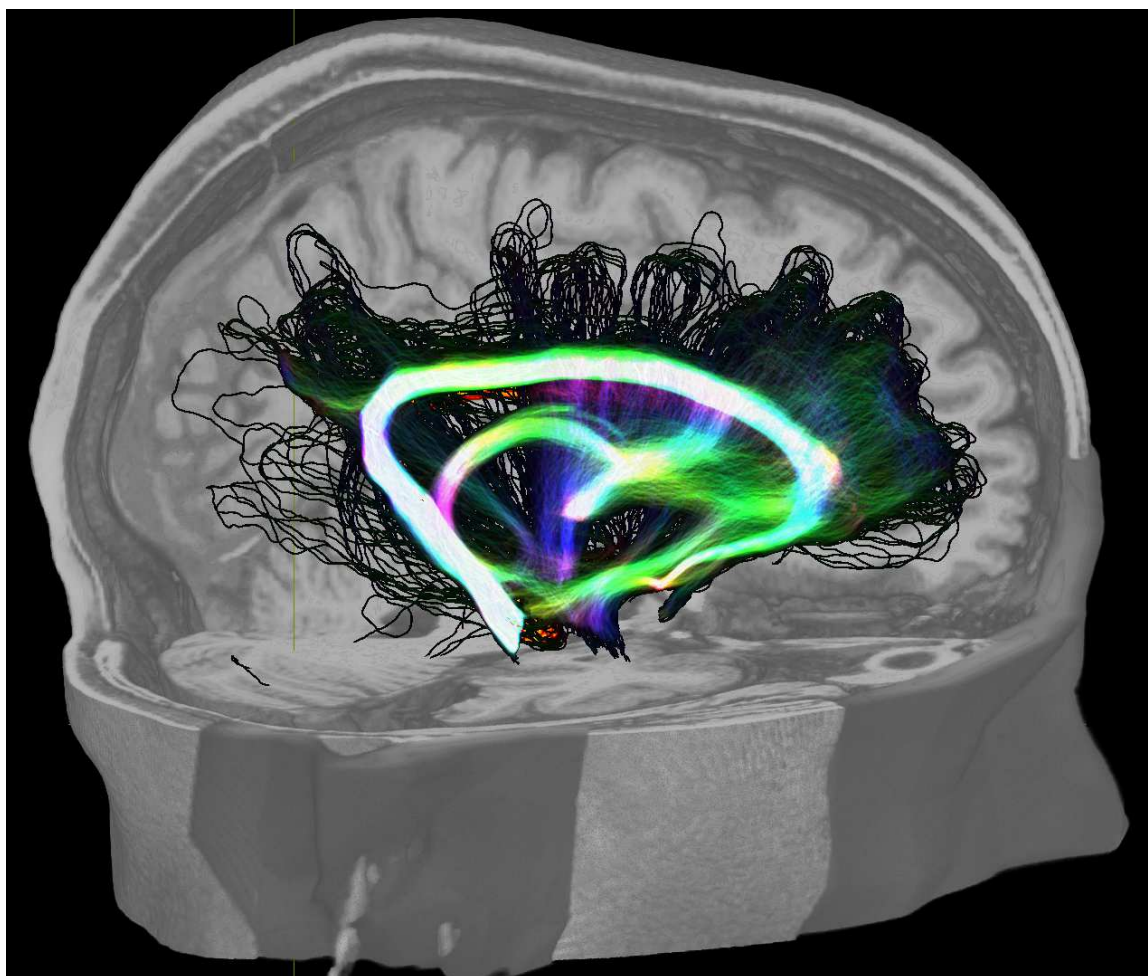
Figure 7-2: The Papez circuit reconstructed using probabilistic tractography. Regions with a high streamline density are colored brightly.

7.2   Structural connectivity measure

The problem of estimating structural connectivity in diffusion-weighted imaging (DWI) is recast into the problem of finding the shortest paths on a Riemannian or Finslerian manifold. The geodesic distance map, introduced in Chapter 6 and demonstrated for synthetic DWI experiments, can be used to compute a *connectivity measure* between two regions (subsets). Given two discrete subsets s_1, s_2 of the manifold $\mathcal{M}$ that are compact and disjoint, and a fiber orientation density function $U : \mathbb{R}^3 \times S^2 \to \mathbb{R}^+$, we can compute the directional connectivity between s_1 and s_2 as:

$$\bar{C}_U(s_1, s_2) = \frac{1}{|s_1|} \sum_{q \in s_2} \left\{ \min_{p \in s_1} \frac{d_{\mathcal{F}_U}(p, q)}{\epsilon(p, q)} \right\}, \tag{7.1}$$

which can be interpreted as the Hausdorff distance between s_1 and s_2, induced by the data-dependent Finsler length $d_{\mathcal{F}_U}(p, q)$ between the point p in s_1 and the point q in s_2, while normalizing for the spatial (Euclidean) length of the minimal Finsler geodesics between these points given by $\epsilon(p, q) = \int_0^1 \|x'_{\min}(t)\| dt$, in which $x'_{\min}(\cdot)$ is the spatial part of the geodesic minimizing the distance $d_{\mathcal{F}_U}(p, q)$. Here, $|s_1|$ indicates the number of points in the subset s_1. The normalization by spatial length of minimizers, similarly to the approach by Pechaud et al. [161], removes a bias towards large spatial distances. In other words, without the normalization the connectivity becomes a true distance satisfying the triangle-inequality.

Due to the varying sizes of the subsets s_1 and s_2, and the possible use of an asymmetric Finsler function $\mathcal{F}_\epsilon^+$ (c.f. Chapter 6), a symmetrized connectivity measure $C_U(s_1, s_2)$ that minimizes both directions is computed according to

$$C_U(s_1, s_2) = \min \left\{ \bar{C}_U(s_1, s_2), \bar{C}_U(s_2, s_1) \right\}. \tag{7.2}$$

The approach that is suggested here has several advantages. Firstly, the symmetrized connectivity measure can be computed by only two runs of the FM algorithm, where even the spatial length normalization can be computed simultaneously [34]. Secondly, the approach is coordinate-free and, unlike Pechaud et al. [161], is not dependent on Euler angles.

7.2.1 Fiber Cup phantom

The "Fiber Cup" is a realistic diffusion-weighted imaging (DWI) phantom that was originally conceived to evaluate the performance of diffusion models and tractography algorithms [64]. The Fiber Cup phantom provides a ground truth of a fiber configuration that resembles a coronal section of the human brain. The phantom contains crossing and kissing fibers as well as bundles of different curvatures, as illustrated in Fig. 7-3 (left).

For the computation of the geodesic distance map of the Fiber Cup using FM, a recently released software phantom of the Fiber Cup created with FiberFox was used [141] since this software allows for a more accurate description of the ground truth fibers. The constrained spherical deconvolution (CSD) model available in Diffusion Imaging in Python (DIPY) was used to compute a fiber orientation density (FOD) function of the Fiber Cup data, the result of which is illustrated in Fig. 7-3 (right).
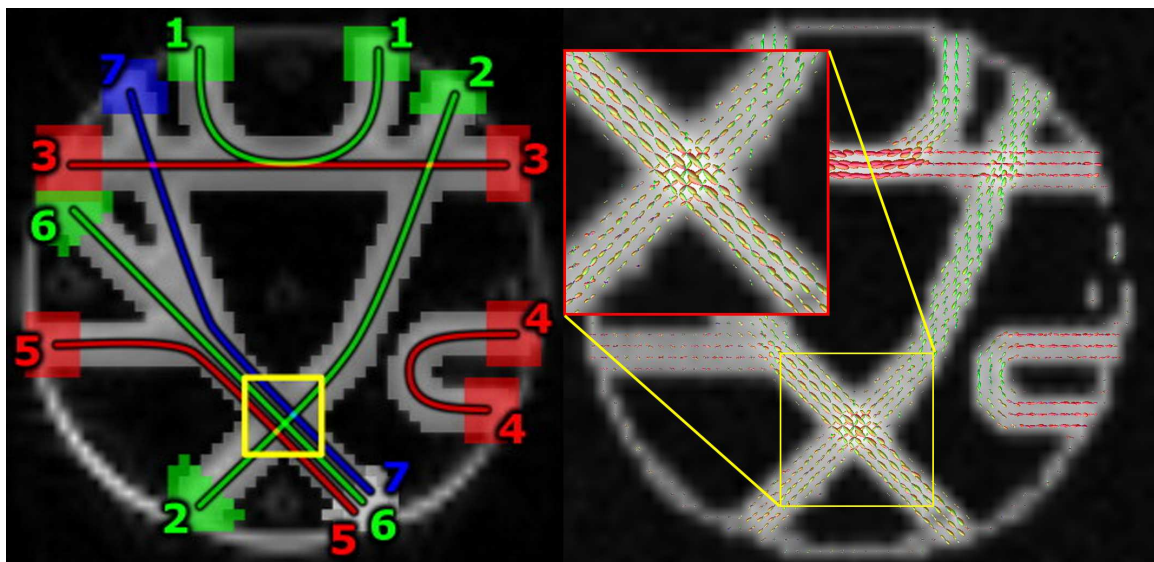
Figure 7-3: Left: the fiber configuration of the Fiber Cup phantom. Right: The FOD of the fiber phantom computed using CSD.

The experimental results of FM applied to the Fiber Cup dataset are shown in Fig. 7-4. For this experiment, three seed regions, or subsets on the manifold $\mathcal{M}$, were selected. To compute a symmetrized connectivity between all these regions, geodesic distance maps were created starting from s_1, s_2 and s_3. The distance map within the seed regions was
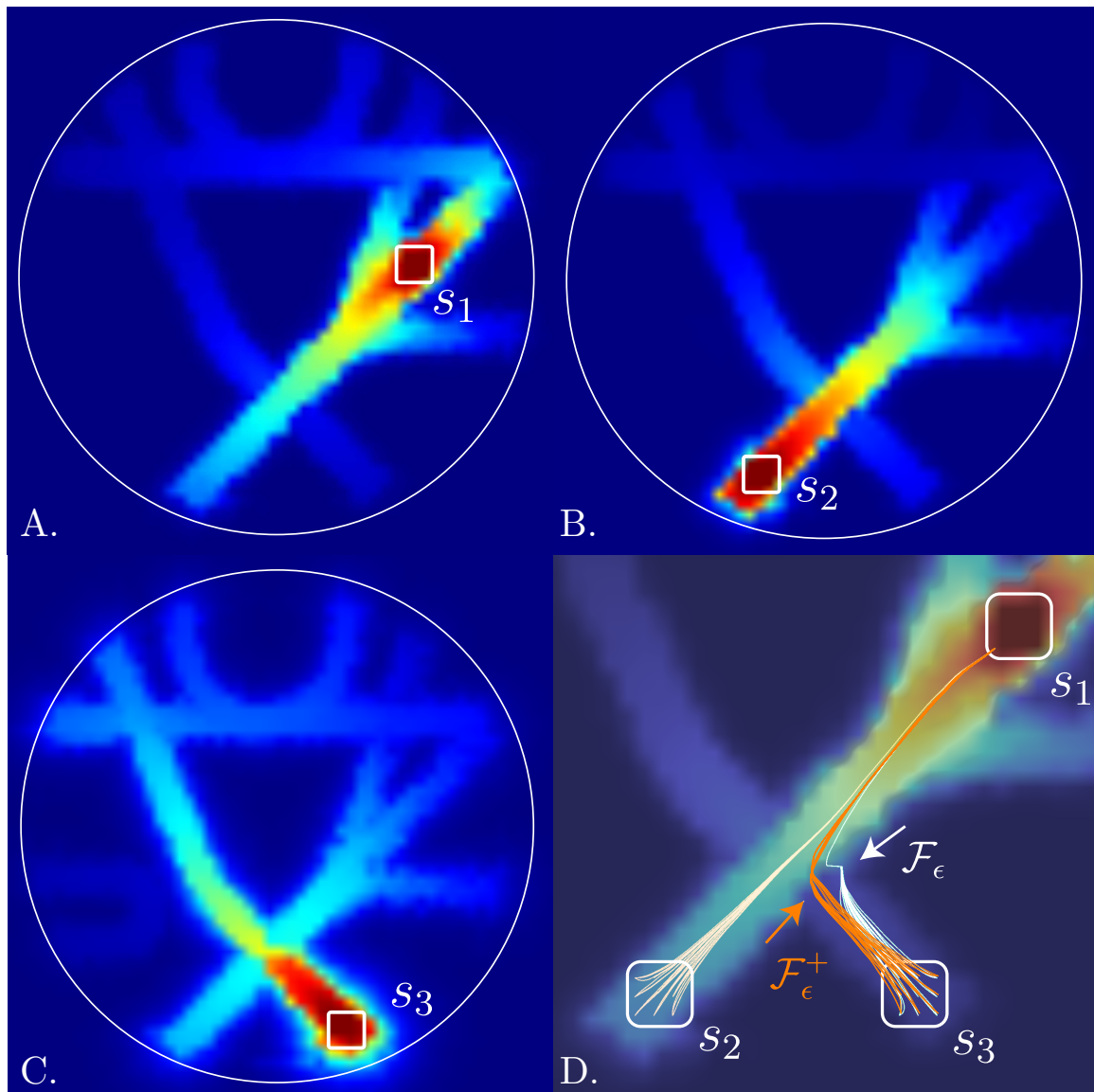
Figure 7-4: Results of the evaluation of geodesic distance maps with the $\mathcal{F}_\epsilon$ metric (c.f. Chapter 6), starting from the subsets s_1 (A), s_2 (B) and s_3 (C). The geodesics from s_1 to s_2 and s_3 are illustrated (with a close-up) in white (D), showing that s_1 and s_2 can be connected by a straight path while the geodesic between s_1 and s_3 contains a cusp (indicated by the white arrow). The experiment repeated with the $\mathcal{F}_\epsilon^+$ metric shows that the cusp is resolved (indicated in orange).

initialized at zero for all orientations on the sphere S_2, i.e. the seeding occurs to all directions equally. Seed regions s_1 and s_2 were placed on the same fiber bundle, see Fig. 7-4 (A and B, respectively), and a third seed region s_3 was placed in another fiber bundle, see Fig. 7-4 (C). For this experiment, the $\mathcal{F}_\epsilon$ metric was used (c.f. Eq. (6.12) of Chapter 6) with $\epsilon = .5$ and $\xi = .5$. Besides the geodesic distance maps, Euclidean distance maps were created for each experiment. The geodesics from s_1 to s_2 and s_1 to s_3 are shown by the white lines in Fig. 7-4 (D) which indicate that a straight path connects s_1 and s_2, while in the path between s_1 and s_3 a cusp appears. Comparison of the symmetrized connectivity measures indicates that $C_U(s_1, s_2)$ is significantly higher than $C_U(s_1, s_3)$ with an increase of 124.4%, which is an expected result since the points s_1 and s_2 are part of the same fiber bundle. If the normalization by the Euclidean distance map is omitted, i.e. $\epsilon(p, q) = 1$ for any p and q, then the $C_U(s_1, s_2)$ is 109.8% higher, indicating that the connectivity difference is mainly contributed by the Finslerian distance.

When the same experiment is applied with the forward metric $\mathcal{F}_\epsilon^+$ it can be observed that the cusp is resolved, as illustrated in Fig. 7-4 (D) by the orange line. The connectivity measure was not significantly affected by the choice of metric $\mathcal{F}_\epsilon$ or $\mathcal{F}_\epsilon^+$ in this particular case, showing that $C_U(s_1, s_2)$ is 123.3% higher than $C_U(s_1, s_3)$.

7.2.2   The Papez circuit

Presented here are the results of preliminary experiments of the reconstruction of the Papez circuit using FM. First of all, it is necessary to have a segmentation of brain areas that are related to the Papez circuit. An accurate segmentation of the ANT is very important since this brain area is the main stimulation target of DBS to treat epilepsy [65]. In this study an atlas of the thalamic nuclei is used to segment the ANT. The so-called Morel's atlas [143] is defined in a standard space, or MNI space, and can be transformed non-linearly to the subject space, e.g. by use of FSL [198], to provide a crude segmentation of the ANT. The quality of the resulting segmentation can vary because of the large inter-patient variability in the thalamic region, however for this preliminary study it is considered acceptable. In future work the thalamic nuclei may be segmented with the use of diffusion tensor imaging (DTI) [234, 245, 176, 122] or HARDI [30, 188]. Furthermore, if 7T neurological data is available then it may be possible to segment the thalamic nuclei based on shape analysis of anatomical images [239, 118].

The FM method was applied to reconstruct the Papez circuit by generating a geodesic distance map starting from the ANT seed region. In Fig. 7-5 the distance map is shown at four sagittal slices of the brain, alongside with the corresponding brain anatomy using a T1-weighted MRI scan. For this experiment the $\mathcal{F}_\epsilon$ metric was used with parameters $\epsilon = \xi = 0.5$. For each slide the anatomical structures are annotated. It can be observed that the distance map reflects relatively shorter paths for structures within the Papez circuit, such as the mammillothalamic fasciculus in slice 1, the fornix in slice 2, the thalamocortical radiation in slice 3 and the cingulum in slice 4. The results presented here indicate that the FM method is effective in finding shortest paths within the Papez circuit and shows promise for an accurate measurement of connectivity.
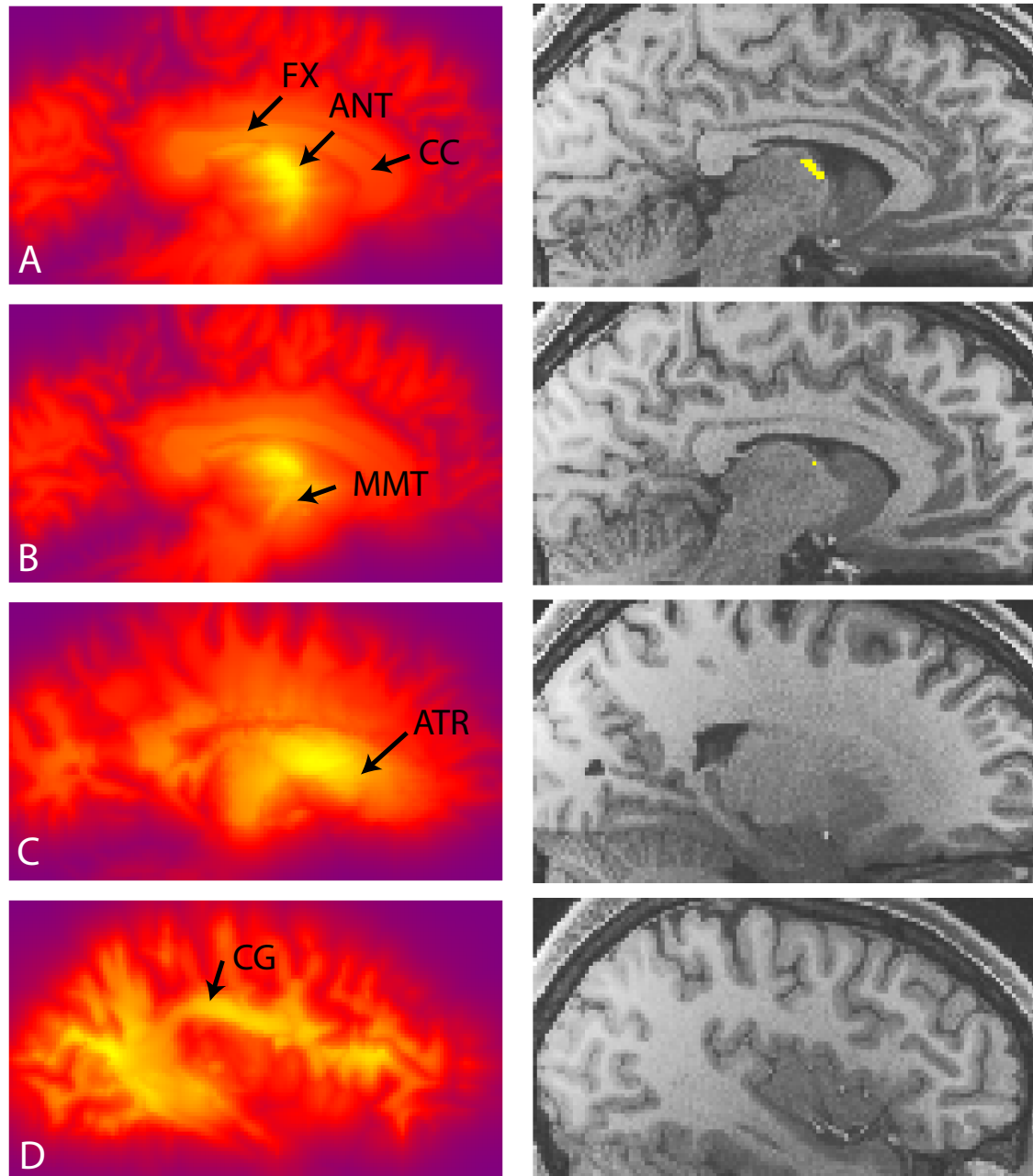
Figure 7-5: Preliminary experiments of Papez circuit identification using FM. A) ANT seed region (yellow) showing parts of the fornix. B) Mammillothalamic fasciculus. C) Anterior thalamic radiation. D) Cingulus. (CC=corpus callosum, FX=fornix, ANT=anterior nucleus of the thalamus, MMT = mammillothalamic fasciculus, CG = cingulus)

7.3   Conclusion and recommendations

Currently, the main challenge is to combine functional and structural methods to solve the problem of unraveling the epileptic network. It was shown (c.f. Chapter 3) that functional connectivity analysis of interictal epileptic discharges (IEDs) yields the brain areas that appear to be the nodes of the underlying network. To better understand the spatiotemporal interactions within this network, it can be useful to reconstruct the structural network that forms the backbone of the functional network. The results of association strength and time delay presented in Chapter 3 can be compared to a measure of structural connectivity as a way of validating each other: a functional analysis pinpoints nodes in the network, while a structural network can aid in explaining the time delays estimated. A promising method to measure the connectivity of the structural network, based on finding the shortest path, is FM, introduced in Chapter 6. The geodesic distance map estimated by FM potentially allows to integrate the structural and functional connectivity measures within a single computational model. To conclude, the preliminary results presented here indicate that structural connectivity analysis using FM has not only potential with regard to the estimation of connectivity of white matter pathways as backbone of functional networks, but also as a method to investigate the efficacy of DBS.

Chapter

Chapter A | **Appendix**

Introduction to the basics of functional modalities (electroencephalography) and structural modalities (magnetic resonance imaging, computed tomography).

A.1   Electroencephalography

An electroencephalogram (EEG) is a measurement of the continuous and changing voltage fields varying with different locations on the brain using electrodes [206]. High density EEG is the main electrophysiological recording technique that is used for the diagnosis of epilepsy. Extracranial EEG provides a broad survey of the electrocerebral activity measured on the scalp. While extracranial EEG has the benefit of being a non-invasive method, it does not provide a complete representation of the brain, since many deep-seated cortical gyri or subcortical regions are unable to be seen, and, secondly, because the volume conduction through the skull leads to significant signal diffusion and attenuation. Another kind of EEG measurement that circumvents these problems is intracranial EEG, which can measure activity from specific targeted areas of the brain. Intracranial EEG can be measured using electrodes on the surface of the cortex, called the electro-corticogram (ECoG), or by using electrodes that are implanted deep in the brain, called stereotactic depth electrodes or stereo-EEG (SEEG) recordings.

Origins of the EEG

Measurements of scalp EEG reflect the activity from a large number of parallelly oriented neurons activated synchronously. It is not the action potential that contributes to the EEG, but the postsynaptic potentials, the so-called local field potentials, which are the result of an influx of positively charged ions, or an active current source, in the *soma* and an outflux of negatively charged ions, or a passive current sink, in the *apical dendrite*, or vice versa [142]. As a result of this extracellular current flow, each neuron can be seen as a current dipole. Many of such tiny dipoles combined in a cortical sheet of synchronously activated neurons result in an equivalent current dipole, which can be measured by scalp EEG. The summation of the current dipoles of a sheet of synchronously activated neurons is measured as a potential field of a dipolar current distribution, underlying the EEG.

Modeling of current sources

To localize current sources in the brain using EEG, a model is required of the *forward problem*, which is the problem of finding the surface potentials, or the external magnetic field, from current sources in the volume [186]. The relation between a current density source and the electric potential field is governed by the Poisson equation, according to

$$\nabla \cdot \sigma \nabla V = \nabla \cdot \mathbf{J}_i \tag{A.1}$$

where $\mathbf{J}_i$ is the current density, σ is the conductivity of the volume, and V is the electric potential. The magnetic field that is produced by the equivalent current dipole or a sheet of neurons can be estimated from the volume and source currents using the Biot–Savart law

$$B = \frac{\mu_0}{4\pi} \int \frac{\mathbf{J} \times \hat{\mathbf{r}}}{r^2} dv \tag{A.2}$$

where $\mathbf{J}$ is the source current density, r is the distance from the volume element dv to the magnetic field point, and $\hat{\mathbf{r}}$ is a unit vector pointing from the volume element dv to the magnetic field point. Note that the magnetic field is perpendicular to the electrical field, as is clear from the use of the cross product $\mathbf{J} \times \hat{\mathbf{r}}$ between the source current density and the unit vector that is perpendicular to the cortical surface. Instead of the forward problem of describing the surface potentials given the current sources, the *inverse* problem is the estimation of current sources inside the volume that match the EEG measurements on the surface. For additional details regarding source localization, the reader is referred to the review on solving the forward problem by Hallez et al. [81] and the review on solving the inverse problem by Grech. et al [78].

With SEEG it is possible to directly measure the localized activity (local field potentials) of brain regions supposed to be responsible for epileptic seizures. A bipolar montage, i.e. the potential differences between two neighboring contacts of a depth electrode, can be used to eliminate all propagated activities generated in distant regions [32]. SEEG provides a high spatial resolution analysis in the axis of the electrodes, but may miss important information in the unexplored brain volume. The feasibility of spatiotemporal modeling of SEEG data is presented in Chapter 3, which is based on independent component analysis and does not rely on the estimation of distance to current sources.

A.2 Magnetic Resonance Imaging

Magnetic resonance imaging (MRI) serves as the primary diagnostic modality for neurology and has been used clinically for more than 30 years. MRI is a safe modality because it doesn't require the use of ionizing radiation. Felix Bloch pioneered the field of nuclear magnetic resonance (NMR) in 1946 by realizing that the atomic nucleus behaves like a magnet: magnetic fields can be produced as protons spin around their own axis. In 1973 it was first demonstrated by Paul Lauterbur that pictures could be made by acquiring location-dependent NMR signals, nowadays referred to as MRI, and in 1977 the first whole-body scanner was developed by Raymond Damadian for medical diagnosis.

Basics of MRI

MRI measures the signal of protons of water molecules in the body as the nucleus of interest because of its abundance in the human body and the inherently low sensitivity of NMR [138]. An object that is devoid of water will have zero intensity. When there is a small amount of water, for example in skin, it looks faint. The brain is composed of roughly 75% water [132] and thus looks more intense. A magnetic field is applied in the direction along the magnet bore, called the B_0 field. The Larmor frequency ω is the rate of precession of magnetic moments of the proton around the external magnetic field B_0

$$\omega_0 = \gamma \|\mathbf{B_0}\|, \tag{A.3}$$

where γ is the gyromagnetic ratio (for a proton $\gamma = 2.675 * 10^8$ rad/(s·T)). In MRI the B_0 field should be kept as homogeneously as possible in order to apply the same frequency to all protons.

The measured signal from all resonating protons in a homogeneous B_0 field is as follows

$$S(t) = \int \rho(\mathbf{r}) s(\mathbf{r}, t) e^{-i\omega_0 t} d\mathbf{r}, \tag{A.4}$$

where $\rho(\mathbf{r})$ is the proton density, assumed to be static, and $\mathbf{r} \in \mathbb{R}^3$ denotes the location and $t \in \mathbb{R}^+$ denotes time. Here, $s(\mathbf{r}, t)$ is a general term for the component of the signal that is measured during the scan by the receiver coil in the transverse plane (i.e. in the x and y directions). The signal is generally characterized by the applied MRI sequence and the effects due to relaxation. The $e^{-i\omega_0 t}$ term describes the oscillating signal at the Larmor frequency due to precession of the atoms induced by the magnetic field. Note that in this case $\omega_0(\mathbf{r}) = \omega_0$ because of the constant magnetic field that is applied, i.e. $\mathbf{B}(\mathbf{r}) = \mathbf{B_0}$.

Using the rotating frame of reference, the following signal remains after demodulation of the oscillation at the Larmor frequency

$$S(t) = \int \rho(\mathbf{r}) s(\mathbf{r}, t) d\mathbf{r}. \tag{A.5}$$

In addition to the $\mathbf{B_0}$ field, magnetic field gradients can be applied so that $\mathbf{B}(\mathbf{r}) = \mathbf{B_0} + \mathbf{B_1}(\mathbf{r}, t)$. Typically the magnitude of these gradients is much smaller than the $\mathbf{B_0}$ field, i.e. $|\mathbf{B_1}| \ll |\mathbf{B_0}|$. A field gradient can be applied along any arbitrary orientation. Generally, a field gradient in the z direction is used for slice selection, while the x and y directions are used to make spins position-dependent within the transversal plane, which is crucial for imaging [225].

Once a field gradient is applied, protons will resonate at different frequencies depending on their position. A field gradient $\mathbf{G}(t)$ applied in an arbitrary direction leads to the following relation between frequency, field strength and position

$$\omega = \gamma|\mathbf{B_0}| + \gamma|\mathbf{B_1}(\mathbf{r}, t)| = \gamma|\mathbf{B_0}| + \gamma\mathbf{G}(t) \cdot \mathbf{r}, \tag{A.6}$$

where $\mathbf{G}(t) \cdot \mathbf{r} = xG_x(t) + yG_y(t) + zG_z(t)$. From Eq. (A.6) it becomes clear that the precession frequency increases with distance $\mathbf{r}$ along the gradient direction, which over time results in a systematic variation of phase among the spins. The accumulation of

phase over time is described by $\mathbf{k}(t)$ as follows

$$\mathbf{k}(t) = \gamma \int_0^t \mathbf{G}(t')dt', \qquad (A.7)$$

where the time origin is at the excitation radio-frequency (RF) pulse of the MRI sequence. Including the effects of the applied gradients, the measured signal is now

$$S(\mathbf{k}(t)) = \int \rho(\mathbf{r})s(\mathbf{r},t)e^{-i\mathbf{k}(t)\cdot\mathbf{r}}d\mathbf{r}. \qquad (A.8)$$

At the end of the measurement, the space spanned by $\mathbf{k}$, referred to as k-space, represents the Fourier domain, or frequency domain, of the image in the spatial domain spanned by $\mathbf{r}$. The k-space can be filled, as time evolves, through the manipulation of gradient fields, in combination with a suitable MRI sequence such as spin echo, gradient echo or echo-planar imaging [225].

Applying an inverse Fourier transform will give ρ, the variable of interest, multiplied by $\beta(\mathbf{r})$ as a weighting factor for contrast, which forms the image I as follows

$$I(\mathbf{r}) = \mathscr{F}^{-1}\{S\}(\mathbf{r}) = \rho(\mathbf{r})\beta(\mathbf{r}). \qquad (A.9)$$

Image contrast can be achieved by designing the MRI sequence to weight the image by e.g. proton density ρ, T_1 and/or T_2 relaxation times. The proton density reflects the water concentration in a tissue. Furthermore, T_1 and T_2 are signal relaxation (decay) times after excitation, which are related to environmental factors, such as viscosity and the type of biological tissue. In Fig. A-1 an example is shown of a medical image acquired with MRI that is weighted by T1 relaxation time.

For more technical details about MRI the reader is referred to books by Vlaardingerbroek [225], Bernstein [23] and Brown [29].
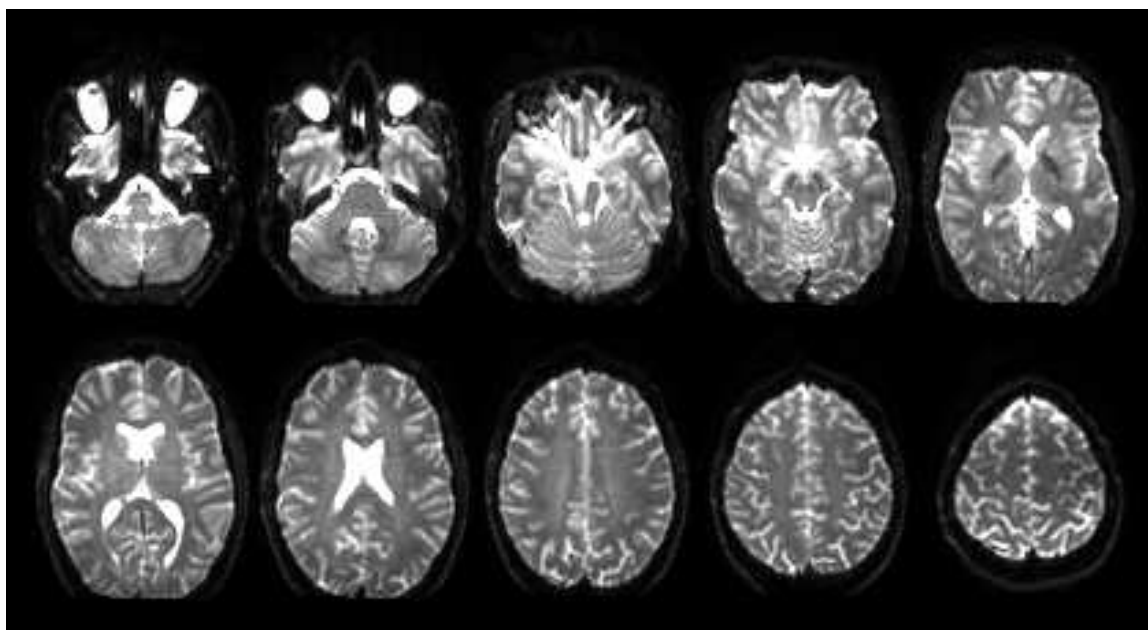
Figure A-1: Images produced using the EPI sequence in a 3.0 T Philips Achieva MR scanner at Kempenhaeghe, Heeze.

Computed tomography

Computed tomography (CT) is an imaging modality that, unlike a conventional x-ray image, uses a rotating arm to capture multiple x-ray signals that, when processed by a computer, results in a cross-sectional image. Most patients who are candidate for epilepsy surgery require a CT scan for the accurate imaging of the skull in order to facilitate the planning of a surgical resection of depth electrode implantation. Tissues are characterized by the attenuation, or dampening, of an x-ray: the denser the tissue, less intense the x-ray beam becomes. The cross-sectional images are produced by a process called *filtered back-projection* in which the attenuation or absorption coefficient $\mu(x, y)$ is estimated for every position $x, y \in \mathbb{R}^2$. The signals acquired by CT in a single rotation is called a sinogram and contains the integrated attenuation of an x-ray for every rotation θ and radial position r. In Fig. A-2 the sinogram of a phantom object is shown.
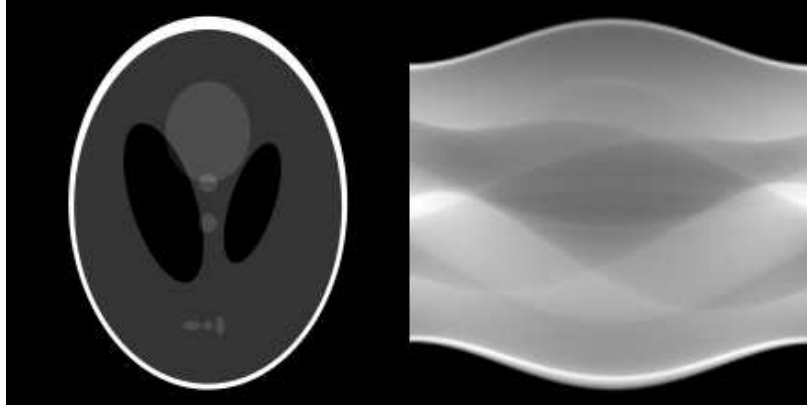
Figure A-2: Cross-sectional image of the Shepp-Logan phantom (left) and the corresponding sinogram (right).

A sinogram is in fact a Radon transformed version of the absorption coefficient:

$$\mathcal{R}\mu(r,\theta) = \int_{-\infty}^{\infty} \mu(r\cos\theta - s\sin\theta, r\sin\theta + s\cos\theta)ds, \qquad (A.10)$$

where $\mathcal{R}$ denotes the Radon transform. To reconstruct the image $\mu(x,y)$, it is required to do an inverse Radon transform, which is called a back-projection transform denoted by $\mathcal{B}$. While an image can be generated through the back-projection, the result is typically blurry and unusable for clinical diagnostics. Therefore, a filtering step is done by applying a Fourier transform $\mathcal{F}$ to the sinogram $\mathcal{R}\mu(r,\theta)$ and subsequently multiplying by the frequency $|\omega|$, which boosts the high frequencies to create a sharper image. Finally, an inverse Fourier transform and back-projection are used to recover the image. These steps are summarized in the following equation

$$\mu(x,y) = \frac{1}{2}\mathcal{B}\Big\{\mathcal{F}^{-1}\big[|\omega|\mathcal{F}(\mathcal{R}\mu)(\omega,\theta)\big]\Big\}(x,y). \qquad (A.11)$$

For more details on the mathematical and physical aspects of CT, the reader is referred to [88].

Chapter B | **Appendix**

Mathematical background information is provided of the embedding of the space of coupled positions and orientations $\mathbb{R}^3 \rtimes S^2$ in the Lie group SE(3).

B.1   Embedding of $\mathbb{R}^3 \rtimes S^2$ in the Lie group SE(3)

The Lie group of rigid body motions SE(3) $= \mathbb{R}^3 \rtimes$ SO(3) is a semi-direct product of the translation group $\mathbb{R}^3$ and the 3D rotation group SO(3). It can be seen as the set of transformations that can be applied to a rigid body, plus the operations of composing and inverting them [80].

To properly regularize functions that are defined on $\mathbb{R}^3 \times S^2$, which is not a group structure, a coupling between positions and orientations is required. This can be obtained by embedding the space $\mathbb{R}^3 \times S^2$ in SE(3). The following procedure is described in Portegies et al. [168]. For an in-depth consideration of these materials the reader is referred to Duits et al. [54, 50] and Oksendal et al. [152].

The space of coupled positions and orientations is defined as a Lie group quotient in SE(3):

$$\mathbb{R}^3 \rtimes S^2 := \text{SE}(3)/(\{\mathbf{0}\} \times \text{SO}(2)). \tag{B.1}$$

For two group elements of SE(3) given by $g = (\mathbf{x}, \mathbf{R})$, $g' = (\mathbf{x}', \mathbf{R}')$, the group product is defined as $gg' = (\mathbf{x} + \mathbf{R}\mathbf{x}', \mathbf{R}\mathbf{R}')$. Because this group product influences the group action in $\mathbb{R}^3 \rtimes S^2$, the semi-product notation $\rtimes$ is used (even though this is usually reserved for the semi-direct product of groups). The group action $\odot$ of $g \in \text{SE}(3)$ onto $(\mathbf{y}, \mathbf{n}) \in \mathbb{R}^3 \times S^2$ is defined by

$$g \odot (\mathbf{y}, \mathbf{n}) = (\mathbf{x}, \mathbf{R}) \odot (\mathbf{y}, \mathbf{n}) := (\mathbf{x} + \mathbf{R}\mathbf{y}, \mathbf{R}\mathbf{n}). \tag{B.2}$$

Within the quotient structure $\mathbb{R}^3 \rtimes S^2$ two elements g, g' (as above) are equivalent if

$$g' \sim g \Leftrightarrow h := (g')^{-1}g \in \{\mathbf{0}\} \times \text{SO}(2) \Leftrightarrow \mathbf{x} = \mathbf{x}'$$

$$\text{and} \quad \exists\, \alpha \in (0, 2\pi] : (\mathbf{R}')^{-1}\mathbf{R} = \mathbf{R}_{\mathbf{e}_z, \alpha} \in \text{SO}(2), \tag{B.3}$$

where $\mathbf{e}_z = (0, 0, 1)^T$ is the reference axis. The notation $\mathbf{R}_{\mathbf{n}, \phi}$ is used for 3D rotations that perform a counter-clockwise rotation about axis $\mathbf{n} \in S^2$ with angle $\phi \in [0, 2\pi]$.

Using the group action, the equivalence relation in Eq. (B.3) amounts to:

$$g' \sim g \Leftrightarrow g' \odot (\mathbf{0}, \mathbf{e}_z) = g \odot (\mathbf{0}, \mathbf{e}_z). \tag{B.4}$$

Thereby, an arbitrary element in $\mathbb{R}^3 \rtimes S^2$ can be considered as an equivalence class of all rigid body motions that map reference position and orientaton $(\mathbf{0}, \mathbf{e}_z)$ onto $(\mathbf{x}, \mathbf{n})$ for arbitrary $\mathbf{x} \in \mathbb{R}^3$ and $\mathbf{n} \in S^2$. Similar to the common identification of $S^2 \equiv \mathrm{SO}(3)/\mathrm{SO}(2)$, we denote elements of the Lie group quotient $\mathbb{R}^3 \rtimes S^2$ by $(\mathbf{x}, \mathbf{n})$.

Functions $U : \mathbb{R}^3 \rtimes S^2 \to \mathbb{R}^+$ are identified with functions $\tilde{U} : \mathrm{SE}(3) \to \mathbb{R}^+$ by the relation

$$U(\mathbf{y}, \mathbf{n}) = \tilde{U}(\mathbf{y}, \mathbf{R_n}), \tag{B.5}$$

where $\mathbf{R_n}$ is *any* rotation matrix such that $\mathbf{R_n} \mathbf{e}_z = \mathbf{n}$ (not to be confused with the notation $\mathbf{R}_{\mathbf{n}, \phi}$). For functions $\tilde{U}$ this leads to the property of invariance $\tilde{U}(\mathbf{y}, \mathbf{R}) = \tilde{U}(\mathbf{y}, \mathbf{R} \mathbf{R}_{\mathbf{e}_z, \alpha})$ for all $\alpha \in (0, 2\pi]$.

Summary

Epilepsy is a chronic neurological disease that affects an estimated 50 million people in the world. Epilepsy is characterized by recurrent seizures that are caused by excessive or synchronous neuronal activity in the brain. If seizures persist despite antiepileptic drug treatment then epilepsy surgery may be a possible solution, which entails the removal of the area of the brain that causes seizures. However, adverse events associated with epilepsy surgery can be severe, e.g. loss of peripheral vision, memory, language and/or emotion. A major goal in epilepsy research is to achieve minimally invasive treatment of epilepsy by combining the clinical information from functional and structural modalities. Stereoelectroencephalography (SEEG), a functional modality, uses depth electrodes to measure the electrical activity in deep-sited anatomical structures of the brain. Magnetic resonance imaging (MRI), a structural modality, is used to study the presence of anatomical anomalies and can furthermore be used to study the white matter architecture of the brain through diffusion-weighted imaging (DWI).

With SEEG it has become possible to pinpoint the areas of the brain where seizures are originating. Epilepsy surgery guided by SEEG is not always successful, however, which is especially the case for patients with complex epilepsies that do not exhibit anatomical abnormalities in the MRI scan. Clinical assessment is mostly based on the recordings of seizure activity. However, SEEG recordings also reflect a vast number of spikes that occur in-between seizures called interictal epileptic discharges (IEDs), which are difficult to interpret due to complex underlying network interactions. In this thesis an analysis framework is developed to unravel the network interactions underlying the IEDs. The three main steps of the framework are: 1) Estimation of the synchronization between

SEEG signals by a non-linear correlation analysis and a robust estimation of time delays; 2) Identification of brain regions actively involved in the generation of the activity underlying the IEDs. This is achieved by relating the variation in correlation over time to the IED density function using the General Linear Model; and 3) Assessment of the interdependency of brain regions that reflect highly synchronized activity by applying Independent Component Analysis followed by a hierarchical clustering of spike clusters. It was concluded that a network approach is imperative in case of patients with complex epilepsies and is considered a valuable addition to the routine review of SEEG recordings, with the potential to increase the success rate of epilepsy surgery.

DWI is increasingly becoming an indispensable tool in the fields of neuroimaging, neurosurgery and neuroscience. In this thesis, a framework is developed for the robust reconstruction of the optic radiation (OR) in support of resective surgery to treat temporal lobe epilepsy. The OR is a white matter structure that facilitates vision, which can be reconstructed using diffusion-weighted tractography by generating streamlines between the thalamus and the visual cortex. In clinical interest is the measurement of the distance between the temporal pole and the tip of the OR. However, results of tractography often reflect spurious (aberrant) streamlines, which hinders an accurate measurement of such a distance measurement. Fiber to bundle (FBC) tractometry measures are introduced to quantitatively measure the alignment of streamlines and to identify and remove spurious streamlines. The developed FBC methodology is made freely accessible to the neuroimaging community as an open-source module in the Diffusion Imaging in Python (DIPY) framework and can be readily included in existing processing pipelines. Related to this work, an efficient implementation has been created as part of DIPY of a crossing-preserving denoising algorithm based on contextual partial differential equations to increase the signal-to-noise ratio of DWI-derived data, which has the potential to further improve the results of tractography. Lastly, a quantitative measure of connectivity was investigated, for which an algorithm was developed based on finding the shortest path using anisotropic fast marching (FM) in the space of positions and orientations. The developed methodology was evaluated on artificial datasets demonstrate that the model with

forward-constrained motion, especially, leads to shortest pathways that may be good candidates for blood vessels or neural fibers in the brain. The new method for anisotropic FM was, furthermore, applied on human brain data to evaluate the estimation of structural connectivity in support of deep brain stimulation.

Overall, the functional and structural methods introduced in this thesis are applicable to improve the minimally invasive treatment of epilepsy, either by identifying focal regions using SEEG (Chapter 2 and Chapter 3), by minimizing functional deficits with an accurate reconstruction of the optic radiation (Chapter 4 and Chapter 5) or by having a method to compute the structural connectivity of relevant subnetworks (Chapter 6 and Chapter 7). A better understanding of the propagation pathways can lead to improved success in epilepsy surgery, and possibly to new methods for treatment, for example by stimulating functionally-relevant white matter bundles using DBS [105]. The FM method can, furthermore, be generically applicable for finding shortest paths in medical imaging data. e.g. as effective application to find the blood vessels of the brain, which is crucial for depth electrode planning.

Acknowledgements

Curriculum Vitae

Stephan Meesters was born on the 8th of January 1990 in Vlijmen, The Netherlands. After finishing his VWO degree in 2008 at the Sint-Jans Lyceum in 's-Hertogenbosch, he studied Biomedical Engineering at the Eindhoven University of Technology. In 2013 he graduated within the group of Biomedical Image Analysis on the reconstruction of the optic radiation with diffusion-weighted tractography. From December 2013 he started a PhD project at the Centre for Analysis, Scientific Computing and Applications (CASA) of which the results are presented in this dissertation.

Bibliography

[1] A. Agrachev and Y. Sachkov (2004). *Control Theory from the Geometric Viewpoint*, volume 87 of *Encyclopaedia of Mathematical Sciences*. Springer Berlin Heidelberg, Berlin, Heidelberg. ISBN 978-3-642-05907-0 978-3-662-06404-7.

[2] G. Alarcon, C. N. Guy, C. D. Binnie, S. R. Walker, R. D. Elwes, and C. E. Polkey, Intracerebral propagation of interictal activity in partial epilepsy: implications for source localisation. *Journal of Neurology, Neurosurgery, and Psychiatry*, 57(4), (1994) pages 435–449.

[3] L. Amini, C. Jutten, S. Achard, O. David, H. Soltanian-Zadeh, G. A. Hossein-Zadeh, P. Kahane, L. Minotti, and L. Vercueil, Directed differential connectivity graph of interictal epileptiform discharges. *IEEE Transactions on Biomedical Engineering*, 58(4), (2011) pages 884–893.

[4] L. Astola, A. Jalba, E. Balmashnova, and L. Florack, Finsler streamline tracking with single tensor orientation distribution function for high angular resolution diffusion imaging. *Journal of Mathematical Imaging and Vision*, 41(3), (2011) pages 170–181.

[5] M. Avoli, Do interictal discharges promote or control seizures? experimental evidence from an in vitro model of epileptiform discharge. *Epilepsia*, 42 Suppl 3, (2001) pages 2–4.

[6] M. Avoli, G. Biagini, and M. de Curtis, Do interictal spikes sustain seizures and epileptogenesis? *Epilepsy Currents*, 6(6), (2006) pages 203–207.

[7] N. Balak, E. Balkuv, A. Karadag, R. Basaran, H. Biceroglu, B. Erkan, and N. Tanriover, Mammillothalamic and mammillotegmental tracts as new targets for dementia and epilepsy treatment. *World Neurosurgery*, 110, (2017) pages 133–144.

[8] D. Bao, S.-S. Chern, and Z. Shen (2000). *An Introduction to Riemann-Finsler Geometry*. Graduate Texts in Mathematics. Springer New York, 1st edition. ISBN 978-1-4612-1268-3.

[9] F. Bartolomei, M. Gavaret, R. Hewett, L. Valton, S. Aubert, J. Regis, F. Wendling, and P. Chauvel, Neural networks underlying parietal lobe seizures: a quantified study from intracerebral recordings. *Epilepsy Research*, 93(2-3), (2011) pages 164–176.

[10] F. Bartolomei, S. Lagarde, F. Wendling, A. McGonigal, V. Jirsa, M. Guye, and C. Benar, Defining epileptogenic networks: Contribution of SEEG and signal analysis. *Epilepsia*, 58(7), (2017) pages 1131–1147.

[11] F. Bartolomei, A. Trebuchon, F. Bonini, I. Lambert, M. Gavaret, M. Woodman, B. Giusiano, F. Wendling, and C. Benar, What is the concordance between the seizure onset zone and the irritative zone? a SEEG quantified study. *Clinical Neurophysiology*, 127(2), (2016) pages 1157–1162.

[12] F. Bartolomei, F. Wendling, J. J. Bellanger, J. Régis, and P. Chauvel, Neural networks involving the medial temporal structures in temporal lobe epilepsy. *Clinical Neurophysiology*, 112(9), (2001) pages 1746–60.

[13] F. Bartolomei, F. Wendling, and P. Chauvel, The concept of an epileptogenic network in human partial epilepsies. *Neurochirurgie*, 54(3), (2008) pages 174–184.

[14] P. J. Basser, Inferring microstructural features and the physiological state of tissues from diffusion-weighted images. *NMR in Biomedicine*, 8(7-8), (1995) pages 333–344.

[15] P. J. Basser, J. Mattiello, and D. LeBihan, Estimation of the effective self-diffusion tensor from the NMR spin echo. *Journal of Magnetic Resonance, Series B*, 103(3), (1994) pages 247–254.

[16] P. J. Basser, S. Pajevic, C. Pierpaoli, J. Duda, and a. Aldroubi, In vivo fiber tractography using DT-MRI data. *Magnetic Resonance in Medicine*, 44(4), (2000) pages 625–32.

[17] T. E. J. Behrens, H. J. Berg, S. Jbabdi, M. F. S. Rushworth, and M. W. Woolrich, Probabilistic diffusion tractography with multiple fibre orientations: What can we gain? *NeuroImage*, 34(1), (2007) pages 144–155.

[18] T. E. J. Behrens, H. Johansen-Berg, M. W. Woolrich, S. M. Smith, C. A. M. Wheeler-Kingshott, P. A. Boulby, G. J. Barker, E. L. Sillery, K. Sheehan, O. Ciccarelli, A. J. Thompson, J. M. Brady, and P. M. Matthews, Non-invasive mapping of connections between human thalamus and cortex using diffusion imaging. *Nature Neuroscience*, 6(7), (2003) pages 750–757.

[19] E. Bekkers, R. Duits, A. Mashtakov, and G. Sanguinetti, A PDE approach to data-driven sub-Riemannian geodesics in SE(2). *SIAM Journal on Imaging Sciences*, 8(4), (2015) pages 2740–2770.

[20] C. F. Benjamin, J. M. Singh, S. P. Prabhu, and S. K. Warfield, Optimization of tractography of the optic radiations. *Human Brain Mapping*, 35(2), (2014) pages 683–697.

[21] J. L. Bentley, Multidimensional binary search trees used for associative searching. *Communications of the ACM*, 18(9), (1975) pages 509–517.

[22] B. C. Bernhardt, Z. Chen, Y. He, A. C. Evans, and N. Bernasconi, Graph-theoretical analysis reveals disrupted small-world organization of cortical thickness correlation networks in temporal lobe epilepsy. *Cerebral Cortex*, 21(9), (2011) pages 2147–2157.

[23] M. Bernstein, K. King, and X. Zhou (2004). *Handbook of MRI pulse sequences*. Elsevier, 1st edition. ISBN 0120928612.

[24] G. Bettus, F. Wendling, M. Guye, L. Valton, J. Régis, P. Chauvel, and F. Bartolomei, Enhanced EEG functional connectivity in mesial temporal lobe epilepsy. *Epilepsy Research*, 81(1), (2008) pages 58–68.

[25] P.-Y. Borius, F.-E. Roux, L. Valton, J.-C. Sol, J.-A. Lotterie, and I. Berry, Can DTI fiber tracking of the optic radiations predict visual deficit after surgery? *Clinical Neurology and Neurosurgery*, 122, (2014) pages 87–91.

[26] U. Boscain, G. Charlot, and F. Rossi, Existence of planar curves minimizing length and curvature. *Proceedings of the Steklov Institute of Mathematics*, 270(1), (2010) pages 43–56.

[27] U. Boscain, R. Duits, F. Rossi, and Y. Sachkov, Curve cuspless reconstruction via sub-Riemannian geometry. *ESAIM: Control, Optimisation and Calculus of Variations*, 20(3), (2014) pages 748–770.

[28] J. Bourien, F. Bartolomei, J. J. Bellanger, M. Gavaret, P. Chauvel, and F. Wendling, A method to identify reproducible subsets of co-activated structures during interictal spikes. Application to intracerebral EEG in temporal lobe epilepsy. *Clinical Neurophysiology*, 116(2), (2005) pages 443–455.

[29] R. W. Brown, Y.-C. N. Cheng, E. M. Haacke, M. R. Thompson, and R. Venkatesan (2014). *Magnetic resonance imaging: physical principles and sequence design.* John Wiley & Sons Ltd, 2nd edition. ISBN 9780471720850.

[30] E. Brunenberg, A Sobolev norm based distance measure for HARDI clustering. *Medical Image Computing and Computer-Assisted Intervention*, 13 (Pt. 1), (2010) pages 175–182.

[31] E. Bullmore and O. Sporns, Complex brain networks: graph theoretical analysis of structural and functional systems. *Nature Reviews Neuroscience*, 10(3), (2009) pages 186–98.

[32] V. Caune, R. Ranta, S. Le Cam, J. Hofmanis, L. Maillard, L. Koessler, and V. Louis-Dorr, Evaluating dipolar source localization feasibility from intracerebral SEEG recordings. *Neuroimage*, 98, (2014) pages 118–33.

[33] M. Chamberland, B. Scherrer, S. P. Prabhu, J. Madsen, D. Fortin, K. Whittingstall, M. Descoteaux, and S. K. Warfield, Active delineation of Meyer's loop using oriented priors through MAGNEtic tractography (MAGNET). *Human Brain Mapping*, 38(1), (2017) pages 509–527.

[34] D. Chen (2016). *New Minimal Path Model for Tubular Extraction and Image Segmentation.* Ph.D. thesis, CEREMADE - CEntre de REcherches en MAthématiques de la DEcision.

[35] X. Chen, D. Weigel, O. Ganslandt, M. Buchfelder, and C. Nimsky, Prediction of visual field deficits by diffusion tensor imaging in temporal lobe epilepsy surgery. *NeuroImage*, 45(2), (2009) pages 286–297.

[36] G. Citti and A. Sarti, A cortical based model of perceptual completion in the roto-translation space. *Journal of Mathematical Imaging and Vision*, 24(3), (2006) pages 307–326.

[37] P. Comon, Independent component analysis, a new concept? *Signal Processing*, 36(3), (1994) pages 287–314. Higher Order Statistics.

[38] M. G. Crandall, H. Ishii, and P.-L. Lions, User's guide to viscosity solutions of second order partial differential equations. *Bull. Amer. Math. Soc.*, 27(1), (1992) pages 1–67.

[39] M. G. Crandall and P.-L. Lions, Viscosity solutions of Hamilton-Jacobi equations. *Transactions of the American Mathematical Society*, 277(1), (1983) pages 1–42.

[40] E. Creusen, R. Duits, A. Vilanova, and L. Florack, Numerical schemes for linear and non-linear enhancement of DW-MRI. *Numerical Mathematics: Theory, Methods and Applications*, 6(1), (2013) pages 138–168.

[41] F. L. da Silva, Interdependence of EEG signals: Linear vs nonlinear associations and the significance of time delays and phase shifts. *Brain Topography*, 2(1/2), (1989) pages 9–18.

[42] A. M. da Silva Braga, E. K. Fujisao, and L. E. Betting, Analysis of generalized interictal discharges using quantitative EEG. *Epilepsy Research*, 108(10), (2014) pages 1740–1747.

[43] A. Daducci, E. J. Canales-Rodriguez, M. Descoteaux, E. Garyfallidis, Y. Gur, Y.-C. Lin, M. Mani, S. Merlet, M. Paquette, A. Ramirez-Manzanares, M. Reisert, P. Reis Rodrigues, F. Sepehrband, E. Caruyer, J. Choupan, R. Deriche, M. Jacob, G. Menegaz, V. Prckovska, M. Rivera, Y. Wiaux, and J.-P. Thiran, Quantitative comparison of reconstruction methods for intra-voxel fiber recovery from diffusion MRI. *IEEE Transactions on Medical Imaging*, 33(2), (2014) pages 384–399.

[44] M. Dayan, M. Munoz, S. Jentschke, M. J. Chadwick, J. M. Cooper, K. Riney, F. Vargha-Khadem, and C. A. Clark, Optic radiation structure and anatomy in the normally developing brain determined using diffusion MRI and tractography. *Brain Structure and Function*, 220(1), (2015) pages 291–306.

[45] M. de Curtis and G. Avanzini, Interictal spikes in focal epileptogenesis. *Progress in Neurobiology*, 63(5), (2001) pages 541–567.

[46] M. de Curtis, J. G. R. Jefferys, and M. Avoli. (2012). Interictal epileptiform discharges in partial epilepsy: Complex neurobiological mechanisms based on experimental and clinical evidence. In *Jasper's Basic Mechanisms of the Epilepsies*. NCBI, 4th edition. ISBN 978-0199746545.

[47] A. Delorme and S. Makeig, EEGLAB: an open source toolbox for analysis of single-trial EEG dynamics including independent component analysis. *Journal of Neuroscience Methods*, 134(1), (2004) pages 9–21.

[48] M. Descoteaux, R. Deriche, T. R. Knosche, and A. Anwander, Deterministic and probabilistic tractography based on complex fibre orientation distributions. *IEEE Transactions on Medical Imaging*, 28(2), (2009) pages 269–286.

[49] E. W. Dijkstra, A note on two problems in connexion with graphs. *Numerische Mathematik*, 1(1), (1959) pages 269–271.

[50] R. Duits, U. Boscain, F. Rossi, and Y. Sachkov, Association fields via cuspless sub-Riemannian geodesics in SE(2). *J Math Imaging Vis*, 49(2), (2014) pages 384–417.

[51] R. Duits, T. Dela Haije, and E. Creusen, Morphological and linear scale spaces for fiber enhancement in DW-MRI. *Journal of Mathematical Imaging and Vision*, 46(3), (2013) pages 326–368.

[52] R. Duits, T. C. J. Dela Haije, A. Ghosh, E. Creusen, A. Vilanova, and B. ter Haar Romeny (2012). *Fiber enhancement in diffusion-weighted MRI*, pages 1–13. Springer, Berlin, Heidelberg. ISBN 978-3-642-24785-9.

[53] R. Duits, M. Felsberg, G. Granlund, and B. Romeny, Image analysis and reconstruction using a wavelet transform constructed from a reducible representation of the Euclidean motion group. *International Journal of Computer Vision*, 72(1), (2007) pages 79–102.

[54] R. Duits and E. Franken, Left-invariant diffusions on the space of positions and orientations and their application to crossing-preserving smoothing of HARDI images. *International Journal of Computer Vision*, 92(3), (2011) pages 231–264.

[55] R. Duits, A. Ghosh, T. Dela Haije, and Y. Sachkov (2014). Cuspless sub-Riemannian geodesics within the Euclidean motion group SE(d). In *Neuromathematics of Vision*, Lecture Notes in Morphogenesis, pages 173–215. ISBN 978-3-642-34443-5 978-3-642-34444-2. DOI: 10.1007/978-3-642-34444-2_5.

[56] R. Duits, A. Ghosh, T. C. J. D. Haije, and A. Mashtakov, On sub-Riemannian geodesics in SE(3) whose spatial projections do not have cusps. *Journal of Dynamical and Control Systems*, 22(4), (2016) pages 771–805.

[57] R. Duits, M. H. J. Janssen, J. Hannink, and G. R. Sanguinetti, Locally adaptive frames in the roto-translation group and their applications in medical imaging. *Journal of Mathematical Imaging and Vision*, pages 1–36.

[58] R. Duits, S. Meesters, J.-M. Mireabeau, and J. Portegies (2017). Optimal paths for variants of the 2D and 3D Reeds-Shepp car with applications in image analysis.

[59] M. Dyrholm, S. Makeig, and L. K. Hansen, Model selection for convolutive ICA with an application to spatiotemporal analysis of EEG. *Neural Computation*, 19(4), (2007) pages 934–955.

[60] U. Ebeling, H. Reulen, and N. Universitfitsklinik, Neurosurgical topography of the optic radiation in the temporal lobe. *Acta Neurochirurgica*, 92(1–4), (1988) pages 29–36.

[61] A. Einstein, On the movement of small particles suspended in a stationary liquid demanded by the molecular-kinetic theory of heat. *Annalen der Physik*, 322(8), (1905) pages 549–560.

[62] D. B. Ennis, G. Kindlman, I. Rodriguez, P. A. Helm, and E. R. McVeigh, Visualization of tensor fields using superquadric glyphs. *Magnetic Resonance in Medicine*, 53(1), (2005) pages 169–176.

[63] Q. Fan, T. Witzel, A. Nummenmaa, K. R. A. Van Dijk, J. D. Van Horn, M. K. Drews, L. H. Somerville, M. A. Sheridan, R. M. Santillana, J. Snyder, T. Hedden, E. E. Shaw, M. O. Hollinshead, V. Renvall, R. Zanzonico, B. Keil, S. Cauley, J. R. Polimeni, D. Tisdall, R. L. Buckner, V. J. Wedeen, L. L. Wald, A. W. Toga, and B. R. Rosen, MGH–USC human connectome project datasets with ultra-high b-value diffusion MRI. *NeuroImage*, 124, (2016) pages 1108–1114.

[64] P. Fillard, M. Descoteaux, A. Goh, S. Gouttard, B. Jeurissen, J. Malcolm, A. Ramirez-Manzanares, M. Reisert, K. Sakaie, F. Tensaouti, T. Yo, J.-F. Mangin, and C. Poupon, Quantitative evaluation of 10 tractography algorithms on a realistic diffusion MR phantom. *Neuroimage*, 56(1), (2011) pages 220–234.

[65] R. Fisher, V. Salanova, T. Witt, R. Worth, T. Henry, R. Gross, K. Oommen, I. Osorio, J. Nazzaro, D. Labar, M. Kaplitt, M. Sperling, E. Sandok, J. Neal, A. Handforth, J. Stern, A. DeSalles, S. Chung, A. Shetter, D. Bergen, R. Bakay, J. Henderson, J. French, G. Baltuch, W. Rosenfeld, A. Youkilis, W. Marks, P. Garcia, N. Barbaro, N. Fountain, C. Bazil, R. Goodman, G. McKhann, K. Babu Krishnamurthy, S. Papavassiliou, C. Epstein, J. Pollard, L. Tonder, J. Grebin, R. Coffey, and N. Graves, Electrical stimulation of the anterior nucleus of thalamus for treatment of refractory epilepsy. *Epilepsia*, 51(5), (2010) pages 899–908.

[66] R. S. Fisher, C. Acevedo, A. Arzimanoglou, A. Bogacz, J. H. Cross, C. E. Elger, J. J. Engel, L. Forsgren, J. A. French, M. Glynn, D. C. Hesdorffer, B. I. Lee, G. W. Mathern, S. L. Moshe, E. Perucca, I. E. Scheffer, T. Tomson, M. Watanabe, and S. Wiebe, ILAE official report: a practical clinical definition of epilepsy. *Epilepsia*, 55(4), (2014) pages 475–482.

[67] R. S. Fisher, H. E. Scharfman, and M. deCurtis, How can we identify ictal and interictal abnormal activity? *Advances in Experimental Medicine and Biology*, 813, (2014) pages 3–23.

[68] O. Friman, G. Farnebäck, and C.-F. Westin (2006). A Bayesian approach for stochastic white matter tractography. In *IEEE Transactions on Medical Imaging*, volume 25, pages 965–978.

[69] N. Fujita, H. Tanaka, M. Takanashi, N. Hirabuki, K. Abe, H. Yoshimura, and H. Nakamura, Lateral geniculate nucleus: anatomic and functional identification by use of MR imaging. *American Journal of Neuroradiology*, 22(9), (2001) pages 1719–1726.

[70] A. Fuster (2014). A novel Riemannian metric for geodesic tractography in DTI. In *Computational Diffusion MRI and Brain Connectivity*, pages 97–104. Springer. ISBN 978-3-319-02475-2.

[71] A. Fuster, T. Dela Haije, A. Tristán-Vega, B. Plantinga, C.-F. Westin, and L. Florack, Adjugate diffusion tensors for geodesic tractography in white matter. *Journal of Mathematical Imaging and Vision*, 54(1), (2016) pages 1–14.

[72] A. Fuster and L. Florack (2014). Riemann-Finsler geometry for diffusion weighted magnetic resonance imaging. In *Visualization and Processing of Tensors and Higher Order Descriptors for Multi-Valued Data*, pages 189–208. Springer. ISBN ISBN 978-3-642-54300-5.

[73] E. Garyfallidis, M. Brett, B. Amirbekian, A. Rokem, S. van der Walt, M. Descoteaux, I. Nimmo-Smith, and Dipy Contributors, Dipy, a library for the analysis of diffusion MRI data. *Frontiers in Neuroinformatics*, 8, (2014) page 8.

[74] G. Girard, K. Whittingstall, R. Deriche, and M. Descoteaux, Towards quantitative connectivity analysis: reducing tractography biases. *NeuroImage*, 98(Supplement C), (2014) pages 266 – 278.

[75] J. Gonzalez-Martinez, J. Bulacio, S. Thompson, J. Gale, S. Smithason, I. Najm, and W. Bingaman, Technique, results, and complications related to robot-assisted stereoelectroencephalography. *Neurosurgery*, 78(2), (2016) pages 169–180.

[76] K. Gorgolewski, C. D. Burns, C. Madison, D. Clark, Y. O. Halchenko, M. L. Waskom, and S. S. Ghosh, Nipype: a flexible, lightweight and extensible neuroimaging data processing framework in Python. *Frontiers in Neuroinformatics*, 5.

[77] J. Gotman, Relationships between interictal spiking and seizures: human and experimental evidence. *Canadian Journal of Neurological Sciences*, 18(4 Suppl), (1991) pages 573–576.

[78] R. Grech, T. Cassar, J. Muscat, K. P. Camilleri, S. G. Fabri, M. Zervakis, P. Xanthopoulos, V. Sakkalis, and B. Vanrumste, Review on solving the inverse problem in EEG source analysis. *Journal of NeuroEngineering and Rehabilitation*, 5(1), (2008) page 25.

[79] M. A. Griswold, P. M. Jakob, R. M. Heidemann, M. Nittka, V. Jellus, J. Wang, B. Kiefer, and A. Haase, Generalized autocalibrating partially parallel acquisitions (GRAPPA). *Magnetic Resonance in Medicine*, 47(6), (2002) pages 1202–1210.

[80] B. Hall (2003). *Lie Groups, Lie Algebras, and Representations: An Elementary Introduction*. Graduate Texts in Mathematics. Springer. ISBN 9780387401225.

[81] H. Hallez, B. Vanrumste, R. Grech, J. Muscat, W. De Clercq, A. Vergult, Y. D'Asseler, K. P. Camilleri, S. G. Fabri, S. Van Huffel, and I. Lemahieu, Review on solving the forward problem in eeg source analysis. *Journal of NeuroEngineering and Rehabilitation*, 4(1), (2007) page 46.

[82] C. H. Halpern, U. Samadani, B. Litt, J. L. Jaggi, and G. H. Baltuch, Deep brain stimulation for epilepsy. *Neurotherapeutics*, 5(1), (2008) pages 59–67.

[83] P. Hastreiter, C. Rezk-Salama, G. Soza, M. Bauer, G. Greiner, R. Fahlbusch, O. Ganslandt, and C. Nimsky, Strategies for brain shift evaluation. *Medical Image Analysis*, 8(4), (2004) pages 447–464.

[84] D. M. Healy, H. Hendriks, and P. T. Kim, Spherical deconvolution. *Journal of Multivariate Analysis*, 67(1), (1998) pages 1–22.

[85] P. A. d. F. R. Højen-Sørensen, O. Winther, and L. K. Hansen, Mean-field approaches to independent component analysis. *Neural Computation*, 14(4), (2002) pages 889–918.

[86] D. Holland, J. M. Kuperman, and A. M. Dale, Efficient correction of inhomogeneous static magnetic field-induced distortion in Echo Planar Imaging. *NeuroImage*, 50(1), (2010) pages 175–83.

[87] M. D. Holmes and D. M. Tucker, Identifying the epileptic network. *Frontiers in Neurology*, 4, (2013) page 84.

[88] J. Hsieh (2009). *Computed Tomography Principles, Design, Artifacts, and Recent Advances.* Wiley, 2nd edition. ISBN 978-0-470-56353-3.

[89] A. Hyvarinen and E. Oja, Independent component analysis: algorithms and applications. *Neural Networks*, 13(4-5), (2000) pages 411–430.

[90] J. S. James, A. Radhakrishnan, B. Thomas, M. Madhusoodanan, C. Kesavadas, M. Abraham, R. Menon, C. Rathore, and G. Vilanilam, Diffusion tensor imaging tractography of Meyer's loop in planning resective surgery for drug-resistant temporal lobe epilepsy. *Epilepsy Research*, 110, (2015) pages 95–104.

[91] M. Jenkinson, C. Beckmann, T. Behrens, M. Woolrich, and S. Smith, FSL. *NeuroImage*, 62(2), (2012) pages 782–790.

[92] B. Jeurissen, A. Leemans, D. K. Jones, J.-D. Tournier, and J. Sijbers, Probabilistic fiber tracking using the residual bootstrap with constrained spherical deconvolution. *Human Brain Mapping*, 32(3), (2011) pages 461–479.

[93] P. Jezzard and R. Balaban, Correction for geometric distortion in echo planar images from B0 field variations. *Magnetic Resonance in Medicine*, 34(1), (1995) pages 65–73.

[94] D. Jones, Challenges and limitations of quantifying connectivity in the human brain in vivo with diffusion mri. *Imaging in Medicine*, 2, (2010) pages 341–355.

[95] D. K. Jones, M. A. Horsfield, and A. Simmons, Optimal strategies for measuring diffusion in anisotropic systems by magnetic resonance imaging. *Magnetic Resonance in Medicine*, 42(3), (1999) pages 515–525.

[96] D. K. Jones, T. R. Knösche, and R. Turner, White matter integrity, fiber count, and other fallacies: the do's and don'ts of diffusion MRI. *Neuroimage*, 73, (2013) pages 239–54.

[97] C. Jutten and J. Herault, Blind separation of sources, part I: An adaptive algorithm based on neuromimetic architecture. *Signal Processing*, 24(1), (1991) pages 1–10.

[98] P. Kahane and F. Bartolomei, Temporal lobe epilepsy and hippocampal sclerosis: lessons from depth EEG recordings. *Epilepsia*, 51 Suppl 1, (2010) pages 59–62.

[99] S. N. Kalitzin, J. Parra, D. N. Velis, and F. H. Lopes da Silva, Quantification of unidirectional nonlinear associations between multidimensional signals. *IEEE Transactions on Biomedical Engineering*, 54(3), (2007) pages 454–461.

[100] A. Kammen, M. Law, B. S. Tjan, A. W. Toga, and Y. Shi, Automated retinofugal visual pathway reconstruction with multi-shell HARDI and FOD-based analysis. *NeuroImage*, 125, (2016) pages 767–779.

[101] S. S. Keller, J. O'Muircheartaigh, C. Traynor, K. Towgood, G. J. Barker, and M. P. Richardson, Thalamotemporal impairment in temporal lobe epilepsy: a combined MRI analysis of structure, integrity, and connectivity. *Epilepsia*, 55(2), (2014) pages 306–15.

[102] J. F. Kerrigan, B. Litt, R. S. Fisher, S. Cranstoun, J. A. French, D. E. Blum, M. Dichter, A. Shetter, G. Baltuch, J. Jaggi, S. Krone, M. Brodie, M. Rise, and N. Graves, Electrical stimulation of the anterior nucleus of the thalamus for the treatment of intractable epilepsy. *Epilepsia*, 45(4), (2004) pages 346–354.

[103] M. Khatami, T. Schmidt-Wilcke, P. C. Sundgren, A. Abbasloo, B. Schölkopf, and T. Schultz, BundleMAP: Anatomically localized classification, regression, and hypothesis testing in diffusion MRI. *Pattern Recognition*, 63, (2017) pages 593–600.

[104] E. L. Kier, L. H. Staib, L. M. Davis, and R. A. Bronen, MR imaging of the temporal stem: Anatomic dissection tractography of the uncinate fasciculus, inferior occipitofrontal fasciculus, and Meyer's loop of the optic radiation. *American Journal of Neuroradiology*, 25(5), (2004) pages 677–691.

[105] M. Z. Koubeissi, E. Kahriman, T. U. Syed, J. Miller, and D. M. Durand, Low-frequency electrical stimulation of a fiber tract in temporal lobe epilepsy. *Annals of Neurology*, 74(2), (2013) pages 223–231.

[106] M. A. Kramer and S. S. Cash, Epilepsy as a disorder of cortical network organization. *Neuroscientist*, 18(4), (2012) pages 360–372.

[107] A. W. Laxton, D. F. Tang-Wai, M. P. McAndrews, D. Zumsteg, R. Wennberg, R. Keren, J. Wherrett, G. Naglie, C. Hamani, G. S. Smith, and A. M. Lozano, A phase i trial of deep brain stimulation of memory circuits in Alzheimer's disease. *Annals of Neurology*, 68(4), (2010) pages 521–534.

[108] D. Le Bihan, J. F. Mangin, C. Poupon, C. a. Clark, S. Pappata, N. Molko, and H. Chabriat, Diffusion tensor imaging: concepts and applications. *Journal of Magnetic Resonance Imaging*, 13(4), (2001) pages 534–546.

[109] D. J. Lee, M. Zwienenberg-Lee, M. Seyal, and K. Shahlaie, Intraoperative computed tomography for intracranial electrode implantation surgery in medically refractory epilepsy. *Journal of Neurosurgery*, pages 1–6.

[110] K. J. Lee, Y. M. Shon, and C. B. Cho, Long-term outcome of anterior thalamic nucleus stimulation for intractable epilepsy. *Stereotactic and Functional Neurosurgery*, 90(6), (2012) pages 379–385.

[111] A. Leemans and D. K. Jones, The B-matrix must be rotated when correcting for subject motion in DTI data. *Magnetic Resonance in Medicine*, 61(6), (2009) pages 1336–1349.

[112] C. Lenglet, R. Deriche, and O. Faugeras (2004). *Inferring White Matter Geometry from Diffusion Tensor MRI: Application to Connectivity Mapping*, pages 127–140. Springer Berlin Heidelberg, Berlin, Heidelberg. ISBN 978-3-540-24673-2.

[113] Y. Lilja, O. Gustafsson, M. Ljungberg, D. Nilsson, and G. Starck, Impact of region-of-interest method on quantitative analysis of DTI data in the optic tracts. *BMC Medical Imaging*, 16(1), (2016) page 42.

[114] Y. Lilja and D. T. Nilsson, Strengths and limitations of tractography methods to identify the optic radiation for epilepsy surgery. *Quantitative Imaging in Medicine and Surgery*, 5(2), (2015) pages 288–299.

[115] J. C. Lim, P. M. Phal, P. M. Desmond, A. D. Nichols, C. Kokkinos, H. V. Danesh-Meyer, A. H. Kaye, and B. A. Moffat, Probabilistic MRI tractography of the optic radiation using constrained spherical deconvolution: A feasibility study. *PLoS ONE*, 10(3), (2015) page e0118948.

[116] T. Lindeberg (1994). *Scale-Space Theory in Computer Vision*. The Kluwer International Series in Engineering and Computer Science. Dordrecht, The Netherlands. ISBN 978-1-4757-6465-9.

[117] T. Lipping, R. Ferenets, P. Puumala, K. Suominen, E. Karvonen, E. Sonkajarvi, S. Alahuhta, E. Heikkinen, T. Erola, G. Baer, and V. Jantti (2003). EEG independent component and coherence analysis from scalp and depth electrodes during propofol anesthesia. In *Engineering in Medicine and Biology Society, 2003. Proceedings of the 25th Annual International Conference of the IEEE*, volume 3, pages 2471–2474 Vol.3.

[118] Y. Liu, P.-F. D'Haese, A. T. Newton, and B. M. Dawant (2015). Thalamic nuclei segmentation in clinical 3T T1-weighted images using high-resolution 7T shape models.

[119] W. E. Lorensen and H. E. Cline, Marching cubes: A high resolution 3D surface construction algorithm. *Computer Graphics*, 21(4).

[120] A. M. Lozano, L. Fosdick, M. M. Chakravarty, J.-M. Leoutsakos, C. Munro, E. Oh, K. E. Drake, C. H. Lyman, P. B. Rosenberg, W. S. Anderson, D. F. Tang-Wai, J. C. Pendergrass, S. Salloway, W. F. Asaad, F. A. Ponce, A. Burke, M. Sabbagh, D. A. Wolk, G. Baltuch, M. S. Okun, K. D. Foote, M. P. McAndrews, P. Giacobbe, S. D. Targum, C. G. Lyketsos, and G. S. Smith, A phase ii study of fornix deep brain stimulation in mild alzheimer's disease. *Journal of Alzheimer's Disease*, 54(2), (2016) pages 777–787.

[121] S. Makeig, T.-P. Jung, A. J. Bell, D. Ghahremani, and T. J. Sejnowski, Blind separation of auditory event-related brain responses into independent components. *Proceedings of the National Academy of Sciences*, 94(20), (1997) pages 10979–10984.

[122] S. C. Mang, A. Busza, S. Reiterer, W. Grodd, Klose, and Uwe, Thalamus segmentation based on the local diffusion direction: a group study. *Magnetic Resonance in Medicine*, 67(1), (2012) pages 118–126.

[123] J. V. Manjon, J. Carbonell-Caballero, J. J. Lull, G. Garcia-Marti, L. Marti-Bonmati, and M. Robles, MRI denoising using non-local means. *Medical Image Analysis*, 12(4), (2008) pages 514–523.

[124] J. V. Manjon, P. Coupe, and A. Buades, MRI noise estimation and denoising using non-local PCA. *Medical Image Analysis*, 22(1), (2015) pages 35–47.

[125] E. Martínez-Heras, F. Varriano, V. Prčkovska, C. Laredo, M. Andorrà, E. H. Martínez-Lapiscina, A. Calvo, E. Lampert, P. Villoslada, A. Saiz, A. Prats-Galino, and S. Llufriu, Improved framework for tractography reconstruction of the optic radiation. *PLoS ONE*, 10(9), (2015) page e0137064.

[126] A. P. Mashtakov, A. A. Ardentov, and Y. L. Sachkov, Parallel Algorithm and Software for Image Inpainting via Sub-Riemannian Minimizers on the Group of Rototranslations. *Numerical Mathematics: Theory, Methods and Applications*, 6(01), (2013) pages 95–115.

[127] S. Meesters, P. Ossenblok, L. Wagner, O. Schijns, P. Boon, L. Florack, A. Vilanova, and R. Duits, Stability metrics for optic radiation tractography: Towards damage prediction after resective surgery. *Journal of Neuroscience Methods*, 288, (2017) pages 34–44.

[128] S. Meesters, G. Sanguinetti, E. Garyfallidis, J. Portegies, and R. Duits (2016). Fast implementations of contextual PDE's for HARDI data processing in DIPY (abstract). 16th Annual Meeting of the International Society for Magnetic Resonance in Medicine.

[129] S. Meesters, G. Sanguinetti, E. Garyfallidis, J. Portegies, P. Ossenblok, and R. Duits (2016). Cleaning output of tractography via fiber to bundle coherence, a new open source implementation (abstract). Human Brain Mapping.

[130] J. Mirebeau, Anisotropic fast-marching on cartesian grids using lattice basis reduction. *SIAM Journal on Numerical Analysis*, 52(4), (2014) pages 1573–1599.

[131] J.-M. Mirebeau, Efficient fast marching with Finsler metrics. *Numerische Mathematik*, 126(3), (2013) pages 515–557.

[132] H. Mitchell, T. Hamilton, F. Steggerda, and H. Bean, The chemical composition of the adult human body and its bearing on the biochemistry of growth. *Journal of Biological Chemistry*, 158, (1945) pages 625–637.

[133] R. Mohanraj and M. J. Brodie, Diagnosing refractory epilepsy: response to sequential treatment schedules. *European Journal of Neurology*, 13(3), (2006) pages 277–282.

[134] I. Moiseev and Y. L. Sachkov, Maxwell strata in sub-Riemannian problem on the group of motions of a plane. *ESAIM: Control, Optimisation and Calculus of Variations*, 16(02), (2010) pages 380–399.

[135] R. Montgomery (2002). *A Tour of Subriemannian Geometries, Their Geodesics, and Applications*. Mathematical surveys and monographs. American Mathematical Society. ISBN 9780821813911.

[136] J. G. Moore, S. A. Schorn, and J. Moore, Methods of classical mechanics applied to turbulence stresses in a tip leakage vortex. *Proceedings of the American Society of Mechanical Engineers*, (78828).

[137] S. Mori and M. Aggarwal, In vivo magnetic resonance imaging of the human limbic white matter. *Frontiers in Aging Neuroscience*, 6, (2014) page 321.

[138] S. Mori and J.-D. Tournier (2013). *Introduction to Diffusion Tensor Imaging*. Elsevier Science, 2nd edition. ISBN 978-0-12-398398-5.

[139] S. Mori and J. Zhang, Principles of diffusion tensor imaging and its applications to basic neuroscience research. *Neuron*, 51(5), (2006) pages 527–39.

[140] D. Mumford (1994). *Algebraic Geometry and Its Applications*, chapter Elastica and computer vision, pages 491–506. Springer-Verlag. ISBN 978-1-4612-2628-4.

[141] P. F. Neher, F. B. Laun, B. Stieltjes, and K. H. Maier-Hein, Fiberfox: facilitating the creation of realistic white matter software phantoms. *Magnetic Resonance in Medicine*, 72(5), (2014) pages 1460–1470.

[142] E. Niedermeyer and F. H. L. da Silva (2005). *Electroencephalography: Basic Principles, Clinical Applications, and Related Fields*. Lippincott Williams & Wilkins, 5th edition. ISBN 9780781751261.

[143] K. Niemann, V. R. Mennicken, D. Jeanmonod, and A. Morel, The Morel stereotactic atlas of the human thalamus: Atlas-to-MR registration of internally consistent canonical model. *NeuroImage*, 12(6), (2000) pages 601–616.

[144] D. Nilsson, G. Starck, M. Ljungberg, S. Ribbelin, L. Jönsson, K. Malmgren, and B. Rydenhag, Inter-subject variability in the anterior extent of the optic radiation assessed by tractography. *Epilepsy Research*, 77(1), (2007) pages 11–16.

[145] NIVEL Zorgregistraties (2016). NIVEL Zorgregistraties eerste lijn.

[146] R. D. Nowak, Wavelet-based Rician noise removal for magnetic resonance imaging. *IEEE Transactions of Image Processing*, 8(10), (1999) pages 1408–1419.

[147] M. Nowell, R. Rodionov, B. Diehl, T. Wehner, G. Zombori, J. Kinghorn, S. Ourselin, J. Duncan, A. Miserocchi, and A. McEvoy, A novel method for implementation of frameless stereo-EEG in epilepsy surgery. *Neurosurgery*, 10 Suppl 4, (2014) pages 525–533.

[148] M. Nowell, R. Rodionov, G. Zombori, R. Sparks, M. Rizzi, S. Ourselin, A. Miserocchi, A. McEvoy, and J. Duncan, A pipeline for 3D multimodality image integration and computer-assisted planning in epilepsy surgery. *Journal of Visualized Experiments*, (111), (2016) page 53450.

[149] M. Nowell, R. Sparks, G. Zombori, A. Miserocchi, R. Rodionov, B. Diehl, T. Wehner, G. Baio, G. Trevisi, M. Tisdall, S. Ourselin, A. W. McEvoy, and J. Duncan, Comparison of computer-assisted planning and manual planning for depth electrode implantations in epilepsy. *Journal of Neurosurgery*, 124(6), (2016) pages 1820–1828.

[150] L. O'Donnell, S. Haker, and C.-F. Westin (2002). *New Approaches to Estimation of White Matter Connectivity in Diffusion Tensor MRI: Elliptic PDEs and Geodesics in a Tensor-Warped Space*, pages 459–466. Springer Berlin Heidelberg, Berlin, Heidelberg. ISBN 978-3-540-45786-2.

[151] L. J. O'Donnell and C.-F. Westin, An introduction to diffusion tensor image analysis. *Neurosurgery clinics of North America*, 22(2), (2011) pages 185–viii.

[152] B. Øksendal (2003). *Stochastic Differential Equations*. Springer-Verlag, 6 edition. ISBN 978-3-642-14394-6.

[153] R. Oostenveld, P. Fries, E. Maris, and J.-M. Schoffelen, Fieldtrip: Open source software for advanced analysis of MEG, EEG, and invasive electrophysiological data. *Computational Intelligence and Neuroscience*, 2011, (2011) page 9.

[154] P. Ossenblok, J. C. de Munck, A. Colon, W. Drolsbach, and P. Boon, Magnetoencephalography is more successful for screening and localizing frontal lobe epilepsy than electroencephalography. *Epilepsia*, 48(11), (2007) pages 2139–2149.

[155] N. Otsu, A threshold selection method from gray-level histograms. *IEEE Transactions on Systems, Man and Cybernetics*, 9(1), (1979) pages 62–66.

[156] E. Ozarslan, C. G. Koay, T. M. Shepherd, M. E. Komlosh, M. O. Irfanoglu, C. Pierpaoli, and P. J. Basser, Mean apparent propagator (MAP) MRI: a novel diffusion imaging method for mapping tissue microstructure. *Neuroimage*, 78, (2013) pages 16–32.

[157] E. Ozarslan, T. M. Shepherd, B. C. Vemuri, S. J. Blackband, and T. H. Mareci, Resolution of complex tissue microarchitecture using the diffusion orientation transform (DOT). *Neuroimage*, 31(3), (2006) pages 1086–1103.

[158] D. Padfield and J. Miller, A label geometry image filter for multiple object measurement. *The Insight Journal, July-December*.

[159] G. J. M. Parker, H. A. Haroon, and C. A. M. Wheeler-Kingshott, A framework for a streamline-based probabilistic index of connectivity (PICo) using a structural interpretation of MRI diffusion measurements. *Journal of Magnetic Resonance Imaging*, 18(2), (2003) pages 242–254.

[160] G. A. Pavliotis and G. A. Pavliotis (2014). *The Fokker–Planck Equation*, pages 87–137. Springer New York, New York, NY. ISBN 978-1-4939-1323-7.

[161] M. Pechaud, M. Descoteaux, and R. Keriven, Brain connectivity using geodesics in HARDI. *Medical Image Computing and Computer-Assisted Intervention*, 12(Pt 2), (2009) pages 482–489.

[162] J. Peltier, N. Travers, C. Destrieux, and S. Velut, Optic radiations: a microsurgical anatomical study. *Journal of Neurosurgery*, 105(2), (2006) pages 294–300.

[163] P. Perona and J. Malik, Scale-space and edge detection using anisotropic diffusion. *IEEE Transactions on Pattern Analysis and Machine Intelligence*, 12(7), (1990) pages 629–639.

[164] F. Pestilli, J. D. Yeatman, A. Rokem, K. N. Kay, and B. A. Wandell, Evaluation and statistical inference for human connectomes. *Nature Methods*, 11(10), (2014) pages 1058–1063.

[165] J. Petitot, The neurogeometry of pinwheels as a sub-Riemannian contact structure. *Journal of Physiology-Paris*, 97(2–3), (2003) pages 265–309.

[166] J. Pijn and F. Lopes da Silva (1993). *Propagation of Electrical Activity: Nonlinear Associations and Time Delays between EEG Signals*, pages 41–61. Birkhäuser Boston.

[167] S. C. Ponten, F. Bartolomei, and C. J. Stam, Small-world networks and epilepsy: graph theoretical analysis of intracerebrally recorded mesial temporal lobe seizures. *Clinical Neurophysiology*, 118(4), (2007) pages 918–927.

[168] J. Portegies and R. Duits, New exact and numerical solutions of the (convection-)diffusion kernels on SE(3). *Differential Geometry and Applications*, 53, (2017) pages 182–219.

[169] J. Portegies, G. Sanguinetti, S. Meesters, and R. Duits (2015). New Approximation of a Scale Space Kernel on SE(3) and Applications in Neuroimaging. Fifth International Conference on Scale Space and Variational Methods in Computer Vision.

[170] J. M. Portegies, R. H. J. Fick, G. R. Sanguinetti, S. P. L. Meesters, G. Girard, and R. Duits, Improving fiber alignment in HARDI by combining contextual PDE flow with constrained spherical deconvolution. *PLoS ONE*, 10(10), (2015) pages 1–33.

[171] V. Prčkovska, M. Andorrà, P. Villoslada, E. Martinez-Heras, R. Duits, D. Fortin, P. Rodrigues, and M. Descoteaux (2015). Contextual diffusion image post-processing aids clinical applications. In *Visualization and Processing of Higher Order Descriptors for Multi-Valued Data*, pages 353–377. Springer, Cham. ISBN 978-3-319-15089-5.

[172] W. Press, S. Teukolsky, W. Vetterling, and B. Flannery (2007). Spherical harmonics. In *Numerical Recipes: The Art of Scientific Computing*. Cambridge University Press, 3rd edition. ISBN 978-0-521-88068-8.

[173] K. P. Pruessmann, M. Weiger, M. B. Scheidegger, and P. Boesiger, SENSE: sensitivity encoding for fast MRI. *Magnetic Resonance in Medicine*, 42(5), (1999) pages 952–962.

[174] W. Qiu, C. Yu, Y. Gao, A. Miao, L. Tang, S. Huang, W. Jiang, J. Sun, J. Xiang, and X. Wang, Disrupted topological organization of structural brain networks in childhood absence epilepsy. *Scientific Reports*, 7(1), (2017) page 11973.

[175] J. A. Reeds and L. A. Shepp, Optimal paths for a car that goes both forwards and backwards. *Pacific Journal of Mathematics*, 145(2), (1990) pages 367–393.

[176] L. Rittner, R. Lotufo, J. Campbell, and G. Pike (2010). Segmentation of thalamic nuclei based on tensorial morphological gradient of diffusion tensor fields. In *Biomedical Imaging: From Nano to Macro, 2010 IEEE International Symposium on*, pages 1173–1176.

[177] R. T. Rockafellar and R. J.-B. Wets (2005). *Variational Analysis*, page 117. Springer-Verlag. ISBN 978-3-642-02431-3.

[178] P. Rodrigues, R. Duits, B. M. t. H. Romeny, and A. Vilanova (2010). Accelerated diffusion operators for enhancing DW-MRI. In D. Bartz, C. Botha, J. Hornegger, R. Machiraju, A. Wiebel, and B. Preim, editors, *Eurographics Workshop on Visual Computing for Biology and Medicine*. The Eurographics Association. ISBN 978-3-905674-28-6.

[179] T. Roine, B. Jeurissen, D. Perrone, J. Aelterman, W. Philips, A. Leemans, and J. Sijbers, Informed constrained spherical deconvolution (iCSD). *Medical Image Analysis*, 24(1), (2015) pages 269–281.

[180] A. Rokem, J. D. Yeatman, F. Pestilli, K. N. Kay, A. Mezer, S. van der Walt, and B. A. Wandell, Evaluating the accuracy of diffusion MRI models in white matter. *PLoS ONE*, 10(4), (2015) pages 1–26.

[181] P. A. Rubino, A. L. Rhoton, X. Tong, and E. de Oliveira, Three-dimensional relationships of the optic radiation. *Neurosurgery*, 57(Supplement 4), (2005) pages 219–227.

[182] Y. L. Sachkov, Cut locus and optimal synthesis in the sub-Riemannian problem on the group of motions of a plane. *ESAIM: Control, Optimisation and Calculus of Variations*, 17(2), (2011) pages 293–321.

[183] S. Sanei and J. A. Chambers (2007). *EEG Signal Processing*. Wiley. ISBN 978-0-470-02581-9.

[184] G. Sanguinetti, E. Bekkers, R. Duits, M. Janssen, Mashtakov, and J. Mirebeau (2015). Sub-riemannian fast marching on se(2). In *CVPR*, volume 9423 of *LNCS*, pages 366–374. Springer International Publishing. ISBN 978-3-319-25751-8.

[185] Y. Sato, S. Nakajima, H. Atsumi, T. Koller, G. Gerig, S. Yoshida, and R. Kikinis (1997). *3D multi-scale line filter for segmentation and visualization of curvilinear structures in medical images*, volume 1205, pages 213–222. Springer Berlin Heidelberg. ISBN 978-3-540-62734-0.

[186] P. H. Schimpf, C. Ramon, and J. Haueisen, Dipole models for the EEG and MEG. *IEEE Transactions on Biomedical Engineering*, 49(5), (2002) pages 409–418.

[187] W. Schroeder, K. Martin, and B. Lorensen (2006). *The Visualization Toolkit–An Object-Oriented Approach To 3D Graphics*. Kitware, Inc., 4th edition. ISBN 978-1930934191.

[188] T. Schultz, Segmenting thalamic nuclei: What can we gain from HARDI? *Medical Image Computing and Computer-Assisted Intervention*, 14 (Pt. 2), (2011) pages 141–148.

[189] T. Schultz, A. Fuster, A. Ghosh, R. Deriche, L. Florack, and L.-H. Lim (2013). Higher-order tensors in diffusion imaging. In B. Burgeth, A. Vilanova, and C.-F. Westin, editors, *Visualization and Processing of Tensors and Higher Order Descriptors for Multi-Valued Data*. Springer. ISBN 978-3-662-51257-9.

[190] N. Sepasian (2011). *Multi-Valued Geodesic Tractography for Diffusion Weghted Imaging*. Ph.D. thesis, Eindhoven University of Technology, Dep. of Biomedical Engineering.

[191] J. A. Sethian (1999). *Level Set Methods and Fast Marching Methods: Evolving Interfaces in Computational Geometry, Fluid Mechanics, Computer Vision, and Materials Science ... on Applied and Computational Mathematics)*. Cambridge University Press, Cambridge, U.K. ; New York, 2 edition edition. ISBN 978-0-521-64557-7.

[192] Y. Shen and Z. Shen (2016). *Introduction to Modern Finsler Geometry*. Higher Education Press, 1st edition. ISBN 9789814704908.

[193] A. Sherbondy, R. Dougherty, M. Ben-Shachar, S. Napel, and B. Wandell, ConTrack: finding the most likely pathways between brain regions using diffusion tractography. *Journal of Vision*, 8(9), (2008) pages 15.1–16.

[194] A. J. Sherbondy, R. F. Dougherty, and B. A. Wandell, Identifying the human optic radiation using diffusion imaging and fiber tractography. *Journal of Vision*, 8(10), (2008) pages 12.1–11.

[195] E. H. Sincoff, Y. Tan, and S. I. Abdulrauf, White matter fiber dissection of the optic radiations of the temporal lobe and implications for surgical approaches to the temporal horn. *Journal of Neurosurgery*, 101(5), (2004) pages 739–46.

[196] S. J. M. Smith, EEG in the diagnosis, classification, and management of patients with epilepsy. *Journal of Neurology, Neurosurgery & Psychiatry*, 76(suppl 2), (2005) pages ii2–ii7.

[197] S. M. Smith, Fast robust automated brain extraction. *Human Brain Mapping*, 17(3), (2002) pages 143–55.

[198] S. M. Smith, M. Jenkinson, M. W. Woolrich, C. F. Beckmann, T. E. J. Behrens, H. Johansen-Berg, P. R. Bannister, M. De Luca, I. Drobnjak, D. E. Flitney, R. K. Niazy, J. Saunders, J. Vickers, Y. Zhang, N. De Stefano, J. M. Brady, and P. M. Matthews, Advances in functional and structural MR image analysis and implementation as FSL. *NeuroImage*, 23 Suppl 1, (2004) pages S208–19.

[199] M. Sprengers, K. Vonck, E. Carrette, A. G. Marson, and P. Boon, Deep brain and cortical stimulation for epilepsy. *Cochrane Database of Systematic Reviews*, (6), (2014) page CD008497.

[200] H. Stefan and F. H. Lopes da Silva, Epileptic neuronal networks: methods of identification and clinical relevance. *Frontiers in Neurology*, 4, (2013) page 8.

[201] G. Stefani, U. Boscain, J. Gauthier, A. Sarychev, and M. Sigalotti (2014). *Geometric Control Theory and sub-Riemannian Geometry*. Springer INdAM Series.

[202] E. Stejskal and J. Tanner, Spin diffusion measurement: spin echoes in the presence of a time-dependent field gradient. *Journal of Chemical Physics*, 42, (1965) pages 288–292.

[203] J. Talairach, P. Tournoux, A. Musolino, and O. Missir, Stereotaxic exploration in frontal epilepsy. *Advances in Neurology*, 57, (1992) pages 651–88.

[204] N. Tanaka, M. S. Hamalainen, S. P. Ahlfors, H. Liu, J. R. Madsen, B. F. Bourgeois, J. W. Lee, B. A. Dworetzky, J. W. Belliveau, and S. M. Stufflebeam, Propagation of epileptic spikes reconstructed from spatiotemporal magnetoencephalographic and electroencephalographic source analysis. *Neuroimage*, 50(1), (2010) pages 217–222.

[205] T. Taoka, M. Sakamoto, S. Iwasaki, H. Nakagawa, A. Fukusumi, S. Hirohashi, K. Taoka, K. Kichikawa, T. Hoshida, and T. Sakaki, Diffusion tensor imaging in cases with visual field defect after anterior temporal lobectomy. *American Journal of Neuroradiology*, 26(4), (2005) pages 797–803.

[206] W. O. Tatum (2014). *Handbook of EEG Interpretation*. Demos Medical, 2nd edition. ISBN 978-1-933864-11-2.

[207] H. F. Tibbals (2010). *Medical Nanotechnology and Nanomedicine*. CRC Press. ISBN 9781439808740.

[208] R. Tibshirani, G. Walther, and T. Hastie, Estimating the number of clusters in a data set via the gap statistic. *Journal of the Royal Statistical Society: Series B (Statistical Methodology)*, 63(2), (2001) pages 411–423.

[209] J.-D. Tournier, F. Calamante, and A. Connelly, Robust determination of the fibre orientation distribution in diffusion MRI: non-negativity constrained super-resolved spherical deconvolution. *NeuroImage*, 35(4), (2007) pages 1459–1472.

[210] J.-D. Tournier, F. Calamante, and A. Connelly, MRtrix: Diffusion tractography in crossing fiber regions. *International Journal of Imaging Systems and Technology*, 22(1), (2012) pages 53–66.

[211] J.-D. Tournier, F. Calamante, D. G. Gadian, and A. Connelly, Direct estimation of the fiber orientation density function from diffusion-weighted MRI data using spherical deconvolution. *NeuroImage*, 23(3), (2004) pages 1176–1185.

[212] J.-D. Tournier, C.-H. Yeh, F. Calamante, K.-H. Cho, A. Connelly, and C.-P. Lin, Resolving crossing fibres using constrained spherical deconvolution: validation using diffusion-weighted imaging phantom data. *NeuroImage*, 42(2), (2008) pages 617–625.

[213] J. N. Tsitsiklis, Efficient algorithms for globally optimal trajectories. *IEEE Transactions on Automatic Control*, 40(9), (1995) pages 1528–1538.

[214] D. S. Tuch, Q-ball imaging. *Magnetic Resonance in Medicine*, 52(6), (2004) pages 1358–1372.

[215] D. S. Tuch, T. G. Reese, M. R. Wiegell, N. Makris, J. W. Belliveau, and V. J. Wedeen, High angular resolution diffusion imaging reveals intravoxel white matter fiber heterogeneity. *Magnetic Resonance in Medicine*, 48(4), (2002) pages 577–582.

[216] M. J. Vaessen, J. F. A. Jansen, H. M. H. Braakman, P. A. M. Hofman, A. De Louw, A. P. Aldenkamp, and W. H. Backes, Functional and structural network impairment in childhood frontal lobe epilepsy. *PLOS ONE*, 9(3), (2014) pages 1–10.

[217] V. N. Vakharia, R. Sparks, A. G. O'Keeffe, R. Rodionov, A. Miserocchi, A. McEvoy, S. Ourselin, and J. Duncan, Accuracy of intracranial electrode placement for stereoencephalography: A systematic review and meta-analysis. *Epilepsia*, 58(6), (2017) pages 921–932.

[218] A. Valentin, E. Garcia Navarrete, R. Chelvarajah, C. Torres, M. Navas, L. Vico, N. Torres, J. Pastor, R. Selway, R. G. Sola, and G. Alarcon, Deep brain stimulation of the centromedian thalamic nucleus for the treatment of generalized and frontal epilepsies. *Epilepsia*, 54(10), (2013) pages 1823–1833.

[219] E. van Diessen, S. J. H. Diederen, K. P. J. Braun, F. E. Jansen, and C. J. Stam, Functional and structural brain networks in epilepsy: what have we learned? *Epilepsia*, 54(11), (2013) pages 1855–65.

[220] P. J. van Houdt, J. C. de Munck, F. S. Leijten, G. J. Huiskamp, A. J. Colon, P. A. Boon, and P. P. Ossenblok, EEG-fMRI correlation patterns in the presurgical evaluation of focal epilepsy: A comparison with electrocorticographic data and surgical outcome measures. *NeuroImage*, 75(238-248).

[221] P. J. van Houdt, P. P. W. Ossenblok, A. J. Colon, P. A. J. M. Boon, and J. C. de Munck, A framework to integrate EEG-correlated fMRI and intracerebral recordings. *Neuroimage*, 60(4), (2012) pages 2042–53.

[222] B. D. van Rooijen, W. H. Backes, O. E. M. G. Schijns, A. Colon, and P. A. M. Hofman, Brain imaging in chronic epilepsy patients after depth electrode (stereoelectroencephalography) implantation: magnetic resonance imaging or computed tomography? *Neurosurgery*, 73(3), (2013) pages 543–9.

[223] D. Van 't Ent, I. Manshanden, P. Ossenblok, D. N. Velis, J. C. de Munck, J. P. A. Verbunt, and F. H. Lopes da Silva, Spike cluster analysis in neocortical localization related epilepsy yields clinically significant equivalent source localization results in magnetoencephalogram (MEG). *Clinical Neurophysiology*, 114(10), (2003) pages 1948–1962.

[224] T. Vaughan, L. DelaBarre, C. Snyder, J. Tian, C. Akgun, D. Shrivastava, W. Liu, C. Olson, G. Adriany, J. Strupp, P. Andersen, A. Gopinath, P.-F. van de Moortele, M. Garwood, and K. Ugurbil, 9.4T human MRI: Preliminary results. *Magnetic Resonance in Medicine*, 56(6), (2006) pages 1274–1282.

[225] M. T. Vlaardingerbroek and J. A. Boer (2003). *Magnetic Resonance Imaging*. Springer, 3rd edition. ISBN 978-3-662-05252-5.

[226] S. Wakana, A. Caprihan, M. M. Panzenboeck, J. H. Fallon, M. Perry, R. L. Gollub, K. Hua, J. Zhang, H. Jiang, P. Dubey, A. Blitz, P. van Zijl, and S. Mori, Reproducibility of quantitative tractography methods applied to cerebral white matter. *NeuroImage*, 36(3), (2007) pages 630–644.

[227] J. H. Ward, Hierarchical grouping to optimize an objective function. *Journal of the American Statistical Association*, 58(301), (1963) pages 236–244.

[228] S. K. Warfield, S. J. Haker, I.-F. Talos, C. A. Kemper, N. Weisenfeld, A. U. J. Mewes, D. Goldberg-Zimring, K. H. Zou, C.-F. Westin, W. M. Wells, C. M. C. Tempany, A. Golby, P. M. Black, F. A. Jolesz, and R. Kikinis, Capturing intraoperative deformations: research experience at brigham and women's hospital. *Medical Image Analysis*, 9(2), (2005) pages 145–162.

[229] F. Wendling and F. Bartolomei, Modeling EEG signals and interpreting measures of relationship during temporal-lobe seizures: an approach to the study of epileptogenic networks. *Epileptic disorders : international epilepsy journal with videotape*, Special Issue, (2001) pages 67–78.

[230] F. Wendling, F. Bartolomei, J. J. Bellanger, and P. Chauvel, Interpretation of interdependencies in epileptic signals using a macroscopic physiological model of the EEG. *Clinical Neurophysiology*, 112(7), (2001) pages 1201–18.

[231] F. Wendling, F. Bartolomei, and L. Senhadji, Spatial analysis of intracerebral electroencephalographic signals in the time and frequency domain: identification of epileptogenic networks in partial epilepsy. *Philosophical Transactions. Series A, Mathematical, Physical, and Engineering Sciences*, 367(1887), (2009) pages 297–316.

[232] what-when how.com (2017). The limbic system (http://what-when-how.com/neuroscience/the-limbic-system-integrative-systems-part-2/).

[233] S. Wiebe, W. T. Blume, J. P. Girvin, and M. Eliasziw, A randomized, controlled trial of surgery for temporal lobe epilepsy. *The New England Journal of Medicine*, 345(5), (2001) pages 311–318.

[234] M. R. Wiegell, D. S. Tuch, H. B. W. Larsson, and V. J. Wedeen, Automatic segmentation of thalamic nuclei from diffusion tensor magnetic resonance imaging. *Neuroimage*, 19(2 Pt 1), (2003) pages 391–401.

[235] B. Wilkins, N. Lee, N. Gajawelli, M. Law, and N. Lepore, Fiber estimation and tractography in diffusion MRI: development of simulated brain images and comparison of multi-fiber analysis methods at clinical b-values. *Neuroimage*, 109, (2015) pages 341–356.

[236] G. P. Winston, P. Daga, J. Stretton, M. Modat, M. R. Symms, A. W. McEvoy, S. Ourselin, and J. S. Duncan, Optic radiation tractography and vision in anterior temporal lobe resection. *Annals of Neurology*, 71(3), (2012) pages 334–341.

[237] G. P. Winston, L. Mancini, J. Stretton, J. Ashmore, M. R. Symms, J. S. Duncan, and T. A. Yousry, Diffusion tensor imaging tractography of the optic radiation for epilepsy surgical planning: A comparison of two methods. *Epilepsy Research*, 97(1-2), (2011) pages 124–132.

[238] T. Yamamoto, K. Yamada, T. Nishimura, and S. Kinoshita, Tractography to depict three layers of visual field trajectories to the calcarine gyri. *American journal of ophthalmology*, 140(5), (2005) pages 781–785.

[239] C. Yang, Q. Wang, W. Wu, Y. Xue, W. Lu, and S. Wu, Thalamic segmentation based on improved fuzzy connectedness in structural mri. *Computers in Biology and Medicine*, 66, (2015) pages 222–234.

[240] J. D. Yeatman, R. F. Dougherty, N. J. Myall, B. A. Wandell, and H. M. Feldman, Tract profiles of white matter properties: Automating fiber-tract quantification. *PLoS ONE*, 7(11), (2012) pages 1–15.

[241] D. Yekutieli and Y. Benjamini, Resampling-based false discovery rate controlling multiple test procedures for correlated test statistics. *Journal of Statistical Planning and Inference*, 82(1–2), (1999) pages 171–196.

[242] M. Yogarajah, N. K. Focke, S. Bonelli, M. Cercignani, J. Acheson, G. J. M. Parker, D. C. Alexander, a. W. McEvoy, M. R. Symms, M. J. Koepp, and J. S. Duncan, Defining Meyer's loop-temporal lobe resections, visual field deficits and diffusion tensor tractography. *Brain*, 132(6), (2009) pages 1656–1668.

[243] T. S. Yoo, M. J. Ackerman, W. E. Lorensen, W. Schroeder, V. Chalana, S. Aylward, D. Metaxas, and R. Whitaker, Engineering and algorithm design for an image processing Api: a technical report on ITK–the Insight Toolkit. *Studies in Health Technology and Informatics*, 85, (2002) pages 586–92.

[244] P. A. Yushkevich, J. Piven, H. Cody Hazlett, R. Gimpel Smith, S. Ho, J. C. Gee, and G. Gerig, User-guided 3D active contour segmentation of anatomical structures: Significantly improved efficiency and reliability. *Neuroimage*, 31(3), (2006) pages 1116–1128.

[245] U. Ziyan, D. Tuch, and C.-F. Westin, Segmentation of thalamic nuclei from DTI using spectral clustering. *Medical Image Computing and Computer-Assisted Intervention*, 9(Pt 2), (2006) pages 807–814.

[246] M. Zucchelli, L. Brusini, C. A. Méndez, and G. Menegaz (2016). *Multi-Tensor MAPMRI: How to Estimate Microstructural Information from Crossing Fibers*, pages 65–74. Springer International Publishing, Cham. ISBN 978-3-319-28588-7.